The Flow in the Surf Zone
A Fully Nonlinear Boussinesq Model for Breaking Waves

by

Rosaria Ester Musumeci, Ib A. Svendsen and Enrico Foti

RESEARCH REPORT NO. CACR-03-05
May, 2003

Center for Applied Coastal Research
Ocean Engineering Laboratory
University of Delaware
Newark, DE 19716

Abstract

A fully nonlinear Boussinesq model for breaking waves is developed. The model is derived from the Reynolds equations by assuming that the motion of the breaking waves is rotational. The vorticity generated by the breaking is determined by solution of the vorticity equation in addition to the Boussinesq equations for the full motion. The model is an extension of the weakly nonlinear model developed by Veeramony and Svendsen (2000) and the fully nonlinear model by Veeramony and Svendsen (1999).

It was found that in the solution of those models, the accuracy of the vertical part of the velocity field was limited by the overall numerical grid being too coarse to resolve the rapid variations in the motion in the neighborhood of the turbulent front of the breaking wave. This results in substantial underestimation of the breaking terms and thereby the energy dissipation in the Boussinesq equations. The latter leads to inaccurate prediction of the wave height decay in the surf zone.

To improve the accuracy of this important detail, a self-adaptive, time-varying sub grid has been implemented in the roller region of the waves. The sub grid moves with the roller and is further refined at the toe where the most rapid variations occur in the relevant variables. The computation of the time derivatives was carefully addressed.

The model results have been compared with laboratory data for both regular waves published by Hansen and Svendsen (1979) (wave heights and selected surface profile only), by Cox *et al.* (1995), and for irregular waves in the form of wave groups by Svendsen and Veeramony (2001). The latter data set included information about time and space varying break points similar to what occurs in random waves.

The two data sets by Hansen and Svendsen (1979) and by Svendsen and Veeramony (2001) mainly contained high density information about the wave height variation which allowed a detailed assessment of wave height decay and hence the accuracy of the breaking terms and the energy dissipation. The data set by Cox *et al.* (1995) made testing of the velocity fields possible. The analysis of the comparisons with experimental data showed that the self-

adaptive, time-varying grid approach allow better prediction of the effect of breaking, particularly the wave height decrease and the changes of the surface profile within the surf zone. Moreover, the comparisons with the very detailed data from Hansen and Svendsen (1979) showed that the model is able to predict quite accurately the flow conditions, both in the shoaling region and inside the surf zone, supporting also the choice of the depth averaged velocity as reference velocity for the Boussinesq model. A comparison with plunging breaker data was also performed using the last dataset in Hansen and Svendsen (1979). The results obtained were quite reasonable, even though, in principle, this kind of breaking cannot be handled by a Boussinesq model.

Another critical point in the use of Boussinesq-type equations to model the flow inside the surf zone is the choice of an appropriate breaking criterion, since the equations by themselves are not able to decide where and when a wave reaches the breaking conditions. The model developed here uses a criterion based on the critical steepness of the wave front (Schäffer *et al.*, 1993). However, the tests performed in the regular wave case showed that the well known and widely accepted breaking criterion, stating that a wave starts to break if the surface velocity is bigger than the wave speed, is satisfied by the model results, even though the breaking criterion adopted is a different one, thus supporting the realistic behavior of the model.

The results about the velocity profiles induced some considerations on the effects and the limits of assuming the eddy viscosity constant over depth. In order to show how the variation of the value chosen for this parameter influences the results, a sensitivity analysis has been carried out, suggesting that the use of an eddy viscosity profile varying over depth would be more suitable.

Finally, the quite good comparisons with the measurements of wave height and surface profile in the case of groupy waves (Svendsen and Veeramony, 2001) also demonstrated that the model is able to recover the moving breaking line, a characteristic of irregular waves, and the effects of the breaking process on the groupiness of the waves.

Contents

Chapter 1

Introduction

1.1 Context and practical relevance

The coastal areas have always had a strategic role in the history of mankind. Indeed, human civilization has had, and has also nowadays, a dual conflictual perception of living close to the sea. Mostly, it tried to take advantage of the enormous resources offered by the littoral regions, connected to the possibility of communications and exchanges. The glorious history of the Italian Marine Republics represents just one of the countless examples of this kind of wealthy development. On the other hand, due to the exposure both to the risk of flooding and to military attacks, the protection of the coasts has always represented one of the major problem to be solved.

In particular, in the last century the human pressure on coastal areas has grown dramatically and at present the majority of the world's population lives along a narrow strip of land close to the sea. Let's just think about the very different situations, from a geographic viewpoint, of Italy and the United States. The former is a narrow peninsula in the Mediterranean Sea, where the majority of the population is forced to live along the coastlines, since the continental part is mainly occupied by mountains, and the insularity index (defined as the ratio of shoreline length to the circumference of the circle equivalent continental area) is pretty high, being nearly equal to 4 (Franco, 1996). The latter is a much larger continental "peninsula" located between two oceans, but also in this case the population is concentrated along the coasts, giving raise to the chains of megapolis, typical of both the Atlantic and Pacific regions.

In this context, both the scientific and the engineering communities have always looked with a great interest at the hydrodynamic and morphodynamic problems generated by the sea motion and its interactions with natural and anthropic elements located in the nearshore region. Nowadays, topics as different as environmental control, survey and planning, water pollution, economics and management of the coastal regions require advanced tools in order to analyze the evolution of the littoral zones or to investigate effectiveness and the consequences of changes in

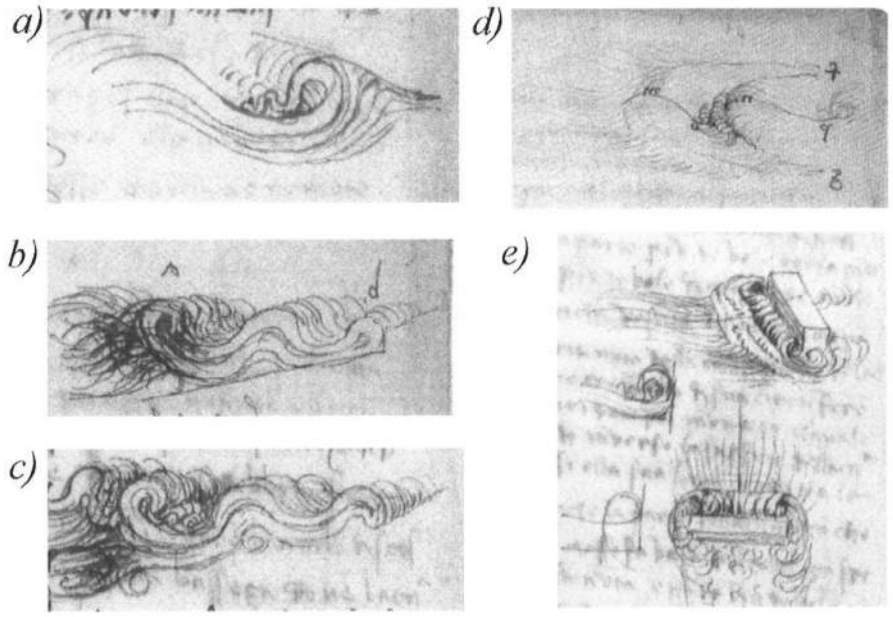

Figure 1.1: Illustrations of wave breaking from the Codex Leicester of Leonardo, *a*) folio 4 v., *b*) folio 26 v., *c*) folio 26 v., *d*) folio 4 v., *e*) folio 25 v.

those areas.

It is maybe superfluous pointing out that the hydrodynamics represents the forcing of any phenomena taking place in the littoral areas, but in particular in the nearshore region it is the wave breaking which plays a key-role in all the marine physical process.

Wave breaking is perhaps one of the most fascinating natural hydrodynamic phenomena, as it can be witnessed by the wide artistic production on this topic (drawings, pictures, poems, etc.), by the attraction exerted on sportsmen, such as surf lovers, or simply on beachgoers.

However, wave breaking is more than this and its importance was understood since the ancient ages. One of the most admirable examples of this interest is represented by the comments and the drawings of Leonardo, who, in Codex Leicester, tried to give a description and a physical explanation of the flow in the surf zone, of the structure of the flow field under breaking waves of its impact on structures, very similar to our modern breakwaters (see Figure 1.1). Leonardo's observations and drawings, where the vortical motion of the flow within the surf zone is detected as one of the most characteristic features, are astonishingly close to what the modern experiments have found out by using advanced measurements techniques, such as Particle Image Velocimetry.

Moreover, from the engineering point of view, wave breaking represents a nat-

ural phenomenon, whose understanding is crucial in order to manage the coastal zone, and particularly to appropriately design coastal structures aimed both to protect and to exploit littoral areas.

The present thesis must be framed in this context, the flow in the nearshore region and particularly inside the surf zone is approached and a contribution to the modelling of wave breaking is attempted through a numerical approach.

1.2 Aim of the study

Wave breaking influences large scale coastal phenomena, however an accurate description of the flow field of a breaking wave, although crucial for the overall understanding of the nearshore hydrodynamics, is still far to be attained. For this reason in the last decades a lot of engineering studies were aimed at analyzing these phenomena, mainly through developing numerical models of such complex processes, which have to satisfy two requirements: to perform an accurate description of the flow and to be able to handle a large scale domain (i.e. significant from an engineering viewpoint).

In particular, in this framework, the derivation and the application of Boussinesq type of models have been largely investigated and developed. The attention devoted to this type of models is essentially due to the fact that their use is suitable to accurately describe the flow and also since they are computationally more economic, with respect to more complicate approaches, like the Computational Fluid Dynamics (CFD), which attempts a three dimensional modelling of the fluid motion. Indeed, as opposed to the simplistic approach of the nonlinear shallow water equations, the Boussinesq models allow to extract information about the vertical structure of the fluid motion, even though the equations are integrated over the water columns. This last point, that is the use of depth averaged equations, allows to reduce the number of independent variables, thus increasing the computational efficiency of this kind of models. With respect to the problem of the surf zone modelling, however, the approaches adopted have been often simplistic, aiming only to model the macroscopic effects of wave breaking.

The aim of this work is to contribute to enhance the modelling capabilities of Boussinesq models within the surf zone, in order to perform better predictions, on a more physical basis, of the effects of wave breaking on the nearshore hydrodynamics and, in turn, on littoral processes. The need for such a type of studies it is even more impelling due to the lack of physical basis of most of the previous approaches and to the demand of extremely accurate large scale models, in order to be able to face many coastal engineering problems.

1.3 Research methodology

A numerical investigation was performed in order to analyze the flow inside the surf zone, through developing a Boussinesq model able to describe the propagation of breaking waves, and, in turn the flow field generated in these conditions. The

weakly nonlinear model by Veeramony and Svendsen (2000) and the fully nonlinear model of Veeramony and Svendsen (1999) were retained as starting points of the model developed in the context of this thesis. The aforementioned approaches seemed more suitable with respect to others proposed in literature, since the hypothesis of irrotationality of the flow is removed. This step is considered crucial from a physical viewpoint since the flow within the surf zone is characterized by a huge amount of vorticity introduced by the breaking.

The rotational approach used in this work forces the adoption of an additional equation to solve the problem; indeed the vorticity equation has to be solved as well. Here an analytical solution to the vorticity transport equation has been carried out by using the perturbation methods, under the assumption of eddy viscosity constant over depth.

The hydraulic similarity between the surface roller on the front of a breaking wave, characterized by strong turbulence and presence of a huge amount of air bubbles, and the recirculating region typical of hydraulic jumps have been here considered in order to specify a source of vorticity for the flow field, by using the experimental analysis on the hydraulic jump peformed by Svendsen *et al.* (2000).

To give a more accurate description of the roller region, responsible of the input of vorticity inside the domain, an original algorithm has been implemented, which changes the uniform fixed grid previously adopted to discretize the domain into a self adaptive time varying grid, more refined corresponding to the roller region.

The performances of such a model have been tested, by comparing the results both with the numerical results obtained using the same model on a uniform fixed grid and with laboratory literature data. In particular the first kind of comparisons were performed in order to verify that the changes introduced gave the desired effects of increasing the breaking generated dissipation within the surf zone, the second ones to test the real effectiveness of the new approach.

Since theoretically the model should be able to handle the casea of both regular and irregular waves, the model results have been compared with the measurements of Hansen and Svendsen (1979), Cox *et al.* (1995) and Svendsen and Veeramony (2001), where the last one refers to the breaking of wave groups.

The time series of the surface profiles, the spatial wave height distribution, the vertical velocity profiles, the undertow profile, the variation of the mean water level and the variation of the position of the breaking point have been analyzed.

The behavior of the model was also tested for different breaking criteria, to verify the realistic prediction of the breaking point.

Finally, a sensitivity analysis of the effects of using different values of eddy viscosity have been carried out, to test the physical validity of the adopted assumption of an eddy viscosity constant over depth.

1.4 Main limits

The main limits of this work are essentially related to the hypothesis used to derive the governing equations of the model.

Since the model is a 1D Boussinesq model, it is of course not able to represent the 2D horizontal hydrodynamics which are related to nearshore circulation processes. Moreover, since the formulation of the problem is done in terms of the stream function, which by definition is a 2D variable (on the vertical plane), the extension to the 2D horizontal case is not a trivial task and it would require complex and computationally intensive procedures, such as the tracking of the wave rays at every point of the domain.

Moreover, the analytical solution of the vorticity transport equation has been derived by assuming a constant eddy viscosity over the water column. Laboratory measurements (Cox *et al.*, 1995; Svendsen *et al.*, 2000) have shown that the real structure of the turbulence under breaking waves is far from being constant over depth, since the turbulence is much higher close to the surface then at the bottom. Moreover a detailed analysis of the numerical results obtained in this study, showed that the model is extremely sensitive to the chosen value of eddy viscosity and that it would be more suitable to adopt a variable profile over the vertical coordinate.

1.5 Outline of the thesis

The aim of this study is to contribute to improve the modelling of breaking waves within the surf zone. As first part of the work, the fully nonlinear Boussinesq model of Veeramony and Svendsen (1999) has been derived anew and the numerical code has been carefully debugged. Therefore, in order to get a more realistic modelling of the breaking terms, a self adaptive time varying grid methodology has been purposely developed and verified against literature laboratory data on regular and irregular breaking waves.

In Chapter 2 a brief overview of the complex hydrodynamics related to the nearshore region is presented, particularly focusing on the mechanics, not yet well understood, of wave breaking. Even though some of this information can be easily found in any textbook, they are reported here for the sake of completeness and to introduce a notation adopted throughout the thesis.

In Chapter 3 the problem of modelling the wave motion in shallow waters is presented, particularly focusing on the mechanics, not still well understood, of wave breaking. Even though some of these information can be easily recovered in any textbook, they are here reported for the sake of completeness end to introduce a notation adopted throught the thesis.

In Chapter 3 the problem of the modelling the wave motion in shallow waters through depth integrated equations is presented and discussed. Particularly the Boussinesq types of models and their evolution is addressed with more attention, focusing on the approaches which have been proposed in literature to model the flow within the surf zone.

In Chapter 4 the governing equations of the present model, that is the continuity and the momentum equations, are derived, after removing the unrealistic hypothesis of irrotational motion.

In Chapter 5, the vorticity transport equation is derived and solved analytically by adopting a perturbation method. Moreover the similarity between breaking

waves and hydraulic jump is presented in order to define the amount of vorticity introduced inside the flow through the roller region.

Chapter 6 describes the procedures adopted in order to numerically integrate the governing equations. The new self-adaptive time varying grid approach is described more extensively along with some preliminary analysis on the effectiveness of adopting such a methodology.

In Chapter 7 the model results using the moving grid methods are compared with the uniform fixed grid case and with experimental data both on regular and groupy waves. Finally some conclusive remarks are reported in Chapter 9.

Chapter 2

Surf zone hydrodynamics

2.1 Overview

The surf zone is defined as the region near the coast between the breaking line, that is where the waves start to break, and the swash zone, that is that part of the beach, right close to the shoreline, which is alternately wet and dry.

In this region most of the relevant coastal processes take place, whose understanding is not only extremely fascinating from a physical point of view but also dramatically important for engineering purposes. Just to consider few examples: the physical phenomena playing inside the surf zone have a tremendous effects on natural processes, such as beach erosion, which, in turn, affect the safety of human artifacts, such as building, roads, railways, which, especially in Italy, are often located close to the coastline. Moreover, as most of the coastal structures, such breakwaters and groins, are located in the shallow water region, the wave-structure interaction represents one of the main problems to be analyzed during the design stage.

It should be noticed that it is on gentle sloping beaches that the aforementioned processes have a dramatic influence, while on very steep coasts the extension of the surf zone is limited or even nonexistent. For this reason, the present work will focus on relatively gentle beaches.

Because of the underlined importance, the surf zone hydrodynamics have been widely investigated, but, despite the interest of the scientific community, still nowadays, it is not possible to affirm that a clear understanding of all the phenomena taking place inside this zone is available yet. For this reason, here, just a "snapshot" of the processes inside the surf zone is given, more aiming both to organize the description of the processes and to present the approaches which have been used, than trying to give a complete and exhaustive picture of the pheonomena.

Indeed, in this narrow region, the wave energy is almost entirely dissipated by the process of wave breaking, which is responsible for the transformation of the organized wave motion into chaotic turbulence, giving raise also to low frequency waves, traveling both in the longshore and cross-shore direction, the latter gener-

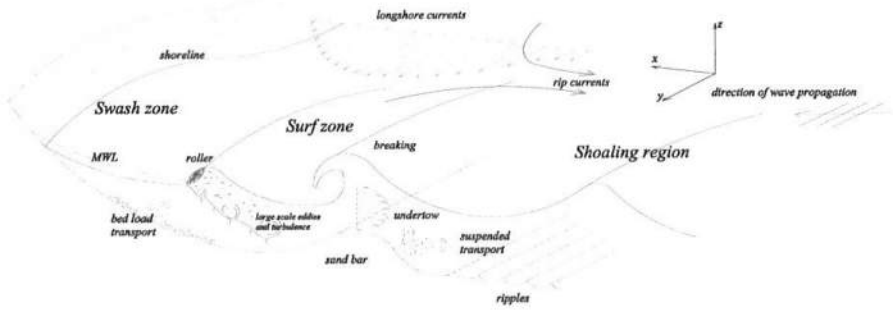

Figure 2.1: Sketch of the complex surf zone hydrodynamics and of the adopted reference system

ating the so-called nearshore circulation. On the other hand, the characteristics of waves inside the surf zone are strongly related to the characteristics of the waves arriving at the breaking point, i.e. after transformation processes in waters with decreasing depth, such as refraction and shoaling, have contributed to change the features of the wave motion from the deep water conditions. Moreover the breaking process plays a complex role in the coastal sediment transport and, in turn, in coastal morphology. In fact, the breaking generated turbulence acts as a mobilizing agent of the sediments comprising the beach, which is then transported as suspended material besides, the breaking generated currents have the capability to transport large amount of sediments from one location to another one, both in the cross-shore and longshore directions.

A nonexhaustive overview of many of the phenomena influencing the flow inside the surf zone is sketched in Figure 2.1. As can be easily seen, a comprehensive and detailed modelling of the three-dimesional surf zone hydrodynamics is very difficult, since it should take into account accurately either the short wave and the steady motion and their interactions, let alone consider the sediment transport problem. It is then necessary often to make some simplifications in the analysis, here this has been done considering the short wave motion in two dimensions, that is following the wave evolution on the vertical plane in the direction of wave propagation. The reason for that is that the main purpose of this work is to contribute to the modelling of the wave breaking process inside the surf zone, which has a strong two dimensional behaviour on this plane, while the wave-wave interactions in the direction perpendicular to that of propagation can be neglected, as a first approximation.

For this reason, the presentation of the surf zone hydrodynamics will be organized here on two different levels. The wave breaking dynamics will be analyzed more deeply, while all the phenomena which influence the breaking process, such as shoaling, refraction, or are influenced by it, such as longshore currents, undertow, set-up, sediment transport, will be briefly presented only for the sake of complete-

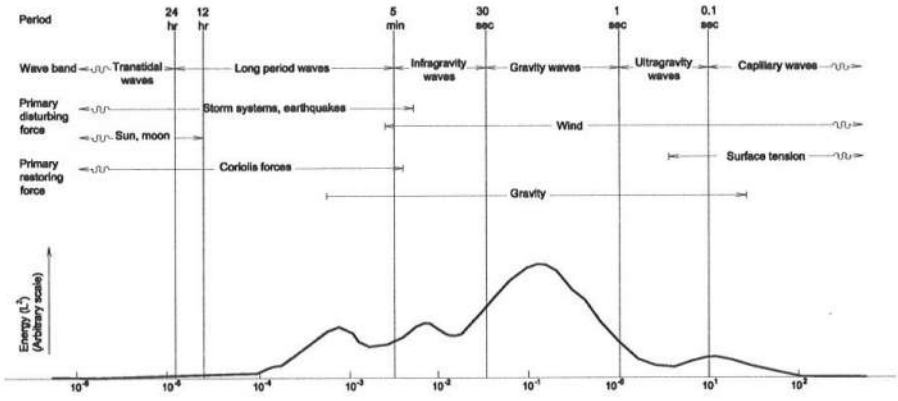

Figure 2.2: Schematic representation of the energy contained in the surface waves of the oceans (from Kinsman (1984))

ness. Some phenomena will be analyzed according to the simple linear wave theory, which in many cases is sufficient to explain the majority of the coastal phenomena, while, in the next chapters, in order to study some of the illustrated coastal processes, related to wave breaking, the nonlinear wave theory in shallow water will be presented and discussed in more details.

Since it is the "history" of the wave, from its generation to the shoreline, which strongly influences the characteristics of the flow within the surf zone, this presentation tries to follow it. In particular, the waves arriving at the beach can be generated by a big variety of phenomena, such as earthquakes, ships in motion or even by the gravitational attraction between the earth and the moon, the difference between these cases being mainly the time scale (see Figure 2.2) of the phenomenon. However, the most common and relevant agent of wave generation, from an engineering point of view, is the wind action. Indeed, blowing on the water surface, the wind transfers its energy to the water waves which then propagates in the same direction of the generating wind, basically unchanged in shape and magnitude until they arrive in regions of intermediate and shallow water, where the interaction with the bottom forces some important changes of the wave characteristics. As the wave propagates toward the shore important phenomena, namely refraction and shoaling, contribute to dramatically change the physical characteristics of the waves, these processes will be described in Section 2.2. Then, in Section 2.3, the wave breaking will be analysed in more details and finally the breaking generated hydro- and morphodynamics will be briefly illustrated in Section 2.4.

2.2 Wave propagation phenomena

From the area of generation, where the surface water waves are induced mostly by the action of the wind, during the propagation toward the shore, the waves meet a region with decreasing water depth. Due to this bathymetric change, the phenomena of wave refraction and wave shoaling take place. These phenomena can be easily explained with the assumption of conservation of energy and gentle sloping beach. Of course these concepts can be found in every coastal engineering manual; however here they are briefly reported for the sake of completeness.

2.2.1 Wave refraction

Wave refraction generates the change in direction of the wave front of a wave propagating from deeper to shallower waters. A simple explanation for this process comes from linear theory, in fact, under the assumption of small amplitude waves, the relationship between the wave frequency f, the local water depth h and the wave lenght L, represented by the wave number $k = 2\pi/L$, is

$$f^2 = gk \tanh kh \tag{2.1}$$

where g is the gravitational acceleration. Since in linear theory the period is assumed to be an invariant, as the water depth decreases, the wave length decreases with the water depth, and so does the wave speed c. In other words, if a wave front is approaching the shore at an angle, the wave is forced to turn with the wave front parallel to the shore, as it is shown in Figure 2.3. The process is analogous to refraction in optics and similarly follows Snell's law, under the hypothesis of straight and parallel off shore contours,

$$\frac{\sin\theta}{c} = \frac{\sin\theta_0}{c_0} \tag{2.2}$$

where θ is the angle representing the direction of wave propagation with respect to the direction perpendicular to the shoreline, c is the wave speed and the pedix $(_0)$ represents the known values at a reference point, typically a location in deeper waters.

The previous approach is the simplest method for calculating the direction of wave propagation and it is also called the wave ray tracing method.

It should be pointed out that the refraction process takes place even after breaking, then the wave keeps refracting, orienting the wave front in a direction parallel to the shoreline, being affected by breaking only in a minor way.

2.2.2 Wave shoaling

Wave shoaling induces a substantial increase of the wave height H as consequence of the energy conservation principle. In fact, always according to linear theory, the wave energy flux $\mathcal{F}$ is proportional to H and to the group velocity c_g. Moving toward shallow waters, the last one decreases as the wave celerity decreases, so,

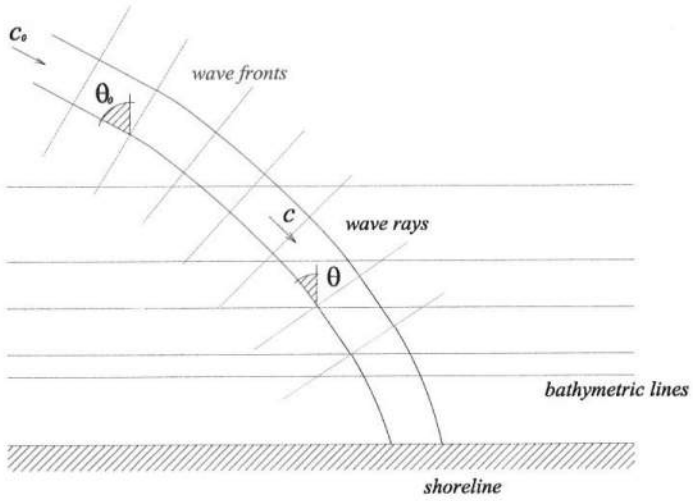

Figure 2.3: Sketch of wave refraction

since the wave energy flux has to be conserved between two transversal sections delimited by two adjacent wave rays, the wave height must, in general, increase.

To take into account the effects of both refraction and shoaling on a wave approaching the shore, a simple formula is provided in linear theory for the prediction of the variation of wave height

$$H = H_0 K_r K_s \tag{2.3}$$

where H_0 is the wave height at a reference point, $K_r = \sqrt{\frac{\cos\theta_0}{\cos\theta}}$ is the refraction coefficient and $K_r = \sqrt{\frac{cg}{c_g}}$ is the shoaling coefficient.

Due to the shoaling process, the wave not only increases its wave height, but is also subjected to a deformation of the wave shape. In fact the wave crest travels faster than the wave trough, making the wave shape asymmetric with respect to both the vertical axis and the horizontal axis. As it can be observed in any field or laboratory measurements of the water surface, in the shoaling region the wave front is much steeper than the rest of the wave, the wave trough is basically flat while the wave crest is much peaker. However this wave shape cannot be substained and at some point, defined as *breaking point* (or *breaking line* in two dimensions), the breaking occurs. From an energetic point of view, during the shoaling process, the strong wave-wave interaction before the breaking point results in a transfer of energy from low frequency to higher frequencies, then breaking occurs when this transfer is not fast enough to balance the increase in energy density. At this stage energy is still transferred to higher frequency, but in a region of energy saturation and the energy excess is dissipated as turbulence (Thornton, 1979).

The linear theory represents a useful tool for describing the two mentioned phenomena of refraction and shoaling. However for a detailed description of both refraction and shoaling, models which consider important nonlinear effects have to be adopted. In literature the most widely-used models for engineering purposes are the ones based on the nonlinear shallow water equations and the Boussinesq equations. Indeed, both models, in particular the second one, give a much more accurate description of the variation of wave heights across the beach, besides performing a better prediction of geometric, kinematic and dynamic features of the waves. The characteristics of these models will be illustrated in the next chapter.

2.3 Wave breaking

Lots of hydrodynamics phenomena take place in the region between the breaking line and the shoreline, where essentially the organized wave motion is transformed into motions of different types and scales. In particular, not only the breaking event generates small scale turbulence and macro vortices at the same time, but also low-frequency waves and currents. Moreover, with respect to the morphodynamics of the coastal regions, the breaking plays a key-role, being responsible for mobilizing a big amount of sediment, and then strongly contributing to the sediment transport in the coastal area.

For more details on wave breaking, the interested reader can be referred to the classical reviews on breaking waves presented in Battjes (1988) and Peregrine (1983). More recently Svendsen (2003) presented a review of the hydrodynamics of the surf zone, while a review of the breaking phenomena in the spilling breaker case has been illustrated in Duncan (2001). Moreover the most recent advances in the numerical modelling and experimental techniques on breaking have been reported in Christensen *et al.* (2002), who focused particularly on the vertical variation of the flow across the surf zone.

For clarity's sake, it should be noticed here that the phenomenon of wave breaking takes place not only inside the surf zone but also in deep waters. In particular, breaking waves can be distinguished in steady breaking waves, such those produced by ships or hydrofoils moving at constant speed, and unsteady, such those inside the surf zone or in the area of wind generation. Even though the focus of this work is the modelling of the wave breaking inside the surf zone, i.e. in shallow waters, it should be acknowledged that many important advances, obtained by looking at waves breaking in deep waters, since, from a fluid mechanics point of view, the phenomenon is very similar in the two cases after the breaking have started and for these reasons in the following reference will be made also to work on this kind of breaking.

The first question in studying the surf zone hydrodynamics is whether the wave breaks or not, distinguishing then if the beach has a reflective (non-breaking) or dissipative (breaking) behaviour. The parameter widely used is the relative beach steepness, also called Iribarren number or surf similarity parameter, introduced by Iribarren and Nogales (1949). It represents the beach slope relative to the wave steepness

$$I_r = \frac{h_x}{\sqrt{H_0/L_0}} \tag{2.4}$$

where h_x is the beach slope, and H_0/L_0 the wave slope, with H_0 wave height and L_0 wave length in deep water.

An analytical solution for the onset of breaking has been proposed by Carrier and Greenspan (1958) for the inviscid, nonlinear shallow water equations. In particular only the case of exact standing waves has been faced by assuming that the critical condition for the starting of the breaking corresponds to a situation where the surface is locally vertical. Keller (1963) then has extended this solution to the case of arbitrary relative water depth, Keller's criteria is similar to the one introduced by Miche (1944) which found large diffusion.

After Galvin (1968), the classification of breaking which is traditionally adopted distinguishes between plunging, spilling, collapsing and surging type of breakers, depending on the Iribarren number (see Tab. 2.I and Figure 2.4)

Plunging breakers are the most spectacular type of breakers, their characteristic is the overturning of the front face of the wave, with a prominent jet falling down on the base of the wave at the plunge point, followed by one or more splash-ups due to the jet impinging on the water surface.

Spilling breakers have aereated water at the crest of the wave, which spills down on the front face, while the wave shape is more or less maintained.

Collapsing breakers appear like truncated plunging breaker which occur on relatively steeper beaches. For this reason the surf zone is a very limited area close to the shoreline where no strong variations of the wave characteristics occur.

Out of this classification, Figure 2.4 shows also the surging breakers often considered, even though these are not true breakers. Indeed for these waves a variation of the wave profile can be detected only close to the moving shoreline.

Focusing on the crest of the spilling breakers, it has been shown that the spilling process starts with a small jet on the crest of the wave, only in the case of long waves or if the surface tension can be considered weak, otherwise a surface-tension-dominated ripple pattern occurs on the front of the wave (Duncan, 2001).

Different types of breakers can appear at the same location, depending on the actual hydrodynamic and morphodynamic conditions of the site. However, the

Table 2.I: Iribarren number for different type of breakers

Type of breaker	*Iribarren number*
spilling	$I_r < 0.46$
plunging	$0.46 < I_r < 3.3$
surging or collapsing	$I_r > 3.3$

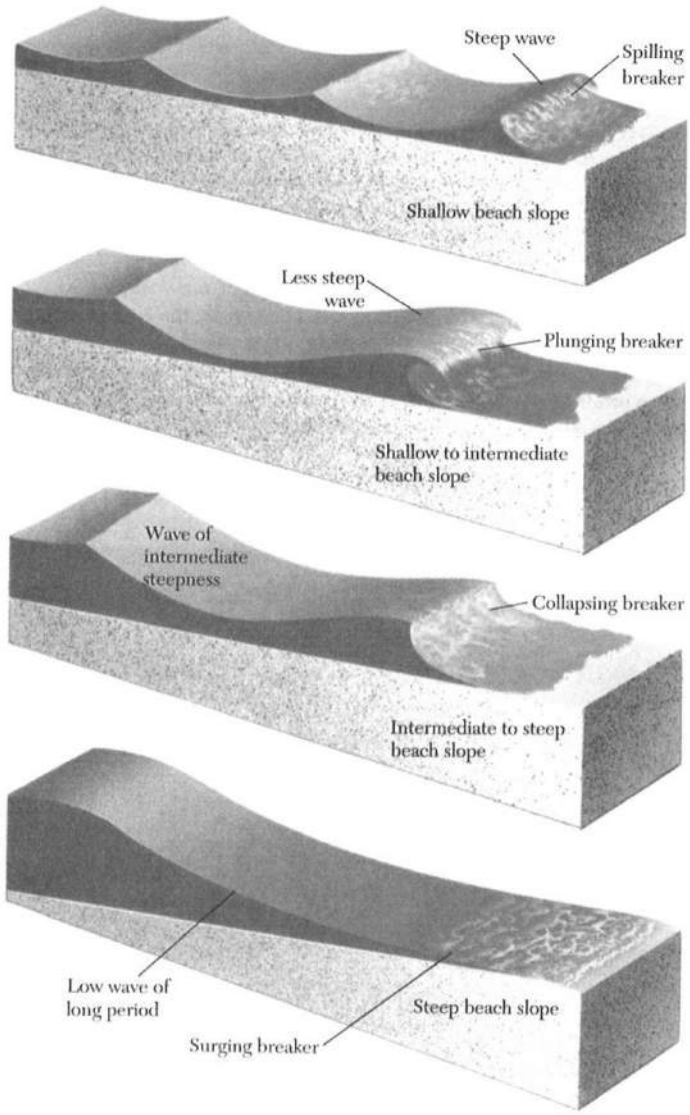

Figure 2.4: Type of breakers for different relative beach slope (Davis, 1997).

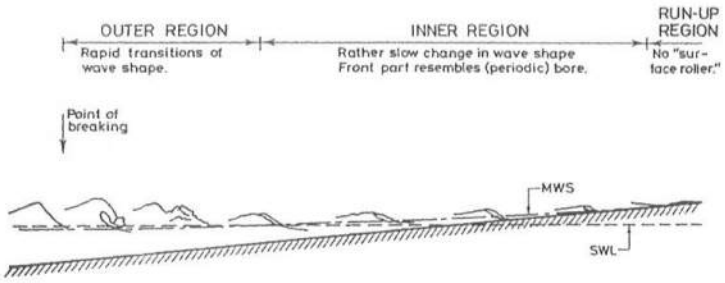

Figure 2.5: Outer and inner region inside the surf zone (from Svendsen *et al.* (1978))

first two classes of breakers, characteristic of gentle sloping beaches, are the most common and important. Indeed, the plunging kind is representative of swell conditions, that is of very regular long waves, whereas the spilling type is characteristic of storm wave conditions, that is to say of waves which are more irregular, both in time and space.

In this work, the analysis has concentrated on the spilling breaker case, considering the fact that, as testified by Duncan (2001), probably this is the type of breaker which occurs more frequently than plunging and gives rise to an important amount of turbulence, spray and bubble generation at the water surface.

As a matter of fact, independently on the breaker types, after the breaking point, the surf zone has been conventionally divided in *outer region*, or *transition region*, and *inner surf zone*. This classification is particularly important for plunging and spilling breakers. Indeed, as it can be seen in Figure 2.5, right after the initiation of breaking the characteristics of the waves change rapidly and dramatically. Macroscopically this can be observed as a strong decrease of the wave height and an abrupt variation of the wave shape. After that, inside the inner surf zone the wave shape is essentially stable, while the gradient of the wave height along the cross-shore direction is much smaller than it is within to the outer region. In this region, which is often the largest inside the surf zone, for beaches with a gentle slope, there is a so-called bore-like propagation, where the definition recall the hydraulic similarity of a breaking wave with a bore. As pointed out by Svendsen (1984), the limit between the two regions is gradual, in particular looking at the records of wave heights throughout the surf zone. Thus Svendsen proposed to define the limit between the two regions as the point where the slope of the mean water level changes. In fact at some distance from the breaking point it can be observed, from measurements, that the mean water level suddenly tends to increase. This is known as the set-up phenomenon and it will be explained better later on in this chapter.

The dissipation of energy during breaking, and the consequent decrease in wave height, are mainly related to the energy exchanges taking place in the surf zone, where the the organized and mainly irrotational wave motion is transformed into vorticity, turbulence and currents. In the subsequent section a review of the studies

dealing with vorticity generation and turbulence structure is given. On the other side, the modelling of breaking waves requires some idealizations, allowing both to simplify the problem and to take into the right account the physics of the phenomenon. Perhaps the most adopted one, in the modelling of breaking, is the concept of the surface roller, which will be presented in Section 2.3.2, assuming that the turbulent region on the front of the wave can be described as a recirculating region which does not participate in the wave motion.

2.3.1 Vorticity and turbulence generated by breaking

The understanding of both the vorticity field and the turbulence structure in the surf zone, both phenomena being strongly related, is crucial for any theoretical, experimental or numerical speculation about the nearshore hydrodynamics.

A review of the study of turbulence in the surf zone has been recently presented by Longo *et al.* (2002). In their paper Longo *et al.* deal also with the turbulence inside the swash zone, as also the shoreline motion is strongly influenced by the breaking processes.

Due to the difficulties in studying an unsteady, highly perturbated process such that of breaking waves on beaches, the attempt to study the turbulence structure in this kind of phenomena has given raise to studies of different flow fields, taking advantage of the hydraulic similarities of the fluid motion inside the surf zone with other kind of hydraulic processes, such as wall jets, hydraulic jumps, bores and wakes.

Another typical characteristic of the breaking process is the presence of a huge amount of air, which is entrained in the fluid, however, it must be stressed that the presence of air bubbles is not a must for a strong turbulent motion, since this can be present even without bubbles (Peregrine and Svendsen, 1978). However the white-caps appearing on the surface and the air bubbles inside the flow make it possible the easy visualization of the structure of vortices generated under the free surface. As a matter of fact, it is very difficult to get three-dimensional measurements of the detailed structure of the turbulence, using Laser Doppler Anemometry (LDA), due to the signal drop-out within the areated region, even though some studies have been successfully perfomed (Nadaoka *et al.*, 1989; Ting and Kirby, 1994, 1995, 1996; Svendsen *et al.*, 2000), but the measurements can be effectively performed only below the trough level. Only very recently the measurements of the breaking generated turbulence started to be done using also Particle Image Velocimeter techniques, which should allow for a simultaneous analysis of the velocity inside the entire flow field to be performed (Haydon *et al.*, 1996; Chang and Liu, 1996; Emarat and Greated, 1999).

The mechanism of vorticity generation near the free surface is still to be established firmly. It seems to be clear that the steepening of the wave naturally induces high curvature and then vorticity inside the flow, even though several theories have been proposed which attribute the breaker generated vorticity to the pressure gradient or to the density gradient close to the overturning roller.

During the initial stages of the breaking event, the formation of the large scale

vortex on the free surface, which gives rise to the generation of the surface roller on the front of the wave, is preceded by a small scale capillary pattern related to the value of the Froude number F_r. This phenomenon has been experimentally investigated by Lin and Rockwell (1995), by using high-density particle image velocimetry in the case of spilling breakers. Lin and Rockwell (1995) showed that the train of capillary waves tends to increase in wavelength, thus contributing to generate vorticity inside a mixing layer beneath the surface. In particular the vorticity has a maximum in the region of intense shear immediately downstream of the separation from the free surface. They identified two mechanisms giving rise to the region of highly concentrated vorticity: one, if the flow is not separated, about the trough and the crest of the capillary pattern; the other, with flow separation, due to the curvature of the free surface of the large scale breaker, which also contributes to convect the vorticity downstrean in the mixing layer.

After its generation from the source region on the free surface, the consequent downward vorticity flux is mainly due to viscous effects. A surface fluid layer is accelerated in order to bring the tangential stress close to the tangential stress at the surface (usually zero). Then, the free surface fluid decelerates with respect to the fluid beneath it, creating a sharp velocity gradient growing into a shear layer and convecting the vorticity downstream.

It is then clear, at this point, that right after the breaking point, the irrotational flow becomes rotational. The rotational component of the flow is mainly related to the presence of macro vortices, which are quickly formed after the onset of breaking. Nadaoka *et al.* (1989) have studied and shown through an experimental investigation that the initially two-dimensional vortices break down forming vortices descending obliquely downward. They attribute to the eddy associated vorticity not only the increase of mass and momentum flux and, then, the consequential decrease of wave height, but also the generation of Reynolds stress in the upper layer of the water and the deformation of the mean flow. Nadaoka *et al.* (1989) refer to the irrotational component of the flow as *wave motion*, and to the rotational component as *eddying motion.*

However, from the earlier work of Duncan (1981) on breaking waves produced by towing a submerged hydrofoil, it is shown that the vertical velocity distribution under the crest of a breaking wave differs from the Stokes linear theory only close to the surface, while near the bottom the hypothesis of irrotational flow, which is the one adopted in linear theory, still holds as a good approximation to the measurements. The experimental investigation on breaking waves on a sloping beach from Cox *et al.* (1995) confirms this behaviour.

More recently, Melville *et al.* (2002) have deeply investigated the velocity field under breaking wave using a DIPV (Digital Particle Image Velocimetry) technique. Taking measurements of the mean velocity and then deriving the breaking generated vorticity and the kinetic energy, they found the presence, under a breaking wave, of a large scale coherent vortex which slowly propagates downstream and deepens. Moreover, from measurements of the Reynolds stresses, responsible for the transfer of horizontal momentum vertically into the water column, Melville *et al.* (2002) found that they are mostly negative, meaning that the horizontal

momentum is transported vertically downwards. Moreover, averaging the mean turbulent kinetic energy, the mean square turbulent vorticity and the Reynolds stresses they found that the maxima of these quantities are not on the surface, but in correspondence of the depth of the core of the mean vortex generated by the breaking.

These recent analysis on breaking wave are in good agreement with the laboratory measurements of velocity and surface elevation in three turbulent hydraulic jumps by Svendsen *et al.* (2000), who used laser-Doppler velocimetry, particularly looking at the flow in the roller region. From the experiments, the resemblance of breaking waves and shear layers has been confirmed qualitatively, since the turbulence generated vorticity by the roller spreads over the entire roller region.

As the breaking develops, the organized vortical motion is transformed into small-scale disorganized motion, which can be treated as turbulence. In particular on the front of the wave the decreasing scale and increasing disorder transform the breaking wave in a turbulent bore propagating shoreward. It is at this stage that the wave is characterized by the presence of a turbulent front and by an area of recirculating flow, the surface roller, located between the so-called *toe*, that is the point on the front where the overturning wave meets the undisturbed or inflowing water, and a point of separation near the wave crest.

The mechanism of dissipation in the inner surf zone is due to continuous shearing generated by the roller which allows for the transfer of energy from the wave motion into turbulence. This phenomenon is responsible not only for the decrease of wave height inside the surf zone but also for a proportional increase of momentum flux. The latter is compensated by a corresponding increase in the mean horizontal pressure gradient, thus resulting in a set-up of the mean water level. Regarding this mechanism several experimental studies have been carried out.

Peregrine and Svendsen (1978), using a visualization of the turbulence under bores and spilling breakers, proposed that the flow in a breaking wave is in part like a mixing layer, in the region of the toe of the surface roller, and in part like a wake, on the back of the crest of the wave, where the turbulence spreads downward deepening the extension of the turbulent region.

For the spilling breaker case, Duncan (1981) demonstrated that the breaking produces a shearing force along the forward face of the wave, while a turbulent wake is left behind with a momentum deficit roughly equal to the maximum momentum flux of a Stokes wave with the same speed as the breaker, with the vertical thickness of the wake incresead according to the square root of the distance behind the wave.

Nadaoka *et al.* (1989) demonstrated that the generation of Reynolds stresses in the region closer to the surface is due to large-scale horizontal eddies which then affect also the deformation of the flow field when the wave is breaking.

Yeh and Mok (1990) proposed the similarity between bores and hydraulic jumps, though pointing out the differences between the two types of flow, in particular with reference to the velocity profiles, the vorticity distribution over depth, the surface roller and the boundary layer. Yeh and Mok (1990) attribute to the presence of the surface roller the turbulence generated inside the two flow fields.

The undertow and turbulence under both spilling and plunging breakers has

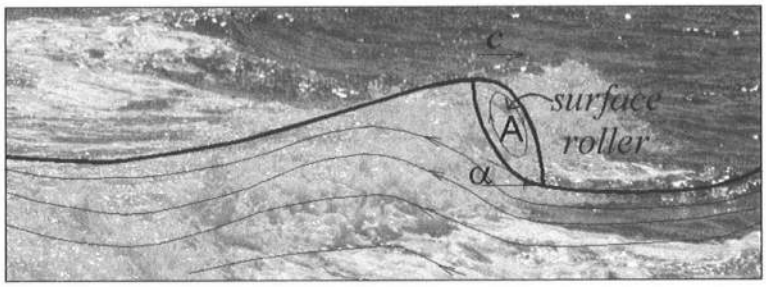

Figure 2.6: Sketch of a surface roller of a breaking wave

been also extensively experimentally investigated by Ting and Kirby (1994), Ting and Kirby (1995), Ting and Kirby (1996) using fiber-optic laser Doppler anemometry. They found that the dynamics of turbulence is quite different in the two type of breakers, in particular the results for the turbulent kinetic energy k_t, show that there is a transport of k_t seaward in the case of a spilling breaker and landward in the case of a plunging breaker. Moreover, under spilling breaking waves the vertical variation of mean flow velocity and turbulence intensity is much more evident than in the plunging breaker case, allowing the large-scale eddies originated from the surface roller to transport the turbulence offshore, slowing down its dissipation mechanism. This kind of study is interesting not only from a fluid mechanics point of view, but also in regard to the direction of the cross-shore sediment transport. In fact when the turbulence is directed offshore, like in the spilling case of steep winter storm waves, the suspended sand is carried relatively far from the beach to create offshore bars, while swell plunging waves move the sand onshore, giving rise to an accretionary beach.

Another topic about the turbulent motion under breaking waves is the wall boundary layer generated turbulence, which is not discussed here, since it has been recognized that the wall turbulence is an order of magnitude smaller than breaker-generated turbulence (Hansen and Svendsen, 1984).

2.3.2 The roller

The idea of the roller, first introduced by Svendsen (1984), is crucially to understanding and to modelling the flow features inside the surf-zone and it is commonly used in the studies of nearshore hydrodynamics. In particular, the roller is defined as the recirculating part of the flow above the dividing streamlines, being located on the front of a breaking wave and moving with approximately the same speed of the wave, being carried shoreward as the wave propagates toward the shoreline In Figure 2.6 a sketch of the roller as it models a breaking waves is presented.

Before being systematically defined by Svendsen (1984), the surface roller, its geometry and its kinematics have been investigated by Duncan (1981). In this work, Duncan was able to optically measure the area A of the roller and the angle of inclination α of the breaking wave.

Then Svendsen (1984) carried out a theoretical analysis in order to predict the wave height and the set-up variation, considering the conservation of the phase averaged energy and momentum and the effects of the roller inside the surf zone. It has been shown that in the inner region, where there is a bore-like propagation, the increases of both energy flux and radiation stresses is mainly due to the presence of the roller, whereas in the outer region jump conditions similar to those used for bores and hydraulic jumps must be considered. Considering the depth integrated phase averaged momentum equation and the depth integrated phase averaged energy equation, Svendsen (1984) found an analytical solution for the variation of wave height for the case of plane beach, which relates the variation of H to a value of the wave height at some reference position, H_0, to the local water depth h, to the water depth at a reference location, to the beach slope h_x, to the wavelength L and to the energy dissipation D. This is clearly an improvement with respect to the assumption that the wave height to the depth ratio is constant throughout all the surf zone. The variation of wave height, in fact, is very different between the transition region and the inner surf zone, as has been already explained. Taking into account the effect of the roller on the flow, even by assuming a simplified vertical velocity profile, with constant velocity under the roller and velocity equal to the wave speed c in correspondence of the roller region and an hydrostatic pressure, Svendsen (1984) found that the presence of the roller contributes to dramatically increase both the energy flux and the radiation stress. Moreover, he noticed that the sudden change of wave shape after the breaking point cannot be immediately transformed into dissipation of energy, but the lost potential energy is converted into forward momentum flux, mainly concentrated in the roller. Therefore, during the first stages of breaking, the radiation stress stays basically constant.

After this initial study the roller idea has been used quite extensively in order to take into account the effects of the breaking waves in the modelling of the surf zone, both in the modelling of the short wave motion inside the surf zone (Deigaard and Fredsøe, 1989; Brocchini *et al.*, 1992; Schäffer *et al.*, 1993; Madsen *et al.*, 1997; Veeramony and Svendsen, 2000, 1999)) and in that of the nearshore circulation, and thus, in turn, in order to determine the short wave forcing terms (Svendsen and Putrevu (1994)).

However, it should be noticed that, even if many scientists use the idea of the surface roller in their theoretical and numerical models, there is not a complete agreement about the role that the surface roller plays in the fluid motion. In Deigaard and Fredsøe (1989) and Brocchini *et al.* (1992), for example, the roller is considered as a solid body, which exert its influence mainly through its own weight, generating an additional pressure. In Veeramony and Svendsen (2000), Veeramony and Svendsen (1999), instead, the action of the roller is modeled considering that through its boundary an injection of vorticity into the remaining part of the fluid domain takes place. This idea is supported by the experimental observations of Lin and Rockwell (1994) on a stationary breaker, who claimed that the real surface roller, intended as a strong , large-scale single vortex does not exists, at least in an instantaneous sense, but showed that there is a concentration of vorticity in the region right beneath the roller.

2.4 Other surf zone phenomena

It has been recognized that the breaking process generates several phenomena, giving rise to the complex picture of the surf-zone hydrodynamics which are the subject of this chapter. Before starting the presentation of the physical processes, the definition of some of the short-wave-averaged quantities, such as mass flux or volume flux and radiation stress should be given, since the analysis of many of the breaking generated phenomena is often pursued using the short-wave-averaged (time averaged over a wave period) depth integrated equations of conservation of mass and momentum.

The flow field is usually decomposed considering a mean flow field $\mathbf{U}$, a flow due to the wave motion $\mathbf{u}_w$ and the one due to the turbulence $\mathbf{u}'$

$$\mathbf{u} = \mathbf{U} + \mathbf{u}_w + \mathbf{u}' \tag{2.5}$$

The volume flux, or mass transport $\overline{Q}_\alpha$, in the horizontal direction α is defined as

$$\overline{Q_\alpha} = \overline{\int_{-h}^{\zeta} u_\alpha dz} \tag{2.6}$$

where ζ is the surface elevation and u_α is the horizontal velocity in the direction α, while the overbar indicates the time average over a wave period. It turns out that, inside the surf zone, this transport is higher under the crest of the wave, and it can be attributed to the contribution given by the surface roller.

The radiation stress is defined as the time average of the local horizontal momentum flux, and, in a synthetic form, can be written as

$$S_{\alpha\beta} = \overline{\int_{-h}^{\zeta} (\rho u_{w\alpha} u_{w\beta} + p\delta_{\alpha\beta}) dz} - \delta_{\alpha\beta} \frac{1}{2} \rho g h^2 \tag{2.7}$$

where the $S_{\alpha\beta}$ is the wave radiation stress in direction α across a surface normal to the direction β, ρ is the water density, $u_{w\alpha}$ and $u_{w\beta}$ are the wave velocity in the horizontal directions α and β respectively, p is the pressure, h is the local water depth and $\delta_{\alpha\beta}$ is the Kronecker's delta. It must be noticed that the radiation stress takes into account not only the momentum due to the convective terms, but also the contribution from the pressure.

Moreover, it can be shown easily, even using the linear theory, that the radiation stress is proportional to wave energy. Since in the surf zone, due to wave breaking, the momentum flux decreases, this has to be balanced by forces acting in the direction opposite to the wave, which are indeed represented by the radiation stress. Using the concept of the radiation stress many of the breaking related phenomena can be explained. To make things simple, the effects in the cross-shore and the longshore direction can be considered separately, both to describe the steady motion generated by the breaking waves and to illustrate the sediment transport processes.

2.4.1 Wave set-up

In the cross shore direction, the variation of the radiation stress S_{xx} due to breaking is balanced by generating a sloping mean water level, within the surf zone. This is the set-up phenomenon, which shows up as an increase of the mean water level with respect to the still water level as the water depth decreases. The wave set-up can be simply described using the short-wave-averaged, depth integrated, horizontal momentum equation in the cross-shore direction:

$$\frac{\partial S_{xx}}{\partial x} = -\rho g(h+\bar{\zeta})\frac{\partial \bar{\zeta}}{\partial x} \tag{2.8}$$

where $\bar{\zeta}$ represents the difference between the mean water level and the still water level, or, in other words, the wave set-up inside the surf zone. The main difficulty in integrating eq. (2.8) is due to the evaluation of the radiation stress inside the surf zone, where no wave theories are available. Since, as shown by Svendsen (1984) there is a strong dependence of S_{xx} on the value of the wave height, the calculation of the set-up are very sensitive to the wave height estimate within the surf zone. Moreover, it has been often observed comparing experimental data and prediction of wave set-up, that whereas the rise of the mean water level is predicted to start at the breaking point, it actually starts a bit shoreward of it. This agrees with the fact that right after breaking the experimental measurements of radiation stress show that this stays constant for a bit, before decreasing inside the surf zone.

A similar phenomenon takes place in the shoaling region, where instead there is an increase of radiation stress, and consequentely the mean water level tends to decrease in the offshore direction. Eq. (2.8) still holds, but $\bar{\zeta}$ assumes negative values.

2.4.2 Undertow

The undertow is a cross-shore seaward current associated with the mass flux near the surface, above trough level, due to breaking waves. In fact, in order to balance the shoreward mass flux associated to the water carried forward with the surface roller, a return flow near the bottom must be generated. It has been found that the undertow is a balance among forces on the fluid particle caused by a combination of the radiation stress, the pressure gradient from sloping mean water surface and turbulent shear stresses. The prediction of undertow is of great importance for engineering purposes, because of its relevance on the sediment transport and the coastal morphology.

2.4.3 Nearshore circulation

The longshore currents are only one of the complex nearshore horizontal circulation driven by the variation of radiation stress due to breaking, but they are extremely important from an engineering and environmental point of view, due to their capability of drifting both sediments and pollutants.

In the alongshore direction, the S_{xy} component of the radiation stress is responsible for driving steady currents, in fact, to balance the change in momentum flux a longshore water level slope can be generated only for the case of bounded shorelines, that is shorelines that are limited in the alongshore direction by some obstacle, natural or man-made. In the case of infinitely long beaches, instead, a longshore current is generated in order to balance the gradients in momentum flux through the generation of bottom shear stresses, τ_y^B and of the lateral transfer of turbulent momentum due to the depth integrated Reynolds stresses, S'_{xy}. In the simplest case of a longshore uniform beach, the equation for the longshore current is simply

$$\frac{\partial}{\partial x}(S_{xy} + S'_{xy} + \tau_y^B) = 0 \tag{2.9}$$

By assuming an expression for the bottom shear stresses term very similar to those used in pipe flow, that is using a Darcy-Weisbach-like friction factor, and by using a simple eddy viscosity model for the turbulent shear stresses Longuet-Higgins (1970) found an analytical solution for the longshore current $V(x)$, showing that the longshore current increases with the water depth and with the incident wave height and decreases with bottom friction factor.

However the causes generating or influencing longshore currents are not only related to the wave action. For example, also longshore topography changes generate pressure gradient which can then drive longshore currents.

Within the nearshore circulation, there are also physical processes like rip currents, which are strong seaward-oriented, jetlike flows, often periodic in the longshore direction, which appear also under piers, alongside jetties, at the side of breakwaters or on the rip channel of a longshore sandbar. This type of phenomenon is extremely dangerous for unaware swimmers, and every year many deadly accidents occur at the beaches due to them. However, field and laboratory observations have shown that they disintegrate outside the surf zone.

2.4.4 Low frequency waves

Low frequency waves, or surf beats, are waves with periods between 20 and 200 sec, they are ubiquitous in the surf zone. The effects of such waves are especially important in the shallow water region, where they increase in magnitude and, being nonbreaking, they do not dissipate energy through breaking, as opposed to wind waves. Moreover the interest devoted to the study of this kind of waves is due to the fact that many coastal regions show morphological characteristics having length scale much larger than a typical length scale related to wind waves and which could be, perhaps, related to this kind of waves.

According to the direction of propagation, it is possible to distinguish: leaky waves, in the cross-shore direction, and edge waves, in the longshore direction.

The first ones seem to be due to the breaking of wave groups, which radiates seaward and shoreward free long waves. Moreover the reflection of this type of waves due to the beach give rise both to a system of standing waves within the

surf zone and to waves which, propagating seaward, superimpose to the outgoing waves previously generated at breaking.

Edge waves are infragravity waves that are trapped in the nearshore region by refraction. It seems they are responsible also for rip currents generation and do influence topographic features. They are difficult to be generated in laboratory experiments and also to find them in the field has been quite hard, due to contemporary presence of leaky waves.

Finally, the shear waves are low frequency waves which appear as oscillation of the longshore currents. They move in the longshore direction, with a wave length of the order of 100 m and period about 100 s and their kinematics seems to be related to the strength of the mean longshore current, while their generation seems to be related to an instability mechanism.

2.4.5 Sediment transport

Similarly to the other kind of breaking generated phenomena previously described, the sediment transport processes can be distinguished according to their direction: in longshore transport and cross-shore transport. Historically, the two types of phenomena have been investigated separately, being the first one being caused by longshore currents and the second one closely associated to the wave motion and to the undertow current. The first one generates beachline erosion or accretion and interacting with coastal structures, such as ports, jetties and groins, the second one is responsible for the evolution of the beach profile and for the generation of longshore sand bar.

On the other hand the sediment transport is usually distinguished as bedload and suspended transport. While this last one is strongly related to the characteristics of the breaking, since a portion of the available energy flux into the surf zone is dissipated by the falling sand grains, it is a widely accepted idea that the longshore transport is strongly related to the wave-driven currents, since it is assumed that while the effects of the breaking is to stir up the sediments from the sandy bottom, longshore currents transport the sand along the coast. It seems that the maximum of the longshore transport is located between the breaking line and the midpoint of the surf zone, however, both field and laboratory data, demonstrated that the distribution of the longshore transport in the cross-shore direction is strongly correlated both to the local beach profile and to the type of breaker. An old, simple model often adopted to calculate the longshore transport is the CERC-formula:

$$P_{ls} = E_{fb} \cos\theta_b \sin\theta_b \tag{2.10}$$

where E_{fb} is the wave energy flux at the breaking point, θ_b is the direction of wave propagation at breaking and P_{ls} is a quantity used to evaluate the submerged weight if the transported sediment I_l

$$I_l = K_c P_{ls} \tag{2.11}$$

with K_c empirical constant. However the CERC-formula does not account neither for the effects of the characteristics of sediments nor for the coastal morphology.

Moreover the features of the longshore transport are closely associated with the irregularities of the waves, since the near-bed orbital motion is irregular and only a fraction of the waves are broken at a given point within the surf zone, while others will break later or never.

The understanding of the cross-shore sediment trasnport is still a matter of debate within the scientific communitee. Inside the surf zone, the wave-breaking-generated turbulence is predominant in influencing the cross-shore transport with respect to the other typical mechanisms. In fact in this region, the strong energy loss due to breaking are compensated by the generation of shear stresses, which strongly affects the vertical velocity distribution, which is also influenced by the effects of the water carried forward by the surface roller on the front of the broken wave and the consequent strong undertow profile close to the bottom and directed offshore. As shown previously, the type of breakers, giving rise to different turbulence structure and to a transport of turbulent kinetic energy seaward, in the case of spilling breaker, and onshore, in the case of plunging, have a dramatic influence on the direction of the net cross-shore transport. The first case, occuring mostly during winter storm, contributes to the building of offshore sand bars.

Chapter 3

Modelling the flow in the surf zone

3.1 Overview

Modelling the flow inside the surf zone is crucial in order to understand and predict the complex surf zone hydrodynamics. It has been shown that, from a fluid mechanic point of view, two different types of motion, both characteristics of the nearshore circulation, can be distinguished: that is the short wave motion and the wave induced steady motion. The approaches to model these processes are consequently different, indeed depending upon whether the wave propagation is solved in time or if the wave properties are averaged over a wave period. Hence the models can be classified as *phase-resolving models* and *phase-averaged models.* The latter are used for nearshore circulation modelling: the wave motion is considered as an input, since the averaged wave properties, such as mass flux, wave energy and radiation stress, represent the forcing of the longshore currents and related phenomena.

Since the main purpose of this work is the modelling of the breaking of the waves as they propagate over a sloping beach, here a closer overview of the most used phase-resolving wave models in shallow and intermediate water regions will be given.

In shallow water, the long wave theory is usually adopted, due to the fact that the wavelength can be assumed as much larger than the wave height, and various sets of equations are available. The level of accuracy performed and the kind of phenomena which are modeled are usually related to the values of two dimensionless parameters

$$\mu = kh \tag{3.1}$$

$$\delta = \frac{a}{h} \tag{3.2}$$

where k is the wave number, h is the local water depth and a is the wave amplitude. The aforementioned parameters represent the dispersiveness of the waves and the nonlinearity of the waves, respectively. Their meaning will be explained later on in more detail.

The linearized equations, both the nondispersive and the dispersive ones, are able to model the long wave motion only to a limited extent. For this reason only the nonlinear depth averaged equations will be considered here, since they provide a better representation of the wave motion in shallow waters. The depth averaged equations are an useful and computationally economic tool for the modelling of large scale phenomena, and have been widely used by the engineering community, since, by reducing by one the number of unknown variables, they allow to speed up the solution. Moreover, in the case of the Boussinesq models, they are also able to give information on the vertical structure of the flow.

In particular, in Section 3.2 the nonlinear shallow water equations, or Airy's equations, will be discussed. In Section 3.3 both the standard versions of the Boussinesq equations and their improved versions will be described in more details, to underline the differences and the advantages of using the first or the second set of equations. The proposed enhanced Boussinesq type of models, with better dispersive and nonlinear characteristics, will be reviewed in Section 3.3.2, while the approaches adopted in literature so far for modelling surf zone waves will be presented in Section 3.3.3.

3.2 NLSWE models

The assumption in the nonlinear shallow water equations is that the wavelength is much larger than the water depth. In terms of the dimensionless parameters previously described, this means that $\mu << 1$, while the parameter δ is assumed to be of order one. The first hypothesis is typical in the long wave approximation, since in this case the horizontal scale is much larger than the vertical scale. Another usual assumption of this type of models is that of gentle water surface slope, which allows to assume that the water particle accelerations are negligible compared with gravity, implying that the pressure has an hydrostatic distribution over depth.

Integrating over the water column, the conservation of mass and momentum leads to the following equations:

$$\frac{\partial \zeta}{\partial t} + \nabla_h(\boldsymbol{u}(h+\zeta)) = 0 \tag{3.3}$$

$$\frac{\partial \boldsymbol{u}}{\partial t} + \boldsymbol{u} \cdot \nabla_h \boldsymbol{u} + g\nabla_h \zeta = 0 \tag{3.4}$$

where ζ is the surface elevation, $\boldsymbol{u}$ is the horizontal velocity vector, ∇_h represents the horizontal gradient operator $\left(\frac{\partial}{\partial x}, \frac{\partial}{\partial y}\right)$, and g is the gravity acceleration, and where the contribution of the bottom stresses has been neglected in the momentum equation (Peregrine, 1972).

The main hypothesis here is that the pressure has an hydrostatic distribution or, what is equivalent, that the horizontal velocity is constant over depth. It must also be noticed that the previous equations do not include any dissipation terms due to wave breaking.

Moreover, the nonlinear shallow water equations, also called finite-amplitude shallow water equations, do not include any frequency dispersion mechanism. Then, when using them, different waves travel with different velocities, according to the dispersion relationship which links the wave speed c to the frequency f and the local water depth h. However the nonlinear shallow water equation do include the mechanism of amplitude dispersion. In order to explain both these statements, it is useful to put eqs. (3.3) and (3.4) in characteristic form (Peregrine, 1972). Let's consider, for simplicity, the two-dimensional case, thus the velocity vector $\boldsymbol{u}$ is reduced to the scalar velocity u, eqs. (3.3) and (3.4) become

$$\frac{d}{dt}(u + \pm 2c) = 0 \tag{3.5}$$

which is valid only along the characteristic curves

$$\frac{dx}{dt} = u \pm c \tag{3.6}$$

Eq. (3.5) states that the wave amplitude and the velocity are constant along the characteristic curve, then each portion of the waves travels at its own speed, $u + c$. The dispersion relationship is represented by the equation

$$c = \sqrt{g(h + \zeta)} \tag{3.7}$$

where the wave celerity c only depends on the local total water depth $h + \zeta$ and not on the wavelength L. Then, eq. (3.7) shows that the crest of the wave travels faster than the wave trough, generating a steepening of the front face of the wave, which, in other words, represents the mechanism of amplitude dispersion. On the other hand, in eq. (3.7) the wave celerity c is independent on the wave number, or on the wave length, then no frequency dispersion mechanism can be modeled by using this kind of equations.

The latter characteristic, even though reasonable in shallow waters, is not appropriate for engineering purposes, since in this case also the accurate modelling of the propagation in deeper waters is extremely important. Indeed, often, the wave conditions (wave height, wave period, direction of propagation, etc.) are known in deep waters, where the wave meters are usually placed. This is the most common case, for example, along the Italian coastlines, where the SIMN (Hydrographic and Mareographic National Service) has installed several buoys far from the beaches, in order to perform the real-time monitoring of the offshore wave conditions. Thus the aim of the wave propagation models is to bring the information about the wave field, available far from the coast, to the nearshore region, where they are required for practical applications.

Also, due to the lack of a frequency dispersion mechanism, the nonlinear shallow water equation are not able to predict any solution of constant form, such as solitary

or cnoidal waves, whose existence in nature has been proven in the case of constant water depth. In fact, according to the nonlinear shallow water equations, the wave will continue to steep until it reaches a vertical front. However, at that point, the assumption that the horizontal scale is much larger than the vertical one does not hold anymore.

Besides, this kind of equations do not include any mechanism representing the dissipation of energy due to breaking, and do conserve energy even inside the surf zone. Therefore, in order to describe the motion of a breaking wave, these equations are often used along with a dissipative numerical scheme (such as the Lax-Wendroff method). This approach has been developed starting with Hibberd and Peregrine (1979), Packwood and Peregrine (1980) and Packwood (1983). Later Kobayashi *et al.* (1989) and Kobayashi and Wurjanto (1992) used it to study the swash zone in very steep bottom conditions, such as the ones characteristic of engineering structures.

Svendsen and Putrevu (1995) give an overview of the advantages and disadvantages of using such an approach. In particular, they recognize the simplicity and robustness of this method, its capability to deal with irregular waves, and, at least in principle, obliquely incident waves and to handle every kind of topography. Moreover, the nonlinear shallow water equations have been widely used in order to model the shoreline motion, that is the uprush and backwash inside the swash zone, on the strength of their simple shoreline boundary condition.

On the other hand, Svendsen and Putrevu (1995) notice that, by using this type of models, the breaking point is strictly dependent on the distance of the offshore boundary, which obviously does not have any physical meaning. In fact, being the dissipation inside the surf zone only numerical, the waves will start to break at a certain distance from the off-shore boundary conditions. This distance is fixed by the grid size, once the distance from the initial computational point is established, regardless the real physics of the phenomenon. Besides, an accurate modelling of the front of the wave cannot be performed, since the front gets unrealistically vertical and it is frozen by the numerical scheme.

On the other hand, Brocchini *et al.* (2001) and Peregrine (2002) claim that this is a simpler and straightforward way to model breaking, compared to the semi-empirical approaches used to insert the breaking effects in the Boussinesq models, which will be discussed in Section 3.3.3. Furthermore, since according to the hypothesis of hydrostatic pressure the horizontal velocity is assumed uniform along the depth, by using the nonlinear shallow water equations only the mean velocity can be determined, not allowing speculations about the velocity profile; whereas the Boussinesq models, which will be presented in the following sections, do specify also the vertical distribution of the horizontal velocity (or flow potential). The importance of a correct prediction of the velocity profiles is even more important in the case of breaking waves, as it will be made clearer later.

3.3 Boussinesq-type of models

The Boussinesq equations, as well as the nonlinear shallow water equations, are depth integrated equations used to model the short wave motion in the nearshore region. Since their introduction, with the paper by Peregrine (1966), for the constant depth case, and by Peregrine (1967), for the variable depth case, these models have been widely adopted for engineering purposes, becoming one the most popular tool for simulating the wave propagation both in the shoaling and, making some simplifications, in the surf zone.

By assuming a velocity profile over depth and a non-hydrostatic pressure distribution, the Boussinesq models include nonlinearity as well as frequency dispersion, while the effects of breaking inside the surf zone has been incorporated following several approaches. It comes out that the standard form of the Boussinesq equations, derived in the case of constant depth, differs from the nonlinear shallow water equations only by a term in the momentum equation. This allows to represents the frequency dispersion, taking into account the effects of the vertical acceleration on both the horizontal velocity and the pressure.

In the following presentation the Boussinesq-type of models have been classified as standard Boussinesq models, described in Section 3.3.1, and extended Boussinesq models, discussed in Section 3.3.2. This is to clarify the difference between the original models, which are rigorously valid in shallow waters, and those with improved dispersive characteristics and better nonlinear properties, which allows to get accurate results even when they are applyed in deeper waters. Since the aim of this work is to contribute to the improvement of the modelling of breaking by using a Boussinesq type of model, in Section 3.3.3 the approaches used in this type of models to incorporate the surf zone energy dissipation, or, in other words, the increase of momentum flux, are discussed.

3.3.1 Standard Boussinesq models

The Boussinesq equations were first derived in Peregrine (1966) and in Peregrine (1967) as a better approximation for steep waves than the Airy equations, in particular by analyzing the case of a solitary wave propagating over constant depth and over a gentle uniform sloping beach respectively. More specifically, Peregrine (1967) derived the equations for varying depth under the assumption of irrotational motion, that is of nonbreaking waves, integrating over depth the Euler's equation of motion and using a pertubation method. He obtained the following continuity and momentum equations:

$$\frac{\partial \zeta}{\partial t} + \nabla[(h+\zeta)\overline{\mathbf{u}}] = 0 \tag{3.8}$$

$$\frac{\partial \overline{\mathbf{u}}}{\partial t} + (\overline{\mathbf{u}} \cdot \nabla)\overline{\mathbf{u}} + \nabla\zeta = \frac{1}{2}h\frac{\partial}{\partial t}\nabla[\nabla \cdot (h\overline{\mathbf{u}})] - \frac{1}{6}h^2\frac{\partial}{\partial t}\nabla(\nabla \cdot \overline{\mathbf{u}}) \tag{3.9}$$

where $\overline{\mathbf{u}}$ is the depth averaged velocity ad the other symbols have the same meaning as before.

It should be stressed that one of the underlying assumptions of these equations is that the slope varies gently, in such a way that the appearance of short waves reflected by the beach, due to a relatively rapid change of water depth compared to the variation of the incident wave, is avoided.

It must also be noticed that another important approximation here is the so called Boussinesq approximation, that is, it is assumed that the nonlinearity effects of the waves balance exactly the dispersive effects. In other words, it is assumed that

$$O(\delta) = O(\mu^2) \tag{3.10}$$

or

$$O\left(\frac{\delta}{\mu^2}\right) = O(U_r) = 1 \tag{3.11}$$

where $U_r = \delta/\mu^2$ is the Ursell number, representing the balance between the shallow water steepening and the effect of water acceleration. Indeed, it is this balance of frequency dispersion and nonlinearity effect which allows for the existence of permanent form solutions for constant water depth, such solitary or cnoidal waves, as exact solutions of the Boussinesq equations.

The aforementioned Boussinesq assumption is made in all the standard Boussinesq models, the main difference being the definition of representative velocity: depth averaged velocity, $\overline{\mathbf{u}}$, depth integrated velocity, $\mathbf{Q}$, velocity at the bottom, $\mathbf{u}_b$, or at the surface, $\mathbf{u}_s$. In some cases, as in Wei *et al.* (1995), also the velocity potential, ϕ_α, has been adopted as dependent variables.

As noticed by Liu (1995), the limitations of the standard Boussinesq models are mainly two. The first one is related to the hypothesis of weak nonlinearity, whereas in very shallow water, close to the breaking point, the nonlinearity of the waves is important. The second one, instead, is directly associated to the Boussinesq approximation. In fact, while in shallow waters the nonlinear parameter δ can reach a relatively high value, the dispersive parameter becomes smaller as the depth decreases. Then, Liu concludes that free surface profile close to breaking obtained as solutions of the Boussinesq waves are usually more symmetric with respect to the wave crest than those observed in the laboratory. Therefore, many efforts have been put into applying the Boussinesq-type of equations within region with larger water depth, i.e. with higher values of the parameter μ, and at the same time to developing fully nonlinear models, i.e. with no limitation on the value of δ.

3.3.2 Extended Boussinesq models

The Boussinesq standard model previously described are called weakly-dispersive weakly-nonlinear. The weak dispersiveness is due to the fact that they are restricted to small values of μ^2, so that their applicability is restricted to the shallow water region, where the dispersive effects are small; while in deep and intermediate waters the exact linear dispersion relationship is not represented accurately by the

linearized equations. It has been proven that different set of equations have different depth limits, depending on the type of horizontal velocity (depth averaged, at the bottom, at the surface, etc.) chosen as independent variable to express the vertical distribution of the horizontal velocity u.

On the other hand, the weak nonlinearity, due to the small values of δ, does not allow for a good representation of the highly nonlinear wave characteristics in the shoaling region, just before the waves start breaking. To extend the validity toward deeper waters, several kind of modified Boussinesq models have been proposed during the last decade.

Witting (1984) used two calibration coefficients in the series expansion for the horizontal velocity, in order to optimize the accuracy of the wave celerity in deeper water, but his approach is difficult to be extended to two horizontal dimensions and it is only valid in water of constant depth.

Madsen *et al.* (1991) noticed that the dispersion relationship can be written in a general form for several kind of Boussinesq equations

$$\frac{c^2}{gh} = \frac{1 + Bk^2h^2}{1 + \left(B + \frac{1}{3}\right)k^2h^2} \tag{3.12}$$

with B constant. In Witting's case, this constant is estimated as $B = 1/15$, corresponding to the choice of the depth averaged velocity. From comparisons with the first-order Stokes theory, it turns out that this is the optimal choice, meaning that the approximation of the exact linear dispersion equation is good for a wider range of water depth and not only in very shallow water.

Madsen *et al.* (1991) rearranged the terms in the standard Boussinesq equations, by adding to the momentum equation some quantities depending on the third derivatives of the velocity and of the surface elevation and from B itself. Without affecting the accuracy of the Boussinesq equation in shallow waters, in this way they improved the dispersive characteristics of the equations.

The same method have been used by Madsen and Sørensen (1992), Madsen *et al.* (1997), Madsen and Schäffer (1998), who applied the linear operator:

$$\mathrm{L} = 1 + B\mu^2h^2\frac{\partial^2}{\partial x^2} \tag{3.13}$$

to the terms in the momentum equation. This is basically equivalent to a rearrangement of the terms in the momentum equation and does not affect the order of accuracy of the model. Veeramony and Svendsen (1999) applied the same operator to its weakly nonlinear model.

In order to perform the same task, that is the enhancement of the dispersive characteristics of the Boussinesq models, a different approach has been presented by Nwogu (1993). He used as reference velocity a velocity at the arbitry level u_α, where the value of the level z_α is chosen in order to minimize the errors between the exact linear dispersion relationship and the one derived from the linearized form of Nwogu's equations. Defining the parameter

$$\alpha = \frac{1}{2}\left(\frac{z_\alpha}{h}\right)^2 + \frac{z_\alpha}{h} \tag{3.14}$$

it was found that the value $\alpha = -0.393$ is the optimal value, i.e. the one that gives the smallest errors.

Even though the approaches described before are quite different and the approach adopted by Madsen and collegues are very similar to those obtained by Nwogu.

Nwogu's approach has been followed by Wei *et al.* (1995), among others. The latter pointed out the importance of removing the weakly nonlinear hypothesis, not only to get a better prediction of the highly nonlinear characteristics of the waves as they approach the breaking, but also to take real advantage from the improved dispersive characteristics. They derived a fully nonlinear Boussinesq model for surface waves, in terms of the velocity potential ϕ, retaining all the terms in δ, hence the attribute of fully nonlinearity.

Following Wei *et al.* (1995), in Gobbi and Kirby (1999) and Gobbi *et al.* (2000), not only a Boussinesq model accurate up to order $O(kh)^4$ is derived, but also, extending Nowgu's original idea, two reference velocities, at two different levels, are adopted in order to give better linear dispersive characteristics.

Moreover, Madsen and Schäffer (1998) and then Agnon *et al.* (1999) have derived a procedure which allows to derive an infinite-order Boussinesq type differential equation, separately solving the linear part of the problem and the nonlinear free-surface boundary conditions.

Kennedy *et al.* (2001), starting from Wei *et al.* (1995) equations, extended Nowgu's approach considering a time-varying component dependent on surface elevation, with the aim of improving the nonlinear properties of the model.

More recently, Kennedy *et al.* (2002) have derived simplified higher-order Boussinesq equations. Their equations were of $O(\mu^4)$ but showed only lower-order terms, up to $O(\mu^2)$, in case of flat bed or slopes of $O(\nabla h)$, obtaining good dispersion and shoaling properties in the case of flat bed and improving the shoaling characteristics on a sloping beach.

3.3.3 The approaches to breaking modelling

Although the Boussinesq model are able to handle very efficiently several nearshore phenomena, such as refraction, diffraction, shoaling, dispersion and nonlinear interactions, nevertheless no Boussinesq model is able to predict by itself if, when and where a wave breaks. Therefore the effects of wave breaking , that is the dissipation of wave energy and the corresponding increase of momentum flux, have to be included into the equations.

Thus, in a Boussinesq model aiming to simulate the propagation of breaking waves in the surf zone two crucial tasks need to be accomplished: first, it is necessary to define a breaking criterion, depending on some wave characteristics, in order to detect the location of the breaking point; second, the modelling of the additional terms representing the excess of momentum needs to be performed in a very accurate manner.

A very simple approach to parameterize the wave breaking is the one adopted in Zelt (1991), where an additional artificial eddy viscosity ν_a is considered in the

momentum equation to model the dissipation of energy, by conserving the overall momentum. The diffusive effect due to ν_a tries to mimic the characteristics and the action of the bore of a breaking wave. The breaking criterion used by Zelt is related to a critical value of the velocity gradient in the cross-shore directions u_x (which for breaking waves should be negative) and to the limiting ratio $H/h = 0.7 \div 0.8$, with H wave height, obtained for solitary waves on constant depth. It can be written as

$$u_x \sqrt{\frac{h+\zeta}{g}} \leq -0.30 \tag{3.15}$$

Karambas and Koutitas (1992) adopted an eddy viscosity approach too, but their model lies on the consideration that the breaking can be treated as unresolved turbulent motion, both in presence of the large scale eddies within the outer surf and within the inner surf zone. By using the mixing length hypothesis, they determined the eddy viscotity coefficient from the numerical integration of the turbulent transport equation. The breaking criterion used, instead, relates the crest elevation at the breaking point, ζ_{cb}, with the wave length in deep water, L_0.

The simple eddy viscosity approach by Zelt has been adopted also by Kennedy *et al.* (2000) and Chen *et al.* (2000) for their 1D and 2D Boussinesq models, respectively, but they considered a different criterion for the onset of breaking, relating the position of the breaking point to the value of the variation in time of the surface elevation, ζ_t. In fact, noticing that once the wave has broken it will stop to break either when it reaches the shoreline or when it attains a stable configuration, they assume that the breaking begins if ζ_t reaches a threshold value, and that then this value decreases in time with the age of the breaking event.

A similar approach was adopted in the breaking criterion proposed by Schäffer *et al.* (1993), where the breaking starts when the slope of the water surface α exceed the threshold α_b (see Figure 3.1)

$$\alpha \geq \alpha_b \tag{3.16}$$

and the breaking stops if

$$\alpha \leq \alpha_0 \tag{3.17}$$

with the values of both α_b and α_0 calibrated by using experimental observations.

Then, after the breaking has started, an exponential decrease in time of α is hypothesized

$$\tan\alpha = \tan\alpha_0 + (\tan\alpha_b - \tan\alpha_0)\exp\left[-\ln 2\frac{t-t_b}{T_b}\right] \tag{3.18}$$

where t_b is the instant of time at which the breaking event starts and T_b is the duration of the breaking event.

Schäffer *et al.* (1993) used the roller approach to incorporate the effects of breaking inside the Boussinesq model. This was previously done by Brocchini *et al.* (1992), who considered the contribution of the roller only by means of a

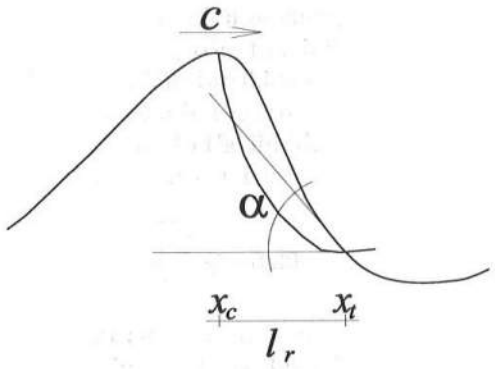

Figure 3.1: Schäffer *et al.* (1993) breaking criterion

pressure term in the momentum equation, due to the weight of the roller. Indeed Brocchini *et al.* (1992), following Deigaard and Fredsøe (1989), treat the roller as a solid body, which does not participate in the fluid motion. In Schäffer *et al.* (1993), instead, taking into account that the generation of the surface roller will introduce a non-uniform velocity, the horizontal velocity is assumed uniform over depth beneath the roller, and equal to u_0, whereas in correspondence of the roller the velocity is assumed equal to the wave speed c, that is

$$u = \begin{cases} c & \zeta - \zeta_e \leq z \leq \zeta \\ u_0 & -h \leq z \leq \zeta - \zeta_e \end{cases} \tag{3.19}$$

where ζ_e is the elevation of the lower edge of the roller (see Fig. 3.2).

This was the same vertical velocity profile assumed by Svendsen (1984) to study the wave height distribution and the set-up inside the surf zone. The introduction of this velocity profile leads to express the excess of momentum flux due to breaking as function of the geometry of the surface roller, i.e. the thickness of the roller ζ_s, which they define through an artificially made-up shape factor.

In all the above models the assumption of irrotational motion is underlined, whereas, as it has been already discussed in Chapter 2, right after the onset of breaking a lot of vorticity from the surface is introduced inside the domain and the hypothesis of irrotationality does not hold anymore. This is why, trying to use a more physical approach, Veeramony and Svendsen (2000) removed the hypothesis of irrotational motion and solved analytically the vorticity transport equation coupled with a weakly nonlinear Boussinesq model with enhanced dispersive characteristics. In their breaker model, Veeramony and Svendsen (2000) considered that the injection of vorticity is due to the dynamics inside the roller and it is spread toward the rest of the domain through the lower edge of the roller. Veeramony and Svendsen (2000) considered the similarity between hydraulic jumps and breaking wave in order to specify both the boundary condition and the roller geometry; in fact they used the findings of the experimental investigations on three hydraulics jumps with low Froude number (Svendsen *et al.*, 2000) to get the values

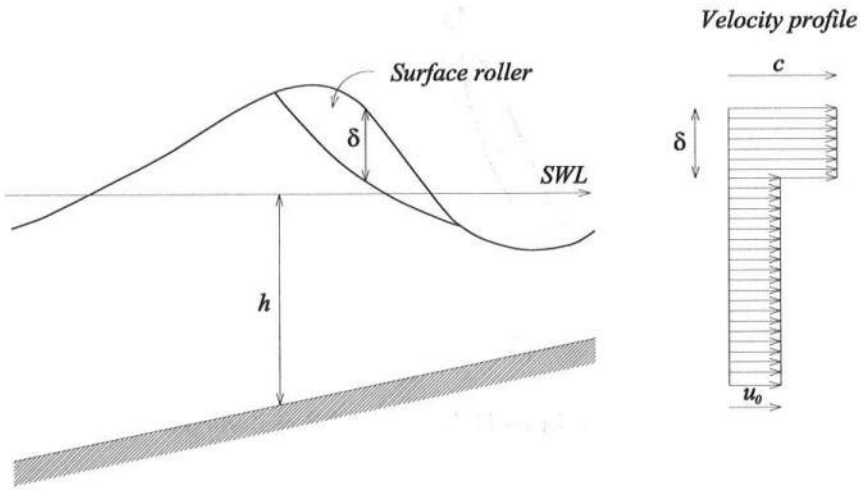

Figure 3.2: Velocity profile assumed under a breaking wave by Schäffer *et al.* (1993)

for the thickness of the roller ζ_s and the value of vorticity at the lower edge of the roller ω_s.

The vertical velocity profile they used, thus, it is a generalization of that of Schäffer *et al.* (1993) and it takes into account the contribution due to presence of vorticity inside the domain. Since this is the approach also adopted in the present work, a more detailed discussion about it will be presented in the following chapters.

Chapter 4

The flow in the surf zone through a 1D Boussinesq model

4.1 Overview

The Boussinesq model adopted in this work is a modified version of the weakly nonlinear model presented by Veeramony and Svendsen (2000) in order to investigate the flow inside the surf zone. In particular the one presented here is a fully nonlinear model, it is worth pointing out that a previous version of it has been already introduced in Veeramony and Svendsen (1999). Thus the model developed in the framework of this thesis can be seen, with respect to the last one an updated version, while from the numerical one a debugged and improved release. The main feature of the Veeramony and Svendsen's model, and the reason for which this model seems to be the most suitable for applications within the surf zone, is that the hypothesis of irrotationality has been removed. This allows to take into account that, after the onset of breaking, the flow cannot be considered to be potential anymore, since, as it has been widely discussed in Chapter 2, a huge amount of vorticity is produced by high surface curvature at breaking and then it is convected inside the flow.

Generally speaking, the Boussinesq equations are depth averaged equations. Indeed the procedure followed to get the equations starts from the continuity and Reynolds equations. Then, assuming incompressible fluid, impermeable and fixed bed, gentle beach slope and neglecting the effects of the bottom boundary layer, by using the free slip condition at the bottom, the equations are integrated over depth and the Leibniz rule is applied along with the boundary conditions at the surface and at the bottom. The pressure term is eliminated from the equations and an expression for the horizontal velocity is given, as a function of the depth averaged velocity $\bar{u}$. Since the Boussinesq equations are depth integrated equations,

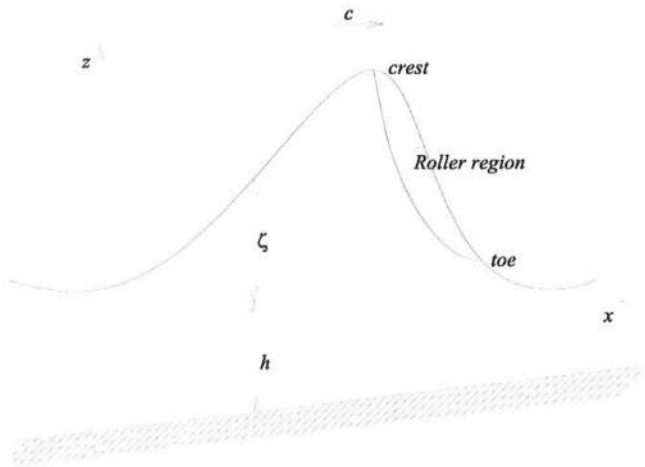

Figure 4.1: Formulation of the problem: reference system.

they cannot handle double connected domain, such as those typical of plunging breaker. For this reason, this model, as all the other Boussinesq type of model, is theoretically valid only for spilling breaker.

Since the aim of the present work is to contribute to an accurate understanding and prediction of the breaking process, the Boussinesq model focus on the analysis of the flow only on the vertical plane corresponding to the direction of wave propagation, or in other words, it is assumed that the waves are propagating in a direction perpendicular to the beach. Indeed, it is right over this plane that the main exchanges of vorticity take place, spreading from the region close to the surface where the vorticity is generated to the interior of the domain. Hence, here, wave-wave interactions in the transverse direction have been neglected.

We have largely followed Veeramony and Svendsen (1999) in the derivations of governing equations, and in the following sections they are presented with some details. This has been done for two reasons: to clearly show how the final expressions are recovered and to clearly show the differences with the previous version of Veeramony and Svendsen (1999). Moreover both a preliminary discussion of the adopted scaling argument and a physical explanation of every term are given.

4.2 Formulation of the problem

Under the hypothesis of incompressible flow and fixed bottom, following Veeramony and Svendsen (1999), the Boussinesq type of equations have been derived by integrating the Reynolds equations over the depth and applying the kinematic and dynamic boundary conditions at the bottom and at the free surface. In particular with reference to the scheme shown in Figure 4.1, by assuming (x, z) as reference

system and by taking (u, w) as horizontal and vertical velocity components respectively, the surface elevation, ζ, and the depth averaged velocity, $\overline{u}$, can be taken as dependent variables of the Boussinesq equations.

The scaling argument is here discussed at first in order to get the dimensionless form of the equations. This is done in order to permit to bias the magnitude of the terms and therefore to allow simplification of some of the smallest ones. The dimensionless parameters,

$$\mu = k_0 h_0 \text{ and } \delta = \frac{a_0}{h_0} \tag{4.1}$$

whose function and importance have been discussed in Chapter 3, are introduced.

In shallow waters it is usually assumed that the changes in the horizontal dimension, scaled through the wave number k_0, are much slower than the change in the vertical direction, scaled by the water depth h_0 (or by the wave amplitude a_0, depending on the vertical scale of variation of the variable considered).

Therefore, it results that the independent variables, i.e. the horizontal coordinates x, the vertical coordinate z and the time t, are scaled as follows:

$$x = k_0 \hat{x}; \qquad z = \frac{\hat{z}}{h_0}; \qquad t = k_0 \sqrt{g h_0}\hat{t} \tag{4.2}$$

while the surface elevation ζ and the stream function ψ becomes

$$\zeta = \frac{\hat{\zeta}}{a_0} \tag{4.3}$$

$$\psi = \frac{\hat{\psi}}{a_0 \sqrt{g h_0}} = \frac{\hat{\psi}}{\delta h_0 \sqrt{g h_0}} \tag{4.4}$$

where the pedix $(_0)$ indicates the values at a reference point in water of constant depth and the symbol $\hat{()}$ indicates the dimensional value of the variables.

As a consequence, from the definition of the horizontal and vertical velocities, u and w, through the stream function, ψ, and of the vorticity, ω, through u and w, the dependent variables are then scaled as

$$\hat{u} = \frac{\partial \hat{\psi}}{\partial \hat{z}} = \frac{\delta h_0 \sqrt{g h_0}}{h_0} \frac{\partial \psi}{\partial z} = \delta \sqrt{g h_0} u \tag{4.5}$$

$$\hat{w} = -\frac{\partial \hat{\psi}}{\partial \hat{x}} = -h_0 \delta h_0 \sqrt{g h_0} \frac{\partial \psi}{\partial x} = \delta \mu \sqrt{g h_0} w \tag{4.6}$$

$$\hat{\omega} = \frac{\partial \hat{u}}{\partial \hat{z}} - \frac{\partial \hat{w}}{\partial \hat{x}} = \frac{\delta \sqrt{g h_0}}{h_0} \frac{\partial u}{\partial z} - \delta \mu \sqrt{g h_0} k_0 \frac{\partial w}{\partial x} = \frac{\delta \sqrt{g h_0}}{h_0} \left(\frac{\partial u}{\partial z} - \mu^2 \frac{\partial w}{\partial x} \right) \tag{4.7}$$

By using this argument, in the case of irrotational motion, $\omega = 0$, the horizontal velocity will be almost constant over depth, since eq. (4.7) will give $\partial u / \partial z \sim O(\mu^2)$, whereas within the surf zone, in presence of rotational motion, it is reasonable to

assume that $\omega \sim O(1)$. Indeed a strong vertical variation of u, particularly close to the wave crest does show up.

It is worth pointing out that the beach slope is scaled as

$$h_x = \mu^2 \hat{h}_x \tag{4.8}$$

Indeed the more obvious scaling argument used above, which would have given $h_x = \mu \hat{h}_x$, would leads to beaches too steep, whereas one of the assumptions of this model is the gentleness of the slope.

4.2.1 Continuity equation

The continuity equation, stating the conservation of mass for an uncompressible flow ($\rho = \text{const}$), reads

$$\frac{\partial \hat{u}}{\partial \hat{x}} + \frac{\partial \hat{w}}{\partial \hat{z}} = 0 \tag{4.9}$$

integrating it over the water column, i.e. between the bottom, $\hat{z} = -\hat{h}$, and water surface, $\hat{z} = \hat{\zeta}$, gives

$$\int_{-\hat{h}}^{\hat{\zeta}} \frac{\partial \hat{u}}{\partial \hat{x}} d\hat{z} + \int_{-\hat{h}}^{\hat{\zeta}} \frac{\partial \hat{w}}{\partial \hat{z}} d\hat{z} = 0 \tag{4.10}$$

or

$$\int_{-\hat{h}}^{\hat{\zeta}} \frac{\partial \hat{u}}{\partial \hat{x}} d\hat{z} + \hat{w}(\hat{\zeta}) - \hat{w}(-\hat{h}) = 0 \tag{4.11}$$

By inserting into eq. (4.11) both the bottom boundary condition, valid under the hypothesis of impermeable and fixed bed,

$$\hat{w}(-\hat{h}) = -\hat{u}(-\hat{h}) \frac{\partial \hat{h}}{\partial \hat{x}} \tag{4.12}$$

and the kinematic free surface boundary condition

$$\frac{\partial \hat{\zeta}}{\partial \hat{t}} + \hat{u}(\hat{\zeta}) \frac{\partial \hat{\zeta}}{\partial \hat{x}} = \hat{w}(\hat{\zeta}) \tag{4.13}$$

and applying to it the Leibniz rule, the following depth integrated continuity equation is obtained

$$\frac{\partial \hat{\zeta}}{\partial \hat{t}} + \frac{\partial}{\partial \hat{x}} \int_{-\hat{h}}^{\hat{\zeta}} \hat{u} d\hat{z} = 0 \tag{4.14}$$

4.2.2 Momentum equation

The horizontal and the vertical Reynolds momentum equation, for uncompressible flow, are respectively

$$\frac{\partial \hat{u}}{\partial \hat{t}} + \frac{\partial \hat{u}^2}{\partial \hat{x}} + \frac{\partial \hat{u}\hat{w}}{\partial \hat{z}} = -\frac{1}{\rho}\frac{\partial \hat{p}}{\partial \hat{x}} + \frac{1}{\rho}\left(\frac{\partial \hat{\tau}_{xx}}{\partial \hat{x}} + \frac{\partial \hat{\tau}_{xz}}{\partial \hat{z}}\right) \tag{4.15}$$

$$\frac{\partial \hat{w}}{\partial \hat{t}} + \frac{\partial \hat{u}\hat{w}}{\partial \hat{x}} + \frac{\partial \hat{w}^2}{\partial \hat{z}} = -\frac{1}{\rho}\frac{\partial \hat{p}}{\partial \hat{z}} + \frac{1}{\rho}\left(\frac{\partial \hat{\tau}_{xz}}{\partial \hat{x}} + \frac{\partial \hat{\tau}_{zz}}{\partial \hat{z}}\right) - g \tag{4.16}$$

where $\hat{\tau}_{xx}$ and $\hat{\tau}_{xz}$ indicates the Reynolds stresses. Integrating over depth and using the Leibniz rule

$$\begin{aligned}
\frac{\partial}{\partial \hat{t}}\int_{-\hat{h}}^{\hat{\zeta}} \hat{u}d\hat{z} \;+\; & \frac{\partial}{\partial \hat{x}}\int_{-\hat{h}}^{\hat{\zeta}} \hat{u}^2 d\hat{z} - \left[\hat{u}\left(\frac{\partial \hat{\zeta}}{\partial \hat{t}} + \hat{u}\frac{\partial \hat{\zeta}}{\partial \hat{x}} - \hat{w}\right)\right]_{\hat{\zeta}} \\
- & \left[\hat{u}\left(\hat{u}\frac{\partial \hat{h}}{\partial \hat{x}} + \hat{w}\right)\right]_{-\hat{h}} = \frac{1}{\rho}\frac{\partial}{\partial \hat{x}}\int_{-\hat{h}}^{\hat{\zeta}} (-\hat{p} + \hat{\tau}_{xx})d\hat{z} \\
+ & \frac{1}{\rho}\hat{p}(-\hat{h})\frac{\partial \hat{h}}{\partial \hat{x}} + \frac{1}{\rho}\left[(\hat{\tau}_{xz} + \hat{p} - \hat{\tau}_{xx})_{\hat{\zeta}}\frac{\partial \hat{\zeta}}{\partial \hat{x}}\right] \\
- & \frac{1}{\rho}\left[\hat{\tau}_{xz}(-\hat{h}) + \hat{\tau}_{xx}(-\hat{h})\frac{\partial \hat{h}}{\partial \hat{x}}\right]
\end{aligned} \tag{4.17}$$

which applying the boundary conditions (4.12) and (4.13) becomes

$$\begin{aligned}
\frac{\partial}{\partial \hat{t}}\int_{-\hat{h}}^{\hat{\zeta}} \hat{u}d\hat{z} \;+\; & \frac{\partial}{\partial \hat{x}}\int_{-\hat{h}}^{\hat{\zeta}} \hat{u}^2 d\hat{z} = \frac{1}{\rho}\frac{\partial}{\partial \hat{x}}\int_{-\hat{h}}^{\hat{\zeta}} (-\hat{p} + \hat{\tau}_{xx})d\hat{z} \\
+ & \frac{1}{\rho}\hat{p}(-\hat{h})\frac{\partial \hat{h}}{\partial \hat{x}} + \frac{1}{\rho}\left[(\hat{\tau}_{xz} + \hat{p} - \hat{\tau}_{xx})_{\hat{\zeta}}\frac{\partial \hat{\zeta}}{\partial \hat{x}}\right] \\
- & \frac{1}{\rho}\left[\hat{\tau}_{xz}(-\hat{h}) + \hat{\tau}_{xx}(-\hat{h})\frac{\partial \hat{h}}{\partial \hat{x}}\right]
\end{aligned} \tag{4.18}$$

The last two terms represents the horizontal components of the forces on the free water surface and at the bottom, respectively,

$$\hat{R}_x^S = \frac{1}{\rho}\left[(\hat{\tau}_{xz} + \hat{p} - \hat{\tau}_{xx})_{\hat{\zeta}}\frac{\partial \hat{\zeta}}{\partial \hat{x}}\right] \tag{4.19}$$

$$\hat{\tau}_x^B = \frac{1}{\rho}\left[\hat{\tau}_{xz}(-\hat{h}) + \hat{\tau}_{xx}(-\hat{h})\frac{\partial \hat{h}}{\partial \hat{x}}\right] \tag{4.20}$$

In dimensional form, the exact depth integrated momentum equation results

$$\frac{\partial}{\partial \hat{t}}\int_{-\hat{h}}^{\hat{\zeta}} \hat{u}d\hat{z}+\frac{\partial}{\partial \hat{x}}\int_{-\hat{h}}^{\hat{\zeta}} \hat{u}^2 d\hat{z} = \frac{1}{\rho}\hat{p}(-\hat{h})\frac{\partial \hat{h}}{\partial \hat{x}}+\frac{1}{\rho}\frac{\partial}{\partial \hat{x}}\int_{-\hat{h}}^{\hat{\zeta}}(-\hat{p}+\hat{\tau}_{xx})d\hat{z}+\hat{R}_x^S-\hat{\tau}_x^B \quad (4.21)$$

where no simplifying assumptions have been introduced yet.

Considering that the present model aims to analyze the flow within the surf zone, where the bottom generated turbulence is at least one order of magnitude of that due to the breaking, it is reasonable here to neglect the effect of the bottom boundary layer. Thus, applying the free slip boundary condition, it is assumed that the shear stresses at the bottom are zero, i.e. $\hat{\tau}_x^B = 0$. From a scaling argument, it can also been shown that the contribution of the deviatoric normal stresses, τ_{xx}, can be reasonably neglected if compared to the pressure, since it is μ time smaller than p. This, on the other hand, indicates that the structure of the turbulence is only weakly anysotropic in the x direction.

Moreover, since the region of interest is the intermediate/shallow water area, where the action of the wind on the free water surface is very weak, also the horizontal forces on the surface, $\hat{R}_x^S$ has been neglected.

According to the previous considerations, eq. (4.21) can be reasonable approximated as:

$$\frac{\partial}{\partial \hat{t}}\int_{-\hat{h}}^{\hat{\zeta}} \hat{u}d\hat{z}+\frac{\partial}{\partial \hat{x}}\int_{-\hat{h}}^{\hat{\zeta}} \hat{u}^2 d\hat{z} = \frac{1}{\rho}\hat{p}(-\hat{h})\frac{\partial \hat{h}}{\partial \hat{x}}-\frac{1}{\rho}\frac{\partial}{\partial \hat{x}}\int_{-\hat{h}}^{\hat{\zeta}}\hat{p}d\hat{z} \quad (4.22)$$

In order to transform eq. (4.22) in dimensionless form, the scaling argument presented above must be applied

$$\frac{\partial}{\partial t}\int_{-h}^{\delta\zeta} udz+\delta\frac{\partial}{\partial x}\int_{-h}^{\delta\zeta} u^2 dz = p(-h)\frac{\partial h}{\partial x}-\frac{\partial}{\partial x}\int_{-h}^{\delta\zeta} pdz \quad (4.23)$$

To eliminate the pressure from eq. (4.23), the vertical momentum equation (4.16) is integrated between $\hat{z}$ and $\hat{\zeta}$, giving

$$\begin{aligned}\frac{\partial}{\partial \hat{t}}\int_{\hat{z}}^{\hat{\zeta}} \hat{w}d\hat{z} &- \hat{w}(\hat{\zeta})\frac{\partial \hat{\zeta}}{\partial \hat{t}}+\frac{\partial}{\partial \hat{x}}\int_{\hat{z}}^{\hat{\zeta}} \hat{u}\hat{w}d\hat{z}-\hat{u}(\hat{\zeta})\hat{w}(\hat{\zeta})\frac{\partial \hat{\zeta}}{\partial \hat{x}}+\hat{w}^2(\hat{\zeta})-\hat{w}^2 \\ &= -g(\hat{\zeta}-\hat{z})+\frac{\hat{p}(\hat{z})}{\rho}+\frac{1}{\rho}\frac{\partial}{\partial \hat{x}}\int_{\hat{z}}^{\hat{\zeta}}\hat{\tau}_{xz}d\hat{z}-\frac{\hat{\tau}_{xz}(\hat{\zeta})}{\rho}\frac{\partial \hat{\zeta}}{\partial \hat{x}} \quad (4.24)\end{aligned}$$

where the Leibniz rule has been applied. Substituting the kinematic free surface boundary condition (4.13) and neglecting the stresses on the surface, the expression for the pressure is

$$\frac{\hat{p}(\hat{z})}{\rho} = g(\hat{\zeta}-\hat{z})-\hat{w}^2+\frac{\partial}{\partial \hat{t}}\int_{\hat{z}}^{\hat{\zeta}}\hat{w}d\hat{z}+\frac{\partial}{\partial \hat{x}}\int_{\hat{z}}^{\hat{\zeta}}\left(\hat{u}\hat{w}-\frac{\hat{\tau}_{xz}}{\rho}\right)d\hat{z} \quad (4.25)$$

The above expression indicates that the pressure is not only composed by the hydrostatic part, as it is assumed in the nonlinear shallow water equations, but has a non-hydrostatic contribution due to the vertical fluid motion, that is to the vertical acceleration and to the action of the adjacent water columns, which contribute to support the weight of the closer water columns.

In order to model the turbulent shear stress τ_{xz}, it is useful now to introduce the concept of the eddy viscosity. The eddy viscosity can be described as the product of some length scale of the turbulence and of some characteristic velocity. From the measurements of Cox *et al.* (1995), the eddy viscosity can be described as

$$\hat{\nu}_t \simeq C_\nu \hat{h}\sqrt{g\hat{h}} \tag{4.26}$$

where C_ν is a constant value, which has been experimentally calibrated and taken in the range $0.01 \div 0.03$. The scaling for $\hat{\nu}_t$ is then

$$\hat{\nu}_t = \mu h_0 \sqrt{g h_0}\nu_t \tag{4.27}$$

where the anisotropy of the turbulence in the z direction has been taken into account.

The scaling for the shear stress $\hat{\tau}_{xz}$ is

$$\hat{\tau}_{xz} = \delta\mu\rho g h_0 \nu_t \left(\frac{\partial u}{\partial z} + \mu^2 \frac{\partial w}{\partial x}\right) \tag{4.28}$$

and the expression for the total pressure, in dimensionless form, results

$$\begin{aligned} p(z) &= (\zeta - \frac{z}{\delta}) - \delta\mu^2 w^2 + \mu^2 \frac{\partial}{\partial t}\int_z^{\delta\zeta} w dz + \delta\mu^2 \frac{\partial}{\partial x}\int_z^{\delta\zeta} uw dz \\ &\quad -\mu^2 \frac{\partial}{\partial x}\int_z^{\delta\zeta} \nu_t \left(\frac{\partial u}{\partial z} + \mu^2 \frac{\partial w}{\partial x}\right) dz \end{aligned} \tag{4.29}$$

Neglecting terms smaller than $O(\mu^2)$, the following approximated relationship is obtained:

$$\begin{aligned} p(z) &= (\zeta - \frac{z}{\delta}) - \delta\mu^2 w^2 + \mu^2 \frac{\partial}{\partial t}\int_z^{\delta\zeta} w dz + \delta\mu^2 \frac{\partial}{\partial x}\int_z^{\delta\zeta} uw dz \\ &\quad -\mu^2 \frac{\partial}{\partial x}\int_z^{\delta\zeta} \nu_t \frac{\partial u}{\partial z} dz + O(\mu^4) \end{aligned} \tag{4.30}$$

Taking the derivatives in x of eq. (4.30)

$$\begin{aligned} \frac{\partial p(z)}{\partial x} &= \frac{\partial}{\partial x}(\zeta - \frac{z}{\delta}) - \delta\mu^2 \frac{\partial w^2}{\partial x} + \mu^2 \frac{\partial^2}{\partial x \partial t}\int_z^{\delta\zeta} w dz + \delta\mu^2 \frac{\partial^2}{\partial x^2}\int_z^{\delta\zeta} uw dz \\ &\quad -\mu^2 \frac{\partial^2}{\partial x^2}\int_z^{\delta\zeta} \nu_t \frac{\partial u}{\partial z} dz + O(\mu^4) \end{aligned} \tag{4.31}$$

integrating over the entire water column and applying again the Leibniz rule, the pressure term to be inserted into the momentum equation is:

$$\begin{aligned}\frac{\partial}{\partial x}\int_{-h}^{\delta\zeta} p dz &= (h+\delta\zeta)\zeta_x - \delta\mu^2\int_{-h}^{\delta\zeta}\frac{\partial w^2}{\partial x}dz + \mu^2\int_{-h}^{\delta\zeta}\frac{\partial^2}{\partial x\partial t}\int_z^{\delta\zeta} w dz dz \\ &+\delta\mu^2\int_{-h}^{\delta\zeta}\frac{\partial^2}{\partial x^2}\int_z^{\delta\zeta} uw dz dz + p(-h)\frac{\partial h}{\partial x} \\ &-\mu^2\int_{-h}^{\delta\zeta}\frac{\partial^2}{\partial x^2}\int_z^{\delta\zeta}\nu_t\frac{\partial u}{\partial z}dz dz + O(\mu^4) \end{aligned} \tag{4.32}$$

By using the continuity equation (4.9) and the bottom boundary condition (4.12), the vertical velocity w can be expressed as function of the horizontal velocity u

$$w(z) = -\frac{\partial}{\partial x}\int_{-h}^{z} u dz \tag{4.33}$$

Substituiting the eqs. (4.32) and (4.33) into the eq. (4.23), the momentum equation is finally obtained

$$\begin{aligned}\frac{\partial}{\partial t}\int_{-h}^{\delta\zeta} u dz &+ \delta\frac{\partial}{\partial x}\int_{-h}^{\delta\zeta} u^2 dz + (h+\delta\zeta)\zeta_x \\ &- \mu^2\int_{-h}^{\delta\zeta}\frac{\partial^2}{\partial x\partial t}\int_z^{\delta\zeta}\frac{\partial}{\partial x}\int_{-h}^{z} u dz dz dz \\ &- \delta\mu^2\int_{-h}^{\delta\zeta}\frac{\partial}{\partial x}\left(\frac{\partial}{\partial x}\int_{-h}^{z} u dz\right)^2 dz - \mu^2\int_{-h}^{\delta\zeta}\frac{\partial^2}{\partial x^2}\int_z^{\delta\zeta}\nu_t\frac{\partial u}{\partial z}dz dz \\ &- \delta\mu^2\int_{-h}^{\delta\zeta}\frac{\partial^2}{\partial x^2}\int_z^{\delta\zeta} u\frac{\partial}{\partial x}\int_{-h}^{z} u dz dz dz = O(\mu^4) \end{aligned} \tag{4.34}$$

Eq. (4.34) is referred as combined momentum equation, since it is basically the horizontal depth integrated Reynolds equation of momentum, where the pressure and the vertical velocity have been eliminated by using the vertical depth integrated Reynolds momentum equation and the continuity equation, respectively.

4.2.3 The approximate equation for the horizontal velocity

The approach followed to solve the Boussinesq equations, namely, in the present model, eq. (4.9) and eq. (4.34), is to specify some reference velocity, such as the depth integrated velocity, the bottom velocity, the surface velocity or the velocity at some reference level, which are in some way representative of the entire velocity profile over the water column. To obtain the expression of the characteristic velocities, an expression for u in terms of the vertical coordinate z must be considered.

In the traditional Boussinesq model this is obtained expanding in powers of z the potential velocity ϕ and then solving the Laplace equation along with the correspondent boundary conditions, valid under the assumption of irrotational motion, in order to obtain the coefficients of the power series and then to express $u = \partial\phi/\partial x$.

For breaking waves a similar assumption is not adequate, since a very big amount of vorticity is produced close to the surface and introduced inside the flow, through the roller region. The hypothesis of irrotationality of the flow results then irrealistic.

Let's take instead the definition of the vorticity ω

$$\mu^2\psi_{xx} + \psi_{zz} = \omega \tag{4.35}$$

where ψ is the stream function, defined as

$$u = \frac{\partial\psi}{\partial z}$$

$$w = -\frac{\partial\psi}{\partial x}$$

The boundary condition at the bottom for the eq. (4.35) is

$$\psi(-h) = 0 \tag{4.36}$$

which express the condition of impermeability of the bed. Considering that

$$\int_{-h}^{\delta\zeta} u dz = \int_{-h}^{\delta\zeta} \frac{\partial\psi}{\partial z} dz$$

$$\psi(\delta\zeta) - \psi(-h) = \int_{-h}^{\delta\zeta} u dz$$

it is found the analogous boundary condition at the free surface

$$\psi(\delta\zeta) = \int_{-h}^{\delta\zeta} u dz \tag{4.37}$$

Thus, integrating eq. (4.35) between $-h$ and z

$$\psi_z = -\int_{-h}^{z} \mu^2\psi_{xx} dz + \psi_z(-h) + \int_{-h}^{z} \omega dz \tag{4.38}$$

since $u(-h) = (\partial\psi/\partial z)_{-h} = u_b$ is the velocity at the bottom (it should be recalled here that in the present model the free slip condition at the bed is considered, so $u_b \neq 0$)

$$\psi_z = -\int_{-h}^{z} \mu^2\psi_{xx} dz + \int_{-h}^{z} \omega dz + u_b \tag{4.39}$$

integrating again between $-h$ and z

$$\psi(z) = -\int_{-h}^{z}\int_{-h}^{z} \mu^2 \psi_{xx} dzdz + \int_{-h}^{z}\int_{-h}^{z} \omega dzdz + (h+z)u_b \tag{4.40}$$

Since the term ψ_{xx} is already of $O(\mu^2)$, in order to derive its expression from eq. (4.40), this last can be approximated up to the lowest order in μ^2

$$\psi(z) = \int_{-h}^{z}\int_{-h}^{z} \omega dzdz + (h+z)u_b + O(\mu^2) \tag{4.41}$$

then deriving twice with respect to x

$$\psi_{xx} = \int_{-h}^{z}\int_{-h}^{z} \omega_{xx} dzdz + (h+z)u_{bxx} + 2u_{bx}h_x + u_b h_{xx} + O(\mu^2) \tag{4.42}$$

Substituting in eq. (4.40)

$$\begin{aligned} \psi &= u_b(z+h) - \int_{-h}^{z}\int_{-h}^{z} \mu^2 \Big[\int_{-h}^{z}\int_{-h}^{z} \omega_{xx} dzdz + u_{bxx}(z+h) \\ &+ 2u_{bx}h_x + u_b h_{xx} \Big] dzdz + \int_{-h}^{z}\int_{-h}^{z} \omega dzdz + O(\mu^4) \end{aligned} \tag{4.43}$$

and expanding the integrals

$$\begin{aligned} \psi &= u_b(z+h) - \frac{\mu^2}{6} u_{bxx}(z+h)^3 - \frac{\mu^2}{2}(2u_{bx}h_x + u_b h_{xx})(z+h)^2 \\ &-\mu^2 \int_{-h}^{z}\int_{-h}^{z}\int_{-h}^{z}\int_{-h}^{z} \omega_{xx} dzdzdzdz + \int_{-h}^{z}\int_{-h}^{z} \omega dzdz \\ &+O(\mu^4) \end{aligned} \tag{4.44}$$

Finally, since $u = \partial\psi/\partial z$, the expression for the horizontal velocity u is obtained as

$$\begin{aligned} u &= u_b - \mu^2[2u_{bx}h_x + u_b h_{xx}](z+h) - \frac{\mu^2}{2} u_{bxx}(z+h)^2 \\ &-\mu^2 \int_{-h}^{z}\int_{-h}^{z}\int_{-h}^{z} \omega_{xx} dzdzdz + \int_{-h}^{z} \omega dz + O(\mu^4) \end{aligned} \tag{4.45}$$

It should be noticed that the splitting of the previous expression as

$$u = u_p + u_r \tag{4.46}$$

follows naturally. Considering that the first term is a contribution having a quadratic formulation in $(z+h)$, as in the classical potential flow formulation of the standard Boussinesq model, which will be called here the *potential velocity* u_p

$$u_p = u_b - \mu^2[2u_{bx}h_x + u_b h_{xx}](z+h) - \frac{\mu^2}{2}u_{bxx}(z+h)^2 + O(\mu^4) \tag{4.47}$$

and that the second term is a contribution due only to the vorticity ω, which will be called the *rotational velocity* u_r

$$u_r = \int_{-h}^{z} \omega dz - \mu^2 \int_{-h}^{z}\int_{-h}^{z}\int_{-h}^{z} \omega_{xx} dz dz dz + O(\mu^4) \tag{4.48}$$

The depth averaged potential velocity can be then express as

$$\begin{aligned}
\overline{u}_p &\equiv \frac{1}{h+\delta\zeta}\int_{-h}^{\delta\zeta} u_p dz \\
&= u_b - \frac{\mu^2}{2}(h+\delta\zeta)[2u_{bx}h_x + u_b h_{xx}] - \frac{\mu^2}{6}(h+\delta\zeta)^2 u_{bxx} + O(\mu^4) \\
&= u_b - \frac{\mu^2}{2}(h+\delta\zeta)(hu_b)_{xx} - \frac{\mu^2}{2}(h+\delta\zeta)\left(\frac{h}{3} + \frac{\delta\zeta}{3} - h\right)u_{bxx} + O(\mu^4) \\
&= u_b - \frac{\mu^2}{2}(h+\delta\zeta)(hu_b)_{xx} + \frac{\mu^2}{2}\left(h^2 - \frac{\delta^2\zeta^2 - \delta\zeta h + h^2}{3}\right)u_{bxx} + O(\mu^4) \\
&= u_b - \frac{\mu^2}{2}(h+\delta\zeta)(hu_b)_{xx} + \frac{\mu^2}{2}\left(h^2 - \frac{\Delta_2}{3}\right)u_{bxx} + O(\mu^4)
\end{aligned} \tag{4.49}$$

where

$$\Delta_2 = \delta^2\zeta^2 - \delta\zeta h + h^2 \tag{4.50}$$

.

Inverting eq. (4.49), the velocity at the bottom can be expressed as

$$u_b = \overline{u}_p + \frac{\mu^2}{2}(h+\delta\zeta)(hu_b)_{xx} - \frac{\mu^2}{2}\left(h^2 - \frac{\Delta_2}{3}\right)u_{bxx} + O(\mu^4) \tag{4.51}$$

Deriving with respect to x and retaining the terms up to $O(\mu^2)$

$$u_{px} = \overline{u}_{px} + O(\mu^2) \tag{4.52}$$

$$u_{pxx} = \overline{u}_{pxx} + O(\mu^2) \tag{4.53}$$

Substituting back into eq. (4.47) it is possible to eliminate the dependence on the velocity at the bottom in order to express the potential velocity

$$
\begin{aligned}
u_p &= \overline{u}_p + \frac{\mu^2}{2}(h+\delta\zeta)(h\overline{u}_p)_{xx} - \frac{\mu^2}{2}\left(h^2 - \frac{\Delta_2}{3}\right)\overline{u}_{pxx} \\
&\quad -\mu^2(z+h)[2h_x\overline{u}_{px} + h_{xx}\overline{u}_p] - \frac{\mu^2}{2}(z+h)^2\overline{u}_{pxx} + O(\mu^4) \\
&= \overline{u}_p + \frac{\mu^2}{2}(h\overline{u}_p)_{xx}[\delta\zeta - h - 2z] - \frac{\mu^2}{2}\overline{u}_{pxx}\left(-\frac{\Delta_2}{3} + z^2\right) + O(\mu^4) \\
&= \overline{u}_p + \mu^2(h\overline{u}_p)_{xx}\left(\frac{\Delta_1}{2} - z\right) + \frac{\mu^2}{2}\overline{u}_{pxx}\left(\frac{\Delta_2}{3} - z^2\right) + O(\mu^4) \qquad (4.54)
\end{aligned}
$$

where

$$\Delta_1 = \delta\zeta - h \qquad (4.55)$$

The total velocity is then written as function of both the depth averaged potential velocity and rotational velocity

$$
\begin{aligned}
u &= \overline{u}_p + \mu^2(h\overline{u}_p)_{xx}\left(\frac{\Delta_1}{2} - z\right) + \frac{\mu^2}{2}\overline{u}_{pxx}\left(\frac{\Delta_2}{3} - z^2\right) \\
&\quad u_r + O(\mu^4) \qquad (4.56)
\end{aligned}
$$

4.2.4 The fully nonlinear model

Once the expression for the total velocity u is obtained in terms of the depth averaged potential velocity $\overline{u}_p$ and of the vorticity ω, the equations, and in particularly the momentum equation, can be specified by substituting eq. (4.56) into eq. (4.34). The denomination *fully nonlinear* is used here, as briefly already discussed in Chapter 3, to remark that no assumption on the order of the nonlinear parameter $\delta = a/h$ has been made. This, in turn, means that the traditional Boussinesq approximation, which postulate the balance between the dispersive and nonlinear effects has been removed, in order to allow for the modelling of the flow close to the breaking point, where the waves have highly nonlinear characteristics.

The characteristic velocity chosen within the present model is the depth averaged velocity

$$\overline{u} = \frac{1}{h+\delta\zeta}\int_{-h}^{\delta\zeta} u dz \qquad (4.57)$$

From eq. (4.14) the continuity equation may be expressed as

$$\frac{\partial\zeta}{\partial t} + \frac{\partial}{\partial x}[\overline{u}(h+\delta\zeta)] = 0 \qquad (4.58)$$

It should be noticed that the continuity expression is exact, since no approximations has been made to get it.

It is convenient here to rewrite again the combined momentum equation expressed by eq. 4.34

$$\begin{aligned}\frac{\partial}{\partial t}\int_{-h}^{\delta\zeta} u dz &+ \delta\frac{\partial}{\partial x}\int_{-h}^{\delta\zeta} u^2 dz + (h+\delta\zeta)\zeta_x \\ &- \mu^2\int_{-h}^{\delta\zeta}\frac{\partial^2}{\partial x\partial t}\int_{z}^{\delta\zeta}\frac{\partial}{\partial x}\int_{-h}^{z} u dz dz dz \\ &- \delta\mu^2\int_{-h}^{\delta\zeta}\frac{\partial}{\partial}\left(\frac{\partial}{\partial x}\int_{-h}^{z} u dz\right)^2 dz - \mu^2\int_{-h}^{\delta\zeta}\frac{\partial^2}{\partial x^2}\int_{z}^{\delta\zeta}\nu_t\frac{\partial u}{\partial z}dz dz \\ &- \delta\mu^2\int_{-h}^{\delta\zeta}\frac{\partial^2}{\partial x^2}\int_{z}^{\delta\zeta} u\frac{\partial}{\partial x}\int_{-h}^{z} u dz dz dz = O(\mu^4)\end{aligned}$$

The first term in eq. (4.34) represents the inertial term, and after substitution of the eq. (4.57) and eq. (4.56) reads

$$\begin{aligned}\frac{\partial}{\partial t}\int_{-h}^{\delta\zeta} u dz &= \frac{\partial}{\partial t}[\overline{u}(h+\delta\zeta)] \\ &= (h+\delta\zeta)\overline{u}_t - \delta\overline{u}[\overline{u}(h+\delta\zeta)]_x \\ &= (h+\delta\zeta)\overline{u}_t - \delta(h+\delta\zeta)\overline{u}\overline{u}_x - \delta^2\overline{u}^2\zeta_x \qquad (4.59)\end{aligned}$$

To calculate the second term in eq. 4.34, which represents the convective contribution, some intermediate results are needed

$$\begin{aligned}u^2 &= (u_p+u_r)^2 = \left[\overline{u}_p + \frac{\mu^2}{2}(h\overline{u}_p)_{xx}\left(\frac{\Delta_1}{2}-z\right) + \frac{\mu^2}{2}\overline{u}_{pxx}\left(\frac{\Delta_2}{3}-z^2\right) + u_r\right]^2 \\ &= \overline{u}_p^2 + u_r^2 + 2\mu^2\left(\frac{\Delta_1}{2}-z\right)(h\overline{u}_p)_{xx}\overline{u}_p + \mu^2\left(\frac{\Delta_2}{3}-z^2\right)\overline{u}_{pxx}\overline{u}_p + 2\overline{u}_p u_r \\ &\quad +2\mu^2\left(\frac{\Delta_1}{2}-z\right)(h\overline{u}_p)_{xx}u_r + \mu^2\left(\frac{\Delta_2}{3}-z^2\right)\overline{u}_{pxx}u_r + O(\mu^4) \\ &= \overline{u}_p^2 + u_r^2 + 2\mu^2\left(\frac{\Delta_1}{2}-z\right)(h\overline{u}_p)_{xx}\overline{u} + \mu^2\left(\frac{\Delta_2}{3}-z^2\right)\overline{u}_{pxx}\overline{u} + 2\overline{u}_p u_r \\ &\quad +2\mu^2\left(\frac{\Delta_1}{2}-z\right)(h\overline{u}_p)_{xx}(u_r-\overline{u}_r) + \mu^2\left(\frac{\Delta_2}{3}-z^2\right)\overline{u}_{pxx}(u_r-\overline{u}_r) \\ &\quad +O(\mu^4) \qquad (4.60)\end{aligned}$$

Moreover, since, from eq. 4.56

$$u = \overline{u}_p + u_r + O(\mu^2) \qquad (4.61)$$

then

$$\overline{u} = \overline{u}_p + \overline{u}_r + O(\mu^2) \tag{4.62}$$

or

$$\overline{u}_p = \overline{u} - \overline{u}_r + O(\mu^2) \;\Rightarrow\; u = \overline{u} + u_r - \overline{u}_r + O(\mu^2) \tag{4.63}$$

It should be also noticed that

$$\overline{u}_p^2 + \overline{u}_r^2 + 2\overline{u}_p\overline{u}_r = \overline{u}^2 + (u_r^2 - \overline{u}_r^2) + 2\overline{u}_p(u_r - \overline{u}_r) \tag{4.64}$$

and that the following integrals are exactly equal to zero

$$\int_{-h}^{\delta\zeta}\left(\frac{\Delta_1}{2} - z\right)dz = \int_{-h}^{\delta\zeta}\left(\frac{\Delta_2}{3} - z^2\right)dz = \int_{-h}^{\delta\zeta}(u_r - \overline{u}_r) = 0 \tag{4.65}$$

Thus, the convective terms can be calculated as

$$\begin{aligned}
\frac{\partial}{\partial x}\int_{-h}^{\delta\zeta} u^2 dz &= \frac{\partial}{\partial x}\int_{-h}^{\delta\zeta}\left[\overline{u}^2 + (u_r - \overline{u}_r^2) + 2\mu^2\left(\frac{\Delta_1}{2} - z\right)(u_r - \overline{u}_r)(h\overline{u}_p)_{xx}\right. \\
&\quad \left. +\mu^2\left(\frac{\Delta_2}{3} - z^2\right)(u_r - \overline{u}_r)\overline{u}_{pxx}\right]dz \\
&= \frac{\partial}{\partial x}\left[\overline{u}^2(h + \delta\zeta)\right] + \frac{\partial}{\partial x}\int_{-h}^{\delta\zeta}(u_r^2 - \overline{u}_r^2)dz \\
&\quad +\frac{\partial}{\partial x}\int_{-h}^{\delta\zeta}\left[2\mu^2\left(\frac{\Delta_1}{2} - z\right)(h\overline{u}_p)_{xx}(u_r - \overline{u}_r)\right. \\
&\quad \left. +\mu^2\left(\frac{\Delta_2}{3} - z^2\right)\overline{u}_{pxx}(u_r - \overline{u}_r)\right]dz
\end{aligned} \tag{4.66}$$

The term

$$(\Delta M)_x = \frac{\partial}{\partial x}\int_{-h}^{\delta\zeta}(u_r^2 - \overline{u}^2)dz \tag{4.67}$$

represents the excess of momentum flux due to the variation of rotational velocity u_r along the water column, while the last integral, after some algebra, becomes

$$(\Delta M_1)_x = \frac{\partial}{\partial x}\left[-\overline{u}_{pxx}\int_{-h}^{\delta\zeta}(2hz + z^2)(u_r - \overline{u}_r)dz + O(h_x)\right] \tag{4.68}$$

and has the same meaning of $(\Delta M)_x$, but has a minor effects into the equations, since it is of $O(\mu^2)$. It should be noticed that here the assumption of gentle sloping beach has been used in order to neglect the terms of $O(h_x)$, considering also that here they would have been considered anyway of order μ^2, i.e. small. The convective term can be then written as

$$\frac{\partial}{\partial x}\int_{-h}^{\delta\zeta} u^2 dz = (h+\delta\zeta)\overline{u}\frac{\partial \overline{u}}{\partial x} + \overline{u}\frac{\partial}{\partial x}[\overline{u}(h+\delta\zeta)] + (\Delta M)_x + \mu^2(\Delta M_1)_x \quad (4.69)$$

The third term in eq. (4.34) represents the hydrostatic pressure and remains unchanged. The fourth and the fifth terms depends on the vertical acceleration $\partial w/\partial t$. In particular, considering eq. (4.63),the third term may be split as:

$$\begin{aligned}\int_{-h}^{\delta\zeta}\frac{\partial^2}{\partial x\partial t}\int_{z}^{\delta\zeta}\frac{\partial}{\partial x}\int_{-h}^{z} u\ dzdzdz &= \int_{-h}^{\delta\zeta}\frac{\partial^2}{\partial x\partial t}\int_{z}^{\delta\zeta}\frac{\partial}{\partial x}\int_{-h}^{z}\overline{u}dzdzdz + O(\mu^2)\\ &+ \int_{-h}^{\delta\zeta}\frac{\partial^2}{\partial x\partial t}\int_{z}^{\delta\zeta}\frac{\partial}{\partial x}\int_{-h}^{z}(u_r-\overline{u}_r)dzdzdz + O(\mu^2) \quad (4.70)\end{aligned}$$

in order to show the dependence of the second component on the rotational velocity u_r.

The first component, after some algebra, results:

$$\begin{aligned}\int_{-h}^{\delta\zeta}\frac{\partial^2}{\partial x\partial t}\int_{z}^{\delta\zeta}\frac{\partial}{\partial x}\int_{-h}^{z}\overline{u}\ dzdzdz &= \frac{1}{3}\overline{u}_{xxt}(h+\delta\zeta)^3\\ &+ (h+\delta\zeta)^2\left[\delta\overline{u}_{xt}\zeta_x + \overline{u}_{xt}h_x + \delta\overline{u}_{xx}\zeta_t + \delta\overline{u}_x\zeta_{xt} + \frac{1}{2}\overline{u}_t h_{xx}\right]\\ &+ (h+\delta\zeta)\Big[\delta^2\overline{u}_x\zeta_x\zeta_t + \overline{u}_x h_x\zeta_t + \delta\overline{u}_t h_x\zeta_x + \delta u_x h_x\zeta_t\\ &\quad +\delta\overline{u}h_{xx}\zeta_t + \delta\overline{u}h_x\zeta_{xt}\Big] \quad (4.71)\end{aligned}$$

From the continuity equation (4.58) it is possible to express the time derivatives of the surface elevation as

$$\zeta_t = -\overline{u}_x(h+\delta\zeta) - \overline{u}h_x - \delta\overline{u}\zeta_x \quad (4.72)$$

$$\zeta_{xt} = -\overline{u}_{xx}(h+\delta\zeta) - 2\overline{u}_x h_x - 2\delta\overline{u}_x\zeta_x - \overline{u}h_{xx} - \delta\overline{u}\zeta_{xx} \quad (4.73)$$

then, substituting eqs. (4.72) and (4.73) into eq. (4.71)

$$\begin{aligned}\int_{-h}^{\delta\zeta}\frac{\partial^2}{\partial x\partial t}\int_{z}^{\delta\zeta}\frac{\partial}{\partial x}\int_{-h}^{z}\overline{u}\ dzdzdz &= (h+\delta\zeta)^3\left[\frac{1}{3}\overline{u}_{xxt} - 2\delta\overline{u}_x\overline{u}_{xx}\right]\\ &+ (h+\delta\zeta)^2\Big[h_x\overline{u}_{xt} + \frac{1}{2}h_{xx}\overline{u}_t + \delta\zeta_x\overline{u}_{xt} - 2\delta h_x\overline{u}\overline{u}_{xx}\\ &\quad -4\delta h_x\overline{u}_x^2 - 2\delta h_{xx}\overline{u}\overline{u}_x - \delta^2\overline{u}\zeta_x\overline{u}_{xx} - 3\delta^2\zeta_x\overline{u}_x^2 - \delta^2\zeta_{xx}\overline{u}\overline{u}_x\Big]\\ &+ (h+\delta\zeta)[-4\delta h_x^2\overline{u}\overline{u}_x - 2\delta h_x h_{xx}\overline{u}^2 + \delta h_x\zeta_x\overline{u}_t\\ &\quad -\delta^2 h_x\zeta_{xx}\overline{u}^2 - 5\delta^2\zeta_x h_x\overline{u}\overline{u}_x - \delta^2 h_{xx}\zeta_x\overline{u}^2 - \delta^3\zeta_x^2\overline{u}\overline{u}_x]\end{aligned} \quad (4.74)$$

The second component, applying the Leibniz rule, becomes

$$
\begin{aligned}
\int_{-h}^{\delta\zeta} & \frac{\partial^2}{\partial x \partial t}\int_z^{\delta\zeta}\frac{\partial}{\partial x}\int_{-h}^{z}(u_r-\overline{u}_r)dzdzdz \\
= & \frac{\partial}{\partial x}\int_{-h}^{\delta\zeta}\frac{\partial}{\partial t}\int_z^{\delta\zeta}\frac{\partial}{\partial x}\int_{-h}^{z}(u_r-\overline{u}_r)dzdzdz \\
& -\delta\left[\frac{\partial}{\partial t}\int_z^{\delta\zeta}\frac{\partial}{\partial x}\int_{-h}^{z}(u_r-\overline{u}_r)dzdz\right]_{\delta\zeta}\frac{\partial\zeta}{\partial x} \\
& -\left[\frac{\partial}{\partial t}\int_z^{\delta\zeta}\frac{\partial}{\partial x}\int_{-h}^{z}(u_r-\overline{u}_r)dz\right]_{-h}\frac{\partial h}{\partial x} \\
= & \frac{\partial^2}{\partial x \partial t}\int_{-h}^{\delta\zeta}\int_z^{\delta\zeta}\frac{\partial}{\partial x}\int_{-h}^{z}(u_r-\overline{u}_r)dzdzdz \\
& -\delta\left[\int_z^{\delta\zeta}\frac{\partial}{\partial x}\int_{-h}^{z}(u_r-\overline{u}_r)dzdz\right]_{\delta\zeta}\frac{\partial\zeta}{\partial t} \\
& -\left[\int_z^{\delta\zeta}\frac{\partial}{\partial x}\int_{-h}^{z}(u_r-\overline{u}_r)dzdz\right]_{-h}\frac{\partial h}{\partial t} \\
= & \frac{\partial^2}{\partial x \partial t}\int_{-h}^{\delta\zeta}\left\{\frac{\partial}{\partial x}\int_z^{\delta\zeta}\int_{-h}^{z}(u_r-\overline{u}_r)dzdz\right. \\
& \left.-\delta\left[\int_{-h}^{z}(u_r-\overline{u}_r)dz\right]_{\delta\zeta}\frac{\partial\zeta}{\partial x}-\left[\int_{-h}^{z}(u_r-\overline{u}_r)dz\right]_{-h}\frac{\partial h}{\partial x}\right\}dz \\
= & \frac{\partial^3}{\partial x^2 \partial t}\int_{-h}^{\delta\zeta}\int_z^{\delta\zeta}\int_{-h}^{z}(u_r-\overline{u}_r)dzdzdz \\
& -\delta\left[\int_z^{\delta\zeta}\int_{-h}^{z}(u_r-\overline{u}_r)dzdz\right]_{\delta\zeta}\frac{\partial\zeta}{\partial x}-\left[\int_z^{\delta\zeta}\int_{-h}^{z}(u_r-\overline{u}_r)dzdz\right]_{-h}\frac{\partial h}{\partial x} \\
= & -(\Delta P)_{xxt}+O(h_x) \qquad (4.75)
\end{aligned}
$$

where ΔP has been defined as

$$
\Delta P = -\int_{-h}^{\delta\zeta}\int_z^{\delta\zeta}\int_{-h}^{z}(u_r-\overline{u}_r)dzdzdz \qquad (4.76)
$$

and it models the contribution to the pressure due to the vertical motion.

The fifth term of eq. (4.34), substituting the expressions in eq. (4.64), becomes

$$\begin{aligned}
\int_{-h}^{\delta\zeta} & \frac{\partial}{\partial x}\left(\frac{\partial}{\partial x}\int_{-h}^{z} u dz\right)^2 dz = \int_{-h}^{\delta\zeta}\frac{\partial}{\partial x}\left(\frac{\partial}{\partial x}\int_{-h}^{z}(\overline{u}+u_r-\overline{u}_r)dz\right)^2 dz + O(\mu^2) \\
&= \int_{-h}^{\delta\zeta}\frac{\partial}{\partial x}\left[\left(\frac{\partial}{\partial x}\int_{-h}^{z}(\overline{u}+u_r-\overline{u}_r)dz\right)\left(\frac{\partial}{\partial x}\int_{-h}^{z}(\overline{u}+u_r-\overline{u}_r)dz\right)\right]dz \\
&\quad +O(\mu^2) \\
&= \int_{-h}^{\delta\zeta}\frac{\partial}{\partial x}\left(\frac{\partial}{\partial x}\int_{-h}^{z}\overline{u}dz\right)^2 dz + \int_{-h}^{\delta\zeta}\frac{\partial}{\partial x}\Big[\Big(\frac{\partial}{\partial x}\int_{-h}^{z}\overline{u}dz\Big)\Big(\frac{\partial}{\partial x}\int_{-h}^{z}(u_r-\overline{u}_r)dz\Big) \\
&\quad +\Big(\frac{\partial}{\partial x}\int_{-h}^{z}(u_r-\overline{u}_r)dz\Big)\Big(\frac{\partial}{\partial x}\int_{-h}^{z}(\overline{u}+u_r-\overline{u}_r)dz\Big)\Big]dz + O(\mu^2) \\
&= \int_{-h}^{\delta\zeta}\frac{\partial}{\partial x}\left(\frac{\partial}{\partial x}\int_{-h}^{z}\overline{u}dz\right)^2 dz \\
&\quad +\int_{-h}^{\delta\zeta}\frac{\partial}{\partial x}\left[\left(\frac{\partial}{\partial x}\int_{-h}^{z}(u_r-\overline{u}_r)dz\right)\left(\frac{\partial}{\partial x}\int_{-h}^{z}(2\overline{u}+u_r-\overline{u}_r)dz\right)\right]dz + O(\mu^2) \\
&= \int_{-h}^{\delta\zeta}\frac{\partial}{\partial x}\left(\frac{\partial}{\partial x}\int_{-h}^{z}\overline{u}dz\right)^2 dz + D_w + O(\mu^2) \qquad (4.77)
\end{aligned}$$

where it has been defined

$$D_w = \int_{-h}^{\delta\zeta}\frac{\partial}{\partial x}\left[\left(\frac{\partial}{\partial x}\int_{-h}^{z}(u_r-\overline{u}_r)dz\right)\left(\frac{\partial}{\partial x}\int_{-h}^{z}(2\overline{u}+u_r-\overline{u}_r)dz\right)\right]dz \qquad (4.78)$$

which represents the excess of momentum due to the vertical motion. The first term in the eq. (4.77) can be rewritten expanding the integrals and derivatives

$$\begin{aligned}
\int_{-h}^{\delta\zeta} & \frac{\partial}{\partial x}\left(\frac{\partial}{\partial x}\int_{-h}^{z}\overline{u}dz\right)^2 dz = \frac{2}{3}(h+\delta\zeta)^3\overline{u}_x\overline{u}_{xx} \\
&+ (h+\delta\zeta)^2[\overline{u}\overline{u}_x h_{xx} + 2\overline{u}_x^2 h_x + \overline{u}\overline{u}_{xx}h_x] \\
&+ (h+\delta\zeta)[2\overline{u}^2 h_x h_{xx} + 4\overline{u}h_x^2\overline{u}_x] + O(\mu^2) \qquad (4.79)
\end{aligned}$$

The turbulent shear stresses, represented by the sixth term in eq. (4.34) can written as

$$D_s = \int_{-h}^{\delta\zeta}\frac{\partial^2}{\partial x^2}\int_{z}^{\delta\zeta}\nu_t\frac{\partial u}{\partial z}dzdz \qquad (4.80)$$

which, if the eddy viscosity ν_t is assumed constant over depth, can be rewritten as

$$\begin{aligned}
D_s &= (h+\delta\zeta)[\nu_t u_r(\delta\zeta)]_{xx} + \delta\zeta_x[\nu_t u_r(\delta\zeta)]_x \\
&\quad +\delta\left[\nu_t u_r(\delta\zeta)\zeta_x\right]_x - [\nu_t\overline{u}_r(h+\delta\zeta)]_{xx} \qquad (4.81)
\end{aligned}$$

Finally, the last term results

$$\begin{aligned}\int_{-h}^{\delta\zeta}\frac{\partial^2}{\partial x^2}\int_{z}^{\delta\zeta} u \quad & \frac{\partial}{\partial x}\int_{-h}^{z} u dz dz dz \\ &= \int_{-h}^{\delta\zeta}\frac{\partial^2}{\partial x^2}\int_{z}^{\delta\zeta}(\overline{u}+u_r-\overline{u}_r)\frac{\partial}{\partial x}\int_{-h}^{z}(\overline{u}+u_r-\overline{u}_r)dzdzdz + O(\mu^2) \\ &= \int_{-h}^{\delta\zeta}\frac{\partial^2}{\partial x^2}\int_{z}^{\delta\zeta}\overline{u}\frac{\partial}{\partial x}\int_{-h}^{z}\overline{u}dzdzdz + D_{uw} + O(\mu^2) \qquad (4.82)\end{aligned}$$

where the last term in eq. (4.82) is defined as

$$\begin{aligned}D_{uw} = & \int_{-h}^{\delta\zeta}\frac{\partial^2}{\partial x^2}\int_{z}^{\delta\zeta}\Big[(u_r-\overline{u}_r)\frac{\partial}{\partial x}\int_{-h}^{z}\overline{u}dz \\ & +(\overline{u}+u_r-\overline{u}_r)\frac{\partial}{\partial x}\int_{-h}^{z}(u_r-\overline{u}_r)dz\Big]dzdz \qquad (4.83)\end{aligned}$$

representing the action that is exerted by the adjacent column of fluid.

The first part of eq. (4.82) is, after some algebra,

$$\begin{aligned}\int_{-h}^{\delta\zeta}\frac{\partial^2}{\partial x^2}\int_{z}^{\delta\zeta}\overline{u} \quad & \frac{\partial}{\partial x}\int_{-h}^{z}\overline{u}dzdzdz \\ & = (h+\delta\zeta)^3\left[\overline{u}_x\overline{u}_{xx}+\frac{1}{3}\overline{u}\overline{u}_{xxx}\right] \\ & +(h+\delta\zeta)^2\Big[2\delta\overline{u}\overline{u}_{xx}\zeta_x+2(h+\delta\zeta)_x\overline{u}_x^2+2\overline{u}\overline{u}_{xx}h_x \\ & +\frac{5}{2}\overline{u}\overline{u}_x h_{xx}+\delta\overline{u}\zeta_{xx}\overline{u}_x+\frac{1}{2}\overline{u}^2h_{xxx}\Big] \\ & +(h+\delta\zeta)[\delta\overline{u}^2h_x\zeta_{xx}+6\delta\overline{u}\overline{u}_x h_x\zeta_x+\delta^2\overline{u}\overline{u}_x\zeta_x^2+2\delta\overline{u}^2h_{xx}\zeta_x] \\ & +O(\mu^2) \qquad (4.84)\end{aligned}$$

Substituting now eqs. (4.59)-(4.83) into the momentum equation (4.34) gives

$$
\begin{aligned}
\overline{u}_t \;+\;& \delta\overline{u}\overline{u}_{xx}+\zeta_x-\mu^2\left[\frac{1}{3}h^2\overline{u}_{xxt}+\frac{1}{2}hh_{xx}\overline{u}_t+hh_x\overline{u}_{xt}\right]\\
+\;& \delta\mu^2\Big[-\frac{1}{3}h^2\overline{u}\overline{u}_{xxx}-h\zeta_x\overline{u}_{xt}+\frac{1}{3}h^2\overline{u}_x\overline{u}_{xx}-\frac{2}{3}h\zeta\overline{u}_{xxt}-\frac{3}{2}hh_{xx}\overline{u}\overline{u}_x\\
&-\frac{1}{2}hh_{xxx}\overline{u}^2-hh_x\overline{u}\overline{u}_{xx}-\zeta h_x\overline{u}_{xt}-h_x\zeta_x\overline{u}_t-\frac{1}{2}\zeta h_{xx}\overline{u}_t\Big]\\
+\;& \delta^2\mu^2\Big[\frac{1}{6}\zeta^2\overline{u}_{xxt}-\frac{1}{3}h\zeta\overline{u}_x-\frac{1}{3}h\overline{u}_{xx}(\zeta\overline{u}_x)+h(\zeta\overline{u}_x^2)_x-\frac{1}{2}(\zeta^2\overline{u}_{xt})_x\\
&-\frac{2}{3}h(\zeta\overline{u}\overline{u}_{xx})_x-\zeta_x h_{xx}\overline{u}^2-\zeta h_x\overline{u}\overline{u}_{xx}-\frac{1}{2}\zeta h_{xxx}\overline{u}^2-\frac{3}{2}\zeta h_{xx}\overline{u}\overline{u}_x-\zeta_x h_x\overline{u}\overline{u}_x\Big]\\
+\;& \delta^3\mu^2\left[-\frac{1}{3}\zeta^2\overline{u}\overline{u}_{xxx}-\zeta\zeta_x\overline{u}\overline{u}_{xx}+\zeta\zeta_x\overline{u}_x^2+\frac{1}{3}\zeta^2\overline{u}_x\overline{u}_{xx}\right]\\
+\;& [\delta(\Delta M)_x+\mu^2(\Delta P)_{xxt}-\mu^2D_s+\delta\mu^2(\Delta M_1)_x+\delta\mu^2D_w\\
&+\delta\mu^2D_{uw}](h+\delta\zeta)^{-1}=O(\mu^4)
\end{aligned}
\tag{4.85}
$$

In order to enhance the dispersion characteristics of the model in deeper water it would have been necessary to include high order terms into the equations. However, some improvement can be obtained by using the approach by Madsen and Schäffer (1998), where the use of the linear operator

$$\mathcal{L}=1+B\mu^2h^2\nabla^2 \tag{4.86}$$

has been proposed in order to obtain, at least, an enhancement of the linear dispertion characteristics, that is to get a better mimic of the exact linear dispersion relationship. After applying the operator $\mathcal{L}$ into eq. (4.85), the following final momentum equation, which has weakly non-dispersive characteristics, is obtained

$$
\begin{aligned}
\overline{u}_t \;+\;& \delta\overline{u}\overline{u}_{xx}+\zeta_x+\mu^2\left[\left(B-\frac{1}{3}\right)h^2\overline{u}_{xxt}-\frac{1}{2}hh_{xx}\overline{u}_t-hh_x\overline{u}_{xt}\right]+B\mu^2h^2\zeta_{xxx}\\
+\;& \delta\mu^2\Big[-\frac{1}{3}h^2\overline{u}\overline{u}_{xxx}-h\zeta_x\overline{u}_{xt}+\frac{1}{3}h^2\overline{u}_x\overline{u}_{xx}-\frac{2}{3}h\zeta\overline{u}_{xxt}-\frac{3}{2}hh_{xx}\overline{u}\overline{u}_x\\
-\;& \frac{1}{2}hh_{xx}\overline{u}^2-hh_x\overline{u}\overline{u}_{xx}-\zeta h_x\overline{u}_{xt}-h_x\zeta_x\overline{u}_t-\frac{1}{2}\zeta h_{xx}\overline{u}_t+Bh^2(\overline{u}\overline{u}_x)_{xx}\Big]\\
+\;& \delta^2\mu^2\Big[\frac{1}{6}\zeta^2\overline{u}_{xxt}-\frac{1}{3}h\zeta\overline{u}_x\overline{u}_{xx}-\frac{1}{3}h\overline{u}_{xx}(\zeta\overline{u})_x+h(\zeta\overline{u}_x^2)_x-\frac{1}{2}(\zeta^2\overline{u}_{xt})_x\\
-\;& \frac{2}{3}h(\zeta\overline{u}\overline{u}_{xx})_x-\zeta_x h_{xx}\overline{u}^2-\zeta h_x\overline{u}\overline{u}_{xx}-\frac{1}{2}\zeta h_{xxx}\overline{u}^2-\frac{3}{2}\zeta h_{xx}\overline{u}\overline{u}_x-\zeta_x h_x\overline{u}\overline{u}_x\Big]\\
+\;& \delta^3\mu^2\Big[-\frac{1}{3}\zeta^2\overline{u}\overline{u}_{xxx}-\zeta\zeta_x\overline{u}\overline{u}_{xx}+\zeta\zeta_x\overline{u}_x^2+\frac{1}{3}\zeta^2\overline{u}_x\overline{u}_{xx}\Big]\\
+\;& [\delta(\Delta M)_x+\mu^2(\Delta P)_{xxt}-\mu^2D_s+\delta\mu^2(\Delta M_1)_x+\delta\mu^2D_w\\
&+\delta\mu^2D_{uw}](h+\delta\zeta)^{-1}=O(\mu^4)
\end{aligned}
\tag{4.87}
$$

It must be noticed that the terms $(\Delta M)_x$,$(\Delta P)_{xxt}$,$(\Delta M_1)_x$, D_w, D_s and D_{uw} are all function of the rotational velocity u_r, which, in turn, is function of the

vorticity ω, injected inside the flow by the breaking mechanism. This is the reason why the aforementioned terms are called *breaking terms* and they represent the excess of momentum flux (i.e. the dissipation of energy) due to breaking, allowing for a modelling of the flow within the surf zone. In particular, D_s is the shear stress inside the fluid, $(\Delta M)_x$ and $(\Delta M_1)_x$ give the excess of momentum flux due to the vertical variation of the rotational velocity, $(\Delta P)_{xxt}$ is the contribution to the pressure due to the vertical motion while D_w is the excess of momentum due to the vertical motion and D_{uw} represents the interaction between the waves and the mean flow.

It may be worth recalling that these terms have been derived from the equations with no artificial assumptions, simply considering the rotationality of the flow as the breaking starts. In order to specify the magnitude of these terms, the vorticity field has to be solved and it will be done in the next chapter.

Chapter 5

The vorticity equation

5.1 Overview

In the previous chapter the governing equations of the proposed fully-nonlinear Boussinesq model have been presented, which describe the conservation of mass and momentum within the flow. These equations are able to model the wave propagation within the shoaling and the surf zone, after determing the unknown variables, that is the surface elevation ζ and the depth averaged horizontal velocity $\overline{u}$.

However, it has also been shown that in order to describe more appropriately the propagation of breaking waves, an additional dependent variable must be introduced: the vorticity ω. Indeed, the total velocity u was expressed as sum of the potential and of the rotational velocity, the latter being function of ω, which allows to take into account the modification of the vertical velocity profile which takes place under a breaking wave.

Since there are three unknowns, namely ζ, $\overline{u}$ and ω, and only two equations, in order to close the problem one more equation has to be considered. Here the vorticity transport equation, which will be derived in Section 5.2, has been taken, which will be solved analytically by following the approach of Veeramony and Svendsen (1999).

The vorticity structure of the flow in the surf zone, induced mostly by the high curvatures attained by the unstable shoaling waves propagating toward the shoreline, has been recognized by most of the experimental studies on wave breaking. Thus, removing the often adopted irrotational hypothesis, by solving the vorticity field, is crucial for any correct and physically based analysis of the surf zone hydrodynamics.

Moreover, within the surf zone a huge amount of vorticity is introduced in the flow, previously irrotational, due to the breaking process, therefore this source of vorticity must also be modeled. The approach which has been used in the works of Veeramony and Svendsen (1999) and Veeramony and Svendsen (2000) is that to schematize the surface roller on the front of a breaking wave as a source of vorticity.

They also adopted the hydraulic similarity between breaking waves and hydraulic jumps in order to specify the amount of vorticity generated by the breaking process. The same approach has been adopted here and will be illustrated in more details in Section 5.3.

5.2 Formulation of the problem

One of the most important hydrodynamic effects of breaking is the generation of vorticity. In the most general case, it has three-components, $\hat{\omega} = (\hat{\omega}_x, \hat{\omega}_y, \hat{\omega}_z)$, but since the aim of this work is the modelling of the propagation of a breaking wave on a vertical plane, the reference to vorticity made here is always to the vertical vorticity $\hat{\omega}_y$, whose axis is horizontal and perpendicular to the flow and will be hereinafter referred simply as $\hat{\omega}$, or ω in dimensionless form. Its definition in terms of the horizontal and vertical velocities, $\hat{u}$ and $\hat{w}$, is

$$\hat{\omega} = \frac{\partial \hat{u}}{\partial \hat{z}} - \frac{\partial \hat{w}}{\partial \hat{x}} \tag{5.1}$$

The vorticity transport equation can be then derived from the horizontal and vertical momentum equations described in (4.15) and (4.16). In fact, cross differentiating these last ones and subtracting the second from the first one, the following equation is obtained

$$\begin{aligned} \frac{\partial}{\partial t}\left(\frac{\partial \hat{u}}{\partial \hat{z}} - \frac{\partial \hat{w}}{\partial \hat{x}}\right) \; + \; & \left[\frac{\partial \hat{u}}{\partial \hat{z}}\frac{\partial \hat{u}}{\partial \hat{x}} + \hat{u}\frac{\partial^2 \hat{u}}{\partial \hat{z}\partial \hat{x}} + \frac{\partial \hat{w}}{\partial \hat{z}}\frac{\partial \hat{u}}{\partial \hat{z}} + \hat{w}\frac{\partial^2 \hat{u}}{\partial \hat{z}^2}\right. \\ & \left. - \frac{\partial \hat{u}}{\partial \hat{x}}\frac{\partial \hat{w}}{\partial \hat{x}} - \hat{u}\frac{\partial^2 \hat{w}}{\partial \hat{x}^2} - \frac{\partial \hat{w}}{\partial \hat{x}}\frac{\partial \hat{w}}{\partial \hat{z}} - \hat{w}\frac{\partial^2 \hat{w}}{\partial \hat{x}\partial \hat{z}}\right] \\ = \; & \frac{1}{\rho}\left[\frac{\partial^2}{\partial \hat{x}\partial \hat{z}}(\hat{\tau}_{xx} - \hat{\tau}_{zz}) - \left(\frac{\partial^2}{\partial x^2} - \frac{\partial^2}{\partial z^2}\right)\hat{\tau}_{zx}\right] \end{aligned} \tag{5.2}$$

Submitting eq. (5.1) and the continuity equation (4.9) into eq. (5.2), gives

$$\frac{\partial \hat{\omega}}{\partial \hat{t}} + \hat{u}\frac{\partial \hat{\omega}}{\partial \hat{x}} + \hat{w}\frac{\partial \hat{\omega}}{\partial \hat{z}} = \frac{1}{\rho}\left[\frac{\partial^2}{\partial \hat{x}\partial \hat{z}}(\hat{\tau}_{xx} - \hat{\tau}_{zz}) - \left(\frac{\partial^2}{\partial x^2} - \frac{\partial^2}{\partial z^2}\right)\hat{\tau}_{zx}\right] \tag{5.3}$$

By using a Newtonian fluid approach in order to model the turbulent shear stresses through the eddy viscosity $\hat{\nu}_t$, the τ-terms can be expressed as

$$\hat{\tau}_{ij} = \rho\left[\hat{\nu}_t\left(\frac{\partial \hat{u}_i}{\partial \hat{x}_j} + \frac{\partial \hat{u}_j}{\partial \hat{x}_i}\right)\right] \tag{5.4}$$

when eq. (5.4) is substituted into eq. (5.3) the final expression for the dimensional vorticity transport equation is obtained

$$\frac{\partial \hat{\omega}}{\partial \hat{t}} + \hat{u}\frac{\partial \hat{\omega}}{\partial \hat{x}} + \hat{w}\frac{\partial \hat{\omega}}{\partial \hat{z}} = \hat{\nu}_t\left(\frac{\partial^2 \hat{\omega}}{\partial \hat{x}^2} + \frac{\partial^2 \hat{\omega}}{\partial \hat{z}^2}\right) \tag{5.5}$$

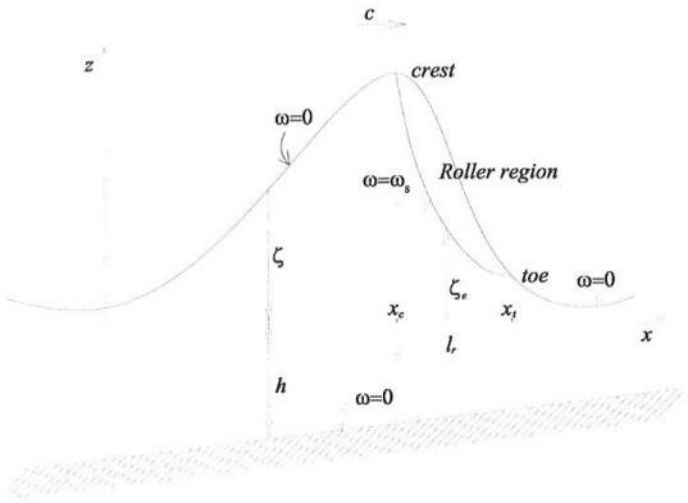

Figure 5.1: Formulation of the problem: boundary conditions of the vorticity transport equation.

It is worth pointing out that a strong hypothesis has been introduced. Indeed, in order to take out the ν_t from the spatial derivatives on the right hand side, the eddy viscosity has been assumed to be constant over the depth.

Eq. (5.5) is able to model the transport of vorticity inside the flow, but in order to have a non-zero vorticity field a source of vorticity must be included somewhere. Being the breaking generated vorticity essentially due to the high curvature of the flow and to the separation of the stream lines in correspondence of the toe of the roller, here the region close to the lower edge of the roller is schematized as source of vorticity. This approach is qualitatively confirmed by the experimental results of Lin and Rockwell (1994), who analyzed the instantaneous structure of a stationary breaking wave, showing as the discontinous slope of the free surface and the occurence of the separation beneath the surface represent a powerful source of vorticity and that a mixing layer is formed in correspondence of the toe of the roller. However, it is useful to stress here that the surface roller does not correspond to a detailed representation of the flow, but to a useful macroscopic schematization. Indeed, as it has been evidentiated also by Lin and Rockwell (1994), the existence of a large scale recirculating vortex with its center on the mixing layer, corresponding to the roller, is an artifact of the particular frame of observation, moving at wave speed.

With reference to the sketch shown in Figure 5.1, the previous considerations allow to formulate the boundary conditions on the lower edge of the roller as

$$\hat{\omega}(\hat{x}, \hat{z} = \hat{\zeta}_e, \hat{t}) = \hat{\omega}_s(\hat{x}, \hat{t}) \tag{5.6}$$

where $\hat{\zeta}_e$ is the elevation of the lower edge of the roller and $\hat{\omega}_s$ is the value of the vorticity at this location, which must be specified. On the other hand, the vorticity at the free surface, outside the roller region, is assumed to be equal to zero.

At the bed, the free slip boundary condition, neglecting the effects of the bottom boundary layer, gives rise to the vorticity bottom boundary condition

$$\hat{\omega}(\hat{x}, \hat{z} = -\hat{h}, \hat{t}) = 0 \tag{5.7}$$

Moreover, since in all the simulation the waves are initially non-breaking, the initial condition is

$$\hat{\omega}(\hat{x}, \hat{z}, \hat{t} = 0) = 0 \tag{5.8}$$

Due to the definition of the previous boundary conditions, the domain where the vorticity transport equation is solved is not the entire fluid domain, but the roller region is left out, being the lower edge of the roller the upper boundary of the computational domain for the vorticity equation. The region for the integration of the vorticity equation is then defined as:

$$-\hat{h} \leq \hat{z} \leq \begin{cases} \hat{\zeta} & \text{outside of the roller region} \\ \hat{\zeta}_e & \text{within the roller region} \end{cases} \tag{5.9}$$

Applying the scaling argument dicussed in Chapter 4 to eq. (5.5) the dimensioless form of the vorticity transport equation is recovered:

$$\frac{\partial \omega}{\partial t} + \delta u \frac{\partial \omega}{\partial x} + \delta w \frac{\partial \omega}{\partial z} = \nu_t \left(\mu^2 \frac{\partial^2 \omega}{\partial x^2} + \frac{\partial^2 \omega}{\partial z^2} \right) \tag{5.10}$$

while the boundary and initial conditions becomes

$$\omega(x, z = \delta\zeta, t) = \omega_s \tag{5.11}$$

$$\omega(x, z = -h, t) = 0 \tag{5.12}$$

$$\omega(x, z, t = 0) = 0 \tag{5.13}$$

$$\tag{5.14}$$

Veeramony and Svendsen (1999) proposed an analytical solution for ω, since a numerical solution of the previous equation would have required an heavy computational effort. Moreover in very shallow water regions the vertical grid size required to get a sufficient accurate description would be very fine, leading to very small time steps to obtain the numerical stability of the model. The approach of Veeramony and Svendsen (1999) will be followed here, the effects and the opportunity of adopting such a solution will be discussed in the next chapters.

In order to get the analytical solution, the physical coordinates (x, z, t) are changed into the computational coordinates (x, σ, t), where the new vertical coordinate is defined as

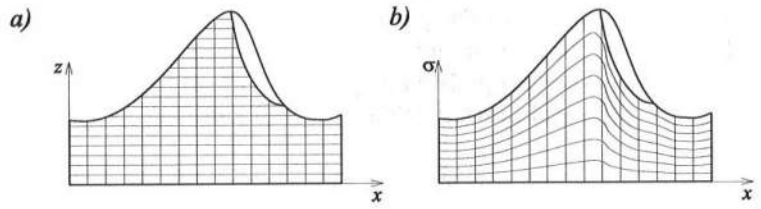

Figure 5.2: *a)* Physical and *b)* computational domain in σ-coordinates

$$\sigma = \frac{h+z}{h+\delta\zeta_e} \tag{5.15}$$

so that the computational domain is changed from $-h \leq z \leq \zeta_e$ to $0 \leq \sigma \leq 1$.

This change of coordinate system allows for stretching the domain in such a way to follow the shape of the domain, so that every vertical section has the same degree of representative points, even if the water is shallower. Moreover, by using σ-coordinates the irregular physical domain is transformed into a regular rectangular computational domain (see Figure 5.2).

Due to the change of coordinate systems, also the expressions of derivatives need to be modified. If q is the generic variable, by using the chain rule

$$\frac{\partial q}{\partial t} = \frac{\partial \sigma}{\partial t}\frac{\partial q}{\partial \sigma} + \frac{\partial q}{\partial t} = -\frac{\delta\sigma}{h+\delta\zeta_e}\frac{\partial \zeta_e}{\partial t}\frac{\partial q}{\partial \sigma} + \frac{\partial q}{\partial t} \tag{5.16}$$

$$\frac{\partial q}{\partial z} = \frac{\partial \sigma}{\partial z}\frac{\partial q}{\partial \sigma} = \frac{1}{h+\delta\zeta_e}\frac{\partial q}{\partial \sigma} \tag{5.17}$$

$$\frac{\partial^2 q}{\partial z^2} = \frac{\partial}{\partial z}\left(\frac{\partial \sigma}{\partial z}\frac{\partial q}{\partial \sigma}\right) = \left(\frac{\partial \sigma}{\partial z}\right)^2 \frac{\partial^2 q}{\partial \sigma^2} = \left(\frac{1}{h+\delta\zeta_e}\right)^2 \frac{\partial^2 q}{\partial \sigma^2} \tag{5.18}$$

$$\frac{\partial q}{\partial x} = \frac{\partial \sigma}{\partial x}\frac{\partial q}{\partial \sigma} + \frac{\partial q}{\partial x} = -\frac{\delta\sigma}{h+\delta\zeta_e}\frac{\partial \zeta_e}{\partial x}\frac{\partial q}{\partial \sigma} + \frac{\partial q}{\partial x} + O(h_x) \tag{5.19}$$

Substituting the derivatives evaluated according to eqs. (5.16)-(5.19) into eq. (5.10) and neglecting terms of $O(\mu^2)$ gives

$$\begin{aligned} \frac{\partial \omega}{\partial t} &- \delta\left[\frac{\sigma}{h+\delta\zeta_e}\frac{\partial \zeta_e}{\partial t}\right]\frac{\partial \omega}{\partial \sigma} + \delta u\frac{\partial \omega}{\partial x} - \delta^2\frac{u\sigma}{h+\delta\zeta_e}\frac{\partial \zeta_e}{\partial x}\frac{\partial \omega}{\partial \sigma} \\ &+ \delta\left[\frac{w}{h+\delta\zeta_e}\right]\frac{\partial \omega}{\partial \sigma} = \frac{\nu_t}{(h+\delta\zeta_e)^2}\frac{\partial^2 \omega}{\partial \sigma^2} + O(\mu^2, \delta h_x) \end{aligned} \tag{5.20}$$

while, in the computational domain, the boundary conditions and the initial condition become respectively

$$\omega(x, \sigma = 1, t) = \omega_s(x, t) \tag{5.21}$$

$$\omega(x, \sigma = 0, t) = 0 \tag{5.22}$$

$$\omega(x, \sigma, t = 0) = 0 \tag{5.23}$$

In order to homogenize the boundary condition, Veeramony and Svendsen (1999) suggested to perform a new change of coordinate

$$\omega = \Omega + \sigma\omega_s \tag{5.24}$$

then the derivatives become

$$\frac{\partial \omega}{\partial t} = \frac{\partial \Omega}{\partial t} + \sigma\frac{\partial \omega_s}{\partial t} - \frac{\delta\sigma\omega_s}{h + \delta\zeta_e}\frac{\partial \zeta_e}{\partial t} \tag{5.25}$$

$$\frac{\partial \omega}{\partial \sigma} = \frac{\partial \Omega}{\partial \sigma} + \omega_s \tag{5.26}$$

$$\frac{\partial^2 \omega}{\partial \sigma^2} = \frac{\partial^2 \Omega}{\partial \sigma^2} \tag{5.27}$$

$$\frac{\partial \omega}{\partial x} = \frac{\partial \Omega}{\partial x} + \sigma\frac{\partial \omega_s}{\partial x} - \frac{\delta\sigma\omega_s}{h + \delta\zeta_e}\frac{\partial \zeta_e}{\partial x} \tag{5.28}$$

By substituting the previous expressions into eq. (5.20) gives

$$\begin{aligned}
\frac{\partial \Omega}{\partial t} &+ \sigma\frac{\partial \omega_s}{\partial t} - \delta\frac{\omega_s\sigma}{h + \delta\zeta_e}\frac{\partial \zeta_e}{\partial t} - \delta\left[\frac{\sigma}{h + \delta\zeta_e}\frac{\partial \zeta_e}{\partial t} - \frac{w}{h + \delta\zeta_e}\right]\left(\frac{\partial \Omega}{\partial \sigma} + \omega_s\right) \\
&+ \delta u\frac{\partial \Omega}{\partial x} + \delta u\sigma\frac{\partial \omega_s}{\partial x} - \delta^2\frac{u\sigma}{h + \delta\zeta_e}\frac{\partial \zeta_e}{\partial x}\left(\frac{\partial \Omega}{\partial \sigma} + \omega_s\right) \\
&= \frac{\nu_t}{(h + \delta\zeta_e)^2}\frac{\partial^2 \Omega}{\partial \sigma^2} + O(\mu^2, \delta h_x)
\end{aligned} \tag{5.29}$$

while the boundary condition becomes homogeneous

$$\Omega(x, \sigma = 1, t) = 0 \tag{5.30}$$

$$\Omega(x, \sigma = 0, t) = 0 \tag{5.31}$$

$$\Omega(x, \sigma, t = 0) = 0 \tag{5.32}$$

Using a pertubation approach, that is by assuming that the solution can be expanded as

$$\Omega = \omega^{(1)} + \delta\omega^{(2)} + \delta^2\omega^{(3)} + O(\delta^3) \tag{5.33}$$

and expanding in Taylor series about zero the following term as well

$$\frac{\nu_t}{(h+\delta\zeta_e)^2} = \frac{\nu_t}{h^2}\frac{1}{\left(1+\frac{\delta\zeta_e}{h}\right)^2}\left[1 - 2\delta\frac{\zeta_e}{h} + O(\delta^2)\right] \tag{5.34}$$

then the vorticity transport equation reads

$$\begin{aligned}\frac{\partial\omega^{(1)}}{\partial t} &+ \delta\frac{\partial\omega^{(2)}}{\partial t} + \sigma\frac{\partial\omega_s}{\partial t} - \delta\frac{\omega_s\sigma}{h+\delta\zeta_e}\frac{\partial\zeta_e}{\partial t} \\ &- \delta\left[\frac{\sigma}{h+\delta\zeta_e}\frac{\partial\zeta_e}{\partial t} - \frac{w}{h+\delta\zeta_e}\right]\left(\frac{\partial\omega^{(1)}}{\partial\sigma} + \delta\frac{\partial\omega^{(2)}}{\partial\sigma} + \omega_s\right) + \delta u\frac{\partial\omega^{(1)}}{\partial x} \\ &+ \delta u\sigma\frac{\partial\omega_s}{\partial x} = \frac{\nu_t}{h^2}\left(1 - 2\delta\frac{\zeta_e}{h}\right)\left(\frac{\partial^2\omega^{(1)}}{\partial\sigma^2} + \delta\frac{\partial^2\omega^{(2)}}{\partial\sigma^2}\right) + O(\delta^3)\end{aligned} \tag{5.35}$$

Therefore, the problem has been decomposed into the sum of an infinite number of simpler linear problems in which the forcing term is function of the solution at the preceding order of approximation. The solutions at each order of approximation, once found, can be added together to give the solution of the original problem. In the following the analytical solution of the problems at $O(1)$ and at $O(\delta)$ will be presented.

$O(1)$: basic state

The problem at $O(1)$ reads

$$\frac{\partial\omega^{(1)}}{\partial t} + \sigma\frac{\partial\omega_s}{\partial t} = \frac{\nu_t}{h^2}\frac{\partial^2\omega^{(1)}}{\partial\sigma^2} \tag{5.36}$$

or, defining,

$$\kappa = \frac{\nu_t}{h^2} \tag{5.37}$$

it becomes

$$\frac{\partial\omega^{(1)}}{\partial t} - \kappa\frac{\partial^2\omega^{(1)}}{\partial\sigma^2} = -\sigma\frac{\partial\omega_s}{\partial t} \tag{5.38}$$

which has to be solved along with the boundary conditions

$$\omega^{(1)}(\sigma = 1, t) = 0 \tag{5.39}$$

$$\omega^{(1)}(\sigma = 0, t) = 0 \tag{5.40}$$

$$\omega^{(1)}(\sigma, t = 0) = 0 \tag{5.41}$$

The right hand side of eq. (5.38) is an odd function in σ, then it can be expanded as half-sine Fourier series

$$-\sigma\frac{\partial\omega_s}{\partial t} = \sum_{n=1}^{\infty} F_n^{(1)} \sin n\pi\sigma \tag{5.42}$$

where, by definition of coefficients of the Fourier series, for each n the corresponding coefficient may be expressed as

$$\begin{aligned} F_n^{(1)} &= \int_{-1}^{1} -\sigma\frac{\partial\omega_s}{\partial t}\sin n\pi\sigma d\sigma = -2\frac{\partial\omega_s}{\partial t}\int_0^1 \sigma \sin n\pi\sigma d\sigma \\ &= 2\frac{(-1)^n}{n\pi}\frac{\partial\omega_s}{\partial t} \end{aligned} \tag{5.43}$$

It is assumed that the solution has the form

$$\omega^{(1)} = \sum_{n=1}^{\infty} G_n^{(1)} \sin n\pi\sigma \tag{5.44}$$

where the coefficients of the series $G_n^{(1)}$ are only function of x and t. Substituting expressions (5.42) and (5.44) in eq. (5.38) gives

$$\frac{\partial}{\partial t}\left[\sum_{n=1}^{\infty} G_n^{(1)} \sin n\pi\sigma\right] - \kappa\frac{\partial^2}{\partial\sigma^2}\left[\sum_{n=1}^{\infty} G_n^{(1)} \sin n\pi\sigma\right] = \sum_{n=1}^{\infty} F_n^{(1)} \sin n\pi\sigma \tag{5.45}$$

which becomes, after expanding the second term on the left hand side:

$$\sum_{n=1}^{\infty}\left[\frac{\partial G_n^{(1)}}{\partial t} + \kappa n^2\pi^2 G_n^{(1)} - F_n^{(1)}\right]\sin n\pi\sigma = 0 \tag{5.46}$$

The last equation must be true for all the values of σ, then it has to be

$$\frac{\partial G_n^{(1)}}{\partial t} + \kappa n^2\pi^2 G_n^{(1)} - F_n^{(1)} = 0 \tag{5.47}$$

This equation is a nonhomogeneous first order differential equation in $G_n^{(1)}$, which may be solved by using the method of variation of parameters (Greenberg, 1988) in order to get the following general solution

$$G_n^{(1)} = Ce^{-\kappa n^2\pi^2 t} + e^{-\kappa n^2\pi^2 t}\int_0^t F_n^{(1)} e^{\kappa n^2\pi^2\tau} d\tau \tag{5.48}$$

where C is an integration constant which can be determined by using the initial condition. In fact since

$$\omega^{(1)}(\sigma, t=0) = \sum_{n=1}^{\infty} G_n^{(1)} \sin n\pi\sigma = 0 \;\Rightarrow\; G_n^{(1)}(x, t=0) = 0 \text{ for } \forall n \tag{5.49}$$

and since the $G_n^{(1)}$'s are the only functions of time in the expression of $\omega^{(1)}$, from the previous equation the value of the constant C results

$$C = 0 \tag{5.50}$$

The solution of the basic state is then given by the following coefficients

$$G_n^{(1)} = (-1)^n \frac{2}{n\pi} \int_0^t \frac{\partial \omega_s}{\partial t} e^{\kappa n^2 \pi^2 (\tau - t)} d\tau \tag{5.51}$$

$O(\delta)$ perturbed state

Considering, now, the problem of $O(\delta)$, this gives rise to the following equation

$$\frac{\partial \omega^{(2)}}{\partial t} - \kappa \frac{\partial^2 \omega^{(2)}}{\partial \sigma^2} = F^(2) \tag{5.52}$$

whith the following boundary and initial conditions

$$\omega^{(2)}(\sigma = 1, t) = 0 \tag{5.53}$$
$$\omega^{(2)}(\sigma = 0, t) = 0 \tag{5.54}$$
$$\omega^{(2)}(\sigma, t = 0) = 0 \tag{5.55}$$

and where the right hand side of eq. (5.52) has been defined as

$$\begin{aligned} F^{(2)} \;=\; & -2\kappa \frac{\zeta_e}{h} \frac{\partial^2 \omega^{(1)}}{\partial \sigma^2} + 2\omega_s \frac{\sigma}{h} \frac{\partial \zeta_e}{\partial t} + \frac{\sigma}{h} \frac{\partial \zeta_e}{\partial t} \frac{\partial \omega^{(1)}}{\partial \sigma} - u \frac{\partial \omega^{(1)}}{\partial x} \\ & - u\sigma \frac{\partial \omega_s}{\partial x} - \frac{w}{h} \left(\frac{\partial \omega^{(1)}}{\partial \sigma} + \omega_s \right) \end{aligned} \tag{5.56}$$

In the last expression the term $(h + \delta\zeta_e)^{-1}$ has been expanded in Taylor series about zero as

$$\frac{1}{h + \delta\zeta_e} \simeq \frac{1}{h} + O(\delta) \tag{5.57}$$

Therefore, as already mentioned, the solution of the $O(1)$ problem, $\omega^{(1)}$, becomes the forcing for the problem to the next order of approximation.

In analogy with the first case, also here it is assumed that the solution has the form

$$\omega^{(2)} = \sum_{n=1}^{\infty} G_n^{(2)} \sin n\pi\sigma \tag{5.58}$$

Since eq. (5.52) is very similar to the eq. (5.38), following the same approach as before, the function F is expanded as half-range sinusoidal series

$$F^{(2)} = \sum_{n=1}^{\infty} F_n^{(2)} \sin n\pi\sigma \tag{5.59}$$

and the coefficients of this series can be calculated as

$$F_n^{(2)} = \int_{-1}^{1} F^{(2)} \sin n\pi\sigma d\sigma = 2\int_{0}^{1} F^{(2)} \sin n\pi\sigma d\sigma \tag{5.60}$$

According to eq. (5.58) the solution to eq. (5.52) is then given by the following coefficients

$$G_n^{(2)} = \int_0^t F_n^{(2)} e^{\kappa n^2\pi^2(\tau-t)} d\tau \tag{5.61}$$

5.2.1 Complete solution

From the results presented in the previous sections, the total expression for vorticity results

$$\omega = \sigma\omega_s + \sum_{n=1}^{\infty} [G_n^{(1)} + \delta G_n^{(2)}] \sin n\pi\sigma \tag{5.62}$$

Considering that the first term in eq. (5.62) can be also written as

$$\sigma\omega_s = \sum_{n=1}^{\infty} G_n^{(0)} \sin n\pi\sigma \tag{5.63}$$

where $G_n^{(0)}$ is determined as

$$G_n^{(0)} = \int_{-1}^{1} \sigma\omega_s \sin n\pi\sigma d\sigma = -2\omega_s \frac{(-1)^n}{n\pi} \tag{5.64}$$

more synthetically the solution for ω can be written as

$$\omega = \sum_{n=1}^{\infty} G_n \sin n\pi\sigma \tag{5.65}$$

where the coefficients G_n have been defined as

$$G_n = G_n^{(0)} + G_n^{(1)} + \delta G_n^{(2)} \tag{5.66}$$

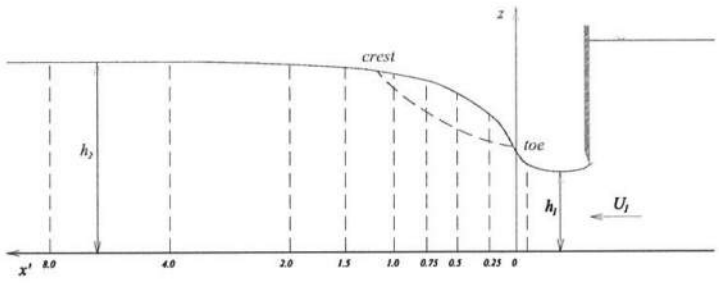

Figure 5.3: Sketch of the experimental set-up used for investigations on hydraulic jump (Svendsen *et al.*, 2000). The reference system is reversed with respect to the conventional representation to stress the similarity with the surface roller.

5.3 Similarity with the hydraulic jump

In the definition of the problem a key-role is played by the definition of the geometry of the domain, which is related to the definition of the geometry of the surface roller, and by the indication of the value of ω_s along the lower edge of the roller, which represents the only input of vorticity for the model. Therefore, in order to close the problem both the horizontal and vertical dimesion of the roller and the value of ω_s have to be determined.

The problem of the horizontal extension of the surface roller is solved if the position of the toe of the roller and of the crest of the roller are specified. The criterion which has been used to perform this task is the one defined by Schäffer *et al.* (1993) based on the wave slope, which has been extensively described in Section 3.3.3. This criterion allows not only to determine the toe location, x_t, and as a consequence of that, the length of the roller, l_r (since the end of the roller is assumed to coincide with the crest of the wave at x_c), but also to take into account the time scale of the evolution of the roller, which as the breaking wave propagates toward the shore tends to stabilize its shape.

As it has been stressed in Chapter 2, due to the difficulty of investigating the breaking waves, many analogies with other different types of flow have been adopted, such as hydralic jumps, bores, wall jets and wakes. In their model, Veeramony and Svendsen (2000) considered the hydraulic similarity between the roller of a breaking wave and the turbulent region on the front of an hydraulic jumps in order to specify the roller thickness, ζ_s, and the vorticity at the lower edge of the roller, ω_s, by using two functions obtained as best fit of the experimental data of Svendsen *et al.* (2000). In that work, three hydraulic jumps with Froude numbers similar to those of breaking waves were investigated, particularly with the aim of extracting information on the flow, on the stresses and on the extension of the recirculating area, i.e. of the roller. The experimental set-up they used is sketched in Figure 5.3

In the channel a steady jump was generated downstream of an undershot weir,

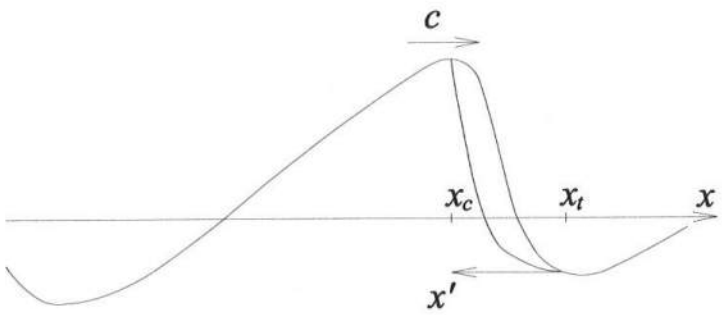

Figure 5.4: Reference system moving with the wave

the sections in Figure 5.3 indicate the locations where both the velocity profiles and the surface profiles have been measured, by using a laser-Doppler velocimeter (LDV) and a capacitance wave gage respectively.

Veeramony and Svendsen (2000) fitted the experimental data in order to get the roller thickness, which in dimensonless form reads

$$\frac{\zeta_s}{h_2\sqrt{\xi}} = 0.78e^{-\frac{x'}{l_r}}\left(\frac{x'}{l_r} - \frac{x'^2}{l_r^2}\right) \tag{5.67}$$

The thickness of the roller is related to the elevation of the lower edge of the roller ζ_e, since

$$\zeta_e = \zeta - \zeta_s \tag{5.68}$$

and the vorticity at the lower edge of the roller, which in dimensionless form is

$$\frac{\omega_s h_2 \xi}{U_1} = 15.75\left(1 - \frac{x'}{l_r}\right) \tag{5.69}$$

where h_1 and h_2 represent the minimum water depth before the jump and the undisturbed water depth downstream with respect to the jump, respectively, ξ is the ratio h_2/h_1 and U_1 is the velocity of the flow beneath the weir. The coordinate system is here fixed with the origin of the x'-axis at the toe of the recirculating region of the hydraulic jump, as it is shown in Figure 5.3. When tranferred to the case of a moving breaking wave, the coordinate x' is equivalent to a reference system moving at the same wave speed. Then the following transformation of coordinate system should be considered (see Figure 5.4)

$$x' = -(x - x_t) \tag{5.70}$$

Eq. (5.69) shows a discontinuity in correspondence of the toe of the roller, where the vorticity goes from zero to its maximum value, decreasing to zero toward the crest of the wave.

Chapter 6

The proposed numerical solution

6.1 Overview

The governing equations of the fully nonlinear Boussinesq model and the analytical solution of the vorticity equation, valid under the assumption of eddy viscosity constant over depth, have been derived and discussed in the previous chapters. Since it is not possible to solve them in a closed form, a numerical integration of the equations must be adopted.

It may be worth to stress that a numerical model such as the one presented in the followings requires a special care about the order of the adopted numerical scheme. Indeed, a careless use of a relative low-order scheme would generate truncation errors having magnitude similar to that of the dispersive terms included into the equations. In this way, the numerical diffusion due to the numerical scheme would be undistinguishable from the physical dispersion due to wave propagation.

After the very simple second order centered in space, explicit in time scheme used by Peregrine (1967) in its pioneeristic model, which required very small grid spacing, both in time and space, Abbott *et al.* (1973) used a second order time centered implicit scheme, with a back substitution of the truncation errors, in order to reduce the numerical diffusion. Finally, Wei *et al.* (1995) found an efficient way to fix the aforementioned problem, by using an higher order finite difference scheme for the spatial derivatives and a high-order predictor-corrector scheme, for the integration in time. The same approach has been adopted by Veeramony and Svendsen (2000) and by Veeramony and Svendsen (1999) and it has been maintained in the present work, since it allows to take advantage both of the relatively fast explicit scheme and of the high accuracy of the spatial derivative discretization.

The adopted finite difference scheme is described in Section 6.2. The problem is formulated in such a way that a tridiagonal system has to be solved in order to determine the velocity and the surface elevation. The use of this pre-calculated

tridiagonal matrix helps to stabilizying the system, without affecting the computational time. The details of the procedure are given in the same Section 6.2, while the description of the numerical integration to be performed for the solution of the vorticity equation is the subject of Section 6.3. Then the treatment of the boundary conditions is presented in Section 6.4.

About the solution of the vorticity equation and the calculation of the breaking terms, it must be considered that the uniform spaced grid adopted to solve the Boussinesq model in Veeramony and Svendsen (1999) seemed too coarse to accurately describe the effect of the roller. Indeed, preliminary analysis have shown that the use of this coarse grid induced losses of vorticity, which, in turn, led to breaking terms with smaller gradient of increase, in particular close to the toe of the roller, and smaller intensity with respect to that expected. In order to overcome this problem in this work an accurate description of the roller has been performed by implementing a self-adaptive-time-varying subgrid, which adjust its definition according to the dimension of the surface roller. This new numerical strategy thus allows to get a better resolution in the region where the vorticity is generated through a nested subgrid, without affecting heavily the computational efficiency of the model.

Moreover, in order to take into account the sudden increase of vorticity due to the passage of the toe of the roller, a continuous tracking both of the roller toe and of the crest is required, as opposite to the discrete tracking which was performed in the previous version of the model. A more detailed description of the adopted methodology will be given in Section 6.5. Finally, the treatment of the breaking terms onto the subgrid will be presented in Section 6.5.2.

6.2 The adopted finite difference scheme

For an efficient numerical solution of the Boussinesq continuity and momentum equations, it is convenient to write the governing equation in a more synthetic form. Thus, let

$$\zeta_t = E \tag{6.1}$$

$$\mathcal{U}_t = F \tag{6.2}$$

where

$$E = -[\overline{u}(h+\zeta)]_x \tag{6.3}$$

$$\mathcal{U} = \overline{u} + \left[\left(B - \frac{1}{3}\right) h^2 \overline{u}_{xx} - \frac{1}{2} h h_{xx} \overline{u} - h h_x \overline{u}_x\right] \tag{6.4}$$

$$F = F'(\zeta, \overline{u}) + F^t(\zeta, \overline{u}_t) + F^b + F^{sp} \tag{6.5}$$

The term F has been conveniently decomposed in order to separate the effects of the spatial variations, F'; of the nonlinear time variations, F^t; of the breaking

terms, F^b, and of the dissipation at the onshore boundary, F^{sp}. This last term is associated to the sponge layer put at end of the domain and it will described in more detail in the next section.

The components of F are then expressed as

$$\begin{aligned} F'(\zeta,\overline{u}) &= -\overline{u\overline{u}}_x - g\zeta_x - gBh^2\zeta_{xxx} \\ &\quad +\frac{1}{3}h^2\overline{u\overline{u}}_{xxx} - \frac{1}{3}h^2\overline{u}_x\overline{u}_{xx} + \frac{3}{2}hh_{xx}\overline{u\overline{u}}_x + \frac{1}{2}hh_{xxx}\overline{u}^2 \\ &\quad +hh_x\overline{u\overline{u}}_{xx} - Bh^2(\overline{u\overline{u}}_x)_{xx} + \frac{1}{3}h\zeta\overline{u}_x\overline{u}_{xx} + \frac{1}{3}h\overline{u}_{xx}(\zeta\overline{u})_x \\ &\quad -h(\zeta\overline{u}_x^2)_x + \frac{2}{3}h(\zeta\overline{u\overline{u}}_{xx})_x + \zeta_x h_{xx}\overline{u}^2 + \zeta h_x\overline{u\overline{u}}_{xx} \\ &\quad +\frac{1}{2}\zeta h_{xxx}\overline{u}^2 + \frac{3}{2}\zeta h_{xx}\overline{u\overline{u}}_x + \zeta_x h_x\overline{u\overline{u}}_x + \frac{1}{3}\zeta^2\overline{u\overline{u}}_{xxx} \\ &\quad +\zeta\zeta_x\overline{u\overline{u}}_{xx} - \zeta\zeta_x\overline{u}_x^2 - \frac{1}{3}\zeta^2\overline{u}_x\overline{u}_{xx} \end{aligned} \tag{6.6}$$

$$\begin{aligned} F^t(\zeta,\overline{u}_t) &= h\zeta_x\overline{u}_{tx} + \frac{2}{3}h\zeta(\overline{u}_t)_{xx} + \zeta h_x\overline{u}_{tx} \\ &\quad +h_x\zeta_x\overline{u}_t + \frac{1}{2}\zeta h_{xx}\overline{u}_t - \frac{1}{6}\zeta^2(\overline{u}_t)_{xx} + \frac{1}{2}(\zeta^2(\overline{u}_t)_x)_x \end{aligned} \tag{6.7}$$

$$\begin{aligned} F_b &= [-(\Delta M)_x - (\Delta P)_{xxt} + D_s - (\Delta M_1)_x - D_w \\ &\quad -D_{uw}](h+\zeta)^{-1} \end{aligned} \tag{6.8}$$

where the hat sign, indicating dimensional variables, has been omitted for the sake of simplicity.

As it has been pointed out by Veeramony and Svendsen (1999), to include the linear terms involving time derivatives in the unknown $\mathcal{U}$ and the nonlinear terms involving time derivatives in the right hand side of eq. (6.2) it is useful to solve the tridiagonal system, thus improving the stability of the model.

The adopted scheme to numerically integrate the continuity and momentum equations is one of the most popular predictor-corrector methods, namely the Adams-Bashforth-Moulton scheme, which has good stability properties (Press *et al.* (1992)). In particular, the scheme used here is the Adams-Bashforth third order predictor, which reads in this case:

$$\zeta_i^{n+1} = \zeta_i^n + \frac{\Delta t}{12}[23E_i^n - 16E_i^{n-1} + 5E_i^{n-2}] \tag{6.9}$$

$$\mathcal{U}_i^{n+1} = \mathcal{U}_i^n + \frac{\Delta t}{12}[23F_i^n - 16F_i^{n-1} + 5F_i^{n-2}] \tag{6.10}$$

being accurate up to $O(\Delta t^3)$. The convention adopted is that the pedix $(_i)$ indicates the section at which the variable is considered and the apix $(^n)$ indicates the instant of time.

At the corrector step the fourth order Adams-Bashforth-Moulton scheme, accurate up to $O(\Delta t^4)$, gives

$$\zeta_i^{n+1} = \zeta_i^n + \frac{\Delta t}{24}[9E_i^{n+1} + 19E_i^n - 5E_i^{n-1} + E_i^{n-2}] \tag{6.11}$$

$$\mathcal{U}_i^{n+1} = \mathcal{U}_i^n + \frac{\Delta t}{24}[9F_i^{n+1} + 19F_i^n - 5F_i^{n-1} + F_i^{n-2}] \tag{6.12}$$

The corrector scheme is repetead until a minimum relative error is reached both in the solution of the surface elevation, e_ζ, and of the depth integrated velocity, $e_{\overline{u}}$

$$e_\zeta = \frac{\sum_{i=1}^N \left|\zeta_i - \zeta_i^*\right|}{\sum_{i=1}^N \left|\zeta_i\right|} \tag{6.13}$$

$$e_{\overline{u}} = \frac{\sum_{i=1}^N \left|\overline{u}_i - \overline{u}_i^*\right|}{\sum_{i=1}^N \left|\overline{u}_i\right|} \tag{6.14}$$

where $i = 1, 2, ..., N$ are the N points of the computational grid in the x direction, ζ_i and $\overline{u}_i$ are the values of the variables at the section i, at the current iteration, while ζ_i^* and $\overline{u}_i^*$ are the values of the variables at the section i, at the previous iteration. The iterations are stopped when both the relative errors are less than 10^{-4}. If the denominator is zero, the iterative cicle ends if the absolute errors on both the variables is less than 10^{-5}.

At the predictor step, the time derivatives of $\overline{u}$, to be inserted in F^t, are evaluated explicitly at every time step as

$$(\overline{u}_t)_i^n = \frac{1}{2\Delta t}[3\overline{u}_i^n - 4\overline{u}_i^{n-1} + \overline{u}_i^{n-2}] \tag{6.15}$$

$$(\overline{u}_t)_i^{n-1} = \frac{1}{2\Delta t}[\overline{u}_i^n - \overline{u}_i^{n-2}] \tag{6.16}$$

$$(\overline{u}_t)_i^{n-2} = -\frac{1}{2\Delta t}[3\overline{u}_i^{n-2} - 4\overline{u}_i^{n-1} + \overline{u}_i^n] \tag{6.17}$$

and at the corrector step

$$(\overline{u}_t)_i^{n+1} = \frac{1}{6\Delta t}[11\overline{u}_i^{n+1} - 18\overline{u}_i^n + 9\overline{u}_i^{n-1} - 2\overline{u}_i^{n-2}] \quad (6.18)$$

$$(\overline{u}_t)_i^{n} = \frac{1}{6\Delta t}[2\overline{u}_i^{n+1} + 3\overline{u}_i^n - 6\overline{u}_i^{n-1} + \overline{u}_i^{n-2}] \quad (6.19)$$

$$(\overline{u}_t)_i^{n-1} = -\frac{1}{6\Delta t}[2\overline{u}_i^{n-2} + 3\overline{u}_i^{n-1} - 6\overline{u}_i^n + \overline{u}_i^{n+1}] \quad (6.20)$$

$$(\overline{u}_t)_i^{n-2} = -\frac{1}{6\Delta t}[11\overline{u}_i^{n-2} - 18\overline{u}_i^{n-1} + 9\overline{u}_i^n - 2\overline{u}_i^{n+1}] \quad (6.21)$$

where the apix $^{n+1}$ on the right hand sides indicates the values calculated at the prediction stage.

For the spatial derivatives, in the interior region a five-point central difference scheme has been adopted, both for the first order and the third order derivatives, accurate up to $O(\Delta x^4)$, while, for the second order derivatives a three-point scheme, accurate up to $O(\Delta x^2)$ have been used. At both the boundaries of the domain a one-sided scheme has been used. The scheme is forward in the case of the offshore boundary and backward in the case of the onshore boundary. The great accuracy of the adopted numerical scheme, as already mentioned, it is required to avoid that the truncation errors have the same magnitude of the dispersive terms presents in the equations. However the aforementioned high-order schemes can generate some instabilities at the boundary, for this reason particularly in the momentum equation a lower order scheme, $O(\Delta x^2)$, has been used at the first and last point of the domain.

The adopted finite-difference approximations of the derivatives, derived from a Taylor series expansion around the point of interest, are reported in Appendix A, for completeness.

In order to extract the information about the average velocity $\overline{u}$ from the computational variable $\mathcal{U}$, since only the first one is the physical variable of interest, the following tridiagonal linear system has to be solved

$$A_{i-1}\overline{u}_{i-1}^{n+1} + B_i\overline{u}_i^{n+1} + C_{i+1}\overline{u}_{i+1}^{n+1} = \mathcal{U}_i^{n+1} \quad (6.22)$$

where the coefficients, A_{i-1}, B_i and C_{i+1}, can be obtained by substituting the expression of the term u_{xx}, discretized according to eq. (A.10), and of the term u_x discretized according to eq. (A.6), into eq. (6.4),

$$A_{i-1} = \left(B - \frac{1}{3}\right)\frac{h_i^2}{(\Delta x)^2} + \frac{h_i(h_x)_i}{2\Delta x} \quad (6.23)$$

$$B_i = 1 - \frac{1}{2}h_i(h_x)_i - \left(B - \frac{1}{3}\right)\frac{2h_i^2}{(\Delta x)^2} \quad (6.24)$$

$$C_{i+1} = \left(B - \frac{1}{3}\right)\frac{h_i^2}{(\Delta x)^2} - \frac{h_i(h_x)_i}{2\Delta x} \quad (6.25)$$

The linear system (6.22) can be solved by using a simple LU decomposition (Press *et al.*, 1992), where the coefficient matrix can be efficiently pre-factorized, before starting the numerical integration, since from eqs. (6.23)-(6.25) it comes out that the matrix coefficients are not related to the flow.

Then, at each time step, the solution procedure is the following:

1. $\mathcal{U}$ is determined from the momentum equation;
2. the linear system in eq. (6.22) is solved to calculate the velocity $\overline{u}$;
3. the values of $\overline{u}$ are substituted in the continuity equation in order to get the surface elevation ζ.

6.3 On the integration of the vorticity equation

Under the hypothesis of an eddy viscosity ν_t constant over depth, but variable in time and space, following Veeramony and Svendsen (1999) the analytical solution of the vorticity transport equation has been determined as

$$\omega = \sum_{n=1}^{\infty} G_n \sin n\pi\sigma$$

where σ represents the stretched vertical coordinate and the expressions for the coefficients G_n's have been defined by perturbing the solution of eq. (5.29). According to eqs. (5.51), (5.61) and (5.64), a numerical integration would be required in order to calculate the coefficients G_n's. Let's consider the simple case of the solution up to order $O(1)$, that is

$$G_n^I = G_n^{(0)} + G_n^{(1)} \tag{6.26}$$

which at the time t may be written as

$$G_n^I\Big|_t = -(-1)^n \frac{2}{n\pi}\omega_s\Big|_t + (-1)^n \frac{2}{n\pi}\int_0^t \frac{\partial \omega_s}{\partial t} e^{n^2\pi^2\kappa(\tau-t)} d\tau \tag{6.27}$$

The use of the classical trapezoidal rule to numerically solve the integral in (6.27), which should be applied rigorously on an uniformly spaced grid, leads to quite inaccurate results if a very high z-resolution is not used, since the entire function to be integrated would be approximated piece-wise like a linear function. Therefore a more efficient approach is adopted in this case and, under some simplificative assumptions, a semi-analytical calculation of the integrals is performed.

At the instant $t + dt$ from eq. (6.27), the coeffiecient G_n^I results

$$
\begin{aligned}
G_n^I\Big|_{t+dt} &= -(-1)^n\frac{2}{n\pi}\omega_s\Big|_{t+dt} + (-1)^n\frac{2}{n\pi}\int_0^{t+dt}\frac{\partial\omega_s}{\partial t}e^{n^2\pi^2\kappa(\tau-t-dt)}d\tau \\
&= -(-1)^n\frac{2}{n\pi}\omega_s\Big|_{t+dt} + (-1)^n\frac{2}{n\pi}e^{-n^2\pi^2\kappa dt}\int_0^{t}\frac{\partial\omega_s}{\partial t}e^{n^2\pi^2\kappa(\tau-t)}d\tau \\
&\quad +(-1)^n\frac{2}{n\pi}e^{-n^2\pi^2\kappa dt}\int_t^{t+dt}\frac{\partial\omega_s}{\partial t}e^{n^2\pi^2\kappa(\tau-t)}d\tau \qquad (6.28)
\end{aligned}
$$

From eq. (6.27) it is also given:

$$
(-1)^n\frac{2}{n\pi}\int_0^t\frac{\partial\omega_s}{\partial t}e^{n^2\pi^2\kappa(\tau-t)}d\tau = G_n^I\Big|_t + (-1)^n\frac{2}{n\pi}\omega_s\Big|_t \qquad (6.29)
$$

and moreover

$$
\int_t^{t+dt} e^{n^2\pi^2\kappa(\tau-t)}d\tau = \frac{e^{n^2\pi^2\kappa dt}-1}{n^2\pi^2\kappa} \qquad (6.30)
$$

Now, for simplicity, it is assumed that the gradient in time of the vorticity at the lower edge of the roller does not vary much instantaneously, that is:

$$
\frac{\partial\omega_s}{\partial t}\Big|_t \approx \frac{\partial\omega_s}{\partial t}\Big|_{t+dt} \qquad (6.31)
$$

Obviously this assumption does not hold properly close to the toe of the roller, since at this point there is an abrupt variation of the value of ω_s.

By adopting the hypothesis in eq. (6.31), and by substituting the results in (6.29)-(6.30) into eq. (6.28), after a little algebra, the final expression for G_n^I at the next time step is

$$
\begin{aligned}
G_n^I\Big|_{t+dt} &= G_n^I\Big|_t e^{-n^2\pi^2\kappa dt} - (-1)^n\frac{2}{n\pi}\left[\omega_s\Big|_{t+dt} - \frac{1}{n^2\pi^2\kappa}(1-e^{-n^2\pi^2\kappa dt})\right. \\
&\quad \left.-\omega_s\Big|_t e^{-n^2\pi^2\kappa dt}\right] \qquad (6.32)
\end{aligned}
$$

The calculations to obtain the term relative to the solution up to $O(\delta)$, $G_n^{(2)}$, are very similar.

6.4 The boundary conditions

In order to perform the numerical simulations a special care is required at the boundaries of the domain, both at the offshore and at the onshore one. The geometry described by the numerical code can be better understood on the basis of Figure 6.1, in which the sketched physical problem and the numerical one are both represented.

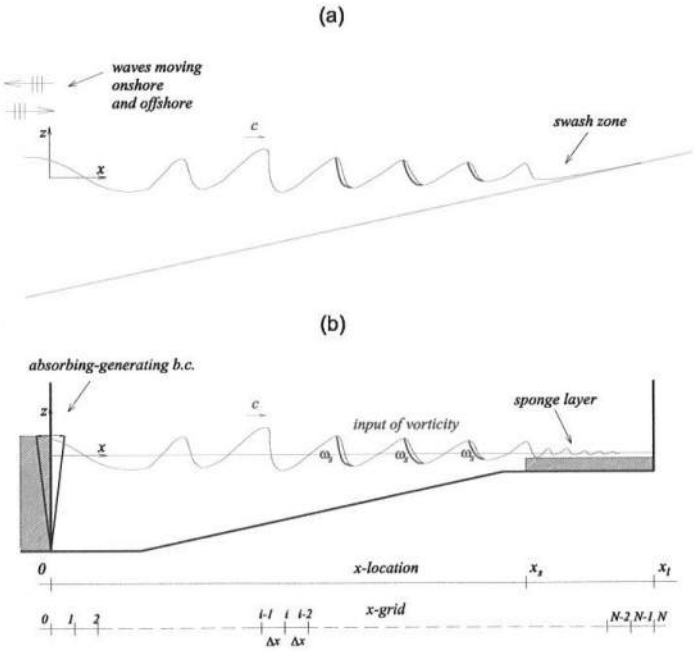

Figure 6.1: Sketch of the physical problem (a) simulated through the numerical wave tank (b).

With reference to the offshore boundary, in nature, when waves propagate toward the coastline, they may be reflected by obstacles or by the beach itself and travel seaward in a direction opposite to that of propagation. To let the waves travelling seaward leave the domain at the offshore boundary, the absorbing-generating boundary condition developed by Van Dongeren and Svendsen (1997) for the case of 2D shallow water models has been adopted. This boundary condition allows not only to specify the incoming waves, but also to radiate of the outgoing waves.

On the other side, at the onshore boundary, in nature the swash zone follows the surf zone. This region is alternatively wet and dry and the run-up and run-down phenomena take place, defining, on average, the position of the shoreline. In this model, the moving shoreline boundary condition is not modelled. Instead, as shown in Figure 6.1, after the slope, a shelf with a sponge layer is adopted. The sponge layer, which is located between the positions x_s and x_l (see Figure 6.1), allows for absorbing the incoming waves and then it reduces as much as possible the reflection from the beach.

At the offshore boundary, by using the mentioned methodology developed by Van Dongeren and Svendsen (1997), the continuity and momentum equations, written in the case of constant water depth and non breaking waves, are expressed in characteristic form as

$$\frac{\partial \beta^+}{\partial t} + \left(\overline{u} + \sqrt{gd}\right) \frac{\partial \beta^+}{\partial x} = \mathcal{G} \tag{6.33}$$

$$\frac{\partial \beta^-}{\partial t} + \left(\overline{u} - \sqrt{gd}\right) \frac{\partial \beta^-}{\partial x} = \mathcal{G} \tag{6.34}$$

where $d = h + \zeta$ is the total water depth and $\mathcal{G}$ is expressed as follows

$$\mathcal{G} = -\left(B - \frac{1}{3}\right) h^2 \overline{u}_{xxt} - Bgh^2 \zeta_{xxx} \tag{6.35}$$

β^+ and β^- are the incoming and outgoing characteristics respectively

$$\beta^+ = \overline{u} + 2\sqrt{gd} \tag{6.36}$$

$$\beta^- = \overline{u} - 2\sqrt{gd} \tag{6.37}$$

The outgoing waves are represented by the negative characteristic and are unknown. In order to specify them, the equations have been linearized and the assumption of linear superposition has been made (Van Dongeren and Svendsen (1997)), then both surface elevation and velocity are decomposed in incoming and outgoing components

$$\zeta = \zeta_i + \zeta_r \tag{6.38}$$

$$\overline{u} = \overline{u}_i + \overline{u}_r \tag{6.39}$$

and considering the exact expression $Q = c\zeta$, valid for wave of permanent shape, it can be written

$$\overline{u}_i = \frac{c\zeta_i}{h + \zeta_i}, \quad \overline{u}_r = -\frac{c\zeta_r}{h + \zeta_r}, \tag{6.40}$$

while, from shallow water theory, the phase speed may be expressed as

$$c = \sqrt{g(h + \zeta)} \tag{6.41}$$

The surface elevations of the incoming and of the reflected wave result then

$$\frac{\zeta_i}{h} = \frac{\overline{u}_i}{c_0} + \frac{1}{2}\frac{\overline{u}_i^2}{c_0^2} + \frac{\overline{u}_i \overline{u}_r}{2c_0^2} + O\left(\frac{\zeta_i^3}{h^3}\right) \tag{6.42}$$

$$\frac{\zeta_r}{h} = -\frac{\overline{u}_r}{c_0} + \frac{1}{2}\frac{\overline{u}_r^2}{c_0^2} + \frac{\overline{u}_i \overline{u}_r}{2c_0^2} + O\left(\frac{\zeta_r^3}{h^3}\right) \tag{6.43}$$

where $c_0 = \sqrt{gh}$.

Substituting eq. (6.39) in the second of (6.37), to determine β^-

$$\frac{\beta^-}{c_0} = -2 - \frac{1}{4}\frac{\overline{u}_i^2}{c_0^2} - \frac{3}{2}\frac{\overline{u}_i\overline{u}_r}{c_0^2} + 2\frac{\overline{u}_r}{c_0} - \frac{1}{4}\frac{\overline{u}_r^2}{c_0^2} \tag{6.44}$$

and then solving with respect to u_r, gives the outgoing component of the depth averaged velocity

$$\frac{\overline{u}_r}{c_0} = \left(-3\frac{\overline{u}_i}{c_0} + 4\right) - 2\sqrt{2\frac{\overline{u}_i^2}{c_0^2} - 6\frac{\overline{u}_i}{c_0} + 4 - \left(\frac{\beta^-}{c_0} + 2\right)} \tag{6.45}$$

where also the still water conditions $\overline{u}_r = 0$, $\overline{u}_i = 0$ and $\frac{\beta^-}{c_0} + 2 = 0$ has been taken into account, in order to select the physical meaningful root between the two roots of the second order equation (6.44). Therefore, at the offshore boundary only the velocity $\overline{u}$ has to be specified.

At the onshore boundary the effect of the sponge layer is modelled by including a dissipation term in the momentum equation (see eqs. (6.2) and (6.5))

$$F_{sp} = W(x)\overline{u} \tag{6.46}$$

where

$$W(x) = \begin{cases} 0, & 0 \le x < x_s \\ \alpha_1 \frac{e^{[(x_{sp})^n]} - 1}{e-1}, & x_s \le x \le x_l \end{cases} \tag{6.47}$$

with the dimensioless x-coordinate inside the sponge layer equal to

$$x_{sp} = \frac{x - x_s}{x_l - x_s} \tag{6.48}$$

where x_s defines where the sponge layer starts and x_l is the length of the computational domain. The sponge layer has then two parameters, α_1 and n. In particular, the first one defines the strenght of the sponge layer (it ranges between 5 and 10 in the simulation) and the second one contributes to ensure a smooth transition into the sponge layer in order to avoid reflection from it (the value used is $n = 2$).

The boundary condition for the vorticity equation has been subject of great attention in this study, since it is maybe one of the most delicate point of the model. A detailed discussion about the reason for a special treatement of this boundary and the description of the adopted methodology will be given in the next sections.

6.5 The self adaptive time varying grid

As it has been described in the Section 5.3, the vorticity at the lower edge of the roller, ω_s, is expressed by the function

$$\omega_s = 15.75\left(1 - \frac{x - x_t}{l_r}\right) \tag{6.49}$$

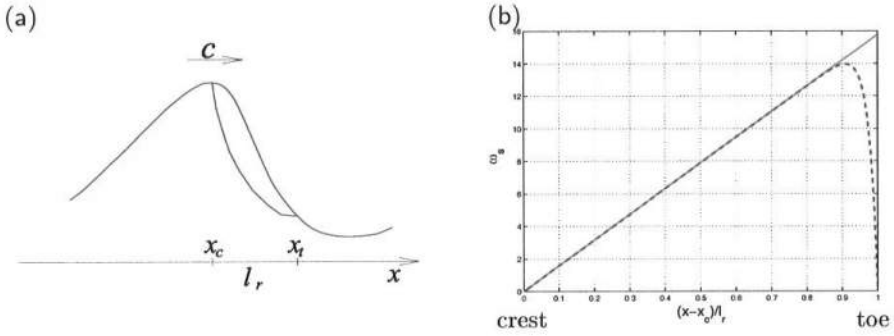

Figure 6.2: (a) Sketch of the roller and (b) vorticity at the lower edge of the roller (solid line fit of data from Svendsen *et al.* (2000); dashed line approximated curve used in the numerical model).

where x_t and l_r are the position of the toe and the length of the roller, respectively. In particular, the length of the roller is defined as the distance between the position of the roller toe x_t and of the wave crest, x_c. Eq. 6.49 is just a fit of the experimental data on hydraulic jumps analyzed in Svendsen *et al.* (2000). At the toe of the roller the vorticity suddenly increases due to the breaking onset. Since the sharp discontinuity at that location caused numerical instabilities during the simulations, in the previous version of the model by Veeramony and Svendsen (1999), the following approximation of eq. (6.49) has been used

$$\omega_s = 15.75 \left(1 - e^{-40\frac{x-x_t}{l_r}}\right)\left(1 - \frac{x - x_t}{l_r}\right) \tag{6.50}$$

In Figure (6.2) the solid line represents the regression of experimental data as given by eq. (6.49) and the dashed line represents the values of ω_s obtained by using eq. (6.50). The maximum value of vorticity occurs right close to the toe of the roller with a very high gradient. Therefore, for an accurate prediction of the flow of a breaking wave, it is crucial to have a good resolution in this region, in order to avoid losses of vorticity and, in turn, underestimate of the breaking terms. Thus, to achieve this resolution, the reduction of the spatial grid size Δx would become so small that the advantages of using a Boussinesq model would be strongly reduced. In fact the length scale of the roller region is much smaller than the one of the waves and, as a consequence of that, a grid optimized to solve the Boussinesq equations is too coarse for modelling the roller. Therefore, a new numerical strategy based on the adoption of a self-adaptive time varying grid has been implemented here, thus getting high accuracy only whereas it is needed. The new grid follows the evolution of the wave, or, in other words, of the surface roller, then it moves and change size as the wave propagates toward the shore. In particular, since a greater accuracy is needed close to the toe of the roller, in the roller region the grid has a finer subdivision.

The multi-grid methods have been developed to describe phenomena where a great accuracy is needed only locally, such as very irregular domain (Wu *et al.*,

1997; Spitaleri and Corinaldesi, 1997; Kania, 1999; Papadakis and Bergeles, 1999; Park and Borthwick, 2001), while time-varying grids have been used in some cases to model phenomena quickly varying in time, but only in some part of the domain, such as the evolution of the front of the free surface profile due to a dam break (Lie *et al.*, 1998; Jeong and Yang, 1998, 1999; Jha *et al.*, 2001). Unfortunately, these methods have been adopted often coupled to Volume of Fluid (VOF) methods, which is not the case in the present work, and very few details are provided, to the knowledge of the writer, by people that used them with finite difference schemes. In the latter case, the difficulty derives from the fact that finite difference schemes are based on uniform size grid, while it is known not only that for the same schemes the accuracy is not exactly defined but also that this kind of schemes looses greatly accuracy when the grid is not uniformly spaced. Moreover, the type of grid needed here is also a time-varying grid, where the grid points move in time, therefore there is also the problem of how to determine the celerity of the numerical cell.

6.5.1 Definition of the moving grid

As a first step, in order to better define the position of the roller, a redefinition of the position of both the wave crest and the toe of the surface roller has been performed. In fact while in the previous version of the model both the crest and the toe are located on the uniform grid points, obtaining a discontinuous movement of these points, in the present work both the crest and the toe are not tied up on the numerical grid but they are allowed to move continuously onto the x-axis.

The position of the crest, x_c, is defined as the point where the slope of the surface is zero, through a second order interpolation. On the other hand, in order to define the position of the toe, x_t, a little more complex procedure is required. As a first approximation, x_t is defined as the point where the second order derivative of the surface elevation is equal to zero, that is the toe location coincides with the position of the inflection point. If the condition $\alpha > \alpha_{toe}$ is satisfied, where α_{toe} is evaluated according to the criteria of Schäffer *et al.* (1993) (see eq. (3.18)), then the position of the toe is then redefined at the point where $\alpha = \alpha_{toe}$, by using a linear interpolation.

Finally the length of the roller is calculated as

$$l_r = x_t - x_c \tag{6.51}$$

For each roller, given the position of the crest x_c and of the toe x_t, a subgrid, which is finer close to the toe, is defined as in Figure 6.3.

The formulation used to define the subgrid is given by the following expression

$$\Delta x_g = \frac{x_t - x_c}{ng}; \qquad \Delta x_{sg} = \frac{\Delta x_g}{ng} \tag{6.52}$$

where Δx_g is the interval for the first subdivision inside the roller, ng is the fundamental number of subdivisions, Δx_{sg} is the interval for the finer subdivision of the roller.

The position x_g^i of a point inside the subgrid is then

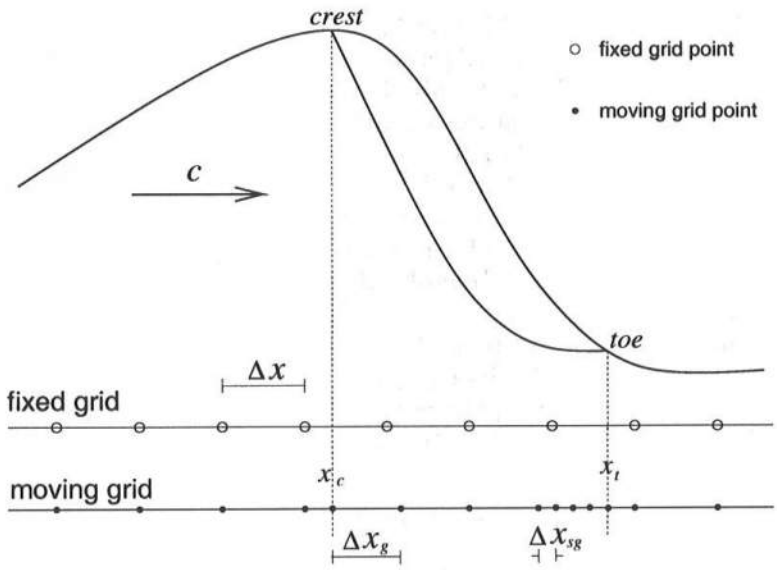

Figure 6.3: Scheme of the fixed grid (circles) and of the self-adaptive time varying grid (dots) under the roller.

$$x_g^i = x_g^{i-1} + \begin{cases} \Delta x_g, & x_c \leq x_g^{i-1} < x_t - \Delta x_g \\ \Delta x_{sg}, & x_t - \Delta x_g \leq x_g^{i-1} < x_t \end{cases} \tag{6.53}$$

Therefore, it can be noticed that the number of representative points inside the roller is fixed, being equal to $2ng$, and does not depend on the length of the roller. Instead, the size of the subdivisions changes according to the roller dimensions, keeping the same degree of accuracy inside, in particular close to the toe, where the grid is finer. Moreover, the subgrid moves according to the movement of the roller, while outside of this region the uniform grid spacing is kept.

By using this approach, the boundary condition for the vorticity transport equation, which represents also the source of vorticity for the model, can be specified avoiding to loose accuracy due to the relatively coarse uniform grid. Both the thickness of the roller, ζ_s, and the vorticity at the lower edge of the roller, ω_s, are then evaluated on the self-adaptive time varying grid points, according to eq. (5.67) and (6.50).

Figures 6.4, 6.5 and 6.6 show the difference in evaluating ω_s using the uniform fixed grid and the subgrid, for three values of ng. It can be noticed that by adopting the subgrid, the calculated ω_s represents eq. (6.49) better, particularly close to the toe, where the sudden increase of vorticity is considered and cumulated in the solution. It should be noticed that assuming a value of $ng = 8$ the behavior is already good.

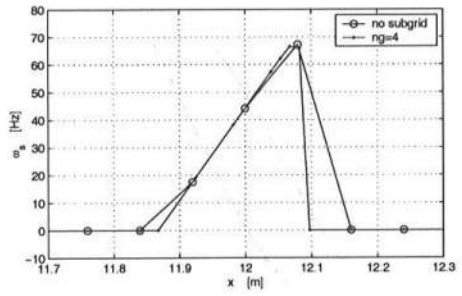

Figure 6.4: Discretization of the vorticity at the lower edge of the roller, ω_s, by using the uniform fixed grid (circle) or the moving grid (dots). Fundamental number of subdivisions $ng = 4$.

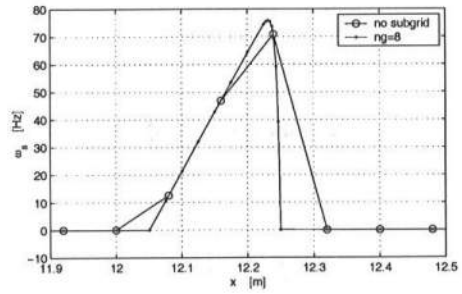

Figure 6.5: Discretization of the vorticity at the lower edge of the roller, ω_s, by using the uniform fixed grid (circle) or the moving grid (dots). Fundamental number of subdivisions $ng = 8$.

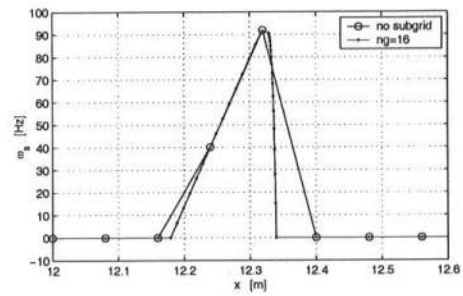

Figure 6.6: Discretization of the vorticity at the lower edge of the roller, ω_s, by using the uniform fixed grid (circle) or the moving grid (dots). Fundamental number of subdivisions $ng = 16$.

6.5.2 On the evaluation of the breaking terms onto the moving grid

As it has been previously discussed, the aim of introducing the aforementioned self-adaptive time varying grid is to avoid vorticity losses inside the model and to have a bigger dissipative effects at the toe of the roller, where the flow separation induces a strong shear layer. This, traduced in terms of the Boussinesq model presented in Chapter 4, requires a more accurate evaluation of the breaking terms $(\Delta M)_x$, $(\Delta P)_{xxt}$, D_u, D_{uw} and D_s, in order to take into account for the right accumulation of vorticity.

In order to evaluate the aforementioned breaking terms, by using the expressions determined in Chapter 4, the following spatial derivatives

$$\frac{\partial \zeta}{\partial x}, \frac{\partial \omega_s}{\partial x}, \frac{\partial u}{\partial x}$$

have to be evaluated. To avoid the loss of accuracy introduced by the use of finite difference scheme with non uniformly spaced grid, the simplest method is to calculate the previous derivates onto the fixed uniform grid and then to transfer them onto the moving non uniform grid, through a linear interpolation.

Since the grid is moving, the procedure to calculate the time derivatives is more complex. Let (x,t) be the real domain and (x^*,t^*) be the image domain

$$x \rightarrow x^* \tag{6.54}$$

$$t \rightarrow t^* \tag{6.55}$$

such that, being f a generic variable, the time derivatives should be evaluated, by using the chain rule, as

$$\left.\frac{\partial f}{\partial t^*}\right|_{x^*} = \left.\frac{\partial f}{\partial x}\right|_t \left.\frac{\partial x}{\partial t^*}\right|_{x^*} + \left.\frac{\partial f}{\partial t}\right|_x \Rightarrow \left.\frac{\partial f}{\partial t}\right|_x = \left.\frac{\partial f}{\partial t^*}\right|_{x^*} - \left.\frac{\partial f}{\partial x}\right|_t \left.\frac{\partial x}{\partial t^*}\right|_{x^*} \tag{6.56}$$

where it could be assumed, as a first approximation, that

$$\left.\frac{\partial x}{\partial t^*}\right|_{x^*} \approx c \approx \sqrt{g(h+\zeta)} \tag{6.57}$$

However, one of this derivation is only valid if there is a perfect correspondence of the number of grid points between the real domain and the image domain, meaning that the grid number have to be the same in both cases. Unfortunately, this is not the case here, in fact the subgrid introduced in the previous section, has a number of points greater than the uniform grid, in order to increase the accuracy within the roller region. Moreover, since the roller moves and new rollers are generated inside the domain as the wave propagates, the number of points of the moving grid is not only greater, with respect to the fixed grid, but also it varies in time. Nevertheless, the formulation in eq. (6.56) has been reported in order to stress the influence of the celerity in the evaluation of the time derivatives.

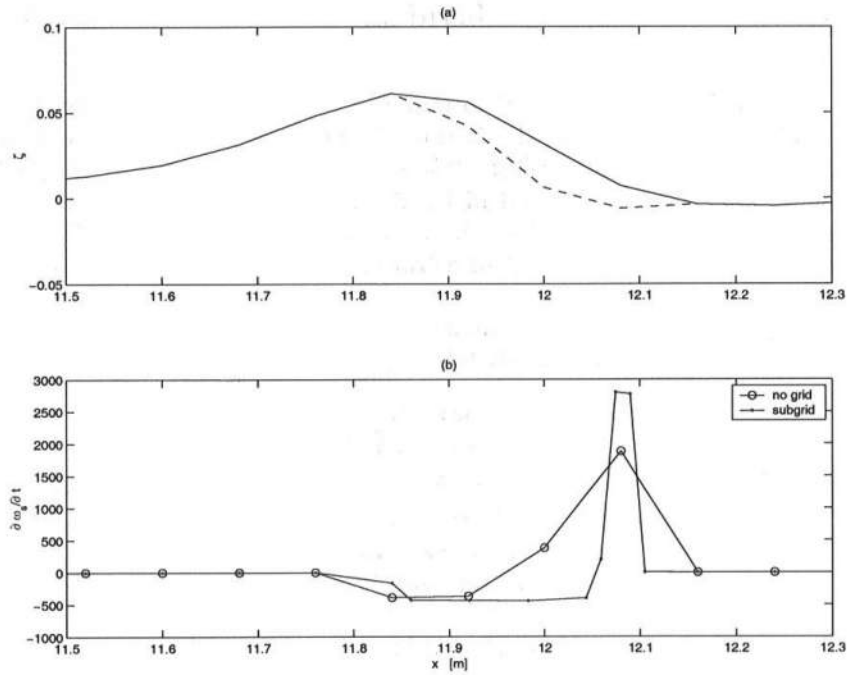

Figure 6.7: (a) Roller profile; (b) Spatial variation of the $\partial\omega_s/\partial t$, by using the uniform fixed grid (circle) or the moving grid (dots). Length of the roller $l_r = 0.245m$.

Due to the aforementioned limit, a different procedure has been then adopted in this work. In order to calculate the time derivatives, the old values of ω_s, $G_n^{(1)}$, $G_n^{(2)}$ and of $G_n^I = G_n^{(0)} + G_n^{(1)}$ have to be stored and transfered, by linear interpolation, from the moving grid at the previous time step, n, onto the moving grid at the next time step, $n+1$. Then, the time derivatives are evaluated at the same point onto the current moving grid.

Some comparisons of the time derivatives of ω_s, using the fixed grid and the moving grid method, are showed in Figure 6.7 and 6.8, for two situations where the surface rollers have different lengths.

The analysis of the effects of using the subgrid to evaluate the term $\frac{\partial\omega_s}{\partial t}$ is particularly relevant, since it is exaclty this term which is cumulated in the evaluation of the integrals of eqs. (5.51), (5.61) and (5.64) to obtain the solution of the vorticity transport equation.

From the analysis of the figures it can be noticed that, when the subgrid is used the sudden change of the term $\frac{\partial\omega_s}{\partial t}$ is better represented, due particularly to the redefinition of the toe position and to the higher resolution obtained close to it. In Figure 6.8, by using the uniform fixed grid, the previous sudden change is not present, while by using the self-adaptive time varying grid this behaviour is still

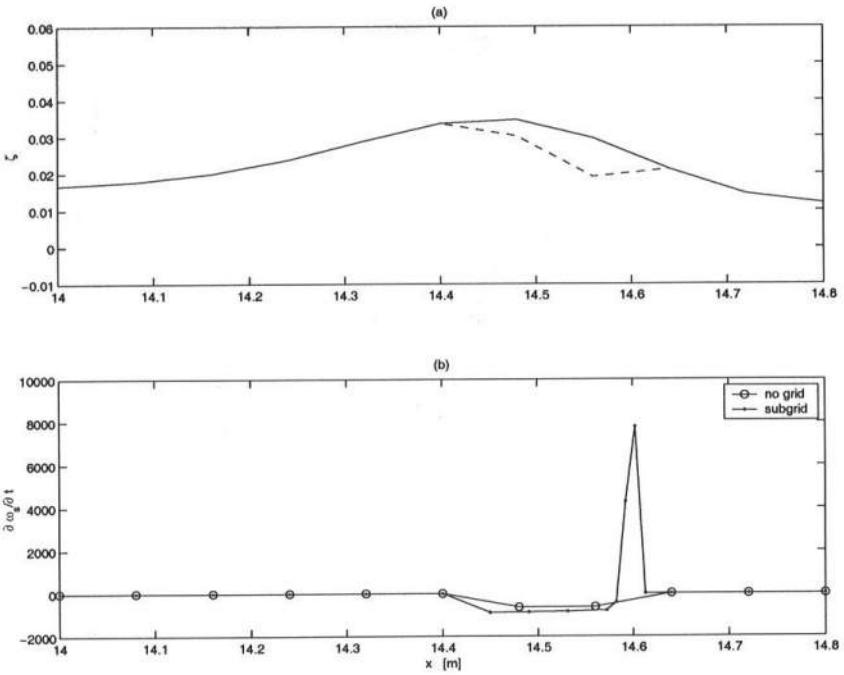

Figure 6.8: (a) Roller profile; (b) Spatial variation of the $\partial\omega_s/\partial t$, by using the uniform fixed grid (circle) or the moving grid (dots). Length of the roller $l_r = 0.163m$.

represented.

Finally, after having cumulate the effects of the roller by using the refined grid, the calculation of the breaking terms $(\Delta M)_x$, $(\Delta P)_{xxt}$, D_u, D_{uw} and D_s is performed onto the fixed grid, since they appear into the momentum equation, whose integration is done only onto the fixed grid.

For example, in Figure 6.9 are shown: the wave profile, with the roller position evaluated both on the fixed uniform grid and on the moving refined grid; the comparison between the excess of momentum ΔM evaluated onto the fixed grid and onto the subgrid, on the same panel the linearly interpolated values of ΔM coming from the subgrid are reported, and, finally, in the last panel the derivatives $(\Delta M)_x$ calculated directly onto the fixed grid and the ones evaluated using ΔM onto the subgrid are shown. As it can be noticed, there is a remarkable difference for the term ΔM in the two cases, as the subgrid evaluation allows to catch its sudden increase, corresponding to the position of the toe of the roller, and its higher values. Besides, the interpolation from the subgrid toward the fixed grid of ΔM does not seem to affect the accuracy too much. This change is also reflected by the results about the the breaking term $(\Delta M)_x$, which increases.

One more consideration need to be discussed here. In all the previous versions of the model, a filter was used in order to smooth out the breaking terms and have a more stable code. Moreover, when a more accurate modeling of the position of the toe is performed, it it should be also expected that the term ΔM is zero before the toe arrives and then it starts to growth. A similar behaviour it is expected also for the term $(\Delta M)_x$. If a filter is used, it is impossible to recover this behaviour as it is shown by Figure 6.9, where $(\Delta M)_x$ is nonzero even when the wave is not breaking yet, that is well outside of the roller region.

Since by using the subgrid approach the model becomes more stable, as it is demonstrated by the fact that no instability problem did show up during the calculations, the aforementioned filter has been removed. As a consequence of that, the expected (ΔM_x) behaviour is recovered, as it is shown by Figure 6.10.

Indeed, defining as x_t the true position of the toe onto the moving subgrid and as x_t^{fixed} the position of the toe onto the fixed grid (which always correspond to the closest position on the fixed grid following the location of the true toe) and by using a second order scheme to calculated $(\Delta M)_x$

$$(\Delta M)_x = \frac{\Delta M_{i+1} - \Delta M_{i-1}}{2\Delta x} \tag{6.58}$$

which gives onto the fixed grid

$$(\Delta M)_x \neq 0 \ \texttt{at} \ x = x_t^{fixed} \tag{6.59}$$

$$(\Delta M)_x = 0 \ \texttt{at} \ x = x_t^{fixed} + \Delta x \tag{6.60}$$

Of course, in order to certainly states the benifits of the proposed new approach, the effects of the changes introduced here must be discussed by comparing the numerical results obtained with the proposed version of the model both with the updated and debugged version of the model by Veeramony and Svendsen (1999),

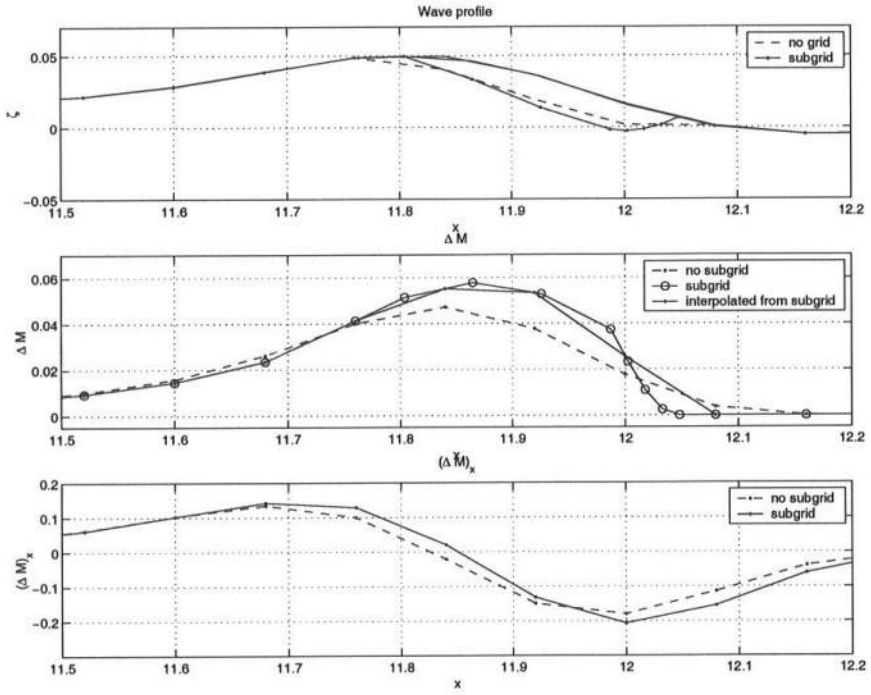

Figure 6.9: Variation of the roller profile (dashed line: fixed grid model, solid line: proposed moving grid model). ΔM (dashed-dot line: fixed grid model, solid-circle line: proposed moving grid model, solid-dot line: results interpolated onto the fixed grid from the self-adaptive time varying grid). $(\Delta M)_x$ calculated by using a filter (dashed-dot line: fixed grid model, solid-dot line: proposed moving grid model)

which uses a uniform fixed grid, and with literature data. This will be presented in the next chapter.

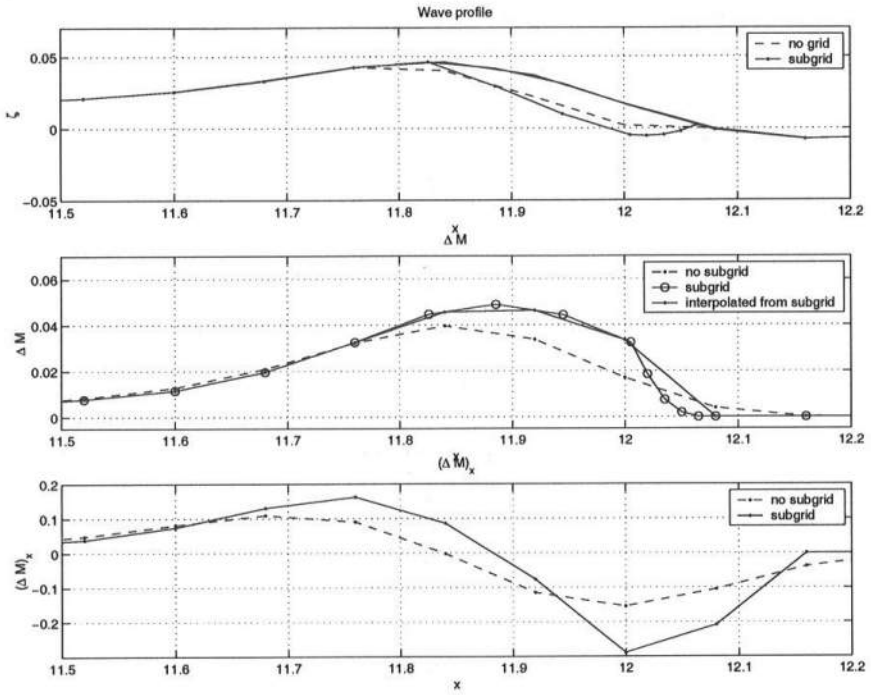

Figure 6.10: Variation of the roller profile (dashed line: fixed grid model, solid line: proposed moving grid model). ΔM (dashed-dot line: fixed grid model, solid-circle line: proposed moving grid model, solid-dot line: results interpolated onto the fixed grid from the self-adaptive time varying grid). $(\Delta M)_x$ calculated by using a filter (dashed-dot line: fixed grid model, solid-dot line: proposed moving grid model)

Chapter 7

Model results

7.1 Overview

The Boussinesq-type model presented here is able to represent the propagation of regular and irregular waves both in the shoaling and in the surf zone. In order to describe more accurately the sudden increase of vorticity due to wave breaking, particularly in the region near to the toe of the surface roller, a new numerical strategy, based on the adoption of a self-adaptive time varying grid, has been implemented (see Chapter 6). The effects of the changes due to the implementation of the proposed moving subgrid have been tested by comparing the results provided by the proposed model, when this approach is adopted (hereinafter referred to as Moving Grid or MG model), with both experimental data and results provided by the same updated and debugged version of the model of Veeramony and Svendsen (1999), in which the moving refined grid was not used (hereinafter referred to as Fixed Grid or FG model). This double comparison allowed to enlighten the effectiveness of the proposed upgraded Boussinesq model, particularly with respect to the one of Veeramony and Svendsen (1999), which represents the starting point of the present work. It is worth pointing out that the model of Veeramony and Svendsen (1999), before being used, was carefully derived again and the numerical code was debugged according to the derivations.

Before presenting the aforementioned comparisons with experimental data, a validation of the model with particular emphasis to the breaking criterion and the effect of the breaking process has been performed. The results about the validation are both quantitative and qualitative: the former based on an agreement with a different breaking criterion with respect to the one adopted in the presented model; the latter was based on the qualitative analysis of the vorticity production due to breaking and, in turn, on the estimate of the breaking terms obtained the momentum equation with the assumption of rotational flow after the wave breaks.

The comparisons with experimental data have been carried out by using literature experimental data on regular breaking waves. The results of the comparisons will be described in Section 7.3, particularly focusing on the main physical charac-

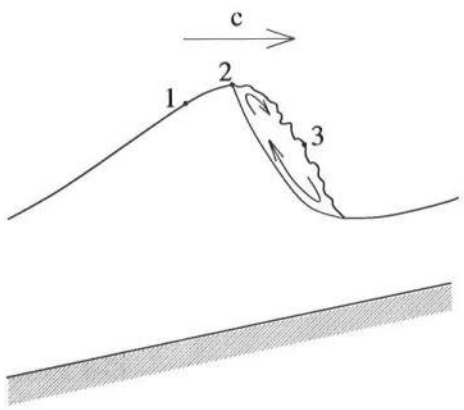

Figure 7.1: Scheme of a breaking wave according to the breaking criterion defined by Eq. (7.1). 1. $u_s < c$. 2. $u_s \approx c$. 3. $u_s > c$.

teristics of the wave motion, such as surface elevation, wave height, velocity profiles under the waves and wave speed. Since one of the peculiarity of the presented model is that to be able to describe the undertow profile due to breaking waves, some comparisons with experimental data about this phenomenon are discussed in Section 7.3.4.

Finally, the model capabilities to simulate the propagation of irregular waves have been tested here, especially with regards to wave groups generated in a wave tank. Indeed, the time series of the surface elevation, the wave height spatial distribution and the position of the breaking point have been deeply analyzed; the results are then discussed in Section 7.4.

7.2 Model performances

7.2.1 Breaking criterion validation

It may be worth to pointing out that, as already stressed, the Boussinesq models have a strong limit given by the fact that they are not able to predict the breaking: an external criterion is thus necessary in order to trigger the breaking. Thus, first of all, the proposed model has been validated by trying to verify that a different breaking criterion, with respect to the one adopted here (Schäffer *et al.*, 1993), was fitted. Among several breaking criterion, the one chosen here to validate the model is a physical based one.

Indeed, it is well known that the initiation of breaking starts when the surface velocity at the crest u_c is equal to the phase velocity c, or, in other words, when

$$\frac{u_s}{c} = 1 \tag{7.1}$$

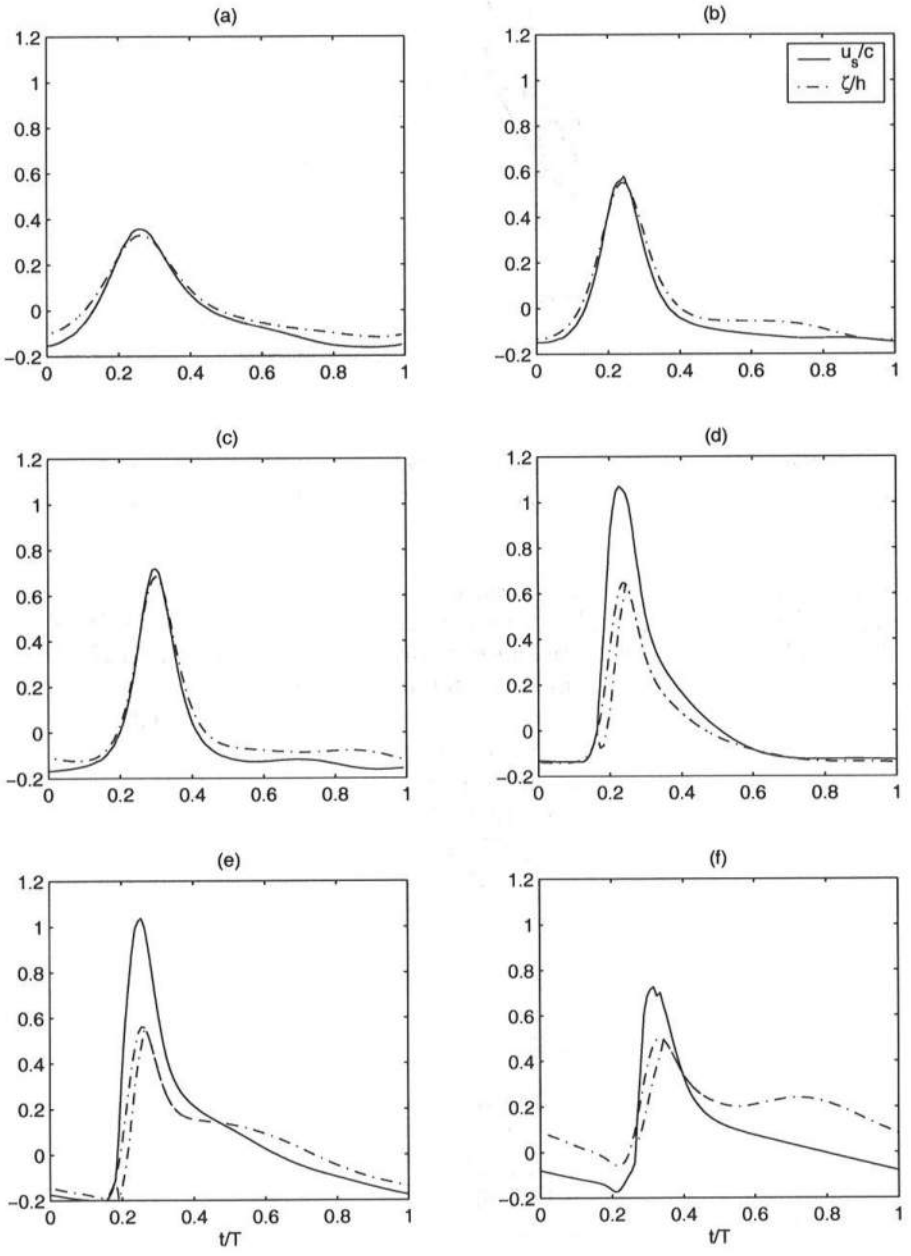

Figure 7.2: Dimensionless surface velocity u_s/c (solid line) and surface profile ζ/h (dash-dot line) time series as obtained from the proposed model, when applied to reproduce the data of the six gauges reported in Cox *et al.* (1995) located over a sloping beach at different depth (see Table 7.I). (a), (b) and (c): transition region. (d), (e) and (f): surf zone.

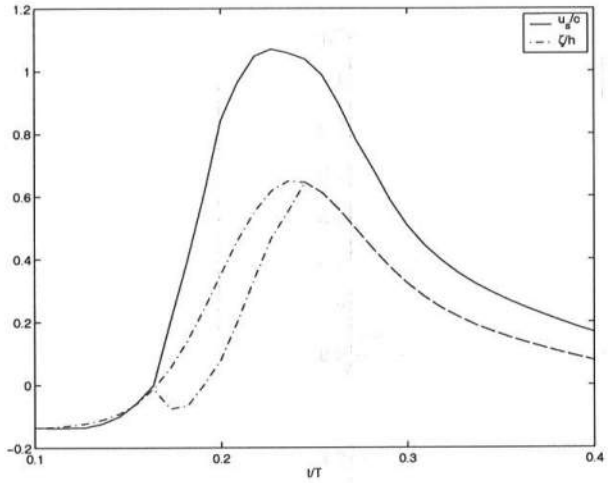

Figure 7.3: Closer view of the surface velocity time series for the Cox *et al.* (1995) case, L4 gauge. (solid line u_s/c; dashed dot line ζ/h).

Indeed the surface particles, which are downstream respect to the crest, are accelerated downward and move faster than the wave, then a turbulent shear is generated to sustain this motion (point 3 in Figure 7.1). The particles on the surface, upstream respect to the crest, move with a velocity smaller than c, since there is no force able of accelerating them upward (point 1 in Figure 7.1), while at the crest the surface velocity is about equal to the wave speed (point 2 in Figure 7.1). Thus, the turbulent front is counterbalanced by the creation of shear at the lower edge of the roller, i. e. from toe to crest. Therefore a very delicate test for the model prediction capabilities is the evaluation of u_s compared to c. Figure 7.2 shows the ratio u_s/c at the six gauge locations of Cox *et al.* (1995). As a reference in the same figure also the dimensionless surface profile ζ/h is reported. It may be noticed that before breaking the ratio u_s/c is always less than one, as expected, while for breaking waves close to the front it is bigger than one. In particular, Figure 7.3 shows a closer view in correspondence of the front region of a breaking wave. From this analysis it turns out that the model results are very close to the reality, at least from a qualitatively viewpoint. In fact, the maximum of the velocity occurs before the crest and the dimensionless surface velocity at the crest is very close to one, satisfying the breaking criterion defined in eq. (7.1) while behind the front the surface velocity is smaller than the wave velocity, thus satisfying a the different situations the breaking criterion defined by eq. (7.1).

It is worth stressing that an important feature of the criterion based on the surface velocity and the wave speed is that there are no empirical parameters to be calibrated. Thus, from a physical point of view, it is remarkable that the model results agree in a fairly good manner with this criterion, even though the breaking

criterion implemented into the model is a different one, i.e. the one proposed by Schäffer *et al.* (1993).

7.2.2 Breaking and vorticity production

The main improvement of the model of Veeramony and Svendsen (1999) and, in turn, of the one presented here, as opposite to the majority of the Boussinesq-type of models proposed in literature, is that the contribution of vorticity due to wave breaking is retained in order to model the flow inside the surf zone. As a matter of fact, the presence of vorticity inside the flow allows to derive the expressions for the breaking terms, which represents the excess of momentum flux and the related energy dissipation due to the breaking process in the nearshore region.

Figure 7.4 shows the contour lines of the time series over a wave cycle of the calculated vorticity distribution under a breaking wave which has just started to break, i.e. within the transition region. In particular, in Figure 7.4(a) the results of the FG model are reported, while Figure 7.4 (b) reports those of the MG model. It is worth to pointing out, for clarity sake, that the direction of wave propagation here is from right to left, as it happens always when the represented results are time series of the variables.

From the comparison with the previous version of the model, it can be noticed that the proposed approach allows to recover greater values of vorticity on the front of the wave, close to the roller region on the front of the wave, since the vorticity losses due to the fixed grid have been removed. As a consenquence of this, the vorticity is clearly spread more upstream in this last case. The increased generation of vorticity leads, in turn, to larger values of the breaking terms. From the analysis of Figure 7.5, which shows the breaking term evolution corresponding to the wave conditions reported in the previous figure, obtained both with the FG model (see Figure 7.5(a)) and the MG model (see Figure 7.5(b)), it happears evident that the biggest breaking terms, which are $(\Delta M)_x$ (excess of momentum flux due to the variation over the water column of the rotational velocity u_r) and $(\Delta P)_{xxt}$ (contribution given to the pressure due to the vertical motion) represented by the dashed line in figure, are basically doubled by using the MG model. Another effects of using the adaptive grid method is to increase the gradient of variation of the breaking terms, modelling the fact that the phenomenon is really a shock process.

Figures 7.6 and 7.7 are similar to the two previous ones, but they refer to a section further onshore, in the inner surf zone. With respect to the situation in the transition region, previously described, it can be noticed that the vorticity did spread remarkably inside the flow, especially by using the MG approach. However, the breaking terms are reduced and in particular, the contribution of $(\Delta P)_{xxt}$, which was predominant before, is decreased.

The previous model of Veeramony and Svendsen (1999) did not provided an accurate prediction of the breaking terms, as, from the analysis of the momentum excess of hydraulic jump, bigger gradients of them where expected to describe the impulsive breaking dissipation (Svendsen, 2001, personal communication). The use

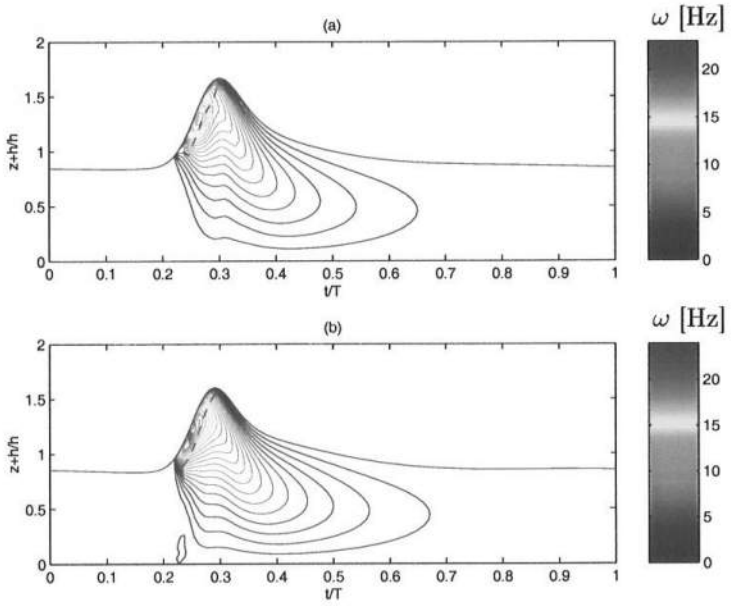

Figure 7.4: Transition region. Contour lines of the vorticity distribution under a breaking wave. (a) FG model results; (b) MG model results (n.b.: the wave propagates from right to left).

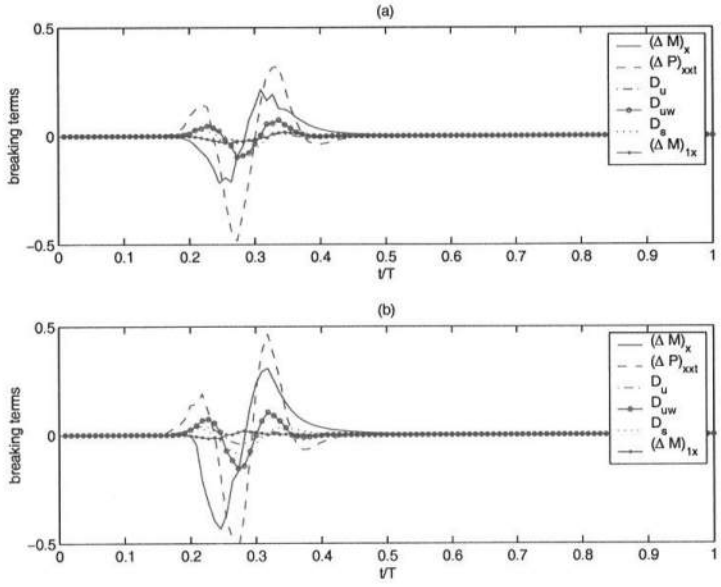

Figure 7.5: Transition region. Time series of the breaking terms. (a) FG model results; (b) MG model results (n.b.: the wave propagates from right to left).

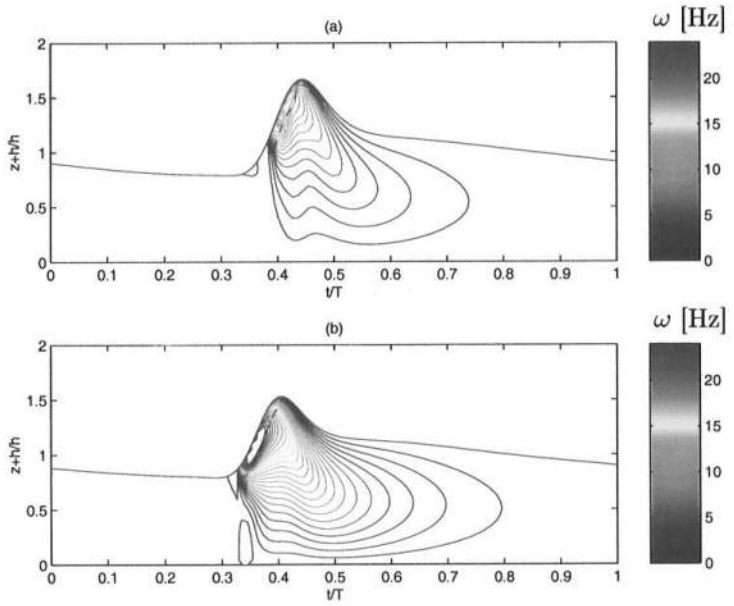

Figure 7.6: Inner surf zone. Contour lines of the vorticity distribution under a breaking wave. (a) FG model results; (b) MG model results (n.b.: the wave propagates from right to left).

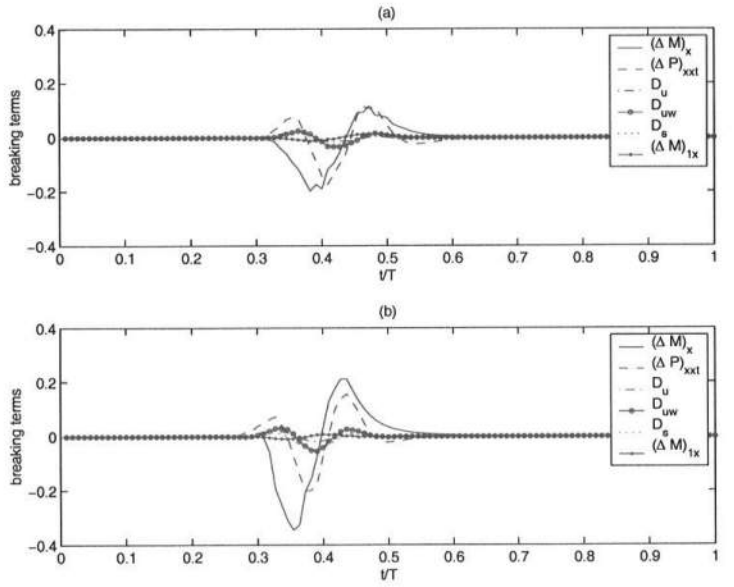

Figure 7.7: Inner surf zone. Time series of the breaking terms. (a) FG model results; (b) MG model results (n.b.: the wave propagates from right to left).

of the subgrid approach leads to a more realistic estimate of the vorticity introduced inside the flow and, in turn, to a bigger dissipation particularly in the transition region, where the fastest changes of the wave characteristics take place.

7.3 Comparison with literature regular wave data

The proposed model performances have been tested here by making at once two different comparisons having different goals: a relative and an absolute one. As a matter of fact the presented model has been implemented to simulate the reality in a fairly good manner: thus comparisons with the experimental data of Hansen and Svendsen (1979), Cox *et al.* (1995), Cox and Kobayashi (1997) have been performed. Moreover, in order to show that the presented model, which adopts a new numerical strategy of integration for the solution of the vorticity transport equation, gives better results than previous similar models, therefore comparisons with the updated and debugged version of the model of Veeramony and Svendsen (1999) are also carried out.

For the sake of completeness, first of all, it is useful to present the aforementioned experiments along with the details of both the numerical setup and the adopted simplifications, considered in order to carry out the numerical simulations with the two aforementioned models.

The experimental studies of Cox *et al.* (1995) on the propagation of regular waves over a constant slope have been carried out at the Ocean Engineering Laboratory of the University of Delaware. The experimental flume was $33m$ long, $0.6m$ wide and $1.5m$ deep, where the steepeness of the sloping part was 1:35, located opposite to the pyston type wavemaker. The bottom was impermeable and it was made rough by gluing natural sand to the bottom ($d_{50} = 1.0mm$, diameters ranging from 0.71 to $1.41mm$). A schematic view of the experimental apparatus is shown in Figure 7.8. The water depth on the horizontal bottom was $h_0 = 0.4m$. Six measuring lines, L1, L2, L3, L4, L5 and L6, were located on the slope, whose positions are reported in Table 7.I. The adopted reference system is the one shown in Figure 7.8, with the origin at the first measuring line. The positions of the measuring lines was chosen in such a way that L1 was in the shoaling region, L2 at the breaking point defined in the experiments as the onset of aeration in the tip of the wave crest, L3 in the transition region where the wave goes from an organized wave motion to a turbulent bore, L4, L5 and L6 are in the inner surf zone. In correspondence of the six measuring lines, surface elevation measurements were obtained by using six capacitance wave gages and the velocities were measured over the water column by using a Laser Doppler Velocimetry (LDV). It is worth pointing out that, due to the dropouts of the LDV signal, the velocity measurements are significant only under the level of the wave trough. Cox *et al.* (1995) simulated only one wave condition, obtaining a spilling type of breaker.

The same experimental set-up and wave parameters were used for the measurements of the undertow current of Cox and Kobayashi (1997).

Since the aim of the proposed numerical model is to describe the flow inside the surf zone, in order to save computational time, the numerical wave tank is shorter

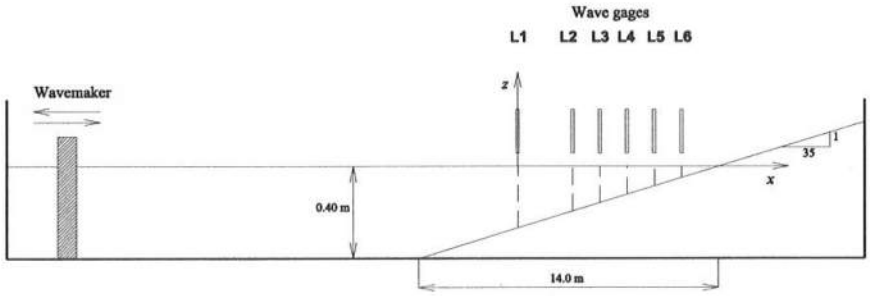

Figure 7.8: Experimental set-up adopted in the experimental investigation on the propagation of regular wave over a sloping beach in Cox *et al.* (1995)

than the real one, having a bathymetry similar to that reported in Figure 6.1, with a total length of $18m$, where the horizontal bottom is $1m$ long, with a water depth of $h_0 = 0.4m$. At the onshore boundary a sponge layer is used, the onshore shelf is $5.65m$ long, the water depth on the onshore shelf is $0.04m$, while the sponge layer starts $1.60m$ after the end of the slope. The wave generated at the offshore boundary are cnoidal waves, with wave height $H = 0.115m$ and period $T = 2.2s$, the critical value of wave slope at which the waves are considered to break is $\alpha_b = 29°$.

The experimental set-up of Hansen and Svendsen (1979) is a wave flume very similar to the one used by Cox *et al.* (1995). The flume was $60cm$ wide, $32m$ long, the slope of the beach was 1:34.26 and the toe of the beach was $14.78m$ far from the piston type wavemaker. The water depth on the horizontal bottom was kept equal to $h_0 = 0.36m$ during all the experiments. Eighteen wave conditions were simulated and the wave heights were accurately measured at an enormous number of locations, by using a wave gage mounted on a movable carriage, which

Table 7.I: Characteristic of gage locations of the measuring lines in the experiments of Cox *et al.* (1995)

Line no.	x [cm]	h [cm]
L1	0	28.00
L2	240	21.14
L3	360	17.71
L4	480	14.29
L5	600	10.86
L6	720	7.43

Table 7.II: Main wave characteristics and dimensionless parameters of the simulated test cases from Hansen and Svendsen (1979) at the toe of the beach

Test	f [Hz]	H [mm]	U_r	I_r
O	0.5	37.5	10.70	0.38
Q	0.4	39.9	17.50	0.44
R	0.3	43.3	32.22	0.52

traveled slowly along the wave flume. Moreover, the time variation of the surface elevation was measured at some locations, providing then measurements of the surface profiles in the shoaling region up to the breaking point.

In order to test the capabilities of the model, only three of the eighteen wave conditions of Hansen and Svendsen (1979) have been chosen here. Indeed breaking did not occur during all the tests and when breaking waves were present, Hansen and Svendsen (1979) recovered both spilling and plunging type of breakers. In particular the cases reproduced here are Tests O, Q and R. Table 7.II reports the wave parameters of the three simulated cases, that is the frequency f, the wave height H, the Ursell number U_r and the Iribarren number I_r.

Specifically the Ursell number, U_r has been calculated as

$$U_r = \frac{H_0 L_0^2}{h_0^3} \tag{7.2}$$

where h_x is the beach slope, the wave height H, the wave length L and the water depth h have been evaluated at the toe of the slope. The Iribarren number I_r is calculated as

$$I_r = \frac{h_x}{\sqrt{H_0/L_0}} \tag{7.3}$$

where the ratio between the wave height H_0 and the wave length L_0 on the horizontal bottom corresponds to the measured value provided by Hansen and Svendsen (1979).

The values of the Ursell number range from short waves (Test O, $U_r = 10.70$), to quite long waves (Test R, $U_r = 32.22$). On the other hand, according to Galvin's criterion (see Table 2.I), Test O and Test Q should correspond to spilling breaker conditions, even though in the second case the I_r value is very close to the critical limit indicated by Galvin, $I_r = 0.46$. Instead, the value of I_r for Test R belongs to the range of the plunging breaker conditions. In particular, this last case was chosen despite of the limit of applicability of the model, which, as any depth integrated model, is strictly valid only for spilling breaker, in order to test the behaviour of the model in these conditions.

The numerical wave tank was shorter also in this case, being $14m$ long, where the slope starts $1m$ far from the offshore boundary and ends after $12.35m$. The

water depth on the shelf is $0.03m$ deep, while the critical surface slope at the breaking point is $\alpha_b = 35°$.

Special attention should be devoted here to the assumed value of eddy viscosity, which, in order to get the best agreement with the experimental data of Cox *et al.* (1995) and of Cox and Kobayashi (1997) it is assumed to be equal to $\nu_t = 0.035h\sqrt{gh}$, while in the Hansen and Svendsen (1979) case it is assumed to be equal to $\nu_t = 0.01h\sqrt{gh}$. This difference is perhaps due to the fact that only in the first case the bottom is rough, since natural sand was glued to the bottom, thus the effects of the dissipation within the bottom boundary layer are magnified.

7.3.1 The surface profile

The time series of the surface profiles at various location, both inside the shoaling region and within the surf zone, obtained by using the proposed model have been also compared with laboratory data and with the numerical results got when the conventional fixed grid approach is adopted.

Considering the wave condition of Cox *et al.* (1995), a comparison of the time variation of the surface elevation at the six measuring sections is shown in Figure 7.9). The panels (a), (b), (c), (d), (e) and (f) correspond to the measuring locations L1, L2, L3, L4, L5 and L6, respectively. The solid line represents the experimental data, which are phase-averaged, the dashed line shows the results obtained by using the FG model and the dashed-dot line shows the model results when the MG approach is adopted. As expected, the two models gives exactly the same results outside of the surf zone (see Figure 7.9 (a), (b) and (c)). Instead, the effects of using the subgrid method start to be evident inside the surf zone. In fact the new numerical strategy allows to have a greater excess of momentum flux, due to the increased vorticity contribution coming from the roller region; this, in turn, leads both to a greater dissipation inside the surf zone and to a faster decaying of wave height. As shown by Figure 7.9 (d), (e) and (f), the model results obtained by using the moving refined grid method are in better agreement with the experimental data, also looking at the shape of the wave profiles, which show more the saw-tooth form, typical of the bore like propagation within the surf zone.

It is worth pointing out that while the numerical results are instantaneous, the experimental ones are phase averaged over a great number of waves (50 waves for each location). The process of phase averaging leads to wave profiles which are smoother than the instantaneous profile. Thus the above mentioned good agreement of the model with experimental data can be considered better than it appears at first sight.

Hansen and Svendsen (1979) provided for each test the instantaneous time series of the surface profile at four sections, which were located inside the shoaling region and, particularly the last one, as close as possible to the breaking point. Being outside of the surf zone, the experimental data have been compared only with the results obtained from the proposed model which uses the subgrid method, as there is no difference between the two models within when the waves are not breaking.

The comparisons with the experimental data are shown in Figures 7.10, 7.11

and 7.12, where the solid line represents the model results and the dashed line are the experimental data. As it can be noticed, the agreement is quite good at all the gage locations of the three cases, even though at the breaking point the wave height is slight overpredicted, particularly for longer waves. Another apparent feature, which could not show up from the comparison with the phase-averaged data of Cox *et al.* (1995), here is that the experimental data show a secondary oscillation of the wave profile, which is recovered also by the Boussinesq model.

The aim of this last analysis was obviously not to support the breaking model adopted, but it helped to confirm the good dispersive and nonlinear properties of the model. On the other hand the choice of the depth integrated velocity $\overline{u}$ as dependent variable seems to be valid, at least in the nearshore region, even though it has been demonstrated by Madsen and Schäffer (1998) and more recently by Kennedy *et al.* (2001) that such a choice should theoretically provide poor results in deeper water.

7.3.2 The wave height

The wave height represents one of the most important characteristics of the wave motion, especially from an engineering point of view, since it represents one of the most important parameter of every design problem. Inside the shoaling region the wave height increases, as the wave propagates toward the shore, and at the breaking point it reaches its maximum value. The breaking point represents the offshore limit of the surf zone, right after that, within the transition region there is an abrupt change of the wave characteristics, therefore the wave height decreases quite quickly. More onshore, in the inner surf zone, where the bore-like propagation takes place, the variation is slower, since the wave reaches a more stable configuration. Here the behaviour of the model has been compared with the experimental data of Hansen and Svendsen (1979). The wave height spatial distribution along the x-axis is shown in Figure 7.13, where the diamonds are the measured wave heights, the solid line represents the model results if the MG approach is adopted and the dashed line represents the FG model results.

In the shoaling region the model results compare well with the experimental data for both the three cases. It could be observed that the slow oscillations, which appear in the measurements, are recovered also from the Boussinesq model simulations, even though the numerical results are out of phase with respect to the data.

About the model results inside the surf zone, which is the specific objective of the present work, the comparisons deserve some more comments. First of all, as already shown in the comparisons with the time series of the surface elevation, the wave height at breaking is slight underpredicted. Moreover, although there is a difference in the evaluation of the two models, this is more evident in the inner surf zone than within the transition region, where the two types of models provide essentially the same results. However, more onshore the results do show some remarkable differences and the subgrid effects, increasing the dissipation, is to reduce the wave height. The last behavior is clearly more consistent with the

experimental data, particularly in the case of longer waves (Test O, see Figure 7.13 (b)). It has been mentioned in Section 7.3, describing the experimental data, that Test Q should corresponds to conditions of plunging breaker, according to Galvin's criterion based on the Iribarren number. At least in principle, no Boussinesq model should be able to handle such a case, since depth averaged equations can describe only simple connected free surface flows, while in a plunging breaker the overturning wave front gives clearly a double connected water surface, at least during the first instant of breaking. The results shown in Figure 7.13 show this difficulty of the model to represents these conditions. In particular within the transition region, the dissipation is not strong enough to make the wave height results compare well with data. However, going toward the inner surf zone the agreement tends to be more acceptable and the overall model prediction, even if not very accurate, results quite reasonable in the case of plunging breakers as well.

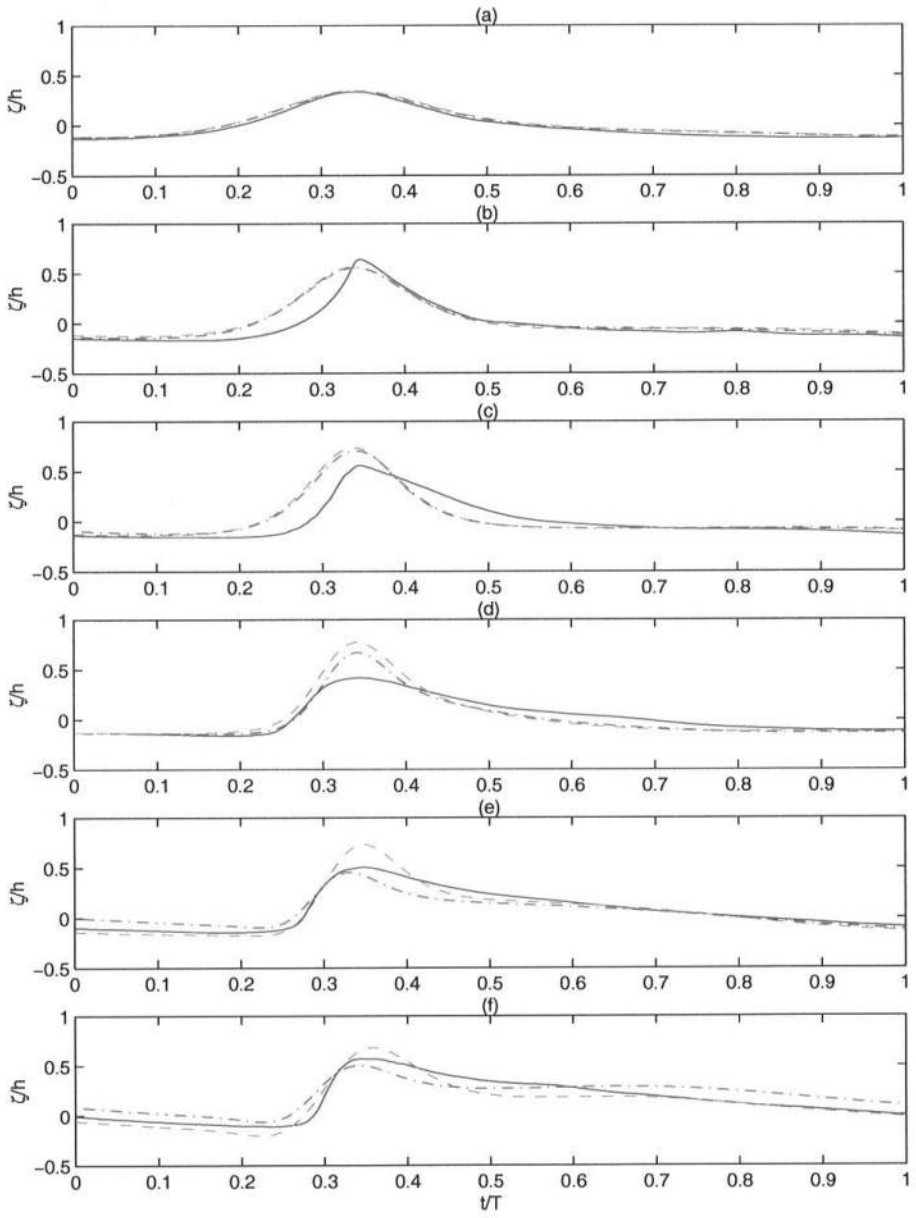

Figure 7.9: Surface profile. Blue solid line: data by Cox *et al.* (1995); green dashed line FG model results; red dash-dot line MG model results. (a) L1 measuring section, (b) L2 measuring section, (c) L3 measuring section, (d) L4 measuring section, (e) L5 measuring section, (f) L6 measuring section

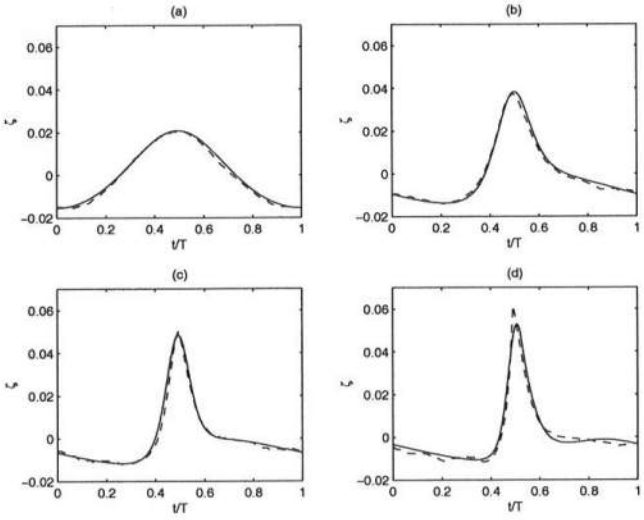

Figure 7.10: Surface profile before breaking. Solid line, MG model results; dashed line data from Hansen and Svendsen (1979) Test O: $T = 2s$, $H_0 = 0.037m$ at (a) $h/h_0 = 1.00$;(b) $h/h_0 = 0.33$; (c) $h/h_0 = 0.25$, (d) $h/h_0 = 0.20$.

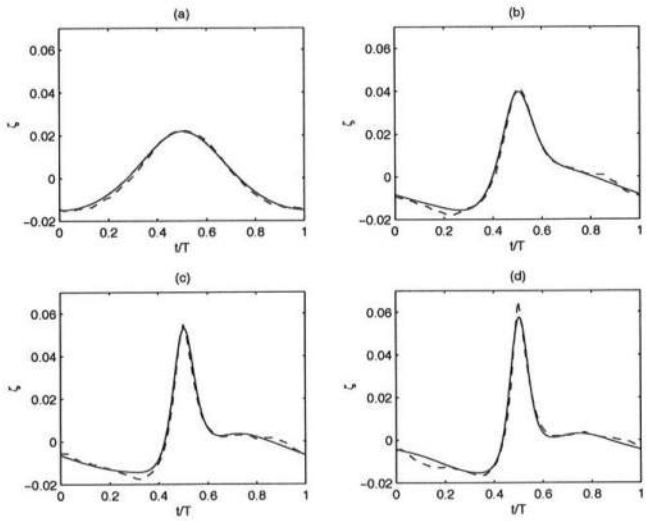

Figure 7.11: Surface profile before breaking. Solid line, MG model results; dashed line data from Hansen and Svendsen (1979) Test Q: $T = 2.5s$, $H_0 = 0.40m$ at (a) $h/h_0 = 1.00$;(b) $h/h_0 = 0.38$; (c) $h/h_0 = 0.29$, (d) $h/h_0 = 0.27$.

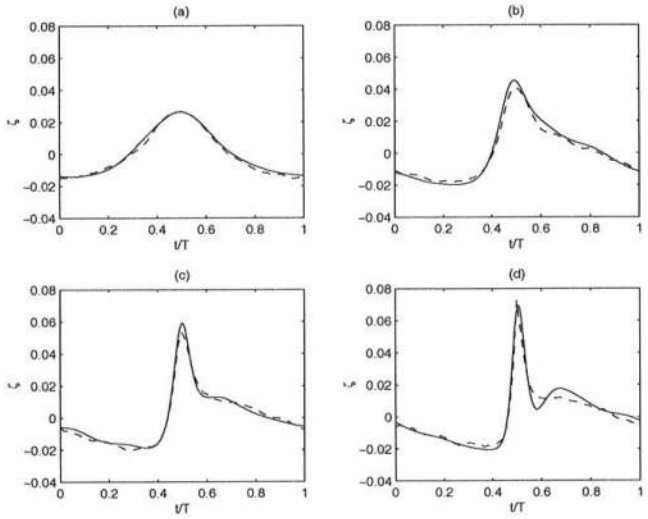

Figure 7.12: Surface profile before breaking. Solid line, MG model results; dashed lines data from Hansen and Svendsen (1979) Test R: $T = 3.33s$, $H_0 = 0.042m$ at (a) $h/h_0 = 1.00$;(b) $h/h_0 = 0.39$; (c) $h/h_0 = 0.31$, (d) $h/h_0 = 0.26$.

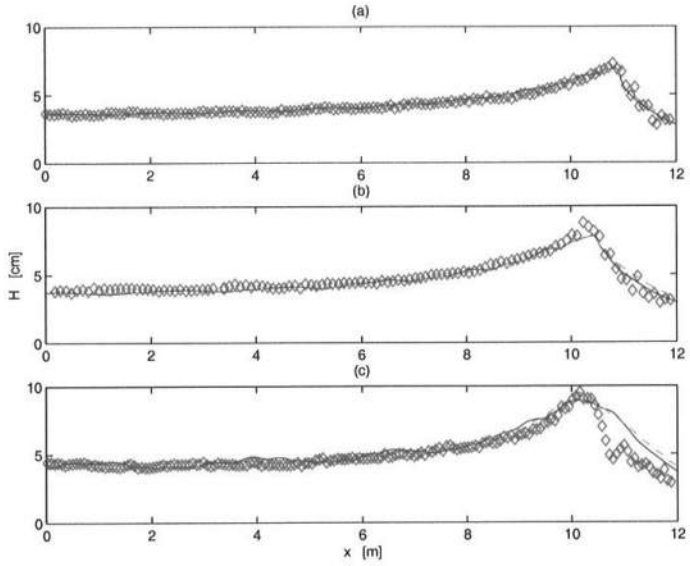

Figure 7.13: Wave height comparisons on a plane beach. Red solid line MG model results; green dashed line FG model results blue diamond Hansen and Svendsen (1979) $h_0 = 0.36m$:(a) Test O: $T = 2.0s$, $H_0 = 0.038m$; (b) Test Q: $T = 2.5s$, $H_0 = 0.040m$; (c) Test R: $T = 3.33s$, $H_0 = 0.043m$.

7.3.3 The velocity profile

One of the key point of the Boussinesq model introduced by the weakly nonlinear model of Veeramony and Svendsen (2000), of the fully nonlinear model of Veeramony and Svendsen (1999) and finally of the present model, is the definition of the velocity, which takes into account the contribution of the vorticity generated by wave breaking, considering the rotational velocity u_r. In fact, under a breaking wave the horizontal velocity strongly deviates from the almost constant profile, characteristic of shallow water conditions, and is much larger close to the surface in correspondence of the wave crest.

The horizontal velocity profiles obtained both with the FG and the MG models have been compared with the experimental results of Cox *et al.* (1995). Figure 7.14 shows the time series of the measured (black dots) and of the calculated horizontal velocity profiles, obtained using both the FG model (green solid lines) and MG model (blues solid line). Again the two models provide the same results in the shoaling region before the breaking starts. The agreement is quite good at section L1, that is the one located more offshore, and it remains good at the next two sections, L2 and L3, where the measured profiles are very similar to the theoric potential velocity profiles. However, as the wave shoals, there are some differences in the region close to the crest, between measured and calculated velocity. Inside the surf zone the measured velocity deviates from the pontential flow shape, especially in correspondence of the wave front, where the profile is pretty constant only in the lower part. The comparison between the FG and the MG numerical results shows that in the surf zone the proposed self-adptive time varying grid approach performs a slight better prediction of the velocity on the back of the front of the wave, indicating that there is a bigger residual vorticity field (bigger than that obtained with the FG model) left over by the moving breaker, which influences also the shape of the velocity profiles. However, under the crest, where the strongest deviation of the velocity from the constant profile takes place, both the FG and the MG model give rise to a stronger deviation than the experimental data. Morever, by using the subgrid approach, the velocity profiles deviate even more just in this region.

To better understanding the reasons of such a behavior, the vertical profiles of the rotational velocity u_r have been also analyzed. Figure 7.15 shows the profiles of u_r obtained using the FG model (magenta dashed line), the MG model (cyan solid line), s a reference, the experimental data (black dots) about the total velocity u are reported too. It must be stressed that no velocity measurements were provided above trough level, due to the dropouts of the signal in this region. In the following figures, all the available data are shown, but it can easily be observed that the upper two or three data are not to be considered as significative measurements.

Before breaking, that is at sections L1, L2 and L3, the rotational velocity is equal to zero. After breaking, at sections L4 and L5 the calculated u_r's show a trend similar to the measured u, confirming that having introduced the rotational velocity is consistent with the physics of the breaking process. However, due to the increased amount of ω inside the flow caused by the adoption of the moving grid, the profiles obtained using the MG model are more inclined with respect to

the vertical than the FG model results.

On the other hand, it may be worth to remind here that the hypothesis of eddy viscosity constant over depth has been made in order to get an analytical solution of the vorticity transport equation. This simplistic hypothesis do not reproduce in a good manner the real structure of the turbulence under a breaking wave. Indeed the turbulence does not spread all over the water column, but it stays confined in the upper part of the flow. This behaviour has been shown in the majority of the studies on breaking generated turbulence, since the early flow visualizations of breaking waves in Peregrine and Svendsen (1978). This phenomenon it is also confirmed even by the velocity measurements of Cox *et al.* (1995), since the profiles are constant in the lower region and only in the upper region deviate and are characterized by larger values. Therefore, by assuming a constant eddy viscosity profile the vorticity is spread uniformly everywhere, whereas it should be concentrated more in the upper part of the flow, this leading in turn to the too much inclined velocity profiles.

7.3.4 Undertow and volume flux

After the analysis of the velocity profiles, presented in the previous section, it may be helpful to investigate another physical quantity related to the velocity field, namely the undertow, that is the offshore current generated to compensate the excess of net onshore volume flux due to wave breaking. The correct prediction of the undertow profiles is extremely important as this phenomenon plays a key role in the transport processes within the nearshore regions and, in turn, in the morphodynamics of the beach profile.

The Boussinesq models, in general, are not able to predict the undertow because they do not consider the roller effects, but only the Stokes' drift, due to the fact that the water goes up and down. Instead, because of the presence of the roller, there is a huge amount of water, the one recirculating inside the roller itself, that is carried with the waves and does not participate to the oscillating motion. Thus the biggest part of the undertow is generated to balance this onshore volume flux. An irrotational velocity profile cannot account for that, while the present model is theoretically able to handle this process, as it takes into account also the roller effects.

However, the simulation of the undertow profile is not as a trivial task as it could seem and some care is required. Indeed, when simulating water waves, either with a physical or a numerical model, a secondary slosh is generated within the wave tank due to the difference of water levels. This secondary currents may affect the estimate of the undertow current and of the wave volume flux, thus, here the undertow current has been evaluated according to the following expression

$$U_{undertow}(z) = u_{mean} - \frac{\overline{Q}}{h_0 + \overline{\zeta}} \tag{7.4}$$

where the estimate of the undertow current is influenced also by the net volume flux $\overline{Q}$ and by the mean water level $\overline{\zeta}$. The second term in eq. (7.4) represent the

slow oscillation within the tank, which has a much longer period and is essentially driven by the pressure gradient. The interested reader can find the details of the derivations of eq. (7.4) in Appendix B.

Figures 7.16 and 7.17 shows the comparisons of the model results (both FG and MG models) with the experimental data of Cox and Kobayashi (1997) at six sections over the slope, which are the same as in Cox *et al.* (1995) as this measurements were obtained by using the same wave characteristics and the same experimental apparatus as the former one. In particular Figure 7.16 refers to the results obtained when it is assumed that $\overline{Q} \neq 0$, while Figure 7.17 considers the sloshing process within the tank ($\overline{Q} \neq 0$). In the aforementioned figures the dots represents the experimental data, the solid line the results obtained by using the proposed moving grid model and the dashed line the results got by using the fixed grid method. Even though the numerically simulated waves have reach an almost steady condition, it can be noticed that by using eq. (7.4), that is by considering the slosh phenomenon within the tank, it helps to improve the matching of the numerical results with the data.

It should be here recalled that one of the limitations of both the MG and FG models is that they do not take into account the presence of a bottom boundary layer, as the free slip condition is introduced at the bottom. Therefore, very close to the bottom, the comparisons are not very good. As expected the bottom boundary layer strongly influences the undertow profiles close to the bottom.

Outside the surf zone the undertow current is constant over depth, see Figures 7.17(a) and (b), and both the calculated profiles match with the experimental data. In the experiments, at section L3 (Figure 7.17(c)) the waves have already started to break, while the two models start to break a little bit more downstream from this section. This explains why the calculated undertow profiles have a constant profile, which is different from the measured one.

Inside the surf zone, (see Figure 7.17 (d), (e) and (f)), the results for the undertow current somehow confirm what was obtained for the instantaneous velocity profiles. In fact the MG model overpredict the undertow at the bottom and the slope of the vertical profiles is slightly larger than that of data. The reason such a behavior could be again addressed to the fact that the vorticity is spread uniformly over depth, due to the constant eddy viscosity adopted to get the analytical solution of the vorticity transport equation. However the effects of the turbulence should be modeled by using an eddy viscosity profile variable over depth, which would be probably much larger only at the surface.

It is worth stressing that the undertow current is generated to balance the net wave volume flux directed onshore. Moreover, as eq. (7.4) states, to evaluate correctly the undertow profile the net volume flux have to be estimated. Therefore the mass transport represents an important parameter to be evaluated. The volume flux time series obtained by using the MG model are reported in Figure 7.18, those obtained with the FG model are shown in Figure 7.19 considering the same six measuring sections (Cox and Kobayashi, 1997). In particular, the total volume flux Q has been evaluated as

$$Q = \int_{-h_0}^{\zeta} u dz \tag{7.5}$$

The expression of Q_{appr} is

$$Q_{appr} = c\eta \tag{7.6}$$

where c is the wave speed and η is the surface elevation with respect to the mean water level. Eq. (7.6) is exactly valid under the hypotheses of wave of permanent form and of no net wave volume flux (Van Dongeren and Svendsen, 1997). Finally, the wave volume flux has been estimated as

$$\overline{Q}_w = \int_{\zeta_t}^{\zeta} u_w dz \approx Q'_w = \int_{\zeta_t}^{\zeta} u dz \tag{7.7}$$

where ζ_t is the wave trough elevation (see Appendix B for a more detailed discussion).

From the analysis of the figures, it may be observed that within the surf zone (see Figures 7.18 and 7.19 (a) and (b)), the differences between Q and Q_{appr} are appreciable, then there is a residual net volume flux $\overline{Q}$ which cannot be neglected and has to be taken into account for the undertow estimation for both models. However, the fixed grid model provides slightly smaller values than the moving grid approach. The aforementioned figures show also that the biggest amount of mass transport is due to the effects of the wave motion above the trough level, more specifically within the surf zone this is almost entirely due to it (see Figures 7.18 and 7.19 (d), (e) and (f)), as the curve for Q coincide with that for Q'_w.

Moreover, Table 7.III reports the values of the net volume flux at the aforementioned six wave locations, got with both models. The net volume flux is a little bit smaller when the proposed numerical approach is used to evaluate the breaking terms, thus highlighting than in this case the steady configuration is reached earlier.

Table 7.III: Calculated net volume flux

Measuring section	$\overline{Q}_{MG}$ $\frac{m^3}{s}$	$\overline{Q}_{MG}$ $\frac{m^3}{s}$
L1	-0.00090	-0.0010
L2	-0.00038	-0.0009
L3	-0.00071	-0.0009
L4	-0.00083	-0.0013
L5	-0.00031	-0.0012
L6	-0.00056	-0.0004

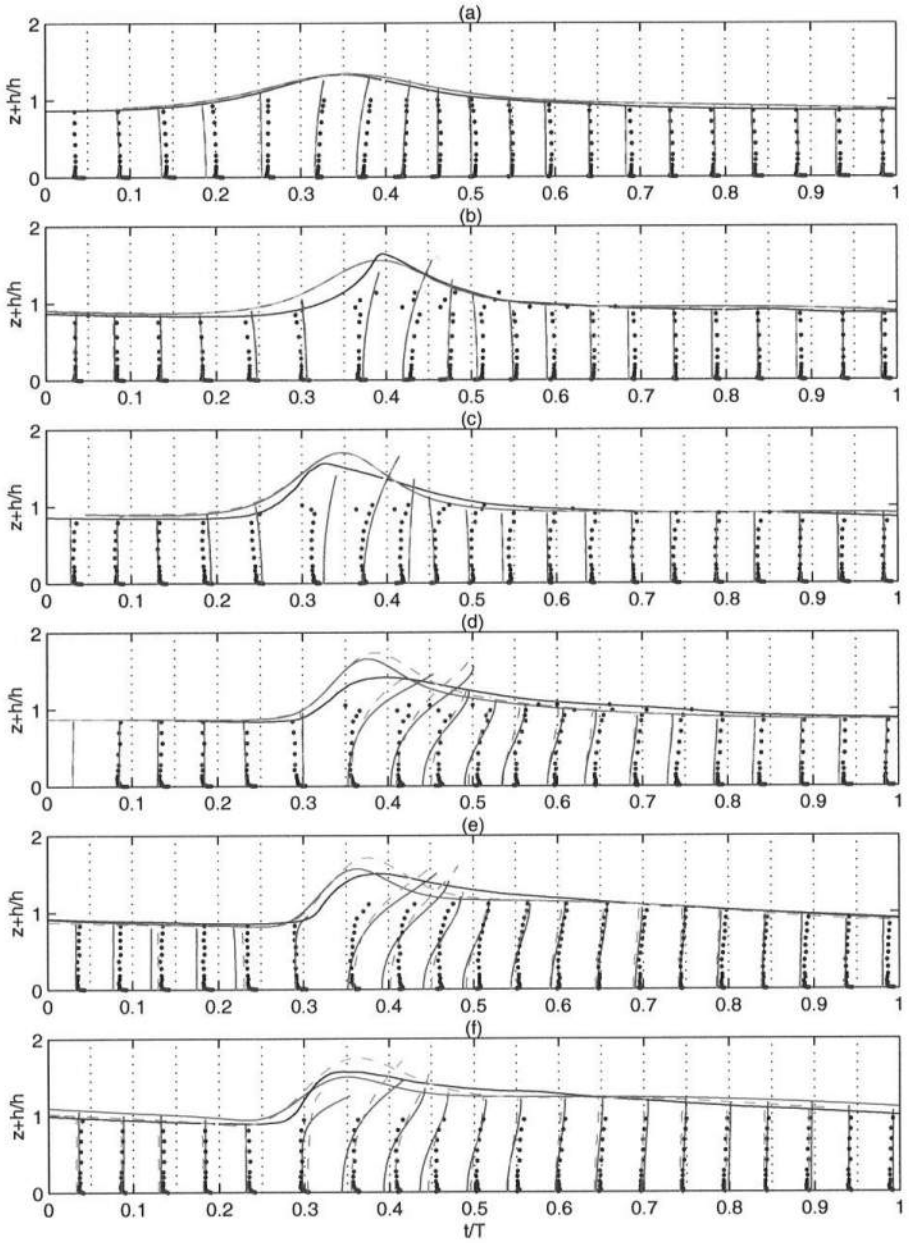

Figure 7.14: Time variation of the total velocity profiles under the waves; dots: total velocity experimental data from Cox *et al.* (1995); cyan solid line: total velocity profiles calculated through the FG model; magenta dashed line: total velocity profiles calculated through the MG model. (a) L1 measuring section, (b) L2 measuring section,(c) L3 measuring section, (d) L4 measuring section, (e) L5 measuring section, (f) L6 measuring section

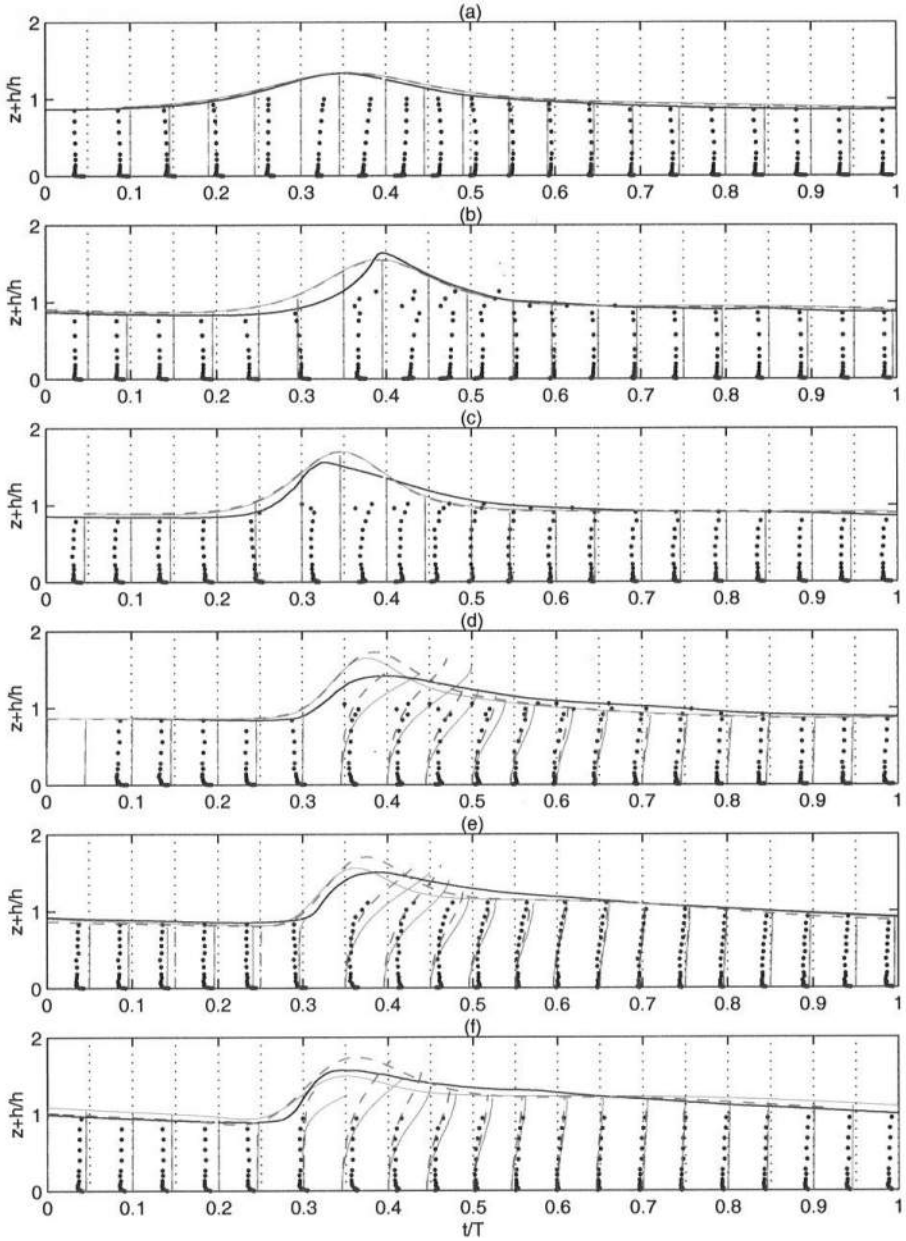

Figure 7.15: Time variation of the rotational velocity profiles under the waves; dots: total velocity experimental data from Cox *et al.* (1995); cian solid line: rotational velocity profiles calculated through the FG model; magenta dashed line: rotational velocity profiles calculated through the MG model. (a) L1 measuring section, (b) L2 measuring section,(c) L3 measuring section, (d) L4 measuring section, (e) L5 measuring section, (f) L6 measuring section

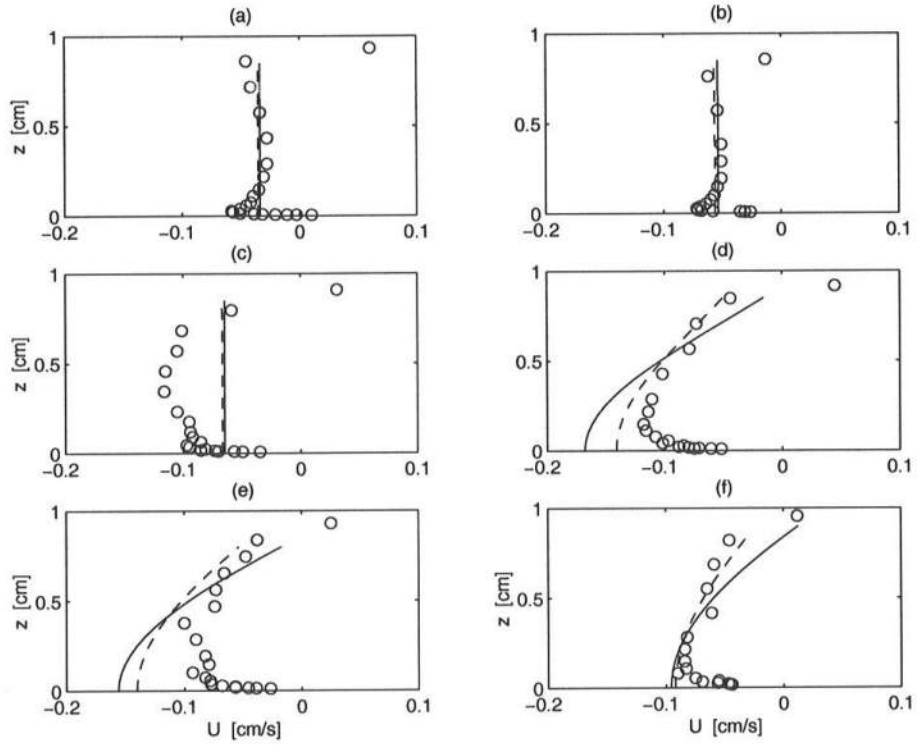

Figure 7.16: Undertow profiles: circle data from Cox and Kobayashi (1997), solid line MG model results, dashed line FG model results, when the slosh phenomenon is not take into account. (a) L1 measuring section, (b) L2 measuring section, (c) L3 measuring section, (d) L4 measuring section, (e) L5 measuring section, (f) L6 measuring section.

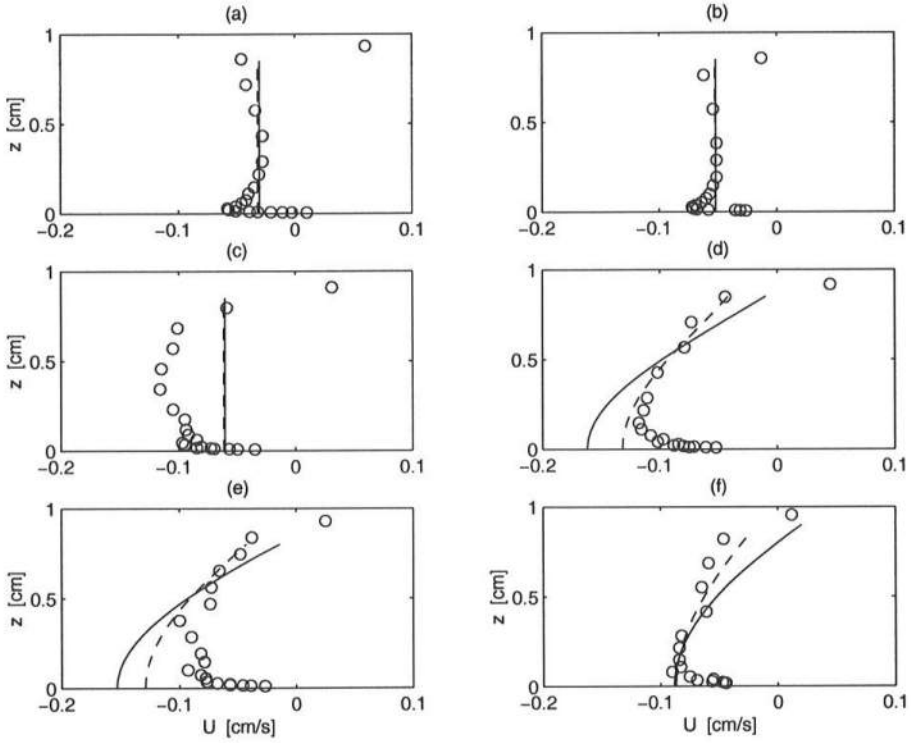

Figure 7.17: Undertow profiles: circle data from Cox and Kobayashi (1997), solid line MG model results, dashed line FG model results, taking into account the slosh phenomenon. (a) L1 measuring section, (b) L2 measuring section, (c) L3 measuring section, (d) L4 measuring section, (e) L5 measuring section, (f) L6 measuring section.

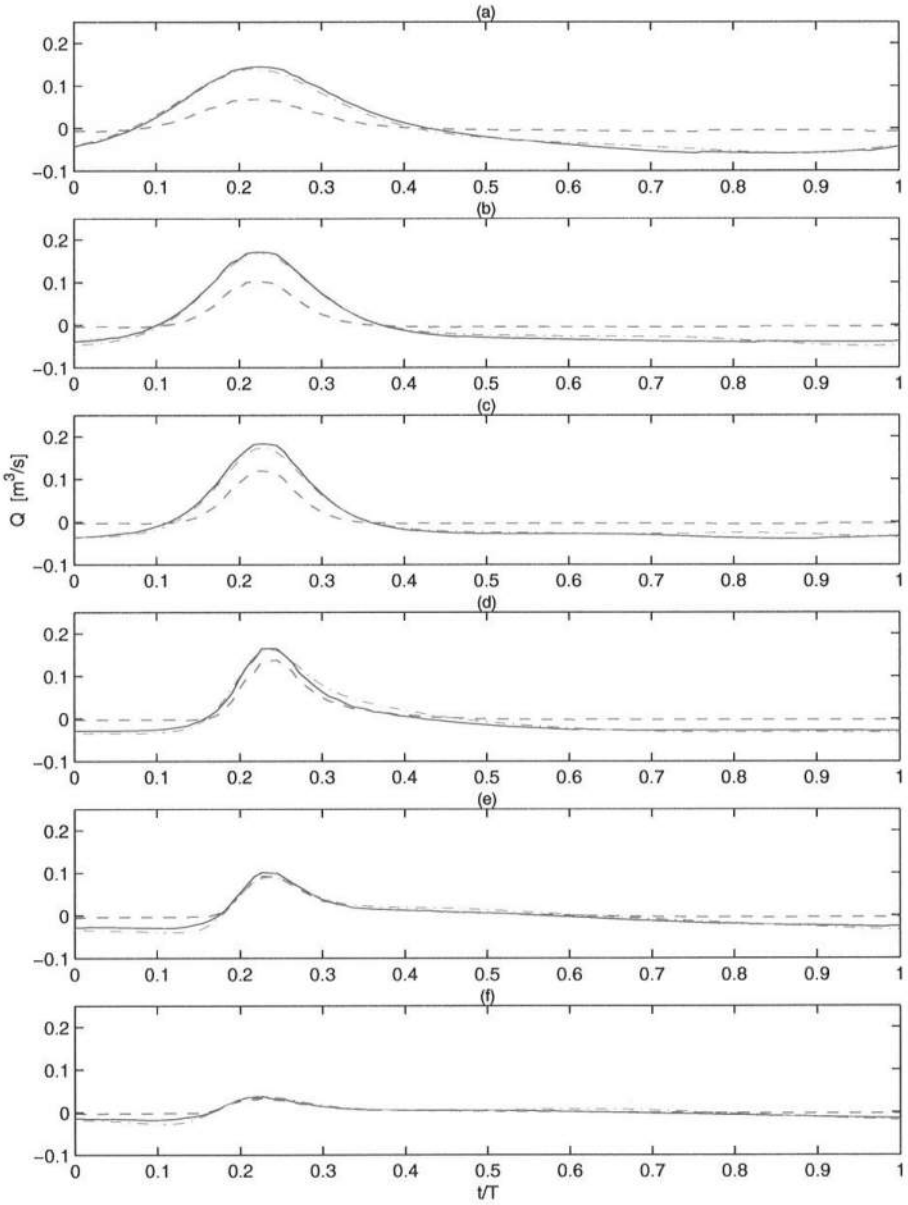

Figure 7.18: Net wave volume flux calculated by the MG model in the case of of Cox and Kobayashi (1997). Solid blue line: Q; dash-dot green line: $Q_{app} = c\eta$; dashed red line: Q'_w. (a) L1 measuring section; (b) L2 measuring section; (c) L3 measuring section; (d) L4 measuring section; (e) L5 measuring section; (f) L6 measuring section.

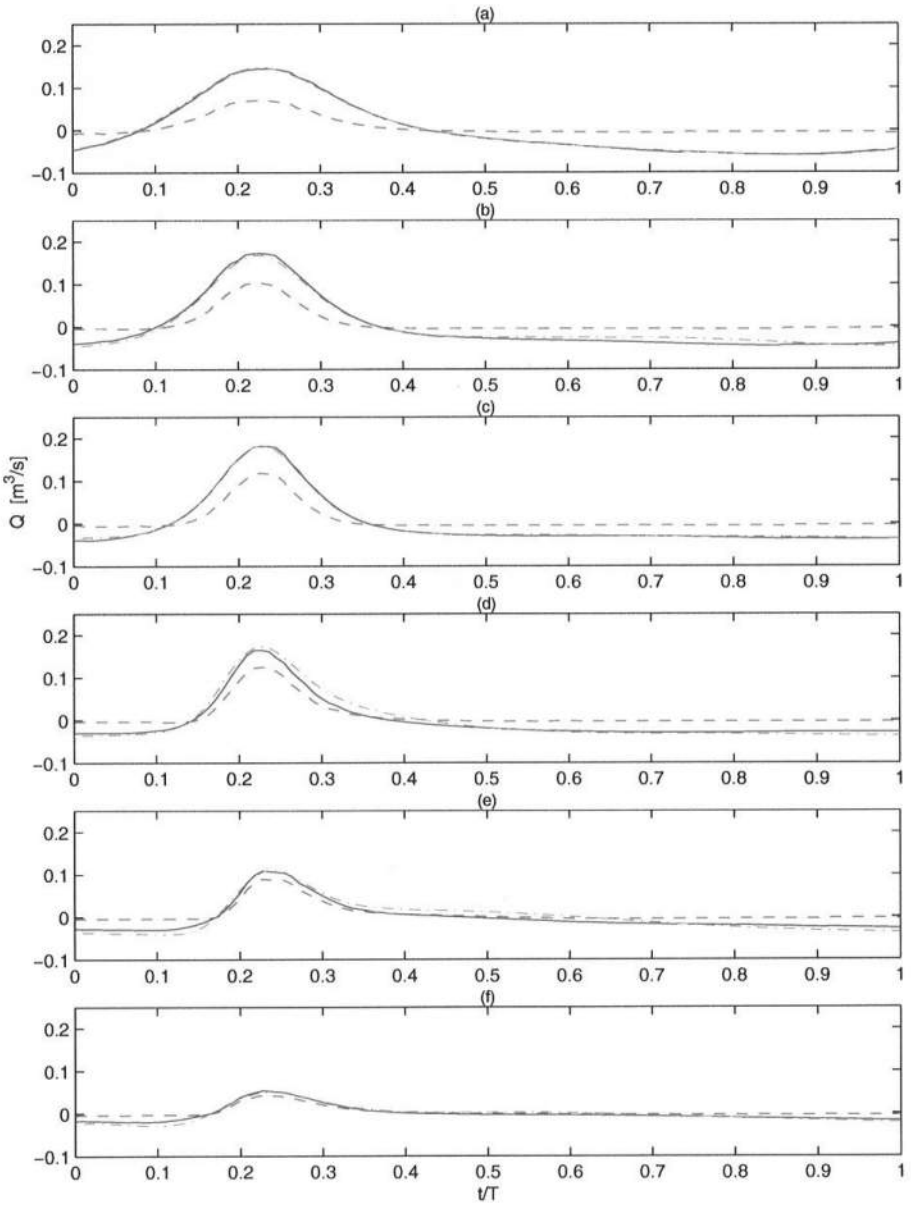

Figure 7.19: Net wave volume flux calculated by the FG model in the case of of Cox and Kobayashi (1997). Solid blue line: Q; dash-dot green line: $Q_{app} = c\eta$; dashed red line: Q'_w. (a) L1 measuring section; (b) L2 measuring section; (c) L3 measuring section; (d) L4 measuring section; (e) L5 measuring section; (f) L6 measuring section.

7.3.5 The wave speed

The wave speed or phase velocity c is defined as the celerity of propagation of the surface profile. In particular a well defined point of the free surface, such as for example the wave crest, is considered in order to determine c at a fixed location.

To obtain the wave speed from the numerical results of the surface profiles, the zero-up crossing point of the surface profile has been chosen here as characteristic point to calculate the phase velocity c. In particular, the mean water level has been subtracted from the time series of the surface profile in order to increase the accuracy of the zero-up crossing identification procedure.

Therefore the wave speed c has been evaluated by moving averaging the celerity c_{inst} of each individual zero-up crossing point, which is expressed as

$$c_{inst} = \frac{\Delta x}{\Delta t_{zero-up}} \tag{7.8}$$

where Δx is the distance between two sections of the numerical grid and $\Delta t_{zero-up}$ is the time for the zero-up crossing point to go from the previous to the next section.

The phase speed c calculated by the proposed moving grid model has been compared with the experimental measurements of Hansen and Svendsen (1979), for the three test conditions described in Table 7.II. In particular, in Figure 7.20, the red diamonds are the experimental measurements, while the blue solid line are the results obtained by using the proposed moving grid model and the green dashed line are those of the fixed grid model. The agreement of the numerical results with the experimental data is always very good. More specifically, for the spilling breaker cases, i.e. Test O and Test Q, the wave speed decreases linearly as the wave propagates on the slope, both in the shoaling and in the surf zone (the breaking point is located around $x = 10m$ in all the three cases). For the conditions of Test R (i.e. the plunging breaker case), the data show an appreciable scatter from the linear trend; however the same variability is also recovered by the proposed numerical model.

7.4 Comparison with literature wave group data

The proposed model, adopting the self-adaptive time varying grid approach, has been tested also for the case of a wave group propagation. The interest for such a particular type of irregular waves is due to the fact that in nature waves approaching the shore often show group characteristics, as a bunch of higher waves are cyclically followed by smaller ones.

Comparisons of the proposed moving grid model results with the experimental data of Svendsen and Veeramony (2001) are presented here, particularly analyzing the agreement with the time series of the free surface and the spatial distribution of the wave heights, both out and inside the surf zone. Moreover, for the case of irregular waves in general the location of the breaking point is not defined uniquely, as it changes in time and space. This is also true for breaking waves groups,

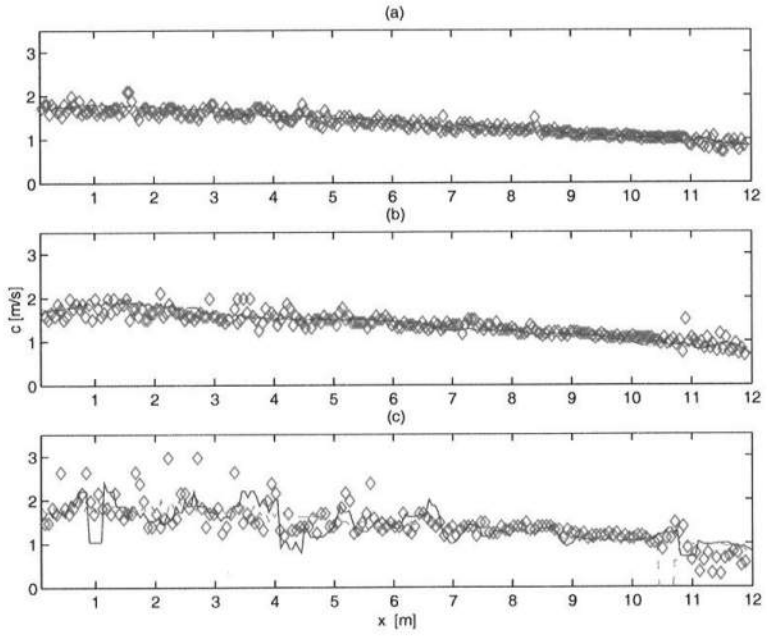

Figure 7.20: Wave speed on a sloping beach (blue solid line, MG model results; green dashed line, FG model results; red diamonds Hansen and Svendsen (1979) $h_0 = 0.36m$:(a) Test O: $T = 2.0s$, $H_0 = 0.038m$; (b) Test Q: $T = 2.5s$, $H_0 = 0.040m$; (c) Test R: $T = 3.33s$, $H_0 = 0.043m$)

therefore the calculated position of the breaking point has been analyzed here, by comparing it with that of the measurements.

The experiments of Svendsen and Veeramony (2001) were carried out in the same wave flume as in Cox *et al.* (1995) experiments, but in this case the adopted 1:35 plane sloping beach was smooth. The water depth at the constant depth section was kept equal to $h_0 = 0.40m$ during all the tests. By using a movable carriage, several wave gages allowed to collect the time series of the surface profile, both in the shoaling and in the surf zone. A wave gage located at a fixed position $7.25m$ offshore from the toe of the slope was used as a reference. In order both to get a large surf zone and to avoid large free second harmonics, the wave groups were generated in a non conventional way. Instead of addying together two sinusoidal waves with slightly different frequencies, the wave groups were generated by packing together five cnoidal waves with the same wave period but different wave heights. Each individual wave of the group was added to the closest wave of the group at the point where the particle velocity is zero, i.e. at the zero-up crossing point of the surface profile. In particular the wave heights were specified as

$$H_i = H_m \left(1 + \frac{G}{2} \sin \frac{2\pi i}{5}\right) \qquad i = 1, .., 5 \tag{7.9}$$

Table 7.IV: Wave group parameters from Svendsen and Veeramony (2001)

Experiment number	Peak frequency fp	H_m/h_0	Groupiness factor G
W03	0.4	0.237	$\pm$ 20
W06	0.625	0.25	$\pm$ 50

where H_i is the height of the ith wave, H_m is the mean wave height within the group and G is the groupiness factor defined as

$$G = \frac{\Delta H}{H_m} \tag{7.10}$$

with ΔH difference between the heights of the highest and of the smallest wave of the group.

Svendsen and Veeramony (2001) carried out seven tests, by considering groupiness factors equal to $\pm 10\%$, $\pm 20\%$ and $\pm 50\%$. Among these, two wave conditions, one with medium groupiness ($G = \pm 20\%$) and one with high groupiness ($G = \pm 50\%$), have been considered here to test the performances of the proposed model when compared with experimental data. Table 7.IV shows the experiments number, the peak frequency f_p, the dimensionless wave height H_m/h_0 (with h_0 water depth at a section with constant depth) and the groupiness factor G, as reported in Table 3 of Svendsen and Veeramony (2001).

As all the individual waves of a group have the same period $T_m = 1/f_p$, the period of the wave group is equal to $5T_m$.

The numerical tank adopted for the simulations was $16.25m$ long, with a water depth equal to $h_0 = 0.4m$ at the section with constant depth and depth of $0.02m$ on the shelf. The wave maker was $1m$ far from the toe of the slope, which ended after $13.3m$ from that. The sponge layer did begin after $0.20m$ from the end of the slope. The critical value of the breaking angle was chosen as $\alpha_b = 27°$, while the chosen eddy viscosity was $\nu_t = 0.01h\sqrt{gh}$. It should be incidentally mentioned that in order to simulate the wave group the numerical code was slightly modified, since at the boundary the irregular signal of velocity had to be specified.

A preliminary analysis of the rough experimental data was carried out, in order to specify the input wave group for the model. Indeed, due to the irregular characteristics of the waves, a long-wave motion was also generated inside the laboratory tank, as waves which have a period much longer than the individual waves of the group were released. It must be stressed also that due to the differences between the laboratory and the numerical wave flume, the infragravity waves generated in the two cases were different, thus requiring the filtering of both the data and the numerical results. As the specific aim of this work is to analyze the short wave motion, a high pass filter has been adopted in order to cut off frequency bigger than the peak frequency f_p.

Since some discrepancies were found between the values of wave heights indi-

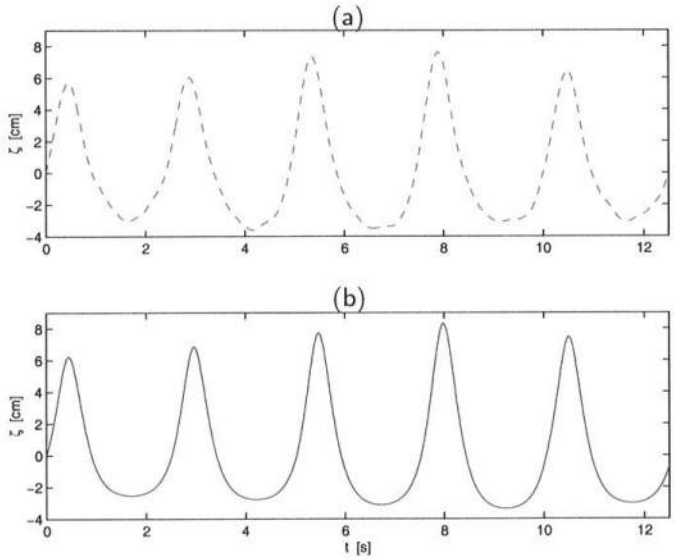

Figure 7.21: Comparison of the surface elevation time series for groupy waves. (a) measured time series at the reference gage. (b) generated input wave group for the numerical model.

cated by Svendsen and Veeramony (2001) as generated at the physical wavemaker and those obtained by processing the time series at the wave gage taken as reference (at $x = 7.25m$ offshore from the toe of the sloper), the latter ones have been considered in order to get the input values for the model. More specifically, after lowpass filtering the rough data, the mean wave group has been determined and from that the wave heights, used to generate the wave groups, have been adopted.

Figure 7.21 shows a comparison between the measured time series at the reference wave gage and the generated wave group, which represent the input for the model.

7.4.1 The surface profile

The comparisons of the surface profiles of groupy breaking waves is a very delicate task. Indeed, as the waves propagating over the slope have different wave heights, they increase the wave heights, due to the shoaling process, differently from one another and an energetic exchange between different frequecies takes place. Therefore each individual wave of the group reaches the breaking condition at a different location and from that point on it continues to evolve. Therefore how and where the single wave starts to break is extremely important to determine the pattern of the free surface inside the breaking zone.

The free surface profiles calculated by the proposed model for both the tests of Svendsen and Veeramony (2001), reported in Table 7.IV, have been tested against the measured time series at eight sections in the wave tank. The comparisons are

shown in Figures 7.22 and 7.23, for Test W03 and W06 respectively.

In particular, in Figures 7.22 and 7.23 the first four and two panels, respectively, are located outside the surf zone, while the others are inside it. The red dashed line represents the experimental measurements, the blu solid line represents the model results

The agreement of the calculated free surface is fairly good, both in the shoaling zone and in the surf zone for both the aforementioned tests. In particular it can be seen that both in the experimental measurements and in the numerical data the groupiness of the waves is still conserved after the breaking point.

It should be noticed that at some section there is a phase shift of some waves within the group with respect to the data, however this is taken again, after a while. As an example, see Figure 7.23 (d) where the four waves following the higher waves are all out of phase with respect to data, and Figure 7.23 (e), where the first two of these waves are again in phase with the measured ones.

Moreover, Svendsen and Veeramony (2001) noticed in their data a change of the position of the highest waves of the group, related to the others. Indeed it seemed that on the slope, higher height waves travel faster than the smaller ones, changing also the period and the wave length. This is more evident when the groupiness is higher. The model recovers pretty well the aforementioned features, such as the changes of wave height distribution inside the group and the period and length variation of the individual waves.

Particularly for the Test W06, with highest groupiness, another phenomenon which can be noticed both in the data and in the numerical results is the bore-bore capturing process, which occurs in the inner surf zone, far from the breaking point. (see Figure 7.23(h)). This process is also often seen on natural beaches. Indeed, two or more waves can be merged into one due to the difference of wave speed, as a wave could be so slow to be reached by the following one and then absorbed by it. As an effect of the wavelength variations and of the bore-bore capturing process, the number of waves within the domain is reduced in the inner surf zone.

7.4.2 The wave height

Since the wave groups at the offshore boundary were generated as in the experiments, i.e. packing together five different cnoidal waves with different wave heights having the same wave period, here for each component of the wave group the spatial distribution of wave height along the x-axis is shown and compared with the experimental data.

The wave heights have been recovered from the time series of the surface profiles by analyzing the history of the waves, that is following the waves as they move forward, by using the zero-up crossing method to identify the individual waves of the group and by numbering each single wave. Figure 7.24) shows the measured time series of the surface profiles at several section along the tank. It is also shown, by the red dashed line which links the different panels, as the Wave 3 propagates in time along the tank. By using such a procedure, it is then possible to distiguish the different component of the wave group.

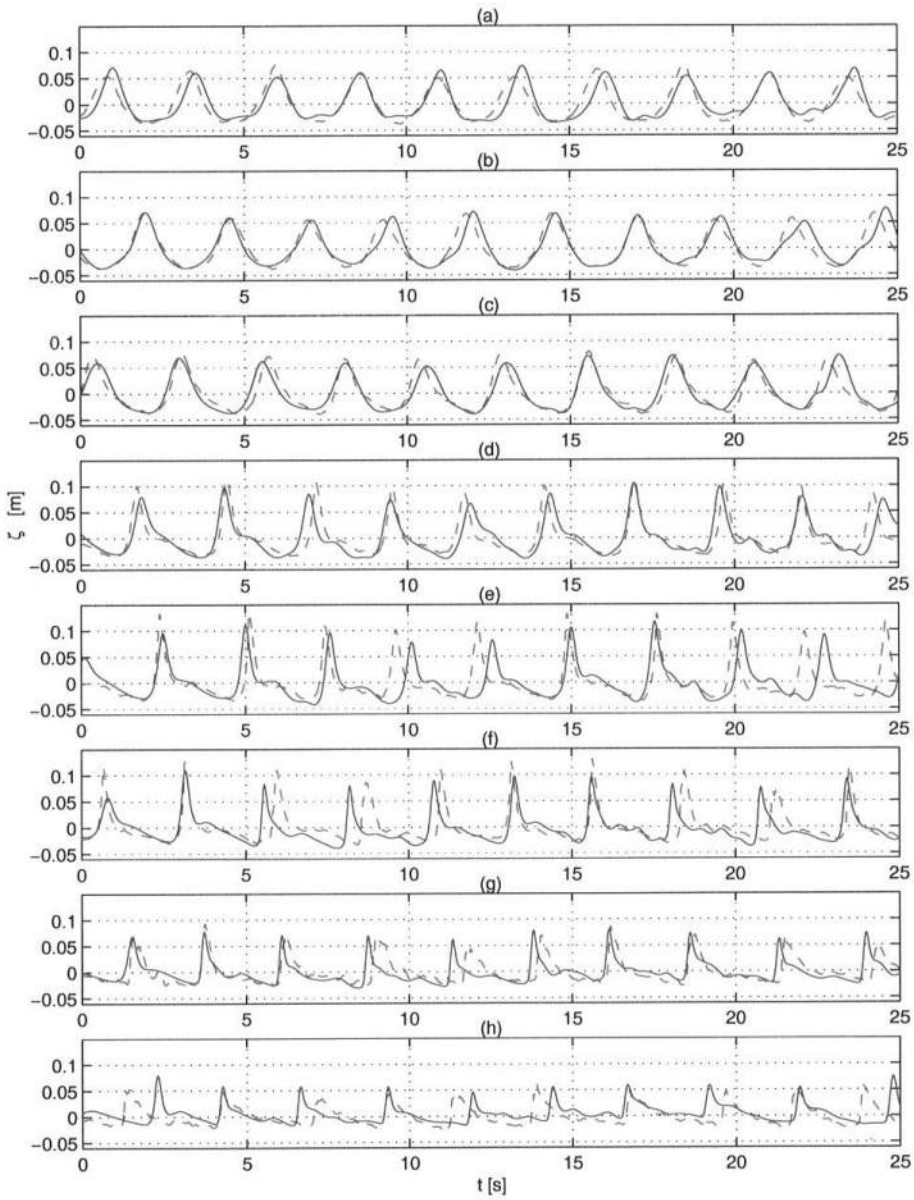

Figure 7.22: Comparison of the surface elevation time series for groupy waves. Solid line: model results, dashed line: data from Svendsen and Veeramony (2001), Test W03, $H_m/h_0 = 0.237$; $G = \pm 20\%$), (a) $h/h_0 = 1$, (b) $h/h_0 = 0.865$, (c) $h/h_0 = 0.730$, (d) $h/h_0 = 0.560$, (e) $h/h_0 = 0.490$, (f) $h/h_0 = 0.417$, (g) $h/h_0 = 0.347$, (h) $h/h_0 = 0.275$)

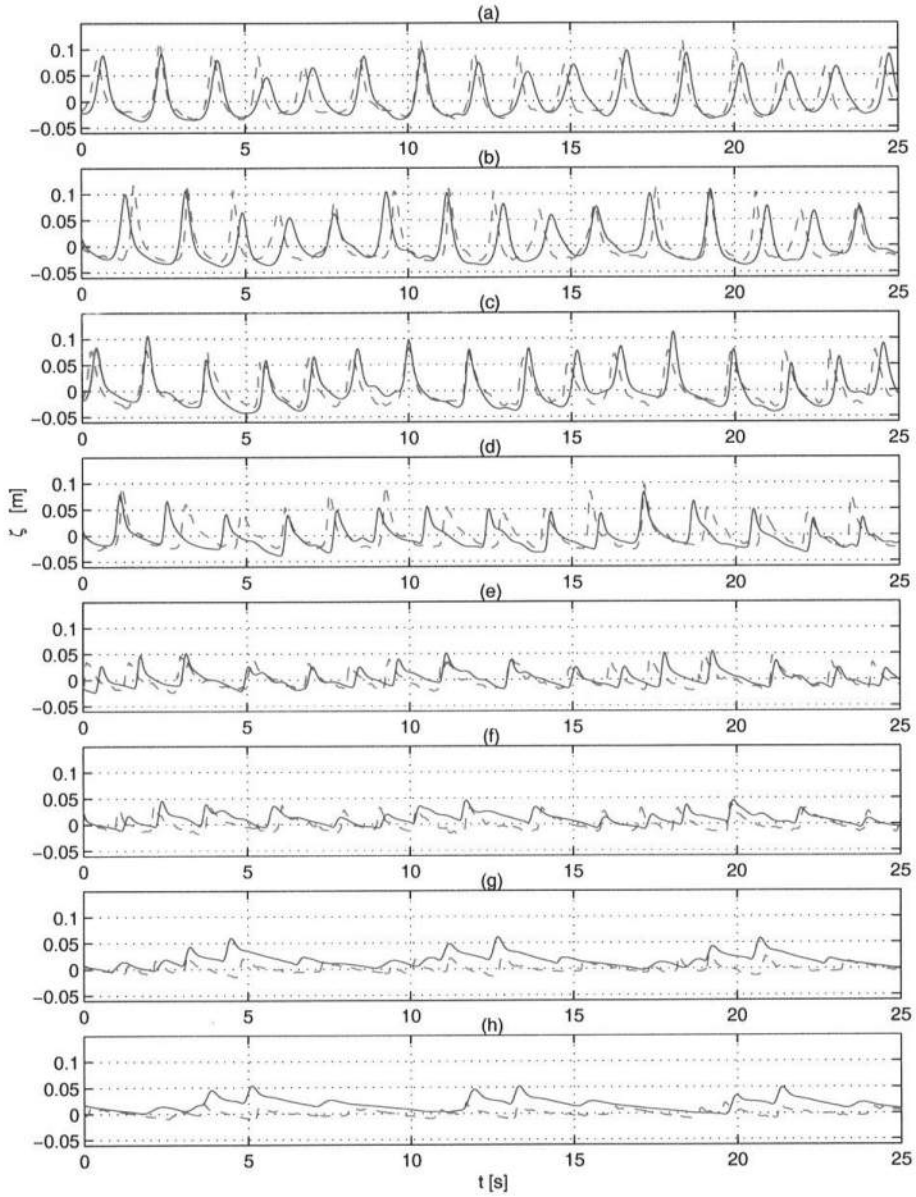

Figure 7.23: Comparison of the surface elevation time series for groupy waves. Solid line: model results, dashed line: data from Svendsen and Veeramony (2001), Test W06, $H_m/h_0 = 0.25$; $G = \pm 50\%$), (a) $h/h_0 = 0.525$, (b) $h/h_0 = 0.454$, (c) $h/h_0 = 0.382$, (d) $h/h_0 = 0.311$, (e) $h/h_0 = 0.239$, (f) $h/h_0 = 0.168$, (g) $h/h_0 = 0.096$, (h) $h/h_0 = 0.054$)

The above described procedure has been adopted both to recover the values of the wave heights from the experimental measurements and to extract the wave height distribution from the calculations. Figures 7.25 and 7.26 shows the comparisons for the W03 case and the W06 case respectively, distinguishing between Wave 1, Wave 2, Wave 3, Wave 4 and Wave 5. It should be noticed that all the available data sets have been taken into account in order to draw the aforementioned plots. Therefore the shown wave heights are referred to different runs of the wavemaker, and this explains why it is possible to find more than one value associated to the same spatial location.

For Test W03, which had a smaller groupiness ($G = \pm\%20$) than the Test W06, the agreement is very good both in the shoaling region and in the inner surf zone. The very satisfactory wave height prediction within such a large surf zone is extremely important, since it confirms the good dissipation properties of the model, which is entirely due to the effects of the roller. In the transition region, particularly for Wave 1 and Wave 2, which are also the smallest waves of the group (see Figure 7.25(a) and (b)), the experimental data show a double trend. One having a positive curvature of the distribution, with a trend more similar to that the other components, the other with a negative curvature. The first type of behavior is physically associated to a well defined position of the breaking point and to smoother changes of the wave characteristics at the first instant of breaking, while the other type could be attributed to the fact that the wave has a unstable equilibrium configuration, such as the breaking can occur sooner or later, as the breaking point is located more onshore when the curvature of the distribution is negative. When the latter condition occurs, however the energy dissipation has to be faster, as the total dissipation has to be always the same, no matter where the wave did break. This is confirmed by the fact that at a certain point within the inner surf zone the two conditions get to the same value of wave height (see Figure 7.25(a)) and from there on have the same trend.

When the groupiness is bigger, as in Test W06 it seems that the shoaling is not predict as well as before, even though the comparisons of the surface profiles were good. This could be perhaps attributed to the difficulty of the zero-up crossing method to correctly identify the individual waves, in order to recover the wave heights values. The prediction of wave height inside the surf zone, however shows an good agreement with the experimental data, particularly for the highest wave of the group (see Figure 7.26(d) and (e)). Both in the measured and calculated wave height distributions, it may be observed that the double trend recovered earlier does not occur in this case.

7.4.3 The breaking point location

As mentioned before, the variation of the position of the breaking point, which defines the offshore limit for the surf zone is extremely important, when looking at surf zone irregular waves. Indeed in the latter case the concept of breaking line should be intended not as real line, but as the average of the breaking locations of the individual waves, which in general occurs in wider or narrower strip.

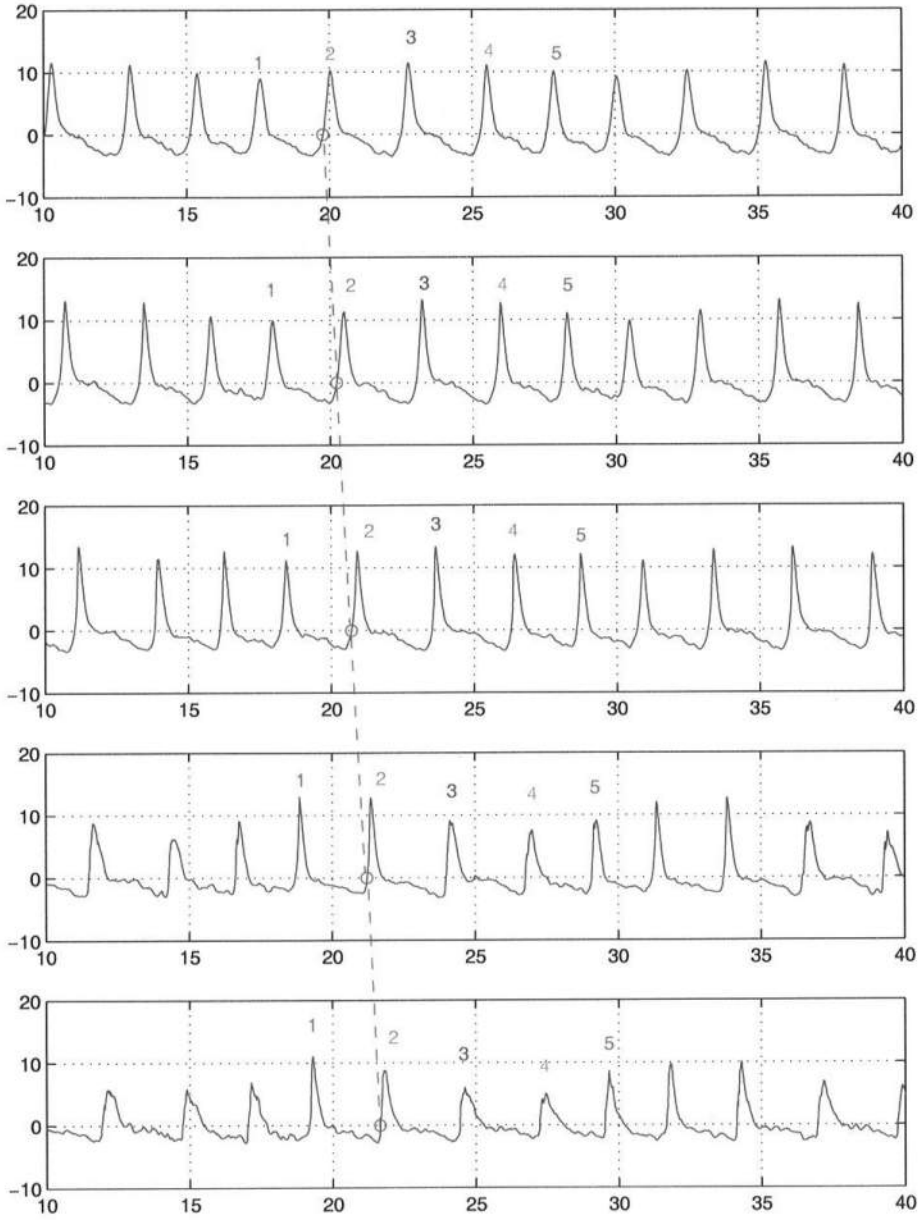

Figure 7.24: Evolution of the wave group. Surface profiles at different section along the tank: (a) $h/h_0 = 0.554$; (b) $h/h_0 = 0.504$; (c) $h/h_0 = 0.454$; (d) $h/h_0 = 0.404$; (e) $h/h_0 = 0.354$.

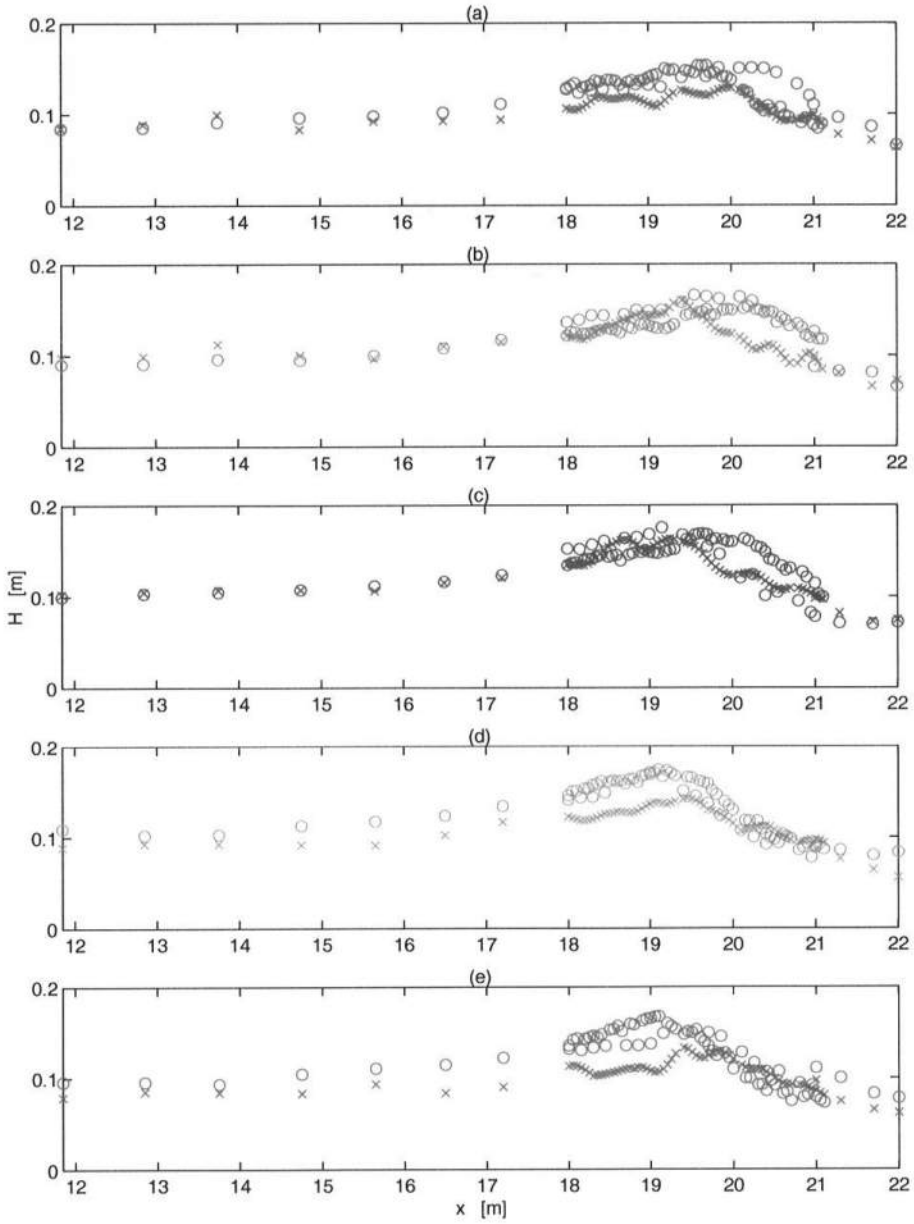

Figure 7.25: Comparison of wave height distribution along the domain (circle: model results, cross: data from Svendsen and Veeramony (2001), case W03. $H_m/h_0 = 0.237$, $G = \pm 20\%$ (a) Wave 1, (b) Wave 2, (c) Wave 3, (d) Wave 4, (e) Wave 5)

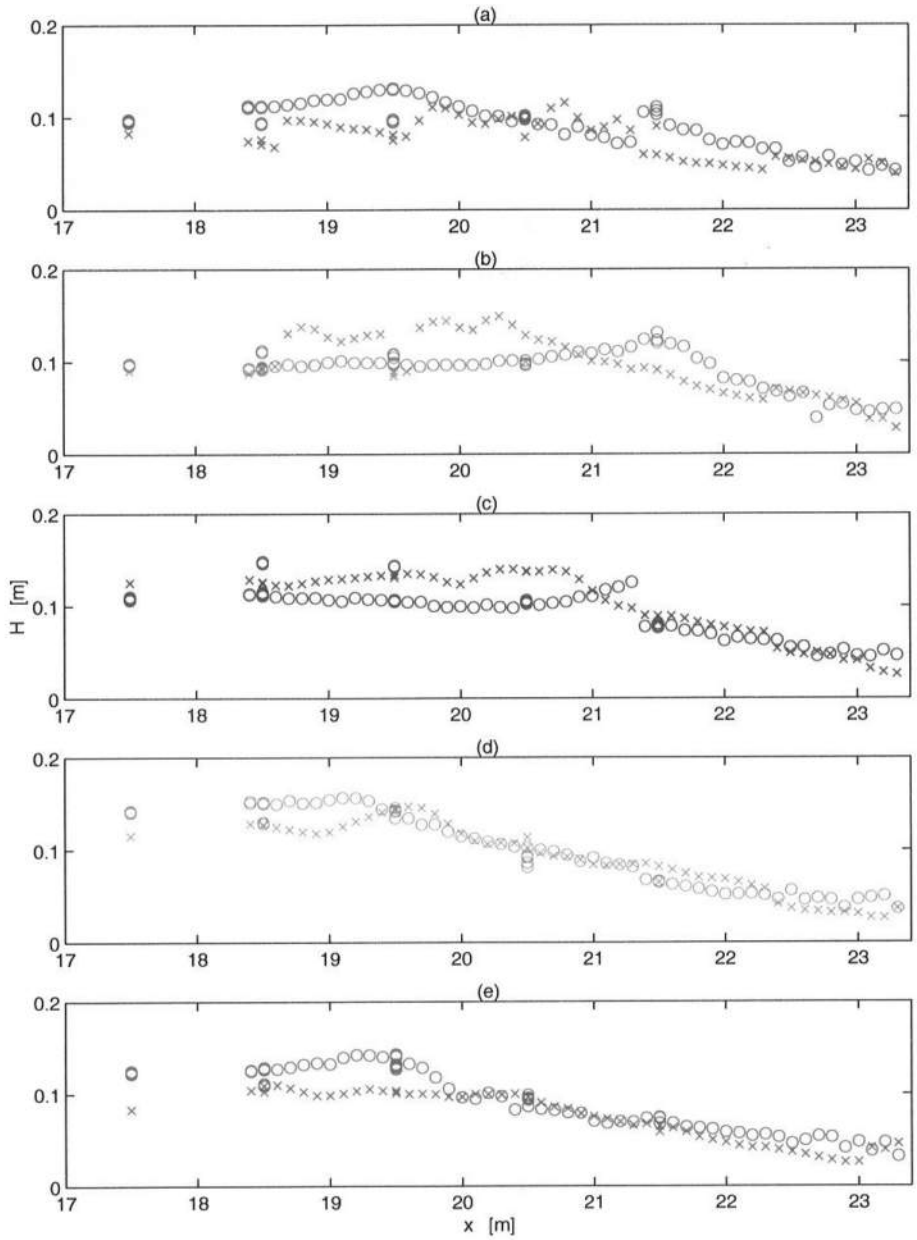

Figure 7.26: Comparison of wave height distribution along the domain (circle: model results, cross: data from Svendsen and Veeramony (2001), case W06. $H_m/h_0 = 0.25$, $G = \pm 50\%$ (a) Wave 1, (b) Wave 2, (c) Wave 3, (d) Wave 4, (e) Wave 5)

Notwithstanding the difficulty of defining a breaking point, the values obtained from the analysis of the experimental measurements, see Table 5 of Svendsen and Veeramony (2001), have been compared with the location calculated by the model, as the point where the breaking criterion defined by Schäffer *et al.* (1993) is satisfied. In particular the mean location of this point have been considered by analyzing the model results.

Figures 7.27 and 7.28 show the x-location of the breaking point for the five individual waves of the group, the red circle-dashed line in the upper panel are the experimental data, while the cross-solid line in the lower one are the model results.

It is clear that in both cases, the width of the region where the different waves start to break is larger in the experimental data. In particular it seems that the smallest waves (such as Wave 1 and Wave 2 in Test W03 and Wave 2 and Wave 3 in Test W06) tends to break later in the experiments than during the numerical simulations. The same behavior was already discussed when analyzing the wave heights results. However the variability of the breaking point recovered in the experiments is also reproduced by the numerical model.

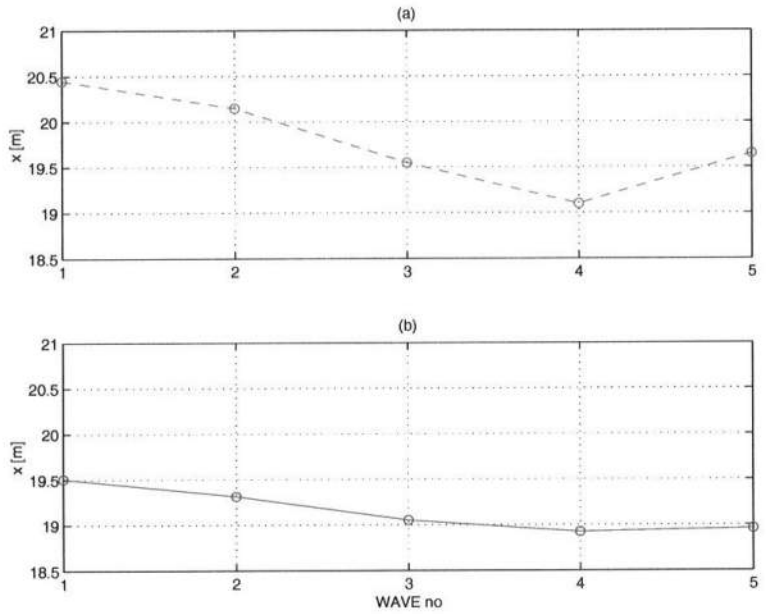

Figure 7.27: Breaking point x-location of the individual waves of the group ($G = \pm 20\%$). (a) Red dash-circle line: experimental data from Svendsen and Veeramony (2001); (b) blu solid-circle line numerical results of the proposed model

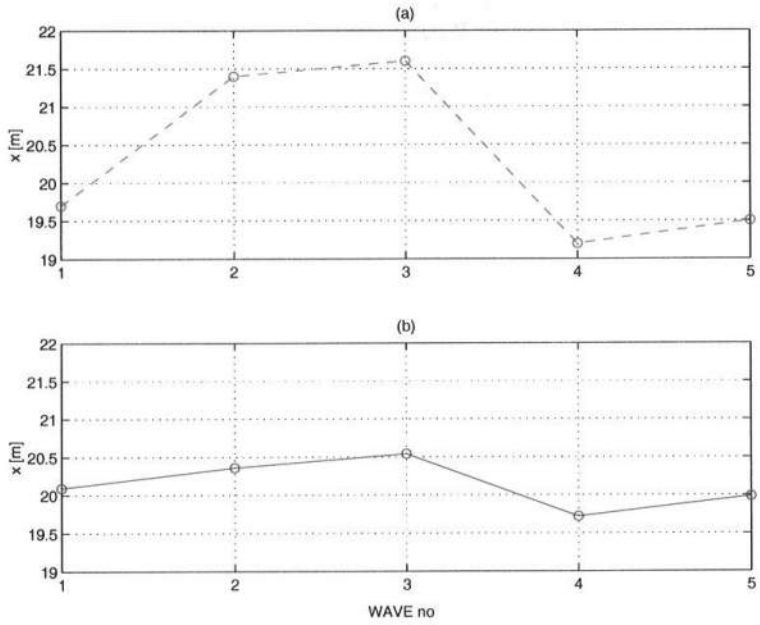

Figure 7.28: Breaking point x-location of the individual waves of the group ($G = \pm 50\%$). (a) Red dash-circle line: experimental data from Svendsen and Veeramony (2001); (b) blu solid-circle line numerical results of the proposed model

Chapter 8

Sensitivity analysis to the eddy viscosity

8.1 Overview

The analysis of the results shown in Chapter 7 have shown that the adopted Boussinesq model has reasonably good prediction capabilities when the self adaptive time varying grid apporach is used. Less good results were recovered for determining the velocity and the undertow profiles. This could be probably associated to a not appropriate representation of the turbulence structure through a model with constant over deth eddy viscosity.

Moreover, even though Cox *et al.* (1995) and Hansen and Svendsen (1979), for example, used a similar wave tank, they used a different bottom situation: being rough in the former case and smooth in the latter one. In order to simulate these two situations with a more or less equal relative error, two different values of the eddy viscosity were used ($\nu_t = 0.035h\sqrt{gh}$ and $\nu_t = 0.010h\sqrt{gh}$, respectively). This suggested to perform a sensitivity analysis of the model with respect to the eddy viscosity. The results of such an analysis are reported here along with a discussion of the influence of ν_t on the vorticity and on other wave characteristics.

It is worth pointing out that the model of eddy viscosity adopted, even though a very simple and probably rough, it takes into account for variations along the cross-shore direction according to the following expression

$$\nu_t = C_{\nu_t} h\sqrt{gh} \tag{8.1}$$

The analyses have been carried out by using the following simplified vorticity transport equation

$$\frac{\partial \omega}{\partial t} = \nu_t \frac{\partial^2 \omega}{\partial z^2} \tag{8.2}$$

in which the horizontal gradient (of order μ^2) has been neglected. Note that the

Table 8.I: Values of dimensionless eddy viscosity $\hat{\nu}_t$ used

Test	$\hat{\nu}_t$
T1	0.035
T2	0.005
T3	0.01

$\hat{}$-sign indicating dimensional variables has been here removed for simplicity sake. Integrating eq. (8.2) between z_1 and z_2, with $z_1 < z_2$ and applying Leibnitz's rule, it follows that

$$\frac{\partial \Omega}{\partial t} = \nu_t \left[\frac{\partial \omega}{\partial z}\Big|_{z_2} - \frac{\partial \omega}{\partial z}\Big|_{z_1} \right] \tag{8.3}$$

where Ω is the total vorticity between section z_1 and section z_2 defined as

$$\Omega = \int_{z_1}^{z_2} \omega dz \tag{8.4}$$

The sensitivity analysis has been carried out here by assuming values of $\hat{\nu}_t$ in the range $0.005 \div 0.035$; in particular the values indicated in Table 8.I have been considered.

8.2 Evolution of the vorticity profile under a breaking wave

The time evolution of the vorticity profiles has been analyzed in order to better understand the mechanisms of diffusion of vorticity within the flow. Moreover, since the total vorticity Ω is related, as a first approximation, to the vertical gradient of the vorticity ω, also the time series of the last quantity have been analyzed.

8.2.1 Test 1 ($\nu_t = 0.035$)

Let's consider the time variation of the vorticity profile at a fixed x-position within the transition region, that is where there are the most rapid and important variations of the wave characteristics due to the breaking. In Figures 8.1 the time evolution of the vorticity profiles is shown within one wave period. The instant $t/T = 0$ is assumed to correspond here to the breaking onset. At the dimensionless vertical location $\sigma = 1$ the vorticity is equal to the value ω_s specified at the lower edge of the surface roller (i.e. forced by the boundary condition). Figure 8.2 shows the history of the vorticity profiles under a breaking wave, holding on the previous profiles in the current plot. Such a representation allows to keep track of the presence of vorticity within the flow field, providing a comprehensive picture of the phenomenon.

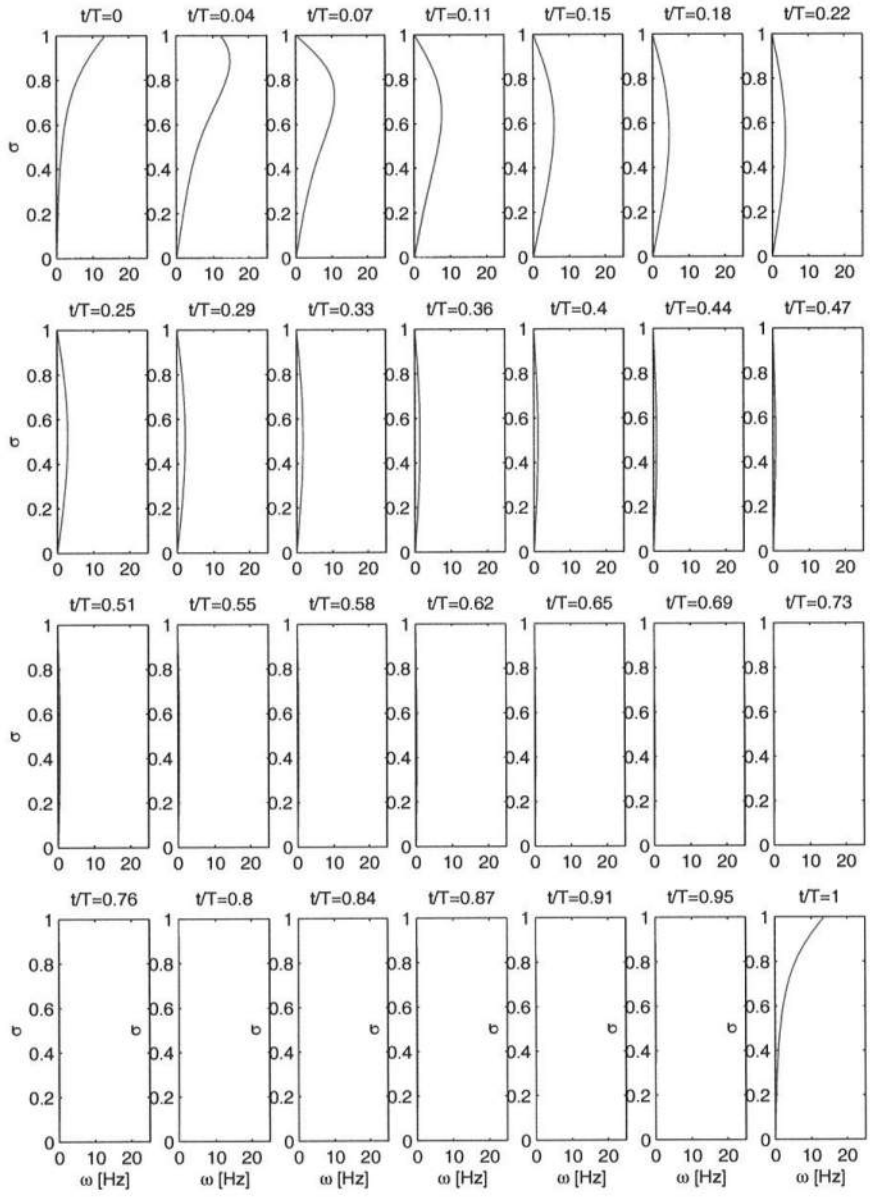

Figure 8.1: Test 1 ($\hat{\nu}_t = 0.035$). Time evolution of the vorticity profiles at a section within the transition region during a wave cycle ($t/T = 0$: initiation of breaking).

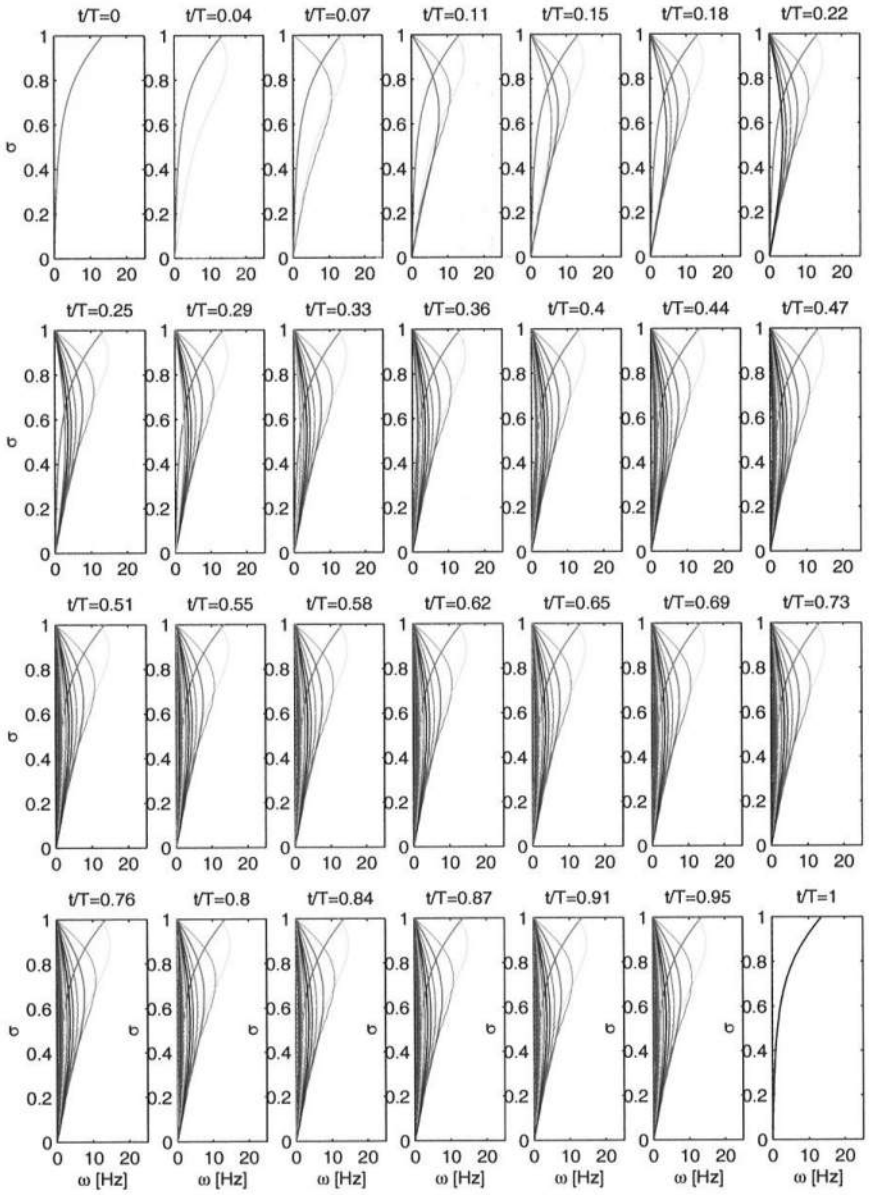

Figure 8.2: Test 1 ($\hat{\nu}_t = 0.035$). History of the vorticity profiles at a section within the transition region during a wave cycle ($t/T = 0$: initiation of breaking).

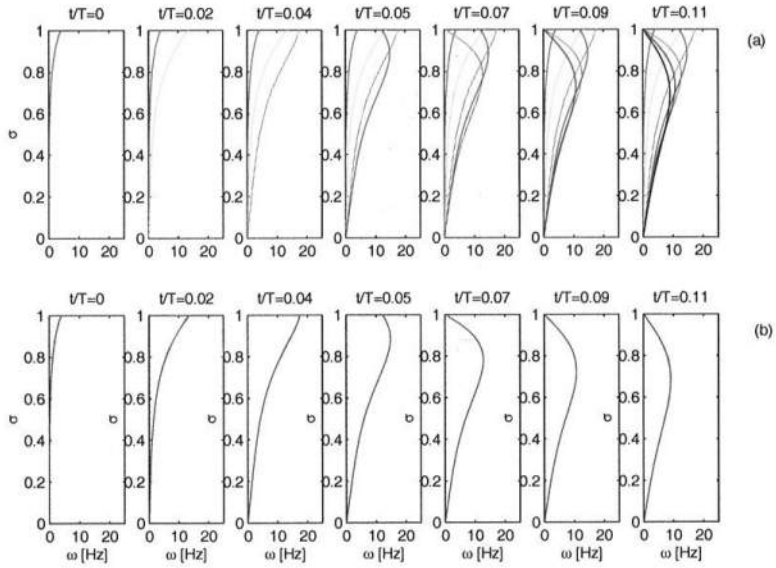

Figure 8.3: Test 1 ($\hat{\nu}_t = 0.035$). (a) History and (b) Time evolution of the vorticity profiles at a section within the transition region ($t/T = 0$: initiation of breaking).

It can be observed that at $\sigma = 1$ $\omega_s = 0$ for most of the wave period. This is due to the fact the roller passes fast at a chosen location.

Moreover, in order to give a closer view of the dynamics of vorticity generation and spreading within the flow, Figure 8.3 shows only the very early stages after the breaker passage.

By analyzing the evolution of vorticity as the roller passes by at the chosen x-location, it is evident that there is an initially fast growth of vorticity up to the time t_{max} at which the vorticity reaches its maximum on the surface and then it starts to decrease. It can be also noticed that by using the chosen value of eddy viscosity (i.e. $\nu_t = 0.035$), the vorticity inside the flow is thoroughly dissipated within half a wave period.

From eq. (8.3), the time variation of the total vorticity Ω between two vertical elevations may be expressed as the difference between the values of the vorticity gradient at two different z-locations. In order to investigate the evolution of the total vorticity at the different stages of breaking, the time variation of ω and of the vertical gradient of it, namely $\frac{\partial \omega}{\partial z}$, at four different elevations z is shown in Figure 8.4. In particular, the four z-elevations represented by the dots in Figure 8.4(a) has been chosen between the bottom and the trough level. It can be noticed that both the initial increase and the later decrease of $\frac{\partial \omega}{\partial z}$ are bigger as z increases. This means that the right hand side of the eq. 8.3 is initially positive, thus the total vorticity Ω increases with time, then in a portion of the vertical profile $\frac{\partial \Omega}{\partial t}$ becomes negative and thus Ω decreases accordingly. This region grows as the time goes on,

or, in other words, as the roller moves shoreward, and the vorticity is dissipated. Where the curves in Figure 8.4 collapse to zero the content of vorticity within the flow is basically zero.

On the other hand, the initial increase of $\frac{\partial \omega}{\partial z}$ is faster then its final decrease, therefore the growth of Ω is larger at the beginning.

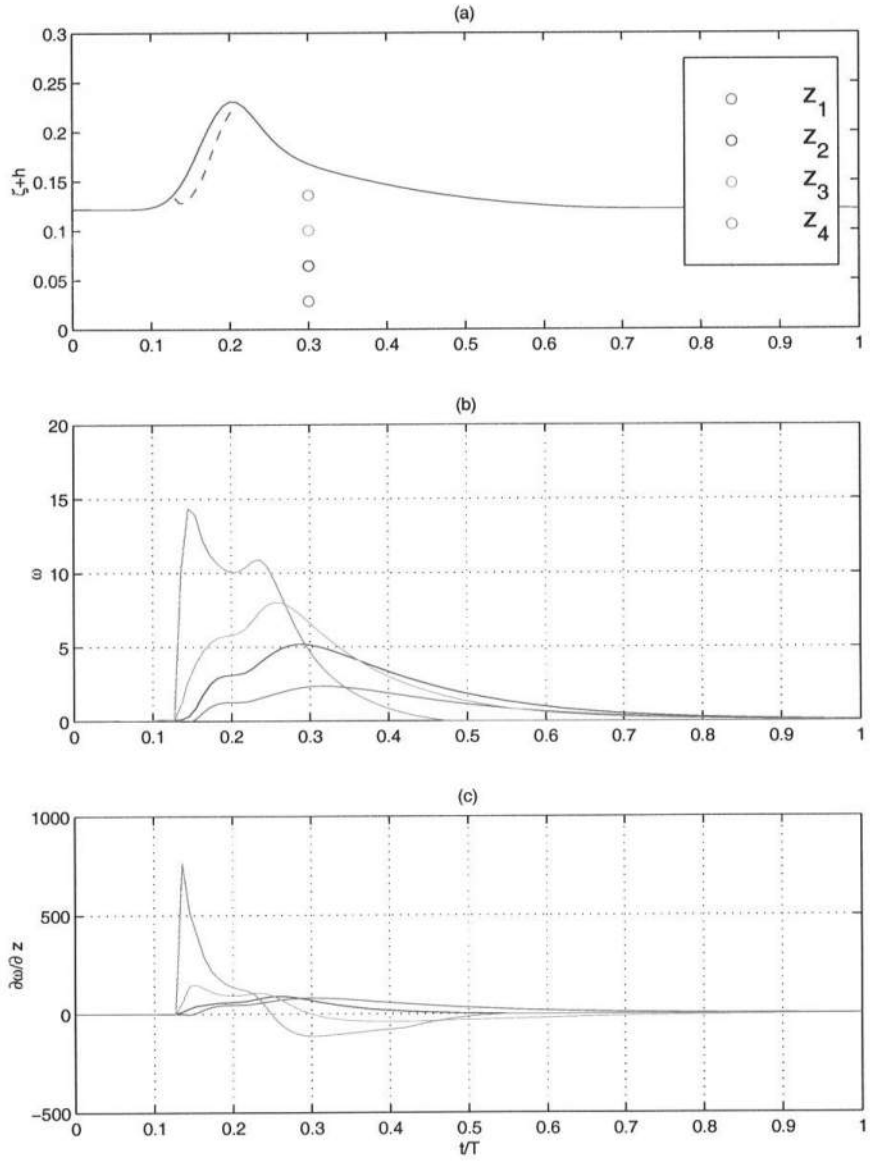

Figure 8.4: Test 1 ($\hat{\nu}_t = 0.035$). (a) Surface elevation, (b) Time variation of vorticity and (c) Time variation of $\frac{\partial \omega}{\partial z}$ at different elevations.

8.2.2 Test 2 ($\nu_t = 0.005$)

The dimensionless eddy viscosity has been then reduced to the value of $\hat{\nu}_t = 0.005$ in order to evaluate the sensitivity of the model to the change of eddy viscosity and thus to have a picture of the limits of applicability of the model with respect to this parameter in presence of breaking waves.

Therefore the evolution of the vorticity profiles at the same section within the surf zone considered in the previous case has been reported in Figures 8.5 and 8.6, by using the same type of representation adopted before. The results show that the vorticity initially does not start from a zero constant distribution, as in the previous case. Indeed, since the eddy viscosity is much more smaller, the modeled turbulence is much weaker and therefore the vorticity ω is spread downward slower. At the time when the roller arrives a residual vorticity due to the previous roller is thus still active.

From the analysis of both the aforementioned figures it is evident that the vorticity is not completely dissipated within a wave cycle but a certain amount of vorticity is available within the flow. As the figures show (for example compare the first, $t/T = 0$, and the last panel, $t/T = 1$ of Figure 8.5), the vorticity left over by the previous roller is basically constant, in other words there is no accumulation of vorticity within the field, as it should be expected.

In order to get a more significant comparison of the latter results with the ones from the previous case, the initial distribution of vorticity may be subtracted from the total vorticity profile, to get the net vorticity only due to the new breaking effects. The results are shown in Figures 8.7 and 8.8 respectively.

Also here the evolution and the history of the vorticity profile related to the first instant of breaking have been reported (see Figures 8.9 and 8.10).

By comparing the results obtained with $\hat{\nu}_t = 0.005$ and with $\hat{\nu}_t = 0.035$, it can be stated some interesting conclusions. Indeed, it should be noticed that, as expected, the values of vorticity are bigger when the eddy viscosity is smaller. Moreover, in the latter situation, there are spurious oscillations in the initial vorticity profiles and there is a not smooth decrease as the roller passes by the location. The vorticity profiles show also a kink near $\sigma = 0.5$, whose size decreases with time. This behaviour is probably due to the fact that the vorticity is spread toward the bottom really slowly, so the "initial" distribution which has been taken off is quite different under the roller, because more vorticity has been included inside the domain due to the roller.

In Figure 8.11, the variation of ω and $\frac{\partial \omega}{\partial z}$ with time, along four different z-locations is reported. Comparing with Figure 8.4, due to the oscillations, there is an initial negative value in $\frac{\partial \omega}{\partial z}$ and then the curves, after reaching a maximum, decrease faster. In this case, then, the decrease of Ω starts earlier than in Test 1 which had a larger eddy viscosity.

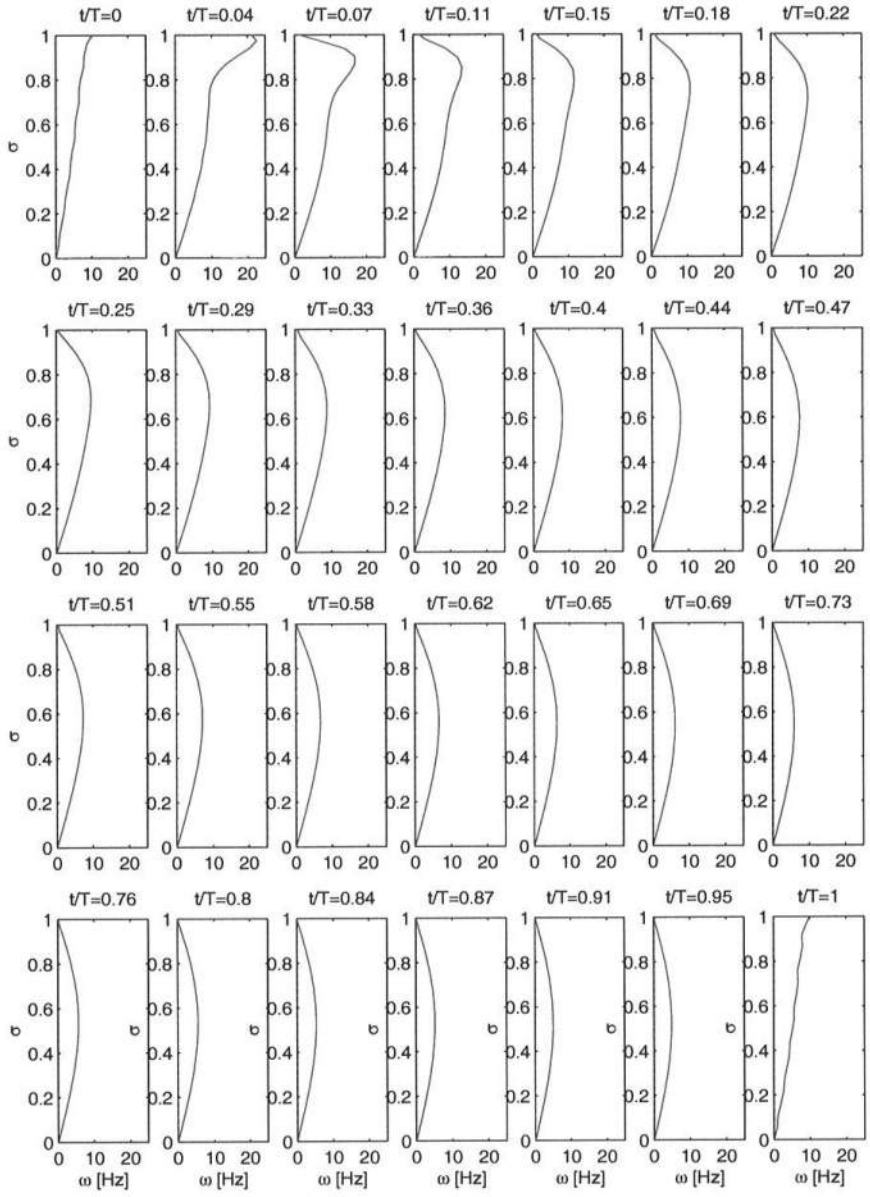

Figure 8.5: Test 2 ($\hat{\nu}_t = 0.005$). Time evolution of the vorticity profiles at a section within the transition region during a wave cycle ($t/T = 0$: initiation of breaking).

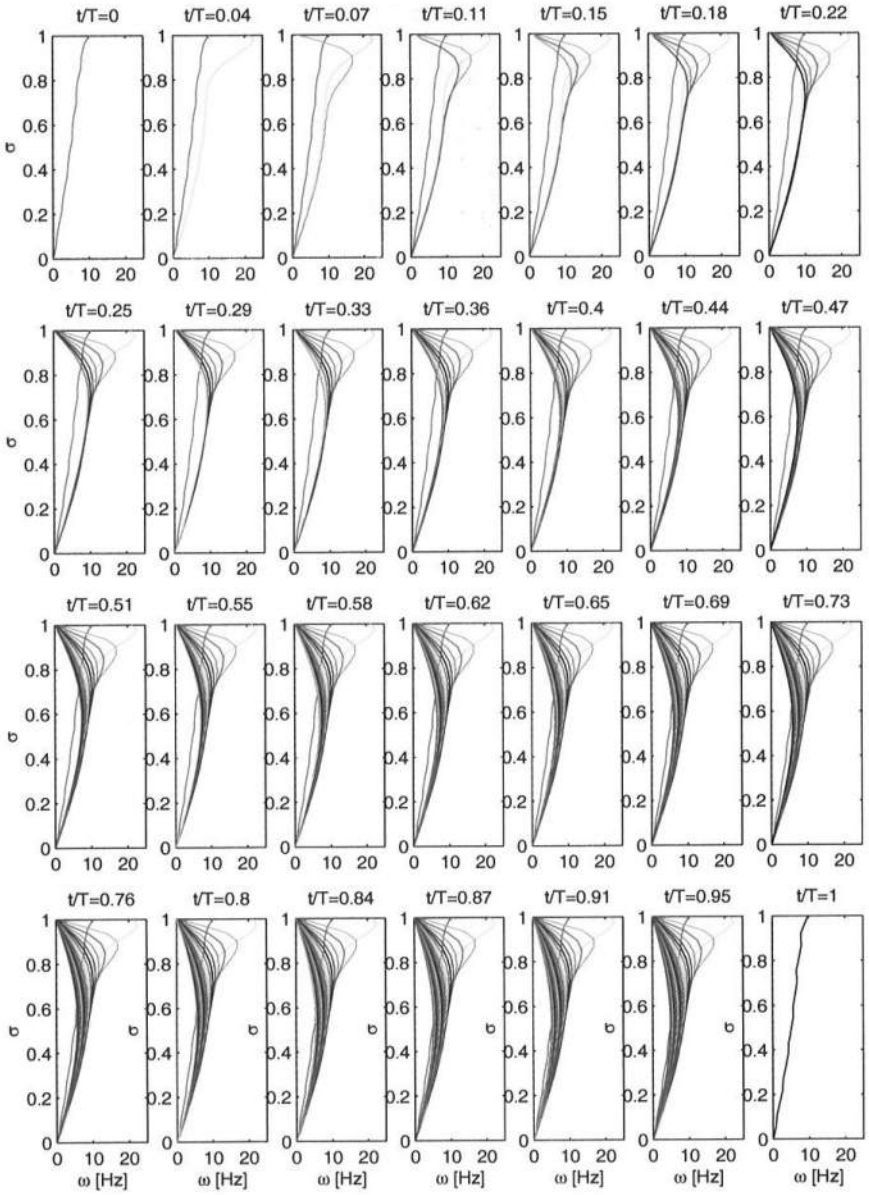

Figure 8.6: Test 2 ($\hat{\nu}_t = 0.005$). History of the vorticity profiles at a section within the transition region during a wave cycle ($t/T = 0$: initiation of breaking).

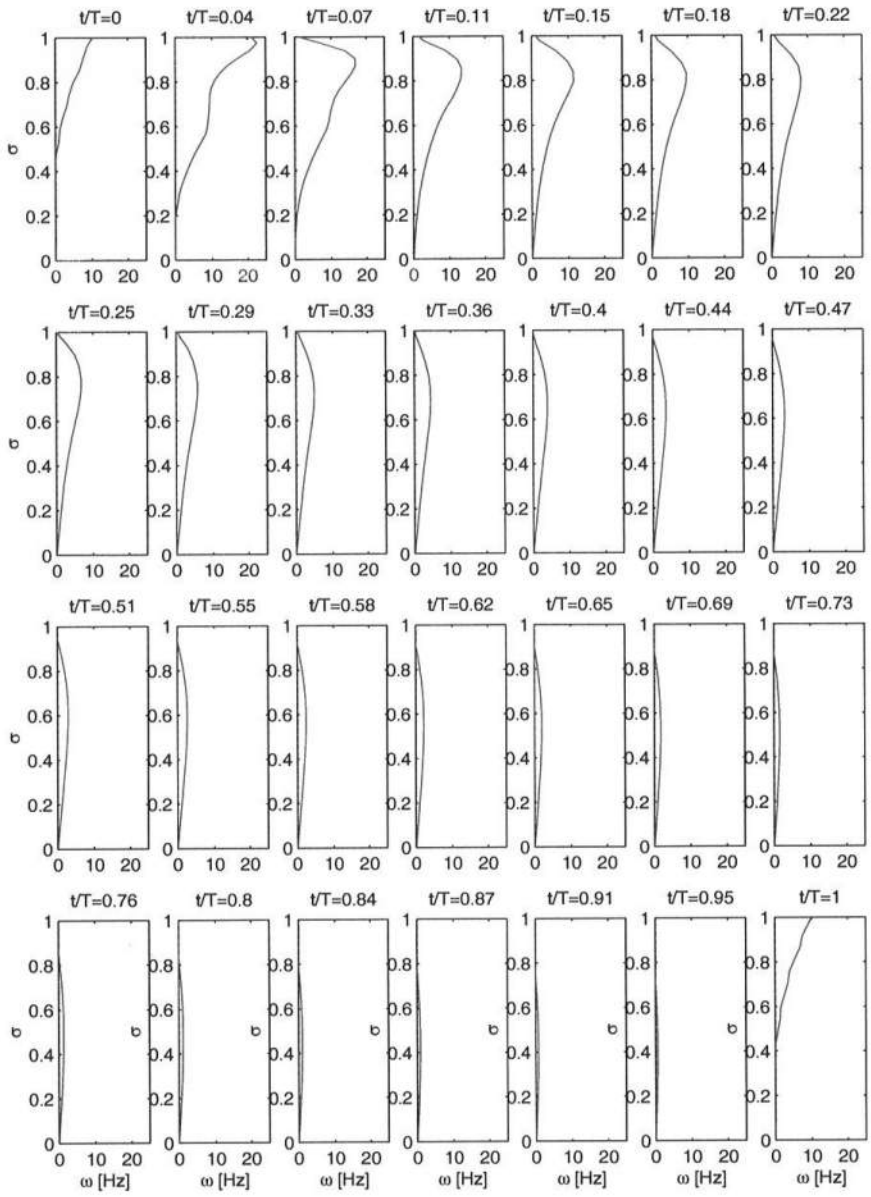

Figure 8.7: Test 2 ($\hat{\nu}_t = 0.005$). Time evolution of the net vorticity profiles at a section within the transition region during a wave cycle ($t/T = 0$: initiation of breaking).

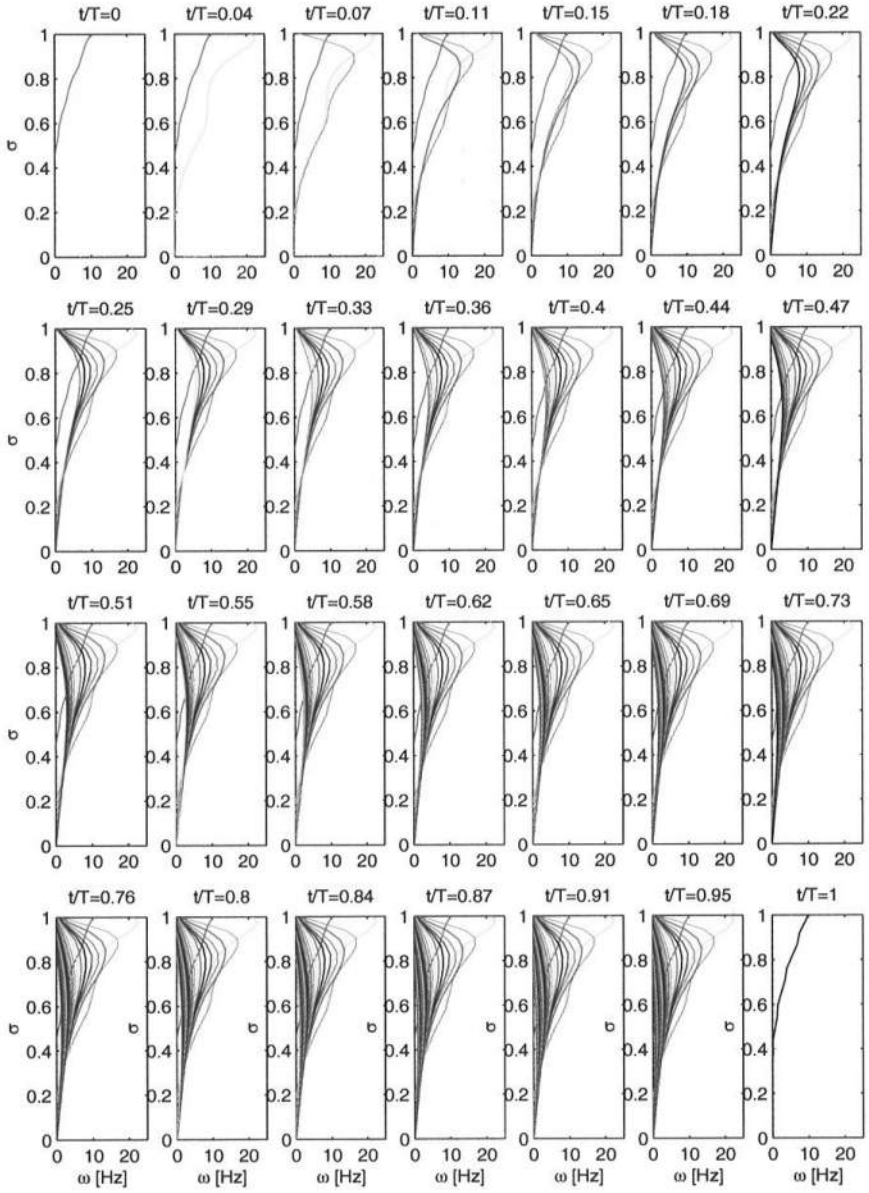

Figure 8.8: Test 2 ($\hat{\nu}_t = 0.005$). History of the net vorticity profiles at a section within the transition region during a wave cycle ($t/T = 0$: initiation of breaking).

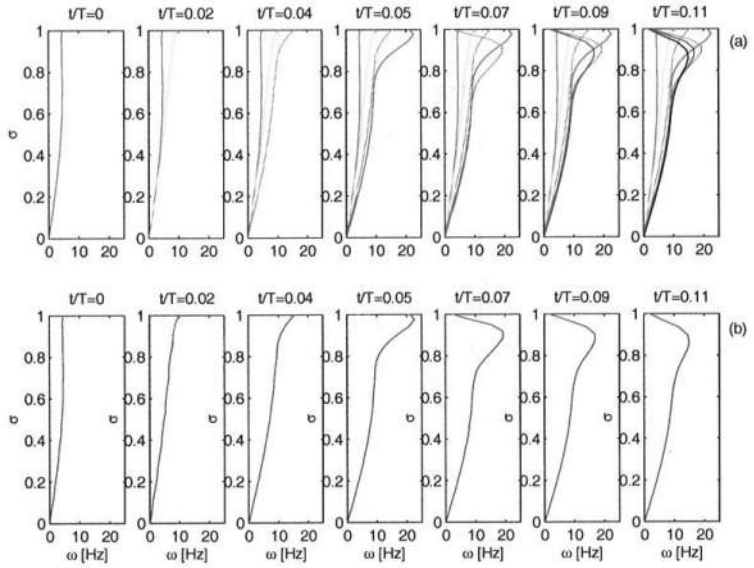

Figure 8.9: Test 2 ($\hat{\nu}_t = 0.005$). (a) History and (b) Time evolution of the vorticity profiles at a section within the transition region ($t/T = 0$: initiation of breaking).

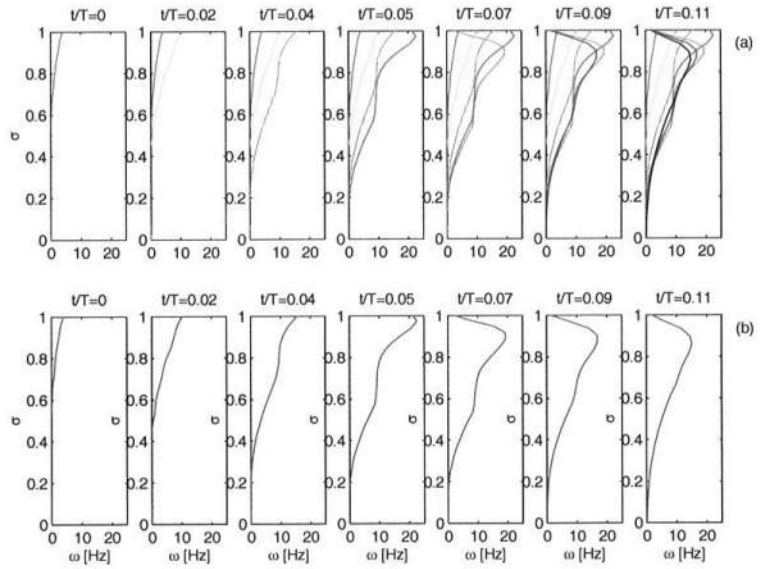

Figure 8.10: Test 2 ($\hat{\nu}_t = 0.005$). (a) History and (b) Time evolution of the net vorticity profiles at a section within the transition region ($t/T = 0$: initiation of breaking).

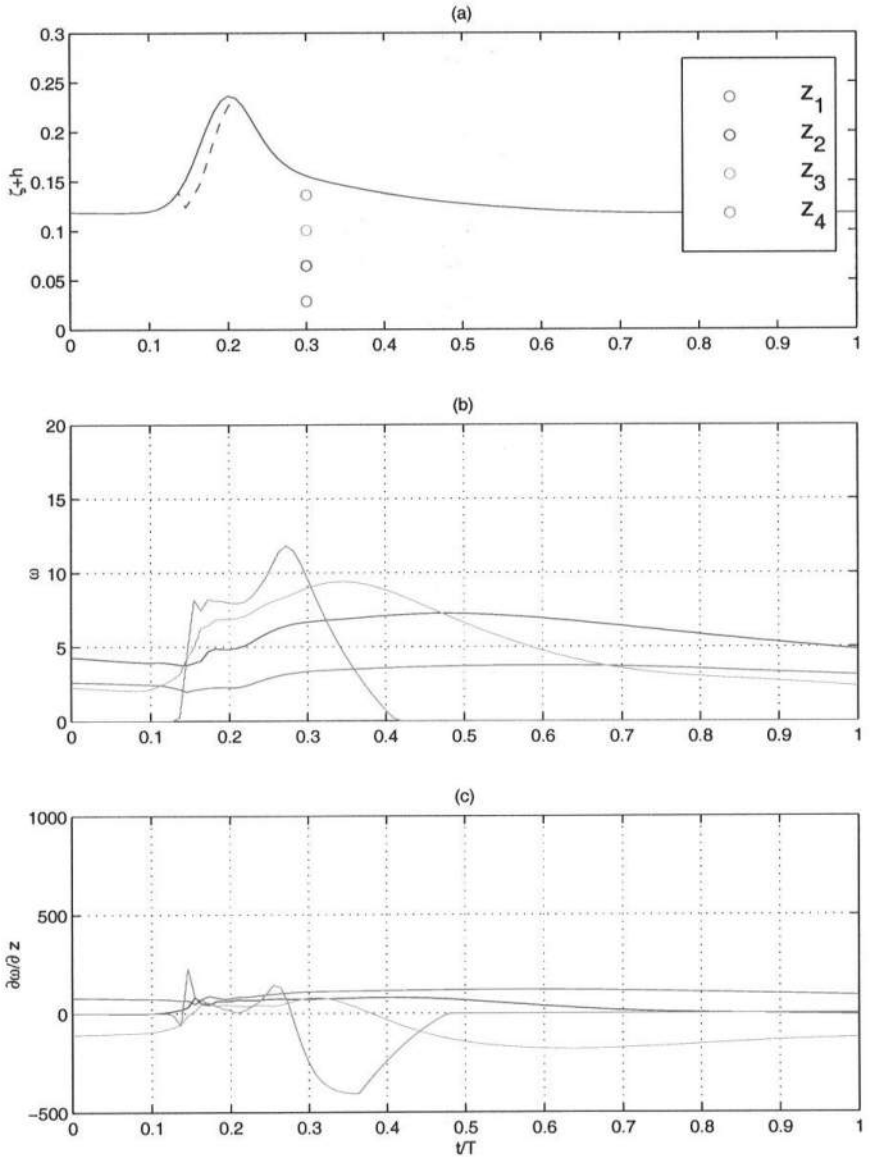

Figure 8.11: Test 2 ($\hat{\nu}_t = 0.005$). (a) Surface elevation, (b) Time variation of vorticity and (c) Time variation of $\frac{\partial \omega}{\partial z}$ at different elevations.

8.2.3 Test 3 ($\nu_t = 0.035$)

With this test a value of vorticity much closer to the original one has been considered, namely $\hat{\nu}_t = 0.01$.

In Figures 8.12, 8.13, the time evolution and the history over the water column of the vorticity and of the net vorticity are shown.

Since also in this case a certain amount of vorticity is left in the field by the breaking waves, the net vorticity has been represented by taking out the initial distribution of vorticity from the field (see Figures 8.14 and 8.15).

For completeness, also here the evolution and the hystory of the vorticity profiles only at the early stages of breaking using a smaller time interval have been reported in Figures 8.16 and 8.17.

It results that by using a value of eddy viscosity more similar to the one normally adopted, the expected smooth behaviour of the vorticity profiles is recovered, even though some small initial oscillation still appears. Then it could be argued that, as a indicative value, in the previous Test 2 the numerical model was not able to handle such a low value of eddy viscosity, representing thus a limit for the model.

Finally, Figure 8.18 shows that the trend of the derivatives is quite similar to the previous case.

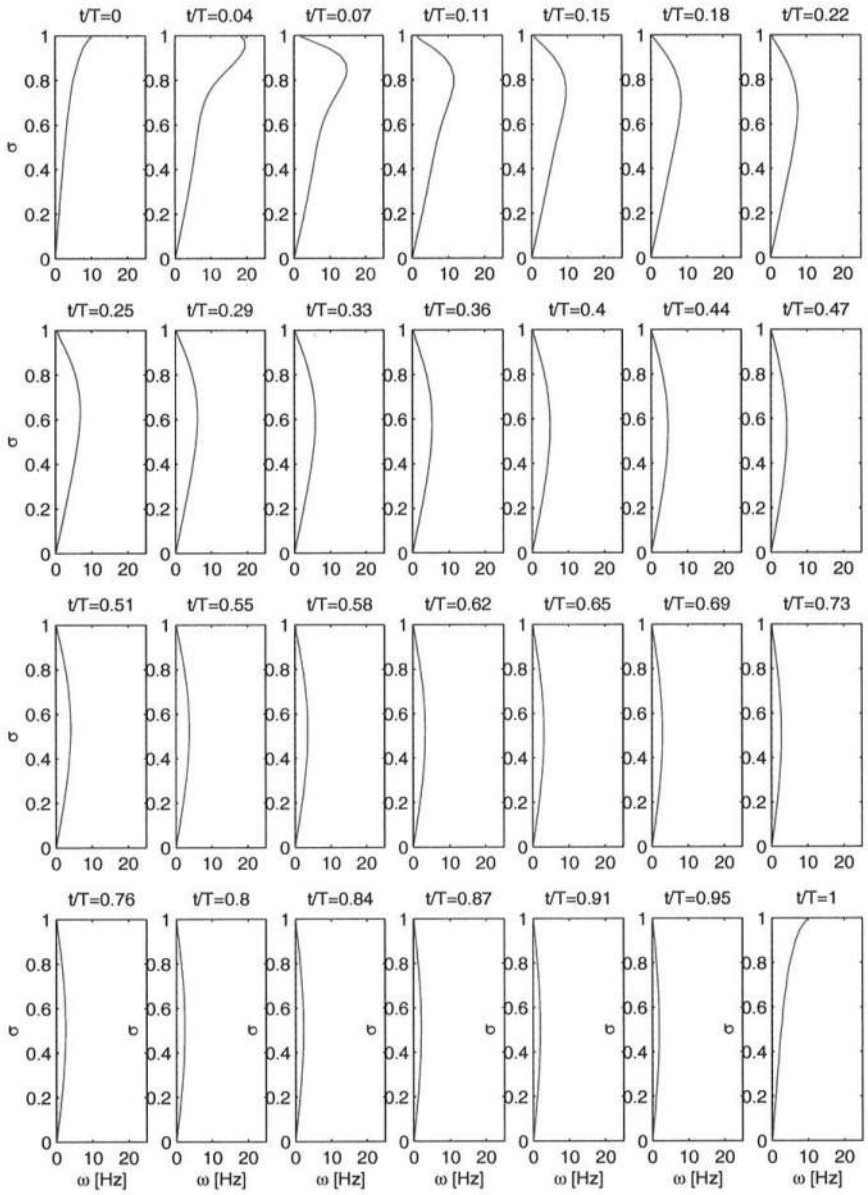

Figure 8.12: Test 3 ($\hat{\nu}_t = 0.010$). Time evolution of the vorticity profiles at a section within the transition region during a wave cycle ($t/T = 0$: initiation of breaking).

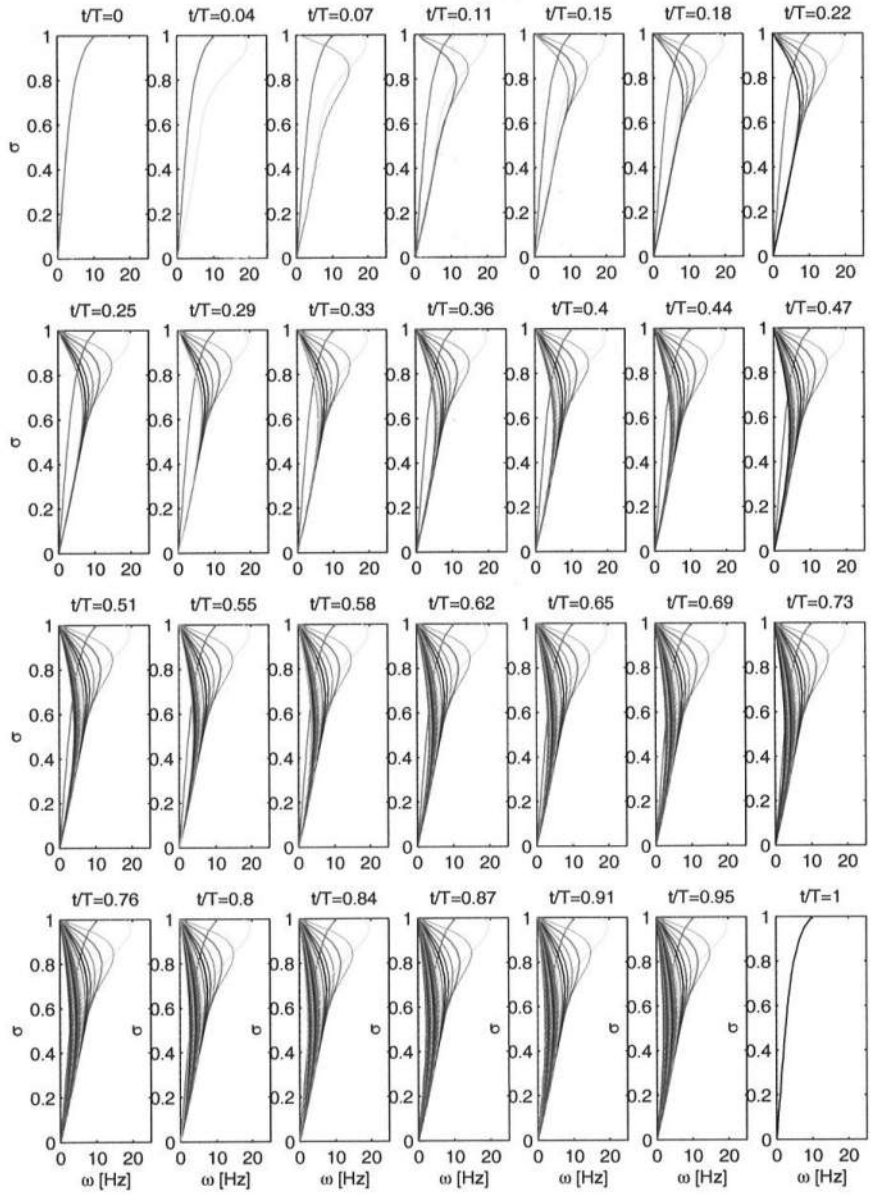

Figure 8.13: Test 3 ($\hat{\nu}_t = 0.010$). History of the vorticity profiles at a section within the transition region during a wave cycle ($t/T = 0$: initiation of breaking).

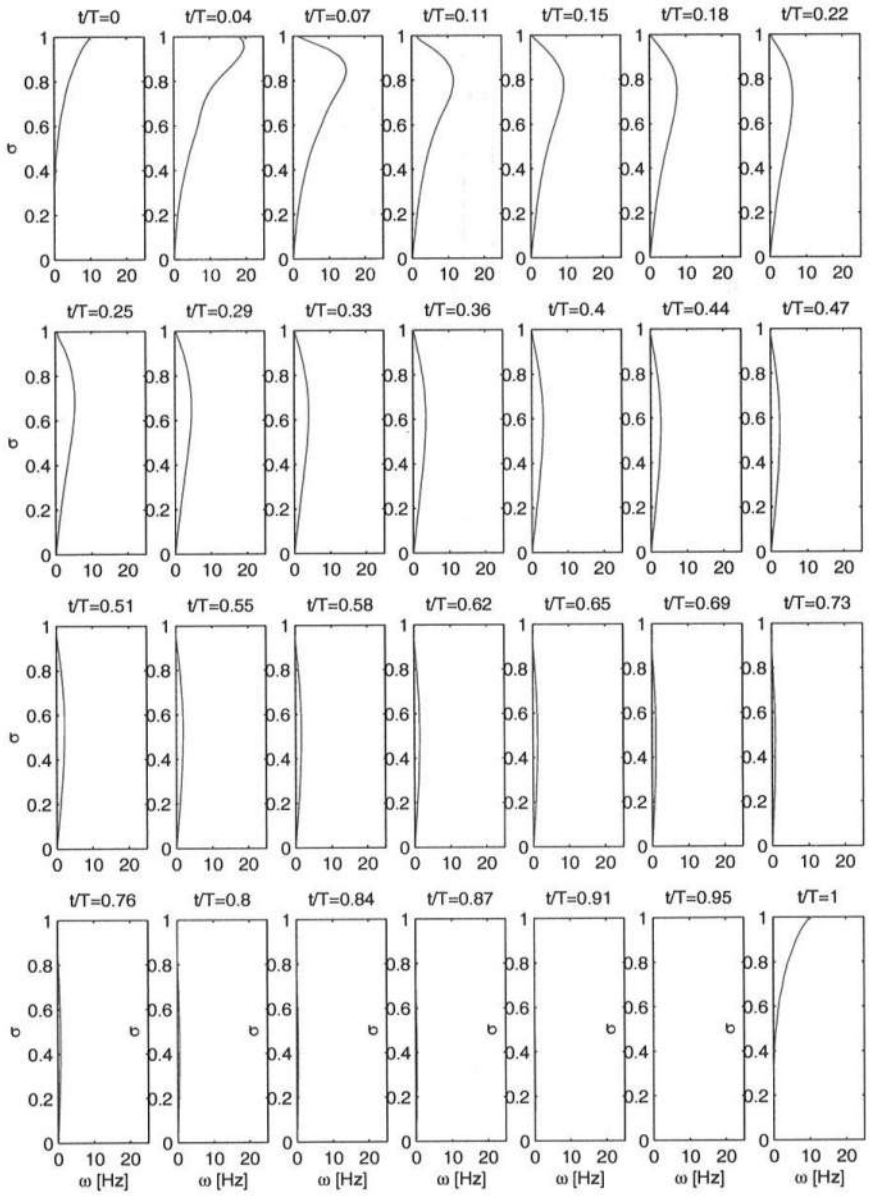

Figure 8.14: Test 3 ($\hat{\nu}_t = 0.010$). Time evolution of the net vorticity profiles at a section within the transition region during a wave cycle ($t/T = 0$: initiation of breaking).

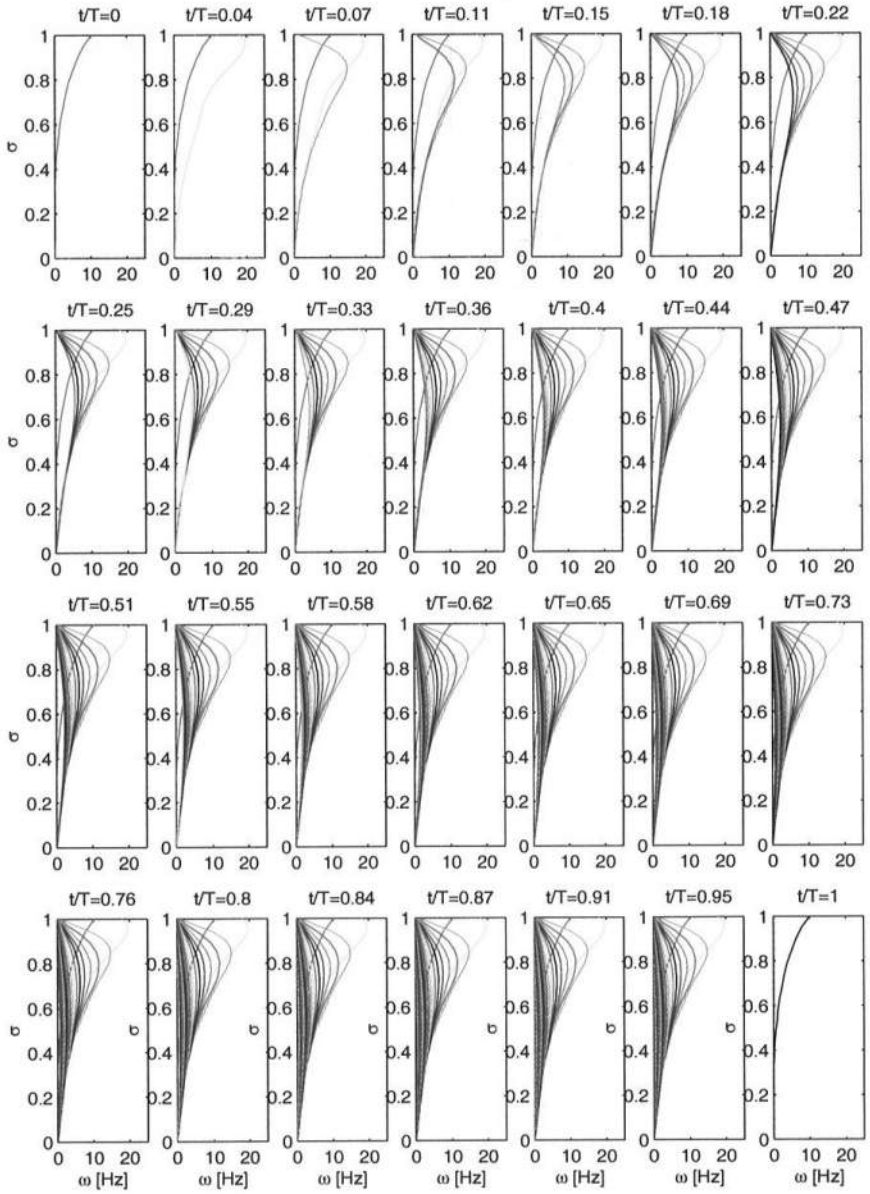

Figure 8.15: Test 3 ($\hat{\nu}_t = 0.010$). History of the net vorticity profiles at a section within the transition region during a wave cycle ($t/T = 0$: initiation of breaking).

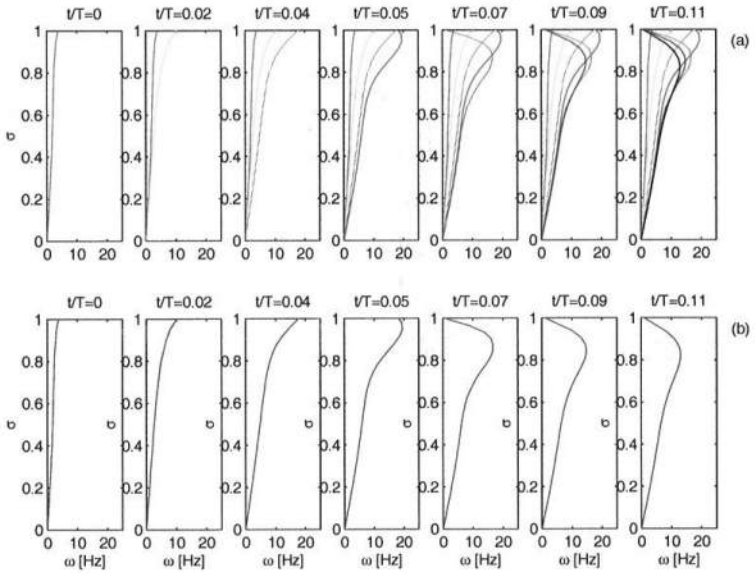

Figure 8.16: Test 3 ($\hat{\nu}_t = 0.010$). (a) History and (b) Time evolution of the vorticity profiles at a section within the transition region ($t/T = 0$: initiation of breaking).

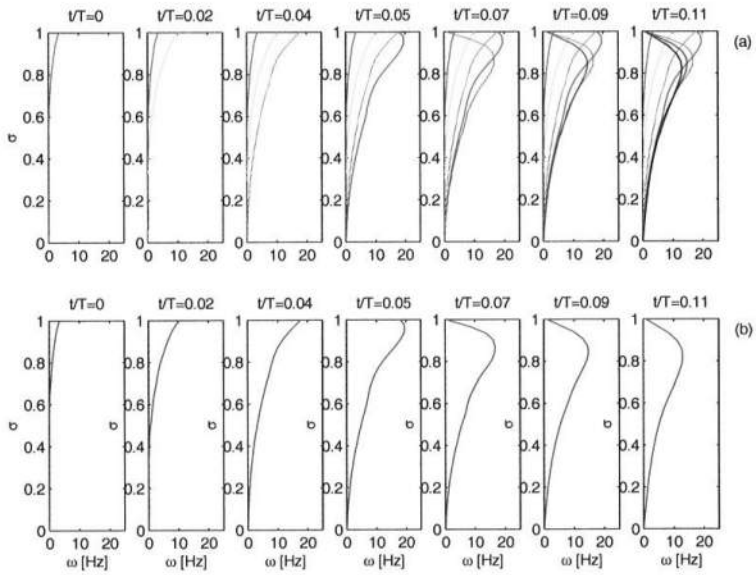

Figure 8.17: Test 3 ($\hat{\nu}_t = 0.010$). (a) History and (b) Time evolution of the net vorticity profiles at a section within the transition region ($t/T = 0$: initiation of breaking).

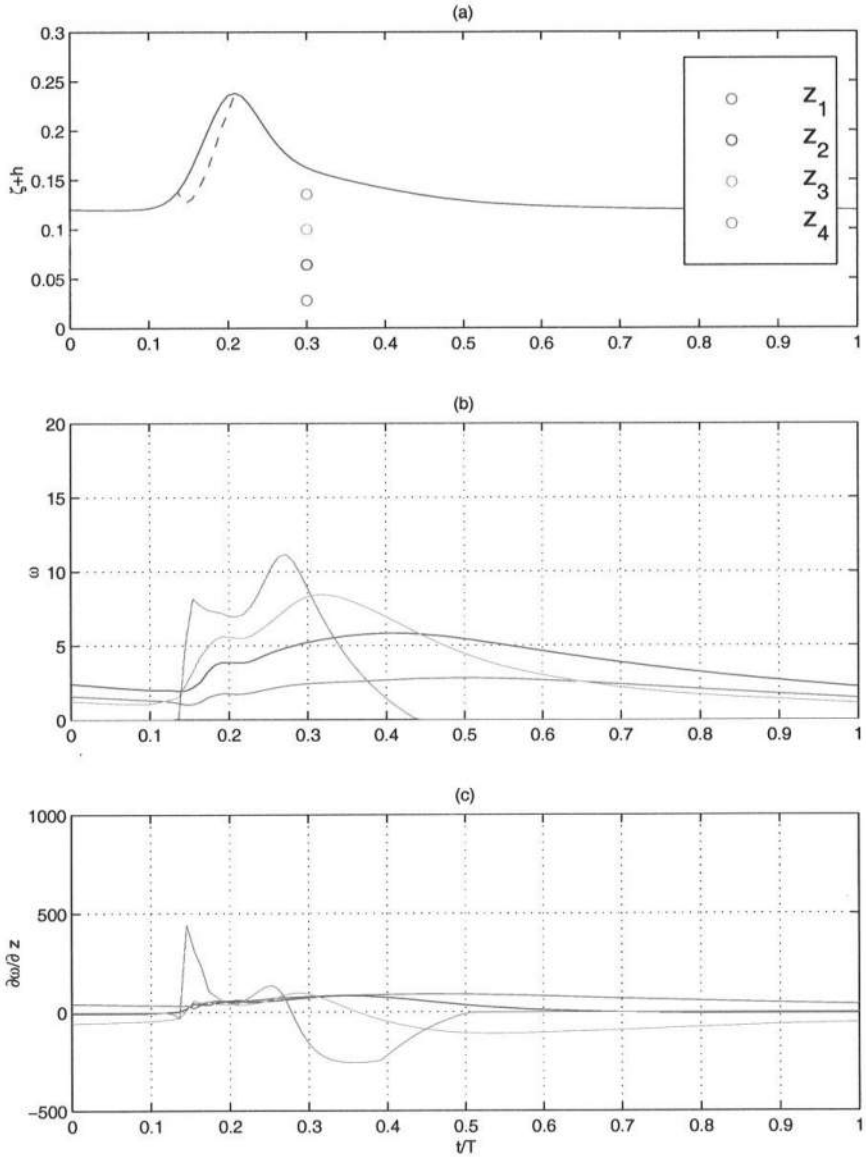

Figure 8.18: Test 3 ($\hat{\nu}_t = 0.010$). (a) Surface elevation, (b) Time variation of vorticity and (c) Time variation of $\frac{\partial \omega}{\partial z}$ at different elevations.

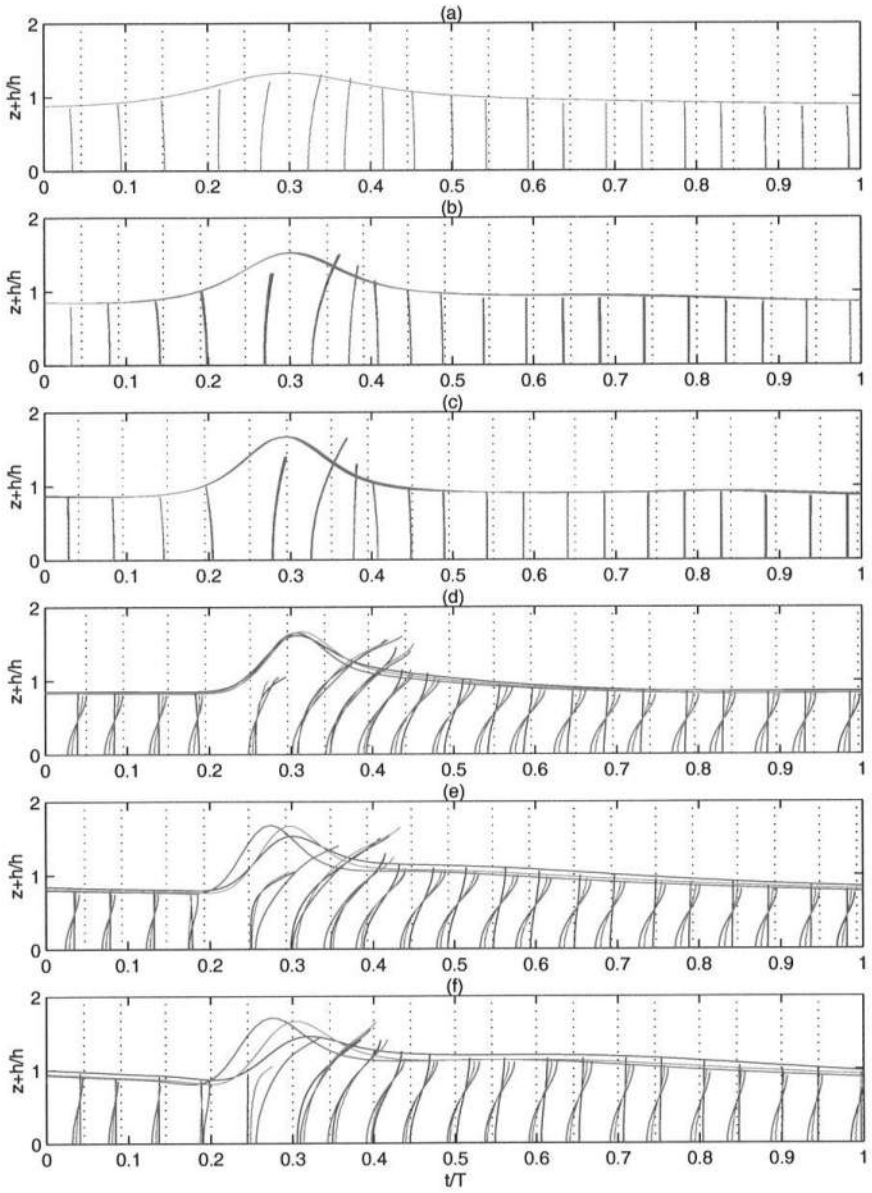

Figure 8.19: Comparisons of the calculated surface and velocity profile for different values of eddy viscosity. Test 1 ($\nu_t = 0.035$): blue solid line ; Test 2 ($\nu_t = 0.005$): red solid line; Test 3 ($\nu_t = 0.010$): green solid line (a) measuring line L1; (b) measuring line L2; (c) measuring line L3; (d) measuring line L4; (e) measuring line L5; (f) measuring line L6

8.2.4 Other results

The effects on the vorticity due to the variation of the eddy viscosity has important consequences on all the other results provided by the model, such as surface elevations, velocities, etc. Here the calculated surface elevation and the velocity profile have been compared when different values of eddy viscosity are adopted (see Figure 8.19). As expected, there are no appreciable differences inside the shoaling zone, while the wave characteristics are strongly affected within the surf zone. Indeed, when the eddy viscosity value is decreased, as the modeled turbulence is weaker, the breaking generated vorticity dissipation, as well as the energy dissipation, are slower. Thus, as a consequence of that, much larger waves are obtained, as the comparisons between the surface profiles in Figure 8.19 shows.

The variation of the eddy viscosity strongly affects also the trend of the horizontal velocity profiles. More specifically, by using smaller eddy viscosity the velocity profiles are more inclined and, in particular, a direction reversal of the horizontal velocity is recovered earlier.

8.3 Suggested values of the eddy viscosity

The previous analysis have shown, as it was expected, that the performances of the proposed model are strongly affected by the chosen value of the eddy viscosity. Indeed, by changing this parameter, it is remarkable that the results on the evolution of the vorticity profiles can be quite different from one another, as a residual vorticity can be left over within the flow ($\nu_t = 0.005$ or $\nu_t = 0.010$) or not ($\nu_t = 0.035$) by the passage of the previous breaking wave. As it has been demonstrated, this, in turn, influences all the model results (surface profile, velocities, etc.). In particular, it has been noticed that for ν_t too small ($\nu_t = 0.005$), the proposed model shows some instabilities. Even though from the comparisons with the velocity profiles it arose that a more realistic eddy viscosity model would be much more suitable, i. e. variable over depth (see for example Section 7.3.3), however, that would prevent from adopting the computationally economic analytic solution for ω and would require a very complicate treatment of the numerical solution of the vorticity transport equation, in order to get an accurate solution. Here, as this simplified model for the eddy viscosity has been used, it can be suggested that, for breaking waves, ν_t should be of the order 10^2, and that smaller values should not be taken into account. Moreover, as even in the suggested range there can be remarkable differences a correct calibration procedure of this parameter has to be considered for the specific case-study.

Chapter 9

Conclusions

This work has been aimed to study the flow driven by breaking waves in the surf zone. Among different numerical approaches to study the hydrodynamics, a new Boussinesq model has been implemented. This model initially started as un updated and debugged version of the existing one by Veeramony and Svendsen (2000, 1999), who removed the usually adopted limiting hypothesis of irrotational flow, in an effort of giving more physical basis to the modelling of the flow within the nearshore region. The studies performed suggested to consider for further enhancements the fully nonlinear version of the aforementioned model, particularly in order to have an improved description of wave characteristics right before breaking occurs. Indeed, as a wave shoals, it acquires highly nonlinear properties, in particular close to the breaking point, in the adopted model no restrictive hypotheses on the order of magnitude of the nonlinear parameter δ have been made. Also, in order to extend the validity of the model toward deeper regions, the dispersive characteristics of the model in deeper waters have been also enhanced by using the methodology proposed by Madsen and Sørensen (1992).

Particular attention has been devoted to the description of the breaking process, which was described here using the well known surface roller approach. Following Veeramony and Svendsen (1999), the coupling of this approach along with the adoption of rotational flow, brought to solve the momentum equation in which so-called breaking terms, which depend on the breaking generated vorticity and then represented the signature of breaking, were present. To model these new terms appropriately, the problem of describing the vorticity as forced by breaking was faced as follows: (i) the vorticity transport equation was solved by assuming the analytical solution obtained by Veeramony and Svendsen (1999) under the hypothesis of a constant eddy viscosity over the depth; (ii) the source of vorticity was assumed to coincide with the lower edge of the surface roller, i.e. the boundary condition which specifies the appropriate amount of vorticity introduced by breaking, was implemented by assuming the hydraulic similarity between the recirculating region of hydraulic jump and the surface roller of a spilling breaking wave.

However, since preliminary analysis did show that the discontinous inclusion

of vorticity at the toe of the roller due to the breaking was not accurately taken into account by the model of Veeramony and Svendsen (1999), a new numerical strategy of solution has been implemented. This new algorithm is based on the adoption of a self-adaptive time varying grid nested inside the uniform fixed grid in the roller region. Two main goals were thus reached: (i) the grid moves following the evolution of the roller, thus refining the position of the crest and of the toe of the roller respectively; (ii) the grid is more refined only right close to the toe of the roller and thus the grid accuracy is independent on the roller length.

The cell celerity was taken into account for the evaluation of the derivatives term. Indeed as the proposed numerical model is more stable, it was also possible to remove the filtering procedure introduced by Veeramony and Svendsen (1999), further increasing the accuracy of the breaking term estimates.

By adopting such a numerical approach, the losses of vorticity observed by using a uniform fixed grid to describe the roller were avoided, and this with a reasonable computational effort.

As regard to the model performances, first of all, the onset of breaking as described by the proposed model was validated. Indeed, the adopted breaking criterion, based on the surface slope (Schäffer *et al.*, 1993), has been validated against the breaking criterion based on the comparisons between the values of the surface velocity and the of wave speed. The advantages of using such a criterion is to avoid any empirical estimates of breaking parameters, such as, for example the critical wave slope or wave height.

The performances of the proposed model where then qualitatively compared with those of a similar model in which the roller was described through a fixed numerical grid, by comparing the vorticity field and the breaking terms. It appeared that the new proposed approach alloed to obatain more reasonable results and particularly a bigger amount of vorticity within the flow and thus higher breaking terms. Indeed, these results were not only consistent with observations of the excess of momentum flux in the hydraulic jump conditions, but the sudden and impulsive effects of the breaking wave was better recovered by the proposed model.

The proposed model results have been then tested against literature data for regular and groupy waves. In most cases also a comparison with the mentioned reference numerical model which uses the fixed grid were also shown.

On the basis of such a comparison, it is possible to state that the new methodology provides more realistic estimates than the previous one especially for what concerns the surface profiles and the wave heights. In particular, inside the surf zone the free surface profile calculated by the proposed model showed more clearly the saw-tooth shape typical of surf zone waves, and the agreement with experimental data of the spatial distribution of the wave height inside the surf zone was improved. Taking the data of Cox *et al.* (1995) on the surface profile, as an example, the error is reduced from about 10% to 3%; while considering the data of Hansen and Svendsen (1979) the error on the wave height prediction is reduced from about 26% (model with a fixed grid) to 14% (proposed model with the moving grid). However, due to the bigger effects of the rotational velocity obtained by using the new numerical strategy, as this velocity component is spread uniformly

over the water column, since it is assumed that the eddy viscosity is constant over depth, the new approach provided profiles of velocity and of undertow different from those of the experimental investigations. These differences were also noticed by applying the model of Veeramony and Svendsen (1999) and could be perhaps overcome by adopting a more realistic eddy viscosity profile (that is by assuming an eddy viscosity profile variable over depth).

The wave speed calculated by the model compares very well with the experimental data of Hansen and Svendsen (1979), in the shoaling and in the surf zone, both for spilling and plunging breakers. It is worth pointing out that the latter situation is outside of theoretical limit of applicability of any Boussinesq model; however not only the magnitude of the predicted phase velocity is the same of that predicted by the model, but also the same scatter observed for this condition in the data is reproduced by the model.

Some interesting conclusions can be drawn also from the comparisons with wave group data. Indeed, not only the time series of the surface profile and the wave height distribution along the domain were predicted in a fairly good manner by the proposed numerical model, but also phenomena such as the conservation of the groupiness after breaking, the change of wave height distribution within the group, the variation of wave length and period and the bore-bore capturing process were recovered by the model results as well as in the data. To give an order of magnitude of the fairly good representativeness of the model, it is worth to stress that inside the inner surf zone, the mean error on the wave height prediction is about 10% on the highest waves of the group. As the individual waves within the groups break at different locations, the prediction of the location of the breaking point was also compared with the one detected during the experiments. It was observed that the model is able to reproduce the same space variability of the breaking point, but it underestimates the breaking point position of the smallest waves of the group of about $1m$, that is about 5% of the length of the domain.

Since, as already mentioned, a weak point of the model results was probably related to the assumption of a constant eddy viscosity over the depth, a sensitivity analysis was performed. It was shown, as expected, that this parameter strongly affects the behavior of the model in terms of the distribution of vorticity over the depth and, in turn, of other results, such as surface and velocity profiles. From the analysis, it turned out that the use of values bigger than $\hat{\nu_t} = 0.005h\sqrt{gh}$ is suggested, in order to avoid numerical instabilities to arise. This analysis thus confirmed the need for treating this parameter in a more physically based way in order to improve the application of such a model as a practical tool for solving engineering problems related to coastal management or to the design of maritime structures.

Appendix A

Adopted finite difference scheme

Let N be the total number of grid points used to discretize the domain, and f be a generic variable:

First order derivatives , accurate up to $O(\Delta x^4)$.

$$(f_x)_1 = \frac{1}{12\Delta x}[-25f_1 + 48f_2 - 36f_3 + 16f_4 - 3f_5] \tag{A.1}$$

$$(f_x)_2 = \frac{1}{12\Delta x}[-3f_1 - 10f_2 + 18f_3 - 6f_4 + f_5] \tag{A.2}$$

$$(f_x)_i = \frac{1}{12\Delta x}[-f_{i+2} + 8f_{i+1} - 8f_{i-1} + f_{i-2}], \quad \text{for } i = 3, 4, ..., N-3, N-2 \tag{A.3}$$

$$(f_x)_{N-1} = -\frac{1}{12\Delta x}[-3f_N - 10f_{N-1} + 18f_{N-2} - 6f_{N-3} + f_{N-4}] \tag{A.4}$$

$$(f_x)_N = -\frac{1}{12\Delta x}[-25f_N + 48f_{N-1} - 36f_{N-2} + 16f_{N-3} - 3f_{N-4}] \tag{A.5}$$

First order derivatives accurate up to $O(\Delta x^2)$. Centered scheme inside the domain:

$$(f_x)_i = \frac{1}{2\Delta x}[f_{i+1} - f_{i-1}] \tag{A.6}$$

One-sided scheme at the boundaries:

$$(f_x)_1 = -\frac{1}{2\Delta x}[3f_1 - 4f_2 + f_3] \quad (A.7)$$

$$(f_x)_N = \frac{1}{2\Delta x}[f_{N-2} - 4f_{N-1} + 3f_N] \quad (A.8)$$

Second order derivatives , accurate up to $O(\Delta x^2)$.

$$(f_{xx})_1 = \frac{1}{(\Delta x)^2}[2f_1 - 5f_2 + 4f_3 - f_4] \quad (A.9)$$

$$(f_{xx})_i = \frac{1}{(\Delta x)^2}[f_{i+1} - 2f_i + f_{i-1}], \quad \text{for } i = 2, 3, ..., N-2, N-1 \quad (A.10)$$

$$(f_{xx})_N = \frac{1}{(\Delta x)^2}[2f_N - 5f_{N-1} + 4f_{N-2} - f_{N-3}] \quad (A.11)$$

Third order derivatives , accurate up to $O(\Delta x^4)$.

$$(f_{xxx})_1 = \frac{1}{(\Delta x)^2}[(f_x)_1 - 2(f_x)_2 + (f_x)_3] \quad (A.12)$$

$$(f_{xxx})_2 = \frac{1}{(\Delta x)^2}[(f_x)_1 - 2(f_x)_2 + (f_x)_3] \quad (A.13)$$

$$(f_{xxx})_i = \frac{1}{2(\Delta x)^3}[f_{i+2} - 2f_{i+1} + 2f_{i-1} - f_{i-2}] \quad \text{for } i = 3, 4, ..., N-3, N-2 \quad (A.14)$$

$$(f_{xxx})_{N-1} = \frac{1}{(\Delta x)^2}[(f_x)_N - 2(f_x)_{N-1} + (f_x)_{N-2}] \quad (A.15)$$

$$(f_{xxx})_N = \frac{1}{(\Delta x)^2}[(f_x)_N - 2(f_x)_{N-1} + (f_x)_{N-2}] \quad (A.16)$$

Appendix B

On the the undertow and the wave volum flux in laboratory and numerical wave tank

In the nearshore region, a shoreward net volume flux is associated to the wave motion. In order to satisfy the conservation of mass, this wave volume flux is balanced by the generation, under trough level, of a current directed offshore, called undertow. When waves are generated in a wave tank, both for laboratory and for numerical wave flumes, the usual initial condition is still water. Then, as the wavemaker starts, together with the waves in the tank a slosh process is generated, having oscillations period much longer than the short waves. The results is that there is not a zero balance until a steady condition is reached.

A brief discussion is presented here to stress the difficulty of computing the undertow and the volume flux according to a wave theory, both from laboratory measurements and numerical calculations. This is mainly due to the definition of the variables itself. Thus, at first, some definitions will be given, then the steady flow case will be considered in order to provide an operational definition of volume flux. Then it will be shown that, by changing the reference system, it is possible to derive some considerations about the definition of the undertow current itself even in the presence of sloshing.

B.1 Definitions

With reference to the scheme reported in Figure B.1, the horizontal velocity u can be split into a mean and an oscillating part as

$$u = u_{mean} + u_w \tag{B.1}$$

where u_{mean} is the velocity averaged over a wave period T and defined as

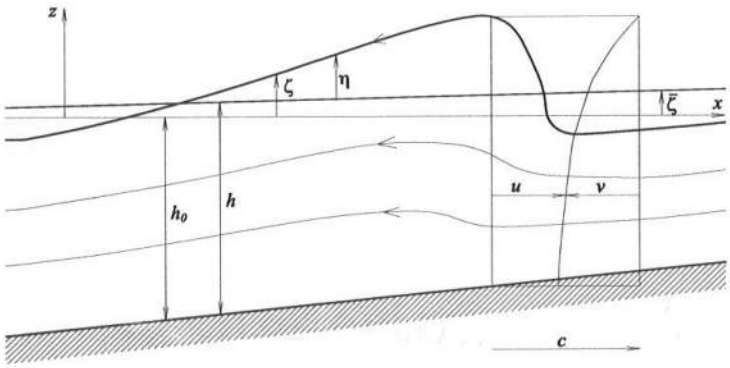

Figure B.1: Adopted reference system

$$u_{mean}(x,y,z) = \frac{1}{T}\int_0^T u(x,y,z,t)dt \tag{B.2}$$

while u_w is the wave velocity, which has to satisfy the following condition

$$\int_0^T u_w dt = 0 \tag{B.3}$$

below the trough level ζ_t. It must be noticed that the reference system used here is the same as before (see Figure B.1), while the adopted symbology is slightly different for notation simplicity. In particular, here the local water depth is indicated as h_0 when is referred to the still water level (which coincides with the x-axis) and h when is referred to the mean water level, that is

$$h = h_0 + \overline{\zeta} \tag{B.4}$$

where $\overline{\zeta}$ is the mean water level.

Moreover, in the case of a laboratory or numerical wave tank to take into account the slosh phenomenon, eq. (B.1) should be rewritten more properly as

$$u = U + U_{slosh} + u_w \tag{B.5}$$

where U is the undertow current directed offshore and U_{slosh} represents the slow oscillation inside the wave tank, generated by the slosh due to the wave motion which starts from a still water condition ($u_{mean} = U + U_{slosh}$). The slosh oscillation is much slower than the wave motion, therefore it may be retained within the definition of the mean flow.

The volume flux is defined instead as

$$Q = \int_{-h_0}^{\zeta} u dz = \int_{-h_0}^{\zeta_t} (u_{mean} + u_w) dz + \int_{\zeta_t}^{\zeta} u dz = \int_{-h_0}^{\zeta_t} u_{mean} dz + \int_{\zeta_t}^{\zeta} u dz \quad \text{(B.6)}$$

In the previous definition, however, u_{mean} can be rigorously defined only below trough level, whether the definition of the same variable above trough level is not trivial, as between ζ_t and ζ there is no water for some time during a wave period.

Moreover the definition of the net volume flux, which is averaged over a wave period, is

$$\overline{Q} = \frac{1}{T} \int_0^T \int_{-h_0}^{\zeta} u dz \quad \text{(B.7)}$$

and, from the last expression, a fictious velocity can be defined as

$$\tilde{V} = \frac{\overline{Q}}{h} \quad \text{(B.8)}$$

It can be defined, but not calculate, the net wave volume flux

$$\overline{Q}_w = \overline{\int_{\zeta_t}^{\zeta} u_w dz} \quad \text{(B.9)}$$

while, from the operational viewpoint, the following quantity $\overline{Q}'_w$

$$\overline{Q}'_w = \overline{\int_{\zeta_t}^{\zeta} u dz} \quad \text{(B.10)}$$

can be instead calculated, which is associated to the volume flux through the following relationship

$$\overline{Q}_w = \overline{Q}'_w - \overline{\int_{\zeta_t}^{\zeta} u_{mean} dz} \quad \text{(B.11)}$$

B.2 Steady flow

If the flow, is steady the net volume flux must be zero, meaning that the wave volume flux must be balanced by a returning flow, the undertow indeed.

$$\overline{Q} = 0 \quad \text{(B.12)}$$

$$\overline{\int_{-h_0}^{\zeta} u dz} = 0$$

$$\overline{\int_{-h_0}^{\zeta_t} u dz} + \overline{\int_{\zeta_t}^{\zeta} u dz} = 0$$

$$\int_{-h_0}^{\zeta_t} u_{mean} dz + u_{mean}(\overline{\zeta} - \zeta_t) + \overline{\int_{\zeta_t}^{\zeta} u_w dz} = 0$$

$$\int_{-h_0}^{\zeta_t} u_{mean} dz + Q'_w = 0 \tag{B.13}$$

B.3 Changing the reference system

In a reference system which moves with the wave at the phase speed c (see Figure B.1) the horizontal velocity seen from this reference system becomes

$$v = u - c \tag{B.14}$$

If there is no net volume flux, that is if $\overline{Q} = 0$, and assuming a wave with quasi-permanent form, it is possible to write the volume flux as

$$Q = \int_{-h}^{\eta} u dz = c\eta \tag{B.15}$$

then in the reference system moving with the wave

$$\int_{-h}^{\eta} v dz = \int_{-h}^{\eta} (u - c) dz = c\eta - c(h + \eta) = -ch \tag{B.16}$$

When there is a nonzero net volume flux ($\overline{Q} \neq 0$) according to Van Dongeren and Svendsen (1997)

$$Q = \int_{-h}^{\eta} u dz = c\eta + \overline{Q} \tag{B.17}$$

then in the moving frame

$$Q = \int_{-h}^{\eta} v dz = \int_{-h}^{\eta} (u - c) dz = c\eta + \overline{Q} - c(h + \eta) = \overline{Q} - ch \tag{B.18}$$

From the previous equation, the depth averaged velocity results

$$\overline{v} \approx \frac{\overline{Q}}{h} - c \tag{B.19}$$

thus recalling the expression for the fictitious velocity $\tilde{V}$ it follows that

$$\tilde{V} = \frac{\overline{Q}}{h} \Rightarrow \tilde{V} \approx \overline{v} + c = u_{mean} \tag{B.20}$$

The equation for the current due to the oscillation in the wave tank is

$$\frac{\partial \frac{\overline{Q}}{h}}{\partial t} = \frac{\partial \tilde{V}}{\partial t} = -\sqrt{gh} \frac{\partial \overline{\zeta}}{\partial x} \tag{B.21}$$

since this current is driven only by the pressure gradient.

Assuming that $\overline{\zeta} << h$, the pressure is hydrostatic and

$$V(z) \approx \tilde{V} \tag{B.22}$$

that is, the current due to the oscillation generated by the slosh inside the wave tank is constant over depth.

B.4 Undertow and wave volume flux

Since the undertow is defined as

$$\tau(z) = \rho\nu\frac{\partial U}{\partial z} \tag{B.23}$$

If the effect of the current $\tilde{V}$, which is constant over depth, is considered, the result due to the undertow is not going to change, indeed

$$\tau(z) = \rho\nu\frac{\partial(U+\tilde{V})}{\partial z} = \rho\nu\frac{\partial U}{\partial z} \tag{B.24}$$

Thus the undertow variation over the water column is not affected by the oscillations (having constant velocity over depth) in the wave tank.

The real undertow should be

$$U_{undertow}(z) = u_{mean} - \frac{\overline{Q}}{h} \tag{B.25}$$

and the wave volume flux

$$Q_w = \overline{\int_{\zeta_t}^{\zeta} u_w dz} = -\int_{-h_0}^{\overline{\zeta}} U_{undertow} dz = \int_{-h_0}^{\zeta_t} \left(u_{mean} - \frac{\overline{Q}}{h}\right) dz \tag{B.26}$$

Acknowledgements

This work was submitted to the University of Catania, Italy as partial fulfillment for the Ph.D. degree in Hydraulic Engineering for Rosaria Ester Musumeci.

The authors gratefully acknowledge for their precious help and suggestions Prof. James T. Kirby, Dr. Jayaram Veeramony and Prof. Maurizio Brocchini.

The project has been funded through a scholarship provided by the Italian Minister of the Education, of the University and Research (MIUR).

Partial financial support was provided also by the "Gruppo Nazionale per la Difesa dale Catastrofi Idrogeologiche" of C.N.R. (Project: Estimation and reduction of the risk in the coastal area), by the Italian Minister of University and Research "Hydrodynamics and Morphodynamics of Tidal forced Environments" and by the SandPit (Contract No. EVK3-CT-2001-00056).

Funding for I. A. Svendsen has been provided by the Office of Naval Research/National Oceanographic Partnership Program (Award No. N00014-99-1-1051).

List of symbols

a	wave amplitude
A	area of the roller region
B	Madsen's constant distinguishing different seto of Boussinesq equations
c	wave speed
c_0	wave speed at a reference location
c_g	group velocity
c_{inst}	instantaneous wave speed
C_ν	experimental parameter of the eddy viscosity model
d	total water depth
d_{50}	median sand diameter
D	energy variation (dissipation if $D < 0$)
D_s	shear stress inside the fluid
D_{uw}	interaction between the waves and the mean flow
D_w	excess of momentum due to the vertical motion
$e_{\overline{u}}$	minimum relative error on the surface elevation
e_ζ	minimum relative error on the depth averaged horizontal velocity
E	total forcing term of the continuity equation
E_f	mean energy flux
E_{fb}	wave energy flux at breaking
f	wave frequency
f_p	peak frequency
F	total forcing term of the momentum equation
F'	forcing term due to spatial variations
F^b	forcing term due to breaking
F^{sp}	dissipation within the sponge layer
F^t	forcing term due to nonlinear time variations
F_r	Froude number
g	gravity accelaration
G	groupiness factor
h	local water depth
h_x	beach slope
h_0	water depth at a reference deep waters
h_1	water depth under the weir

h_2	water depth downstream with respect to the hydraulic jump
H	wave height
H_i	wave height of the ith wave in the group
H_m	mean wave height
H_0	wave height at a reference point
I_r	Irribaren number
k	wave number
k_t	turbulent kinetic energy
k_0	wave number in deep waters
K_c	empyrical constant for sediment transport
K_r	refraction coefficient
K_s	shoaling coefficient
l_r	lenght of the roller
L	wave length
L_0	wave length in deep water
L	Madsen's linear operator to improuve the dispersive properties
n	parameter of the sponge layer
ng	fundamental number of grid subdivisions
N	number of the uniform grid points
p	pressure
P_{ls}	dimensionless longshore transport defined in the CERC-formula
Q	depth integrated velocity or volume flux
Q_w	wave volume flux
Q'_w	operational wave volume flux
$\overline{Q}$	net volum flux over a wave period
$\overline{Q}_w$	net wave volum flux over a wave period
$\overline{Q}'_w$	net operational wave volum flux over a wave period
Q_α	volume flux in the direction α
$\hat{R}_x^S$	horizontal component of the force on the free water surface
$S_{\alpha\beta}$	radiation stress in the α direction across a plane normal to the direction β
S'_{xy}	lateral turbulent stress
t	time in the physical domain
t^*	time in the image domain
T	wave period
T_m	mean wave period of a groupy wave
T_b	duration of the breaking event
u	horizontal velocity
$\mathbf{u}_w$	wave velocity
$\mathbf{u}'$	turbulent velocity
$\boldsymbol{u}$	horizontal velocity vector
$\overline{u}$	depth averaged velocity
u_b	velocity at the bottom
u_{mean}	time averaged velocity
u_p	potential velocity

$\overline{u}_p$	depth averaged potential velocity
u_r	rotational velocity
u_s	velocity at the surface
u_α	horizontal velocity in the direction α
u_α	Nwogu's reference velocity
$u_{w\alpha}$	horizontal wave velocity in the direction α
$u_{w\beta}$	horizontal wave velocity in the direction β
U	undertow current
U_{slosh}	slosh velocity
U_1	average velocity upstream with respect to the jump
$\mathcal{U}$	mean velocity
$\mathbf{U}$	generalized u variable of the momentum equation
U_r	Ursell number
V	longshore current
$\tilde{V}$	fictious velcocity
v	horizontal velocity in a frame moving with the waves
W	dissipation function of the sponge layer
x	horizontal coordinate in the cross-shore direction
x'	x-axis moving at the wave speed
x^*	horizontal coordinate in the image domain
x_c	x-position of the crest
x_g^i	x-position of the point inside the subgrid
x_l	length of the computational domain
x_s	x-position where the sponge layer starts
x_{sp}	dimensionless horizontal coordinate within the sponge layer
x_t	x-position of the toe
x_t^{fixed}	position of the toe onto the fixed grid
y	horizontal coordinate in the longshore direction
z	vertical coordinate
z_α	Nwogu's reference level
$\mathcal{F}$	wave energy flux
α	angle of inclination of a breaking wave
α_b	critical value of the water slope for the onset of breaking
α_0	threshold value of the water slope for the end od breaking
α_1	parameter of the sponge layer
β^+	incoming characteristic at the offshore boundary
β^-	outgoing characteristic at the offshore boundary
δ	nonlinear parameter
$\delta_{\alpha\beta}$	Kroenecker's delta
ΔH	difference between the height of the highest wave and that of the smallest wave of the group
$(\Delta M)_x$	excess of momentum flux due to the vertical variation of the rotational velocity, $O(1)$
$(\Delta M_1)_x$	excess of momentum flux due to the vertical variation of the rotational velocity, $O(\mu^2)$

$(\Delta P)_{xxt}$	contribution to the pressure due to the vertical motion
Δt	uniform time grid step
$\Delta t_{zero-up}$	time for the zero-up crossing point to move from the previous to the next section
Δx	uniform space grid step
Δx_g	interval for the first grid subdivision inside the roller
Δx_{sg}	interval for the finer grid subdivision of the roller
Δ_1	$\delta\zeta - z$
Δ_2	$\delta^2\zeta^2 - \delta\zeta h + h^2$
ζ	surface elevation with respect to the still water level
$\bar{\zeta}$	difference between the mean water level and the still water level
ζ_{cb}	crest elevation at the breaking point
ζ_e	elevation of the lower edge of the roller
ζ_s	thickness of the surface roller
ζ_t	trough elevation
η	surface elevation with respect to the mean water level
θ	angle representing the direction of wave propagation
θ_0	angle representing the direction of wave propagation at a reference location
θ_b	angle representing the direction of wave propagation at the breaking point
κ	ratio between the eddy viscosity and the depth
μ	dispersiveness parameter
ν_t	eddy viscosity
ν_a	Zelt's artificial viscosity
ξ	ratio between h_2 and h_1
ρ	water density
σ	stretched vertical coordinate
τ_b	bottom shear stress
τ_{xx}	normal Reynolds stress in the x direction
τ_{xz}	shear Reynolds stress in the z direction
$\hat{\tau}_x^B$	horizontal component of the force on the bottom
ϕ	velocity potential
ϕ_α	velocity potential at a reference level
ψ	stream function
$\hat{\omega}$	3D vorticity
ω	vertical vorticity
ω_s	vorticity at the lower edge of the roller

List of Figures

List of Tables

References

Abbott, M. B., Damsgaard, A., and Rodenhuis, G. S. (1973). System 21, Jupiter, a design system for two-dimensional nearly horizontal flows. *J. Hydraulic Res.*, **11**, 1–28.

Agnon, Y., Madsen, P. A., and Schäffer, H. A. (1999). A new approach to high order Boussinesq models. *J. Fluid Mech.*, **399**, 319–333.

Battjes, J. A. (1988). Surf-zone dynamics. *Ann. Rev. Fluid Mech.*, **20**, 257–293.

Brocchini, M., Drago, M., and Iovenitti, L. (1992). The modelling of short waves in shallow waters. Comparisons of numerical models based on Boussinesq and Serre equations. In *Proc., 23rd Int. Conf. Coast. Eng.*, pages 76–88, New York. ASCE.

Brocchini, M., Bernetti, R., Mancinelli, A., and Albertini, G. (2001). An efficient solver for nearshore flows based on the WAF method. *Coastal Engineering*, **43**, 105–129.

Carrier, G. F. and Greenspan, H. P. (1958). Water waves of finite amplitude on a sloping. *J. Fluid Mech.*, **4**, 97–109.

Chang, K. A. and Liu, P. L. (1996). Measurements of breaking waves using particle image velocimetry. In *25th Int. Conf. on Coastal Eng.*, volume 1, pages 527–537, Orlando FL. ASCE.

Chen, Q., Kirby, J. T., Dalrymple, R. A., Kennedy, A. B., and Chawla, A. (2000). Boussinesq modeling of wave transformation, breaking and run-up. I: 2D. *J. Waterway, Port, Coastal and Ocean Engng*, **126**, 48–56.

Christensen, E. D., Walstra, D.-J., and Emerat, N. (2002). Vertical variation of the flow across the surf zone. *Coastal Engng.*, **45**, 169–198.

Cox, D. T. and Kobayashi, N. (1997). Kinematic undertow model with logarithmic boundary layer. *Journal of Waterway, Port, Coastal and Ocean Engineering*, **123**(6), 354–360.

Cox, D. T., Kobayashi, N., and Okaiasu, A. (1995). Experimental and numerical modeling of surf zone hydrodynamics. Research report CACR–95–07, Center For Applied Coastal Research, University of Delaware.

Davis, R. A. (1997). *The evolving coast*. Scientific american library.

Deigaard, R. and Fredsøe, J. (1989). Shear stess distribution in dissipative water waves. *Coastal Engng*, **13**, 357–378.

Duncan, J. (1981). An experimental investigation of wave breaking produced by a towed hydrofoil. *Proceedings of the Royal Society London*, **Series A**(377), 331–348.

Duncan, J. (2001). Spilling breakers. *Annu. Rev. Fluid Mech.*, **33**, 519–547.

Emarat, N. and Greated, C. A. (1999). Turbulence study in breaking waves on a beach using PIV. In *Proc. 3rd Int. Workshop on Particle Image Velocimetry*, pages 427–432, Santa Barbara, CA, 16-18 September.

Franco, L. (1996). Hystory of coastal engineering in Italy. In N. C. Kraus, editor, *Hystory and heritage of coastal engineering*, pages 275–335. ASCE.

Galvin, C. J. (1968). Breaker type classification on three laboratory beaches. *J. Geophys. Res.*, **73**, 3651–3659.

Gobbi, M. F. and Kirby, J. T. (1999). Wave evolution over submerged sills:tests of a high order Boussinesq model. *Coastal Engng.*, **37**, 57–96.

Gobbi, M. F., Kirby, J. T., and Wei, G. (2000). A fully nonlinear Boussinesq model for surface waves. Part 2: Extension to $O(kh)^4$. *J. Fluid Mech.*, **405**, 181–210.

Greenberg, M. D. (1988). *Advanced Engineering Mathematics*. Prentice Hall.

Hansen, J. and Svendsen, I. (1984). A theoretical and experimental study of undertow. In *Proc. 19th Int. Conf. on Coast. Eng.*, pages 2246–2262. ASCE.

Hansen, J. B. and Svendsen, I. A. (1979). Regular waves in shoaling water experimental data. Series Paper 21, Institute of Hydrodynamics and Hydraulic Engineering, Technical University of Denmark.

Haydon, T. R., Hann, D. B., Davies, P., Greated, C. A., and Barnes, T. C. D. (1996). Turbulence structures in the surf zone. In *25th Int. Conf. on Coastal Eng.*, volume 1, pages 214–220, Orlando FL. ASCE.

Hibberd, S. and Peregrine, D. H. (1979). Surf and runup on a beach: a uniform bore. *J. Fluid Mech.*, **95**, 323–345.

Iribarren, C. R. and Nogales, C. (1949). Protection des ports, Section II. In *17th Int. Nav. Congr*, pages 31–80, Lisbon.

Jeong, J. H. and Yang, D. Y. (1998). Finite element analysis of transient fluid flow with free surface using VOF (Volume-Of-Fluid) method and adaptive grid. *International Journal for Numerical Methods in Fluids*, **26**, 1127–1154.

Jeong, J. H. and Yang, D. Y. (1999). Three dimensional finite element analysis of transient fluid flow with free-surface using marker surface method and adaptive grid refinement. *International Journal for Numerical Methods in Fluids*, **29**, 657–684.

Jha, A. K., Akiyama, J., and Ura, M. (2001). High resolution flux-difference-splitting scheme on adaptive grid for open-channel flows. *International Journal for Numerical Methods in Fluids*, **36**, 35–52.

Kania, L. (1999). Elliptic adaptive grid generation and area equidistribution. *International Journal for Numerical Methods in Fluids*, **30**, 481–491.

Karambas, T. V. and Koutitas, C. (1992). A breaking wave propagation model based on the Boussinesq equations. *Coastal Engnrng.*, **18**, 1–19.

Keller, J. B. (1963). Tsunamis-water waves produced by earthquakes. In *Int. Union Geod. Geophys. Monogr. 24, Tsunami Hydrodyn. Conf*, pages 154–166, Honululu.

Kennedy, A. B., Chen, Q., Kirby, J. T., and Dalrymple, R. A. (2000). Boussinesq modeling of wave transformation, breaking and run-up. I: 1D. *J. Waterway, Port, Coastal and Ocean Engng*, **126**, 39–47.

Kennedy, A. B., Kirby, J. T., Chen, Q., and Dalrymple, R. A. (2001). Boussinesq-type equations with improved nonlinear performance. *Wave Motion*, **33**, 225–243.

Kennedy, A. B., Kirby, J. T., and Gobbi, M. F. (2002). Simplified higher-order Boussinesq equations I. Linear simplifications. *Coastal Engng.*, **44**, 205–229.

Kinsman, B. (1984). *Wind Waves Their generation and propagation on the ocean surface*. Dover Publications, Inc, second edition.

Kobayashi, N. and Wurjanto, A. (1992). Irregular wave setup and runup on beaches. *J. of Waterway, Port, Coastal and Ocean Engng.*, **118**, 368–386.

Kobayashi, N., DeSilva, G. S., and Watson, K. D. (1989). Wave transformation and swash oscillation on gentle and steep slopes. *J. Geophys. Res.*, **C1**, 951–966.

Lie, K.-A., Haugse, V., and Hvistendahl Karlsen, K. (1998). Dimensional splitting with front tracking and adptive grid refinement. *Numerical Methods for Partial Differential Equations*, **14**(5), 627–648.

Lin, J. C. and Rockwell, D. (1994). Istantaneous structure of a breaking wave. *Phys. Fluids*, **6**(9), 2877–2879.

Lin, J. C. and Rockwell, D. (1995). Evolution of a quasi-steady breaking wave. *J. Fluid Mech.*, **302**, 29–44.

Liu, P. L.-F. (1995). Model equations for wave propagations from deep to shallow water. In P. L.-F. Liu, editor, *Advances in Coastal and Ocean Engineering*, volume 1, pages 125–157. World Scientific, Singapore.

Longo, S., Petti, M., and Losada, I. J. (2002). Turbulence in the swash and surf zones: a review. *Coastal Engineering*, **45**, 129–147.

Longuet-Higgins, M. S. (1970). Longshore currents generated by obliquely incident sea waves, 1. *J. Geophys. Res.*, **75**, 6778–6801.

Madsen, P. and Schäffer, H. A. (1998). A review of Boussinesq-type equations for gravity waves. In P. L.-F. L. (Ed.), editor, *Advances in Coastal and Ocean Engng*, volume 5, page 90. World Scientific, Singapore.

Madsen, P. A. and Sørensen, O. R. (1992). A new form of the Boussinesq equations with improved linear dispersion characteristics: Part 2. A slowly varying bathymetry. *Coastal Engng.*, **18**, 183–204.

Madsen, P. A., Murray, R., and Sørensen, O. R. (1991). A new form of the Boussinesq equations with improved linear dispersion characteristics. *Coastal Engng.*, **15**, 371–388.

Madsen, P. A., Sørensen, O. R., and Schäffer, H. A. (1997). Surf zone dynamics simulated by a Boussinesq type model. Part I. Model description and cross-shore motion of regular waves. *Coastal Engng.*, **32**, 255–287.

Melville, W. K., Veron, F., and White, C. J. (2002). The velocity field under breaking waves: coherent structures and turbulence. *J. Fluid Mech.*, **454**, 203–233.

Miche, R. (1944). Mouvements ondulatoires de la mer en profondeur constante ou décroissante. *Ann. Ponts Chaussées*, **114**, 25–78,131–164,270–292,369–406.

Nadaoka, K., Hino, M., and Koyano, Y. (1989). Structure of the turbulent flow field under breaking waves in the surf zone. *J. Fluid Mech.*, **204**, 359–387.

Nwogu, O. (1993). Alternative form of Boussinesq equations for nearshore wave propagation. *J. Waterway, Port, Coast. and Ocean Eng.*, **119**(6), 618–638.

Packwood, A. (1983). The influence of beach porosity on wave uprush and backwash. *Coastal Engineering*, **7**, 29–40.

Packwood, A. and Peregrine, D. H. (1980). The propagation of solitary waves and bores over a porous bed. *Coastal Engineering*, **3**, 221–242.

Papadakis, G. and Bergeles, G. (1999). A local grid refinement method for three-dimensional turbulent recirculating flows. *International Journal for Numerical Methods in Fluids*, **31**, 1157–1172.

Park, K.-Y. and Borthwick, A. G. (2001). Quadtree grid numerical model of nearshore wave-current interaction. *Coastal Engineering*, **42**, 219–239.

Peregrine, D. H. (1966). Calculations of the development of an ondular bore. *J. Fluid Mech.*, **25**, 321–331.

Peregrine, D. H. (1967). Long waves on a beach. *J. Fluid Mech.*, **27**, 815–827.

Peregrine, D. H. (1972). Equations for water waves and the approximation behind them. In R. E. Meyer, editor, *Waves on Beaches and the resulting sediment transport*, pages 95–121, New York. Academic Press.

Peregrine, D. H. (1983). Breaking waves on beaches. *Ann. Rev. Fluid Mech.*, **15**, 149–178.

Peregrine, D. H. (2002). Waves on beaches: modelling surf and swash. In *SIMAI 2002, VI National Congress*, Chia Laguna (Italy).

Peregrine, D. H. and Svendsen, I. (1978). Spilling breakers, bores and hydraulics jumps. In *16th Proceedings of the Coastal Engineering Conference*, 30, pages 540–550.

Press, W. H., Flannery, B. P., Teukolsky, S. A., and Vetterling, W. T. (1992). *Numerical recipes in Fortran (2nd ed.)*. Cambridge University Press.

Schäffer, H. A., Madsen, P. A., and Deigaard, R. (1993). A Boussinesq model for waves breaking in shallow water. *Coastal Engng*, **20**, 185–202.

Spitaleri, R. M. and Corinaldesi, L. (1997). A multigrid semi-implicit finite difference method for the two dimensional shallow water equations. *International Journal for Numerical Methods in Fluids*, **25**, 1229–1240.

Svendsen, I. A. (1984). Wave heights and set-up in a surf zone. *Coastal Engineering*, **8**, 303–329.

Svendsen, I. A. (2003). Hydrodynamics of the surf zone. In *International Handbook of Coastal Engineering and Management*. A. Watanabe, M. Isobe and N. Kraus, Academic Press. (in press).

Svendsen, I. A. and Putrevu, U. (1994). Nearshore mixing and dispersion. *Proceedings of the Royal Society London A*, **445**, 561–576.

Svendsen, I. A. and Putrevu, U. (1995). Surf-zone hydroddynamics. In P. L.-F. Liu, editor, *Advances in Coastal and Ocean Engineering*, volume 2, pages 1–78. World Scientific, Singapore.

Svendsen, I. A. and Veeramony, J. (2001). Wave breaking in wave groups. *J. Waterway, Port, Coastal and Ocean Engng*, **127**, 200–212.

Svendsen, I. A., Madsen, P. A., and Hansen, J. B. (1978). Wave characteristics in the surf zone. In *Proc. 16th Coast. Eng. Conf.*, volume I (Chap. 29), pages 520–539, Hamburg.

Svendsen, I. A., Veeramony, J., Bakunin, J., and Kirby, J. (2000). The flow in weak turbulent hydraulic jump. *J. Fluid Mech*, **418**, 25–57.

Thornton, E. B. (1979). Energetics of breaking waves within the surf zone. *J. Geoph. Res.*, **84**(C8), 4931–4938.

Ting, F. C. K. and Kirby, J. T. (1994). Observation of undertow and turbulence in laboratory surf zone. *Coastal Engng.*, **24**, 51–80.

Ting, F. C. K. and Kirby, J. T. (1995). Dynamics of surf-zone turbulence in a strong plunging breaker. *Coastal Engng.*, **24**, 177–204.

Ting, F. C. K. and Kirby, J. T. (1996). Dynamics of surf-zone turbulence in a spilling breaker. *Coastal Engng.*, **27**, 177–204.

Van Dongeren, A. R. and Svendsen, I. A. (1997). Absorbing-generating boundary condition for shallow water models. *J. of Waterway, Port, Coast. and Oc. Engnrg*, **123**(6), 303–313.

Veeramony, J. and Svendsen, I. A. (1999). Modeling the flow in surf zone waves. Research report CACR –99–04, Center for Applied Coastal Research, University of Delaware.

Veeramony, J. and Svendsen, I. A. (2000). The flow in the surf-zone waves. *Coastal Engineering*, **39**, 93–122.

Wei, G., Kirby, J. T., Grilli, S. T., and Subramanya, R. (1995). A fully nonlinear Boussinesq model for surface waves. I. Highly non linear, unsteady waves. *J. Fluid Mech*, **294**, 71–92.

Witting, J. M. (1984). A unified model for the evolution of nonlinear water waves. *J. Comput. Phys.*, **56**, 203–236.

Wu, J., Ritzdorf, H., Oosterlee, K., Steckel, B., and Scüller, A. (1997). Adaptive parallel multigrid solution of 2D incompressible Navier-Stokes equations. *International Journal for Numerical Methods in Fluids*, **24**, 875–892.

Yeh, H. and Mok, K. (1990). On turbulence in bores. *Physics of Fluids*, **2**, 821–828.

Zelt, J. A. (1991). The run-up of nonbreaking and breaking solitary waves. *Coastal Engng.*, **15**, 205–246.